Fluorescence Spectroscopy as a Technique for Diagnosis of Pathologic Conditions in Human Arterial, Urinary Bladder, and Gastro-Intestinal Tissues

by

Rebecca Rae Richards-Kortum

M.S., Physics
Massachusetts Institute of Technology
(1987)

B.S., Physics and Mathematics
University of Nebraska, Lincoln
(1985)

SUBMITTED TO THE DEPARTMENT OF
HEALTH SCIENCES AND TECHNOLOGY
IN PARTIAL FULFILLMENT OF THE
REQUIREMENTS FOR THE DEGREE OF
DOCTOR OF PHILOSOPHY IN MEDICAL PHYSICS

at the
Massachusetts Institute of Technology
June, 1990

Signature of Author: _____
Department of Health Sciences and Technology
May 4, 1990

Certified by: _____
Michael S. Feld
Professor, Department of Physics
Thesis Supervisor

Accepted by: _____
Roger Mark, Co-Director
Department of Health Sciences and Technology

Fluorescence Spectroscopy as a Technique for Diagnosis of Pathologic Conditions in Human Arterial, Urinary Bladder, and Gastro-Intestinal Tissues

by

Rebecca Richards-Kortum

Submitted to the Department of Health Sciences and Technology
on May 4, 1990 in partial fulfillment of the requirements for the
Degree of Doctor of Philosophy in Medical Physics

ABSTRACT

This thesis presents a method for developing fluorescence based diagnostic algorithms for pathologic conditions which can be applied *in vivo* in real time. This method is illustrated for two diseases - atherosclerosis and neoplasia - in three model systems: atherosclerosis in human aorta and coronary artery, transitional cell carcinoma in human urinary bladder and adenomatous polyps in human colon. The method of algorithm development presented is stepwise. Fluorescence excitation-emission matrices are first used to identify excitation regions optimal for the differentiation of normal and pathologic tissues. At these excitation wavelengths, the morphologic and molecular basis of tissue fluorescence are determined using a combination of fluorescence and light microscopy, and studies of individual biomolecules. A model of tissue fluorescence is presented which relates tissue physico-chemical composition to fluorescence spectra. The parameters of this model are then used to develop statistically optimized diagnostic algorithms for the presence of pathology. Finally, *in vivo* trials of these techniques are undertaken, to begin to assess their role in clinical medicine.

Thesis Supervisor: Michael Feld, PhD

Title: Professor, Dept. of Physics

Table of Contents

Acknowledegements:

Many people deserve to be recognized for their contributions to this thesis. Several members of the LST and LAS groups at MIT and the Cleveland Clinic Foundation, including Gary Hayes, Joe Baraga, Rim Cothren, Robert Petras, Howard Levin, John Kramer and Michael Sivak, made important contributions to this work. The members of my thesis committee spent much time discussing my results and conclusions with me and improving drafts of my thesis.

There are several people without whose help and encouragement this thesis would not exist. Carter Kittrell introduced me to this project and helped me through the first two years of graduate school and research. Maryann Fitzmaurice taught me immeasurable amounts about pathology and fluorescence microscopy, and always provided thoughtful comments about research in progress. Rich Rava devoted many hours to this project, teaching me about molecular spectroscopy and working with me to achieve a quantitative interpretation of tissue spectra. Michael Feld provided enthusiasm and guidance in setting the directions for this research. More than anyone, he helped me to develop confidence as a scientist. Finally, throughout the last five years, Phil and the Vic-man were always there to help me to keep things in perspective. Thanks.

1: Introduction and Overview

1:1: Ultimate Goal: Developing *in vivo* Methods of Histochemistry

The diagnosis of disease is more and more becoming a technological task. The clinician's goal is to assess the structural and functional changes in diseased tissue, infer the identity and stage of the disease, and predict the ultimate consequences to the organism as a whole, intervening with the proper treatment whenever possible [1].

The diagnostic ordnance varies both for the suspected disease and with the specialty of the clinician. Radiologists, for example, assess gross structural abnormalities utilizing variations in tissue or contrast agent absorption of x-rays [2]. Similar information can be obtained from sonograms, due to variations in tissue reflection of ultra-sonic waves [2]. This structural information, although useful diagnostically, provides limited insight into the chemical and molecular etiology and pathogenesis of the disease, factors that are now appreciated to be important prognostically and in selecting appropriate therapy [1]. Magnetic resonance (MR) spectroscopy has the potential of demonstrating this chemical information in the living patient; however, there are several technical barriers to overcome before this technique is a clinical reality [3].

Pathology provides the most widely used clinical method of elucidating chemical information from diseased tissues [1, 4]. Traditional techniques of histology can be used to probe the microscopic structural alterations of diseased tissue [1]. Utilizing histochemical stains, many of the corresponding chemical alterations accompanying disease can be mapped on a microscopic scale [4]. The chief disadvantage of these techniques is that they can only be applied *in vitro*, necessitating the removal of tissue [1, 4]. The requirement of biopsy limits the utility of this approach; it implies that, using histologic techniques, only small areas of tissue, accessible either to biopsy forceps or needles, can be sampled.

A more useful diagnostic technique would combine the advantages of pathologic and radiologic methods, allowing for real time imaging of tissue *in vivo* to extract diagnostically relevant structural and histochemical information. Tissue fluorescence spectroscopy is a new technique in the field of medical diagnostics which may ultimately provide these features at a lower cost and level of technology compared to that of MR spectroscopy [5-10].

Fluorescence spectroscopy has long been an important tool in analytical chemistry; no other non-destructive methods available at comparable cost can equal fluorimetry in analytical sensitivity. Concentrations of fluorescent materials as low as 10^{-9} molar can be routinely determined [11]. This sensitivity is particularly utilized in biomedical applications to monitor, for example, low concentrations of fluorescent metabolites [12]. The emergence of fiber optic technology, however, has enabled the development of remote sensing and monitoring systems based on fluorescence spectroscopy [13]. This technology has been applied to such diverse fields as the remote detection of air pollution [14], where three dimensional mapping of air pollutants in real time has been achieved [15].

Fiber optic technology is routinely used in medicine. Fiber-optic endoscopy is a recently developed screening method for identifying epithelial or mucosal tumors in the interior of hollow organs, such as the colon and urinary bladder [16]. Similarly, fiber-optic angioscopy is utilized to view atherosclerotic obstructions in blood vessels [17]. These systems utilize the reflection of white light to identify gross architectural changes associated with pathology [16, 17]. Their limitations are similar to those of radiologic methods described above; with these techniques, documentation of the microscopic or biochemical changes associated with disease is currently not possible without biopsy.

We are developing a new, endoscope-compatible, diagnostic technique which can be used to screen the entire surface of a hollow organ for both the gross and microscopic structural and biochemical changes associated with disease without the need for biopsy [18]. This method is based on fluorescence spectroscopy, which can yield information about the physico-chemical composition of tissue [5]. Our technique would combine the advantages of endoscopic methods - the gross architectural changes associated with disease could be visualized with reflected white light - with those of biopsy and histochemistry - the microscopic and biochemical alterations could be probed with fluorescence. The resulting system would provide a method of obtaining correlated gross structural and histochemical information for the identification of disease *in vivo* in real time without the need for biopsy [18].

Such a system could be easily adapted to incorporate the capability for laser surgery, which is rapidly becoming an important treatment modality for atherosclerosis [19] and many mucosal tumors [20]. Thus, such a system could ultimately provide both

real-time diagnosis of disease and guidance of its treatment via interactive spectroscopic feedback.

This thesis considers a central problem in the development of such a system. Herein is presented a general method for developing fluorescence based algorithms for real time diagnosis of disease *in vivo*. The method is based on steady state fluorescence and absorption spectroscopy in the ultra-violet (UV) and visible regions of the spectrum. The development of this method, its general features, and its utility are illustrated with three specific examples in which a clinically useful diagnostic algorithm for the presence of pathology is developed.

1:2: Clinical Problems Addressed in this Work

The clinical problems addressed in this work include the development of diagnostic algorithms for atherosclerosis in human arteries, and for neoplasia in the human colon and urinary bladder. These conditions and the rationale for selecting them are briefly reviewed here.

1:2.1: Spectroscopic Determination of Chemical Composition of Atherosclerotic Lesions *in vivo*: Applications in Cardiology

1:2.1.1. Brief Review of Clinical Considerations

Atherosclerosis is a disease of medium sized and large arteries, in which progressive narrowing of the arterial lumen occurs as atherosclerotic lesions form in the arterial intima [21]. The most commonly affected arteries include the aorta and those of the coronary and cerebral systems [21, 22]. In the coronary arteries, a primary result of atherosclerosis is compromised blood flow to the heart, the consequences of which can be particularly severe, including myocardial infarction [21, 22]. Current estimates indicate that approximately 25% of deaths in the US can be attributed to coronary atherosclerosis [21, 22].

Symptoms of coronary artery disease (CAD) are produced by the resulting imbalance of myocardial oxygen supply and demand [22]. Therapies of CAD are therefore directed towards restoring this balance [22, 23]. This can be achieved in primarily two ways:

• reducing the mechanical workload of the heart, thus reducing its oxygen demand, or

• augmenting myocardial blood flow; thus increasing oxygen supply [23].

The first goal can be achieved primarily through medical management of CAD, using drugs such as nitrates and calcium channel blockers. These drugs work chiefly by relaxing vascular smooth muscle, reducing venous return, and thus reducing the workload of the heart [23]. These drugs also relax the smooth muscle in the media of the coronary arteries, resulting in arterial dilatation, increasing both coronary blood flow and myocardial oxygen supply [23].

Many therapies have been designed with the goal of bypassing, reducing or removing the atherosclerotic lesions which can obstruct coronary blood flow. Three of these will be discussed here. A major interventional form of treatment for CAD is coronary artery bypass grafting (CABG) [24]. In this procedure, coronary revascularization is achieved via either a venous or arterial bypass [24].

CABG is a major surgical procedure; associated mortality rates vary from center to center and with patient risk factors; overall rates of 1-3% are routinely reported [25]. Despite this risk, it is clear that CABG is superior to medical therapy in relieving symptoms and signs of severe myocardial ischemia [24]. Five year survival rates are significantly higher for surgically treated patients with severe ischemia than for those treated medically [24]. The mortality of mildly symptomatic patients treated surgically is not significantly lower than that for medically treated patients; however, quality of life, as measured by complete relief of chest pain and improvement in functional status, is superior for surgically treated patients [25]. It is clear, however, that CABG is not a curative operation, but merely palliative. Atherosclerosis and intimal fibroplasia progress in the grafted vessels, and as a result of this progression, eventually the benefits of surgery are eliminated [24, 26].

Early restenosis (within one year of CABG), although unusual, does occur, and is influenced by the coronary artery grafted, and the presence of angina [27]. During 1-5 years following CABG, the rate of restenosis is quite low; however, after this time period, the rate of restenosis following CABG increases [27]. Restenosis is more frequent in vein than arterial grafts; one study reported significant restenosis or occlusion in 44% of 786 vein grafts at a mean follow up of 88 months [27]. In contrast, only 5%

of 135 arterial grafts were stenotic or occluded within this time period [27]. Several risk factors have been associated with the occurrence of late restenosis, including time following CABG, myocardial infarction, angina, diabetes, hypercholesterolemia, and hypertriglyceridemia [27-29]. Lower high density lipoprotein levels, and cigarette smoking have also been correlated to increased frequency of late restenosis [28]. Hypertension has been correlated to the progression of intimal fibroplasia in grafts [29, 30]. Many of these risk factors have been previously identified as important risk factors for the initial development of atherosclerosis [21, 22].

In addition, several risk factors have been associated with greater early and late mortality following CABG, including single or multi-vessel disease in which lumen diameter is reduced by more than 50%, female gender, age, diabetes, and incomplete revascularization [31]. Many of the risk factors for mortality and restenosis can be assessed prior to CABG, and controlled with appropriate medical therapy [31].

Another major therapy for CAD is percutaneous transluminal coronary angioplasty (PTCA) [23]. In this procedure a balloon tipped catheter is introduced via a peripheral vessel and advanced to the site of obstruction [32]. Inflation of the balloon causes rupture of the plaque and dilatation of the remaining artery wall, allowing increased blood flow, even though the plaque has not been removed [32].

Although PTCA is less invasive than CABG, and is successful in increasing coronary lumen diameter in over 90% of cases [33], there are currently several significant complications associated with PTCA. Two of these are restenosis and abrupt reclosure [33, 34]. Restenosis after successful PTCA occurs in 20 to 40% of patients [34 - 36]. Typically this restenosis occurs by 4 to 6 months following the procedure; long-term studies indicate that the incidence of restenosis after 12 months is small [35, 37]. Currently, no alterations in PTCA technique or pharmacologic management have proved effective in decreasing this incidence of restenosis [35]. The mechanism of restenosis appears to be arterial trauma at the site of PTCA, resulting in platelet adhesion and subsequent activation of the tissue injury response [35, 36].

There are certain predisposing characteristics of patients who experience restenosis: male gender [38], lesions greater than 15 mm in length [38], and cigarette smoking have all been associated with a higher frequency of restenosis [39]. Despite these correlations, it has not been possible to predict accurately which patients who undergo angioplasty will develop restenosis [40]. Laboratory tests related to lipoprotein

metabolism, coagulation, and platelet function, factors which influence the development of coronary atherosclerosis, did not correlate to the development of recurrent restenosis following PTCA in one study of over 400 patients [40]. In studies at autopsy, atherosclerotic plaque composition has been strongly correlated to the development of restenosis; the ideal coronary arterial atherosclerotic narrowing for clinically successful PTCA appears to be one in which the plaque contains relatively little calcium and extracellular lipid [41]. Unfortunately, no reliable methods of assessing plaque composition *in vivo* exist.

The standard method for evaluating the location and severity of arterial atherosclerosis is x-ray angiography [42]. In this technique, the ostium of each main coronary artery is selectively catheterized by a specially designed catheter introduced percutaneously. Upon catheterization, radio-opaque contrast material is injected into the coronary artery, which is then visualized using an external fluoroscopic viewing system [43]. With this technique, the percent narrowing of the lumen diameter due to focal atherosclerosis can be estimated [42, 43]. However, this technique images primarily the contrast medium, rather than the artery, and thus provides little information about lesion composition [42]. The exception is that severely calcified lesions, which may be radio-opaque, can sometimes be recognized [42, 43].

Several more recently developed techniques for imaging atherosclerotic obstructions include angioscopy [44], ultrasound [45] and magnetic resonance imaging (MRI) [46]. Of these, only MRI has the potential to give information about both the gross architecture and chemical composition of atherosclerosis. Because of limitations on sensitivity and the fact that the heart is in constant motion, imaging of the coronary arteries themselves has not yet been accomplished with this technique [46]. Thus, with any of the currently available imaging techniques, little information can be obtained about the morphologic or molecular composition of the atherosclerotic plaque.

A second major limitation of PTCA is abrupt reclosure. With current techniques of PTCA, acute closure after an initially successful dilatation occurs in 2 to 6% of attempts [47, 48]. Yet, this phenomenon is the major cause of morbidity and mortality in this procedure [47]. Risk factors for closure include female gender, unstable angina, multi-vessel disease, stenosis at a bend or branch point, lesion calcification and lesion length [47]. Although many of these risk factors can be assessed angiographically, more accurate methods of predicting those patients at risk for abrupt reclosure would reduce the mortality associated with PTCA.

Thus, CABG and PTCA both represent effective methods of treatment for CAD, in which the deficit in myocardial oxygen supply is corrected by increasing coronary blood flow. Although PTCA is associated with more complications, it is a less invasive, better tolerated procedure [48]. For these reasons, PTCA remains the therapy of choice for patients with early, discrete obstructions in single vessels [49]. It is within this subset of patients that the complications of PTCA are minimal. For patients with severe ischemia, particularly those with complete or near complete single or multi-vessel obstructions, CABG remains the preferred therapy [49]. One drawback of both procedures is that neither can be used to effectively treat diffuse atherosclerosis [50]. In fact, it is believed that the many discrepancies between experimental results of these techniques in animal studies and clinical applications in patients are due to the absence of diffuse coronary atherosclerosis in animals and its variable presence in patients [50].

A better treatment of atherosclerosis would combine the percutaneous approach of PTCA, the wide range of applicability and lower restenosis rate of CABG, and the ability to treat diffuse atherosclerosis. Although still in the experimental stage, it appears that the technique of laser angiosurgery (LAS), the treatment of atherosclerosis with laser radiation via fiber optic catheters, may provide these important advantages [51-60]. In this method of treatment, a catheter containing optical fibers is inserted percutaneously through a peripheral vessel and advanced to the site of the obstruction. Laser radiation is delivered to the blockage site via the optical fibers, vaporizing the atherosclerotic plaque and restoring lumenal patency [51-60].

Unlike PTCA, which redistributes atherosclerotic plaque and CABG, which bypasses atherosclerotic obstructions, LAS removes plaque. By reducing the bulk of the obstruction, and leaving behind a smooth vascular surface, LAS has the potential to reduce the restenosis rate associated with PTCA [51]. Studies of LAS in animal models indicate that thrombogenesis is minimal at the site of treatment, with re-endothelialization occurring within two weeks [52]. As a percutaneous procedure, LAS potentially would have many of the same advantages as PTCA. Furthermore, complete obstructions and diffuse disease could be treated using this procedure, with the catheter being advanced as the lumen is cleared [53].

Vaporization of atherosclerotic plaque can be accomplished with minimal damage to surrounding tissue using relatively low fluences of light from many laser sources [54]. Unfortunately, these lasers are also capable of vaporizing healthy artery wall; thus, the

risk of perforation of the arterial wall is a serious complication of LAS [51-60]. Early use of a bare optical fiber catheter to recanalize coronary arteries under direct vision during CABG resulted in one perforation in five attempts [55]. Subsequent improvements in catheter technology have resulted in better performance [60]; however, perforation is still a significant problem associated with LAS.

1.2.1.2. Fluorescence Spectroscopy in the Management of CAD

It is our belief that fluorescence spectroscopy may ultimately impact on and improve each of these treatments for CAD. It has been suggested by many groups that fluorescence spectroscopy may be used to provide a guidance system for LAS catheters and significantly reduce the risk of perforation [5-8, 95-99]. These groups have shown that there are significant differences in the fluorescence spectra of normal and atherosclerotic vessel wall which can be exploited in the diagnosis of atherosclerosis. Incorporating the capability to record fluorescence spectra through the optical fiber catheters used in LAS is not a difficult procedure [57].

Furthermore, fluorescence spectra contain information about the morphologic and biochemical composition of tissue [5, 11]. Deconvoluting tissue spectra to yield this information, may both improve guidance techniques for LAS catheters and the manner in which the most appropriate treatment for an individual with CAD is selected.

In LAS, spectroscopic determination of the chemical composition of atherosclerotic lesions could ultimately be used to tailor parameters of the ablating radiation, providing the most precise and selective removal of plaque. The efficacy of the many therapies of CAD have been correlated to the chemical composition of the atherosclerotic obstruction [41]; thus, fluorescence spectroscopy may be useful in selecting appropriate therapy. It promises to provide a method of assessing the chemical composition of plaque *in vivo*, allowing accurate prediction of those lesions which are truly ideal candidates for PTCA, and those which require CABG. In addition, using fluorescence spectroscopy, it may be possible to determine when medical therapy is most appropriate, if those chemical constituents of atherosclerotic lesions which can be probed using fluorescence are related to the pathogenesis of atherosclerosis. For example, the presence of the autofluorescent oxidized lipoprotein, ceroid, has been correlated with the formation of irreversible atherosclerotic lesions [61]. Thus, fluorescence detection of ceroid may provide a method of assessing which patients will benefit most from conservative therapies, such as reduction of CAD risk factors and medical treatment.

1:2.2: Endoscope Compatible Spectroscopic Methods for Diagnosing Neoplasia: Guide/Replacement for Biopsy

According to present incidence rates, one in three Americans now living will eventually develop cancer [62]. The management of different types of cancers is becoming increasingly individualized; however, because tumors become progressively more aggressive in their behavior as they develop, it is important to detect them as early as possible [62, 63]. As neoplasms develop, they proceed, in a stepwise fashion, through qualitatively different stages [63]. In fact, it is now recognized that many epithelial cancers are preceded by premalignant changes, such as dysplasia or adenoma [64, 65]. Identification of these premalignant changes has proven to be crucial in the battle against cancer. If diagnosed, many of these premalignant changes are treatable. However, currently, no truly effective clinical methods of recognizing them exist. If such methods are developed, physicians will be provided with the opportunity to reduce the ultimate incidence and avert the adverse consequences of subsequent carcinoma [66].

The features of these epithelial pre-cancers are varied, and include morphologic and biochemical changes, such as an increase in the ratio of nuclear to cytoplasmic size [64, 65]. These are sometimes accompanied by changes in gross architecture, as occur in adenomatous polyp formation [64]. Many techniques have been developed in an attempt to identify these premalignant changes. Fiber-optic endoscopy is a recently developed screening method for identifying mucosal tumors in the interior of hollow organs [67]. However, endoscopy relies on largely architectural changes to identify neoplasms and is less useful in clinical situations where these morphologic or biochemical premalignant changes do not lead to alterations in gross architecture, or when the normal architecture of the non-neoplastic mucosa is disrupted [68, 69]. Although endoscopically directed biopsies can be obtained to screen for precancerous changes in these situations, such screening is limited because the surface area of the mucosa is generally orders of magnitude larger than that sampled by biopsy.

In view of the need for better early detection methods, we are developing an endoscope compatible method which can be used to screen the entire mucosal surface of a hollow organ for morphologic and biochemical premalignant changes. This method does not rely on changes in gross architecture. We have selected two clinically relevant examples of neoplasia for initial development of this technique: colo-rectal dysplasia in ulcerative colitis and transitional cell carcinoma in the urinary bladder. These diseases

share a theme, common in the management of many types of neoplasia. In both, it is desirable to detect premalignant and malignant morphologic and biochemical changes (dysplasia and carcinoma in situ (CIS)) in order to identify patients at risk for developing invasive carcinoma, who then face the possibility of surgery. In both, endoscopic methods are insufficient to screen for dysplasia, and are currently supplemented by selected mucosal biopsy, followed by histologic analysis. The utility of these techniques is limited because only a small portion of the mucosal surface of the organ is screened. In some cases, large areas of dysplasia or CIS may not be discovered, resulting in the failure to identify a patient at risk. The rationale for selecting these two conditions will be described in more detail in the following sections.

1.2.2.1. Brief review: Dysplasia in the Gastro-Intestinal Tract

Mucosal ulcerative colitis (MUC) is a recurrent ulcero-inflammatory disorder, affecting primarily the rectum and left colon [70]. Patients with MUC have a much greater risk of developing carcinoma of the large bowel than does the general population [70, 81]. The estimated risk varies somewhat, but cumulative rates as high as 60% at 30 years have been reported [71-74]. Because of this dramatically increased risk of developing carcinoma, prophylactic colectomy has been advocated for all patients with extensive long-standing MUC [75, 76]. However, this surgery is not without risk. The death rate for elective colectomy is low, but deaths do occur. Removal of the rectum can result in sexual dysfunction in both men and women [77]. Many patients, particularly those without severe chronic symptoms of MUC, find it difficult to accept surgery as a means of preventing cancer [76].

In those MUC patients not electing initial colectomy, physicians recommend regular colonoscopy with biopsy to screen for either early, potentially invasive carcinoma, or for dysplasia, the earlier premalignant change [72, 78]. If these changes are found, the physician recommends colectomy. Surveillance colonoscopy with biopsy has a number of limitations, the most important of which is that participation does not guarantee that the presence of a lethal cancer will be detected [72]. In one series, carcinoma developed in 13 of 186 patients with a history of disease for ten years or more despite regular colonoscopic surveillance [79]. A major contributing factor to these surveillance failures is the fact that carcinoma and dysplasia do not often cause grossly observable lesions at endoscopy. This coupled with the fact that dysplasia and carcinoma foci can be very small, can lead to tremendous sampling error [78, 80, 81].

Thus, because of limitations in current methods of screening for colo-rectal dysplasia, the ideal result, the prevention of cancer and restriction of operations to patients with demonstrated precancer has not been realized. Spectroscopic diagnosis of dysplasia has the potential to reduce the sampling error associated with colonoscopy and biopsy, both through better direction of biopsy placement and by allowing the entire surface area of the colon to be screened for dysplasia. This will be of immense practical value in the management of patients with MUC.

1:2.2.2. Brief Review of Transitional Cell Carcinoma in the Urinary Bladder

There are 38,000 new cases of bladder cancer in the US each year, resulting in 10,000 deaths annually [82]. Most (~90%) are transitional cell carcinomas (TCC) [82]. These carcinomas are subclassified based on their gross morphology (papillary or flat), the degree of atypia exhibited by the cancer cells, and the extent of invasion [82]. The extent of tumor invasion is the most important prognostic factor for the patient. Once the tumor has penetrated the outer layer of the bladder musculature, the chances of 5 year survival become 10% or less [65]. There is substantial evidence to indicate that invasive TCC is the final stage in a sequence of progressive mucosal dysplasia, rendering it theoretically subject to early detection in a more curable phase [65]. It is generally accepted that invasive cancers begin as non-invasive carcinomas, either non-invasive papillary carcinomas, or as carcinoma in situ (CIS), a flat, non-invasive lesion [82]. There is reasonable good evidence that CIS may either progress directly to invasive non-papillary carcinoma or to a papillary carcinoma that may in turn become invasive [82].

When initially discovered, most TCCs are non-invasive and of low histologic grade [82]. However, once removed, TCCs often recur at different sites. With each recurrence, TCC may be of higher grade, implying worse prognosis. In one series of over 250 patients, with grade I, non-invasive papillary carcinoma, 46% of patients exhibited a recurrence within 5 years, 81% within 15 years [83]. Because of this risk of higher grade recurrence, patients with a history of non-invasive TCC are followed closely. Surveillance of patients with TCC at present consists of evaluation of voided urine cytology, cytology of bladder washings after instrumentation, DNA ploidy analysis of cells obtained from bladder washings and cystoscopy with repeated biopsies [84]. Cytologic evaluation is reliable when cells are obtained from a high grade tumor [85, 86]. Cells from a low grade tumor may not be recognizable on cytologic analysis. DNA ploidy analysis is useful, but does not invariably identify malignant cells [87].

Cytologic analysis, even if positive, and DNA ploidy analysis, even if aneuploid, do not identify the site of tumor. This can only be accomplished with biopsy at cystoscopy. Bladder biopsy diagnosis of TCC at cystoscopy is reliable if a biopsy was obtained from a cancerous site. This is usually not a problem in the case of papillary or infiltrating tumors. However, the identification of foci of flat, non-invasive TCC or dysplasia is often a problem [88]. In one series of 399 biopsies obtained from endoscopically normal mucosa, it was found that 4.5% contained CIS, and an additional 13.5% contained dysplasia [69]. When cystoscopic appearance was flat and erythematous, abnormalities were observed in 51% of biopsies, 14% containing carcinoma, and when the typical cystoscopic appearance of CIS was observed, 42% of biopsies contained carcinoma, with 11% indicating severe dysplasia [69]. It has been demonstrated that these microscopic changes have important prognostic significance: 38% of 29 patients who had a prior abnormal biopsy developed a subsequent tumor, compared to 16% of 32 patients who did not have a prior positive biopsy [89].

Thus, patients displaying severe dysplasia or CIS will have their treatment plan altered, as they are at higher risk of developing invasive bladder cancer. The most critical decision encountered in the clinical management of these patients, concerns the role of cystectomy [90]. While cystectomy can cure a certain portion of these patients, it is an operative procedure which is accompanied by significant morbidity and mortality [91]. The mutilation and functional loss associated with this procedure is a heavy burden for these patients. Therefore, there is much interest in improving diagnostic techniques for dysplasia and CIS, in order to accurately separate patients at most risk for developing invasive bladder cancer, requiring cystectomy, and patients who can be treated with less aggressive therapies. Spectroscopic diagnosis of these conditions has the potential to reduce the sampling error associated with cystoscopy and biopsy, either through better direction of biopsy placement or by allowing the entire surface area of the bladder to be screened.

1:3: Goals of this Work

The goal of this work was to develop a general method, based on fluorescence spectroscopy, of defining diagnostic algorithms for pathology which can be applied to human tissue *in vivo* in real time. Furthermore, this method was to be applied to the diagnosis of the three specific pathologies described in the preceding section.

1:3.1: Can Fluorescence Spectroscopy be Used to Differentiate Normal and Pathologic Tissues?

Fluorescence spectroscopy was chosen as the basis of our algorithm for primarily two reasons. The first is that the technical requirements of this goal - gathering chemical information sensitively, remotely and non-destructively in real time - can be achieved using fluorescence. Secondly, there is much evidence to indicate that the chemical alterations accompanying many diverse diseases can be probed using fluorescence spectroscopy [5-10]. Many naturally occurring fluorophores, such as NADH, NAD(P)H and the flavins, are intimately involved in important cellular processes such as respiration, growth and even necrosis [92, 93, 94]. Thus, fluorescence has the potential to provide an algorithm which achieves real time *in vivo* histochemical diagnosis and staging of disease, but in addition may also yield novel methods of studying the pathogenesis of disease *in vivo*.

1:3.1.1. Brief Review of Tissue Spectroscopy Literature

Many groups have shown that fluorescence spectroscopy can be used to develop diagnostic algorithms for disease which are effective when applied *in vitro* [5-10, 95-110]. Tissues investigated have been diverse, including atherosclerosis in arterial tissues [5-8, 95-99], neoplasia in many organs such as oral mucosa [10], gastrointestinal tissues [10, 108, 109] and tissues of the upper urinary tract [96]. Preliminary results have suggested that even dental caries [110] can be detected using fluorescence spectroscopy.

The most advanced studies have been carried out in arterial tissue. These will be reviewed here, and in Chapter 3. Early work, with visible excitation, demonstrated that fluorescence spectroscopy could be utilized to diagnose the presence of atherosclerosis in human cadaver aorta. Kittrell suggested that, with 480 nm excitation, the peak to valley ratio of the fluorescence intensity at 600 nm to that at 580 nm indicated the presence of fibrous atherosclerosis [95]. This algorithm was tested in a small set of six samples of human cadaver aorta, and all were correctly classified as normal or atherosclerotic. Sartori demonstrated that, with 457.9 nm excitation, the peak fluorescence intensity could be used to delineate regions of calcific plaque in six samples of human cadaver aorta [6].

Much subsequent work has been done with ultra-violet excitation. Deckelbaum demonstrated that 337 nm excited laser induced fluorescence (LIF) spectra could be used to differentiate 21 samples of normal cadaver aorta, white fibrous plaque and yellow fatty

plaque, based on the ratios of fluorescence intensities at 448 nm, 514 nm and 538 nm [96].

Deckelbaum subsequently showed that, with 325 nm excitation, a fluorescence based algorithm could be used to classify over 180 unknown samples of cadaver aorta as normal or atherosclerotic with an accuracy of 92% when compared to histology [8]. In this study, however, only advanced atherosclerotic plaques, with an intimal thickness of greater than 900 μm, were considered. At 325 nm excitation, Deckelbaum attributes the fluorescence signal to collagen and elastin fluorescence [8]. His algorithm consists of extracting the relative contributions of these proteins from the fluorescence spectrum [8]. Diagnosis is accomplished because the fluorescence spectrum of atherosclerotic aorta is dominated by contributions from collagen, while that of normal aorta resembles primarily that of elastin [8]. He notes that this algorithm can not be extrapolated successfully to diagnosis of atherosclerosis in muscular arteries, such as the coronary arteries, because the elastin content of these arteries is much different than that of the elastic aorta [97].

Leon has reported studies of over 250 samples of cadaver aorta and coronary artery at 325 nm excitation. He observed a single emission peak near 465 nm in the fluorescence spectrum of both normal and atherosclerotic tissues [7]. Differences were observed in the maximum fluorescence intensity and fluorescence lineshape of non-calcified atherosclerotic samples and normal tissues. The peak fluorescence intensity of these plaques was only 45% that of normal tissue and the full width at half maximum (FWHM) of this single peak was larger for non-calcified plaques than for normal tissues [7]. The fluorescence intensity of calcified atherosclerotic plaques was more similar to that of normal tissue at this excitation wavelength; these plaques had an average fluorescence intensity 7% greater than that of normal tissues [7]. Leon did not present an algorithm for classification of sample type based on these fluorescence features. In addition, he reported no differences in the fluorescence properties of aorta and coronary artery at this excitation wavelength [7].

In a preliminary study, Clarke indicated no significant differences in the fluorescence of native calcified and normal aortic valves when excited in the UV [98]. In a more recent paper, however, he presented work at 325 nm excitation and showed that fatty, fibrous and calcific plaque content as well as maximal intimal thickness in cadaver coronary artery could be correlated to features of the fluorescence spectrum [99]. He investigated over 300 samples *in vitro* and used multiple and stepwise regression analysis to correlate over 78 ratios of fluorescence intensities at 13 wavelengths between 390 and

600 nm to intimal thickness and lesion composition [99]. When regression analysis was applied to the total sample set, correlation coefficients approached 0.8 for intimal thickness, fibrous, fatty and calcified plaque content [99]. The correlation coefficients were greater when the data sets were restricted to include only particular types of atherosclerotic plaques [99]. In all cases, the parameters estimated by fluorescence spectroscopy were compared to values measured using standard histologic methods [99].

In addition, many studies have shown that the autofluorescence properties of normal and neoplastic tissues differ over a wide range of UV and visible excitation and emission wavelengths [9, 10, 100-109]. These will be briefly reviewed here, and those involving tumors of the colon will be described in more detail in Chapter 4. Alfano and colleagues have demonstrated that 488 nm excited laser-induced autofluorescence spectra of normal and cancerous tissue are appreciably different in rat kidney and prostate tissues [100]. In addition, Alfano has shown that an observational comparison of 457.9, 488 and 514.5 nm excited LIF spectra of normal and cancerous human tissue can be used to diagnose the presence of tumor with a sensitivity of 87.5% and a specificity of 86.6% in 31 samples *in vitro* [9]. Similar results have been reported by Alfano in human lung tissue as well [101, 102]. He suggests that autofluorescence in these tissues may be due to flavins and porphyrins, which may have different environments in normal and neoplastic tissues [9, 100-102]. Other groups have measured increased levels of red fluorescence in tumors, and suggest that this is due to higher concentrations of endogenous porphyrins in tumors than in corresponding normal tissues [10, 103-106].

Additional empirical studies have demonstrated that UV LIF spectra can be used to develop diagnostic methods for neoplastic human tissue. Montan demonstrated that at 337 nm excitation, autofluorescence of meningiomas was significantly different than that of normal white and gray matter, while astrocytoma spectra were similar to that of normal brain tissue [107]. Yakshe observed differences in the autofluorescence spectra of resected normal colonic mucosa and invasive carcinoma of the colon with 337 nm excitation [108]. Kapadia and colleagues have shown *in vitro*, that at 325 nm excitation, fluorescence spectroscopy can be used to differentiate normal colonic mucosa, hyperplastic polyps and adenomatous polyps with an overall accuracy of 92% [109].

Thus, in many preliminary studies, most of which were empirical in nature, autofluorescence spectroscopy has been shown to be useful for developing diagnostic algorithms for pathology *in vitro*. However, in the development of these systems there are many improvements which can be made. For example, the selection of excitation

wavelength in many previous studies seems largely to be a function of the laser available in the researcher's laboratory. Human tissue likely contains many different chromophores which can contribute to the fluorescence spectrum; this implies that both the intensity and lineshape of the fluorescence emission spectrum will be a function of excitation wavelength [11]. In addition, in the development of these algorithms, a detailed understanding of the morphologic and molecular basis of tissue fluorescence spectra has not been undertaken. Empirical interpretation of fluorescence spectra neglects a vast amount of morphologic and biochemical information. It is likely that a more scientific approach to this interpretation will yield both more sensitive and accurate diagnostic algorithms. Furthermore, a morphologic or molecular interpretation of the fluorescence spectrum will be more meaningful to the clinician, enabling the most direct correlation of spectroscopic algorithms with the identity, stage, prognosis and choice of treatment of the particular disease.

This thesis addresses these shortcomings; here is presented a systematic approach to defining spectroscopic diagnostic algorithms for pathology. This method includes optimization of the excitation wavelength and development of morphologic/molecular models of fluorescence. This method can be applied to any pathology in any tissue; it is illustrated here with three specific examples. Our general approach is described concisely below, and in more detail with respect to each of the examples in Chapters 3, 4, and 5.

1:3.2: What is the Optimal Way to Achieve Spectroscopic Diagnosis of Disease? Our Approach in Brief.

Our approach to defining spectroscopic diagnostic algorithms for disease is a stepwise procedure. It begins with the initial step of forming the hypothesis that, at specific excitation wavelengths, fluorescence spectroscopy can be used to distinguish normal and pathologic tissues for the clinical condition of interest. These excitation wavelengths are selected on the basis of a comparison of the fluorescence properties of normal and pathologic tissues over a wide range of ultra-violet and visible excitation wavelengths.

At these excitation wavelength(s), studies are then conducted to determine the biochemical and morphologic basis of tissue fluorescence. Tissue fluorescence spectra are interpreted utilizing a simple mathematical model of tissue fluorescence to extract parameters related to the concentration and spectral properties of tissue chromophores.

Diagnostic algorithms for the diagnosis and staging of disease are then developed, utilizing parameters extracted with the model.

Much of this procedure must be carried out *in vitro*; however, in our protocol, clinical trials of fluorescence spectroscopy are carried out *in vivo* in parallel with *in vitro* studies. In these clinical trials, the hardware and software with which fluorescence spectra are collected and analyzed are tested and modified as necessary. In addition, these trials ensure that algorithms developed *in vitro* are applicable *in vivo*.

This method is illustrated schematically in Fig. 1. Each of these steps in our procedure is described below in more detail.

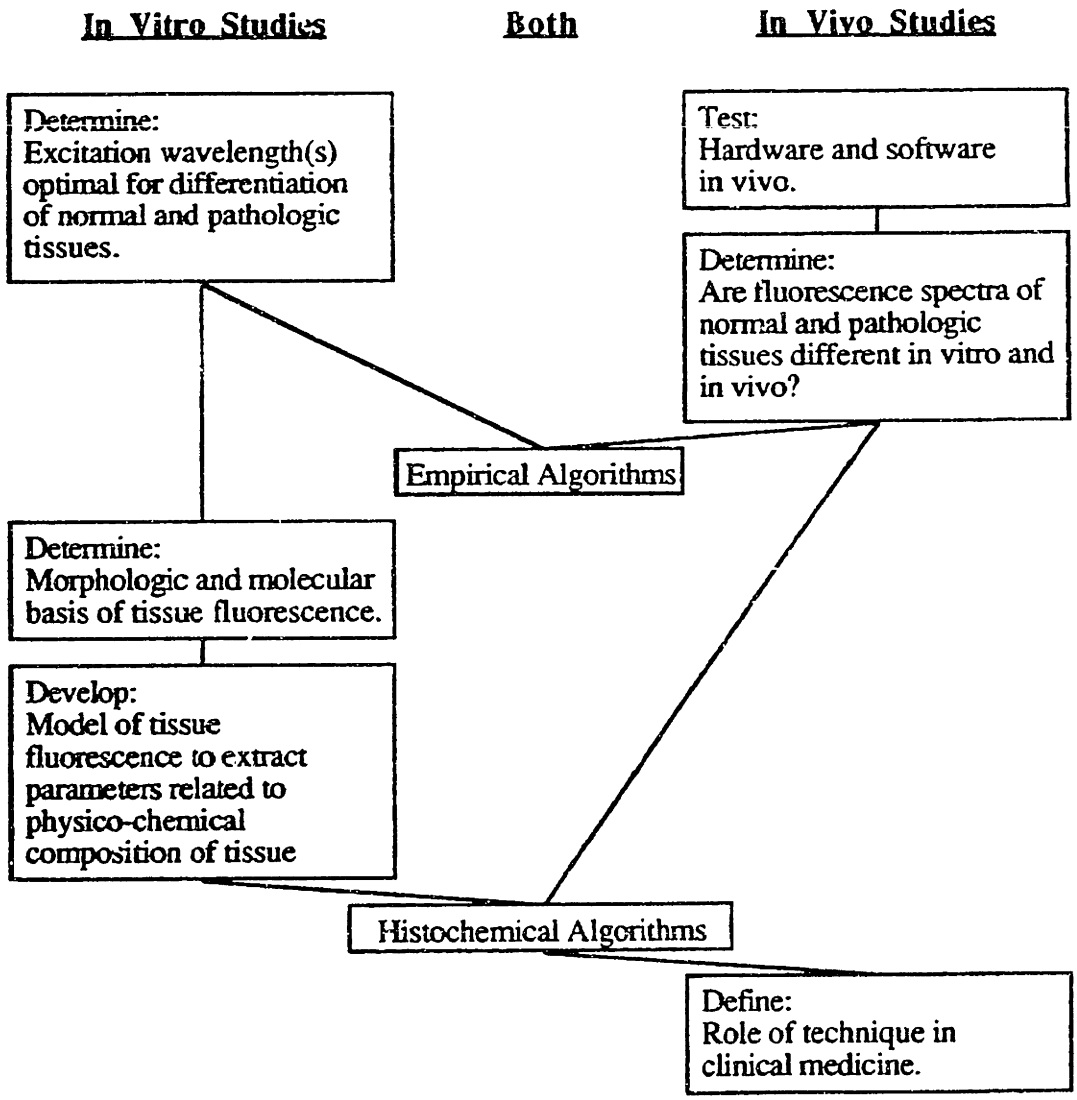

Figure 1: Schematic diagram illustrating the steps involved in our approach to defining spectroscopic algorithms for real time diagnosis of disease *in vivo*.

1:3.2.1. Clinical Considerations - Record emission spectra

Before describing our procedure in more detail, it is necessary to explain why our algorithms are based on features of the fluorescence emission spectra at selected excitation wavelengths. In principle, the same information could be obtained from parameters of fluorescence excitation spectra at selected emission wavelengths. However, our goal is to achieve real time diagnosis of pathology; to achieve this, technical considerations suggest that emission spectra are superior to excitation spectra, because, with current technology, than can be collected more rapidly. At a single excitation wavelength, using multi-channel detection, an entire fluorescence emission spectrum can generally be collected within a single shot of a pulsed excitation source. Fluorescence spectra even at several excitation wavelengths can then be collected very rapidly. Fluorescence excitation spectra, on the other hand, are more difficult to collect in such a rapid fashion.

1:3.3: Fluorescence Excitation-Emission Matrices

The first step of our approach is to form the hypothesis that, at specific excitation wavelengths, fluorescence spectroscopy can be used to differentiate normal and pathologic tissues for a particular clinical condition. These excitation wavelengths are identified by recording tissue fluorescence intensities over a wide range of UV and visible excitation and emission wavelengths. This data is then assembled into a fluorescence excitation-emission matrix (EEM), a matrix containing the fluorescence intensity as a function of excitation and emission wavelength [111]. Fluorescence EEMs are acquired for a small group of normal and pathologic samples *in vitro*. Average EEMs are calculated for each class of tissue to be differentiated. They are displayed as fluorescence contour maps, where contour lines are used to connect points of equal fluorescence intensity. We have developed two methods of comparing fluorescence EEMs to determine excitation wavelength(s) optimal for diagnosing disease. These require calculating both the ratio and difference of the average normal and pathologic EEMs. From these we determine the minimal number of excitation wavelengths required to collect all possible diagnostically relevant physico-chemical information about the tissue.

1:3.4: Basis of Tissue Fluorescence

Our goal is to develop methods for minimally invasive diagnosis of pathology based on histochemical features which can be extracted from tissue fluorescence spectra.

The third step in our procedure then is to elicit the morphologic and molecular basis of tissue autofluorescence at the excitation wavelength(s) of interest.

1:3.4.1. Molecular: EEMs of Tissue and Biological Molecules

The fluorescence EEMs provide important clues about the biochemical components which contribute to the fluorescence of tissue. For the purpose of interpreting fluorescence EEMs, we can regard tissue as a multi-component, optically thick, turbid solution, containing species which can absorb and/or scatter radiation, and which, following absorption, can potentially fluoresce. Definitive identification of tissue chromophores[1] from fluorescence EEMs is thus a difficult task. Here, we use a simple method of interpretation, in order to preliminarily determine the biochemical identity of tissue fluorophores and absorbers. A list of potential tissue chromophores is established by a comparison of fluorescence excitation-emission maxima in tissue EEMs to fluorescence excitation-emission maxima of naturally occurring fluorophores [112].

1:3.4.2. Morphologic/Biochemical:Fluorescence microscopy

Definitive identification of the morphologic structures contributing to the tissue fluorescence spectrum (chromomorphs) is achieved using microscopy. Unstained frozen sections of tissue are viewed through the fluorescence microscope to determine which regions of the tissue fluoresce; serially stained sections are then viewed through the light microscope to determine the morphologic identity of these fluorescing structures. The spectroscopic properties of individual chromomorphs are characterized by microspectrofluorimetry.

This morphologic characterization provides important clues about the molecular identity of tissue fluorophores. The location of a chromomorph, i.e. extracellular, intra-cellular, intra-nuclear, membranous, gives clues about the chemical nature of the associated fluorophore(s). In addition, the spectroscopic properties of chromomorphs can be compared with those of individual biomolecules. A comparison of the spectrum of

---

[1]Here, we use several terms to describe tissue constituents which may contribute to the fluorescence spectrum. We use the term chromophore to indicate a specific chemical structure which absorbs radiation in the UV or visible regions of the spectrum, and following absorption may emit fluorescence. We use the term absorber to represent those chromophores which do not fluoresce and fluorophore to represent those chromophores which do fluoresce. In contrast, we use the term chromomorph to indicate those morphologically distinct structures which absorb radiation in the UV and/or visible region of the spectrum, and following absorption may emit fluorescence. The distinction between the terms chromophore and chromomorph is in the level at which the identitiy of the tissue constituent is known - chemical or morphologic.

a particular chromomorph with those preliminarily identified from EEM studies can result in definitive molecular fluorophore identification.

1:3.5: Models of Tissue Fluorescence

1:3.5.1. General Overview

To extract the histochemical composition of tissue from the fluorescence spectra of bulk tissue two conditions must be met. First, the histochemical basis of tissue fluorescence must be known, and the spectroscopic properties of individual tissue components must be characterized. Secondly, a model of tissue fluorescence is required to describe light propagation within the tissue. There are many approaches to developing such a model; however, there are three features which must be included no matter what the approach.

1:3.5.1.1: Absorption, Scattering, Fluorescence

The first feature to model is the fate of photons which are incident on or generated within tissue. UV or visible electro-magnetic radiation in tissue can either be scattered or absorbed [113]. There are many theories to describe this process [114]. The scattering and absorption of incident radiation control the distribution of excitation light within the tissue [114], and thus determine what structures within the tissue can potentially absorb radiation. When light in this spectral range is absorbed by a chromophore, a variety of consequences can result, one of which is emission of a fluorescence photon. The UV and visible absorption and emission characteristics of a particular chromophore are governed by quantum mechanics and can be described in terms of energy level diagrams, as shown in Fig. 2 [92, 113]. The scattering and re-absorption of fluorescence photons generated within the tissue determines the distribution of fluorescence photons emanating from the surface of the tissue. Only those photons reaching the tissue surface and entering the detection system are collected [115].

1:3.5.1.2: Multi-component sample

The second essential feature of any model of tissue fluorescence is the inclusion of contributions from multiple chromophores, including scatterers, absorbers and fluorophores. The properties of dilute solutions containing a single fluorophore are considerably different than those of multi-component, optically thick, turbid materials such as tissue. For example, the fluorescence emission lineshape of a dilute solution

containing a single fluorophore is independent of excitation wavelength; as the excitation wavelength is varied, only the overall fluorescence intensity changes [113]. On the other hand, both the fluorescence intensity and lineshape of multi-component solutions change with excitation wavelength, as the relative contribution of various fluorophores is a function of excitation wavelength.

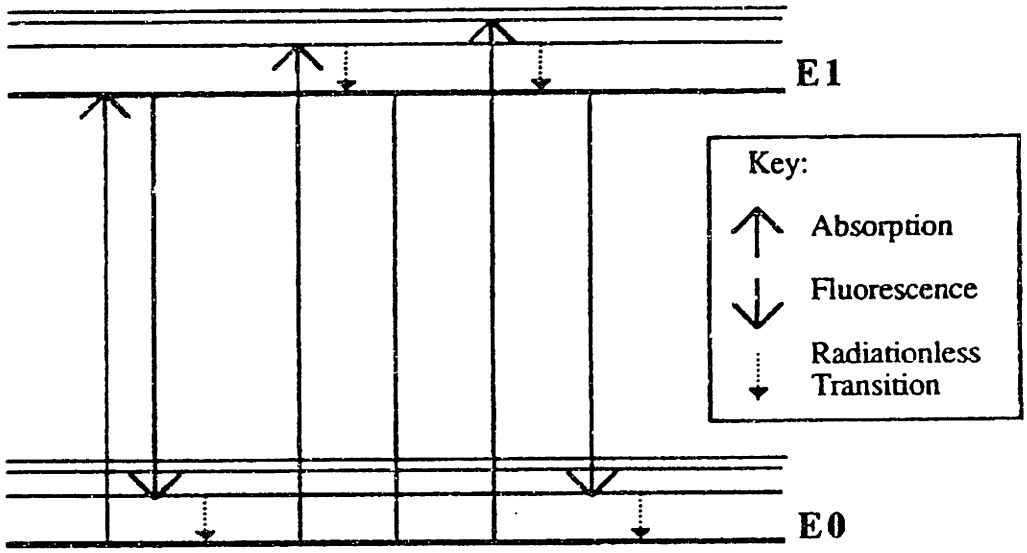

Figure 2: Energy level diagram depicting the process of absorption and emission of photons in the UV and visible regions of the spectrum.

1:3.5.1.3: Multi-layer samples

Finally, it is necessary to incorporate the geometry of tissue into a model of tissue fluorescence in order to extract physical properties of the tissue from fluorescence spectra. The layered structure of many tissues simplifies this task; the artery, for example, is composed of three layers, the intima, media and adventitia [116]. These layers are distinct histochemically; thus, must be treated separately within a model of tissue fluorescence.

1:3.5.2. Models for light attenuation

A key feature of any model of tissue fluorescence incorporating these three elements is the manner in which the propagation of light within the tissue is described. In non-scattering media, light intensity decreases exponentially along the axis of propagation, according to Beer's law [117]. The large amount of scattering in tissue, however, precludes a simple determination of the functional form of attenuation. Light

propagation in a highly scattering medium is commonly treated using the equation of transfer [118]. Unfortunately, a general solution is not known. This has led many workers to develop reasonable approximations which lead to analytical solutions for estimating light propagation in scattering media [118, 119]. Monte Carlo simulations have been extensively utilized, offering the advantage that complex geometries and inhomogeneities can be modeled [120]. However, the time required to obtain sufficient photon statistics obviously precludes the use of this technique in a real time system.

In our model of tissue fluorescence, we will, for simplicity, treat the processes of absorption and scattering together, considering only the total effects of attenuation. We will assume that light is attenuated exponentially, and can be described by a wavelength dependent attenuation coefficient. The ramifications of this simplifying assumption will be discussed in Chapter 2:3.2.2, comparing our model of attenuation to results of Monte Carlo simulations and the diffusion theory approximation to the equation of transfer.

1:3.6: Algorithm Development

The model of tissue fluorescence provides a method of extracting parameters related to the morphologic and biochemical composition of tissue from fluorescence spectra. To utilize these parameters in making clinical decisions concerning the presence, identity, stage and treatment of disease requires a diagnostic algorithm. The process of algorithm development is well studied in the field of medical statistics [121].

Basically this iterative procedure can be broken down into two consecutive steps. First, parameters which have the greatest diagnostic capability must be selected. Then a decision surface which separates this parameter space into various diagnostic categories must be defined. The performance of the algorithm is described in terms of several quantities, including sensitivity, specificity and positive predictive value [121]. The decision surface is usually defined to optimize a certain measure of algorithm performance; the choice of which measure is optimized depends on the particular clinical application of the algorithm.

In this thesis several methods of algorithm development are utilized. Each utilizes fluorescence spectra from a representative data set for which tissue type has been characterized by histologic methods, known as the defining set. These methods will be briefly described below.

1:3.6.1. Choice of Parameters

We utilize an empirical method of selecting the parameters to include in the diagnostic algorithm. In this process, we employ a simple analog of stepwise variable selection to choose which variables have the greatest diagnostic capability [121]. This technique uses the misclassification rate for the defining data set to test the diagnostic capability of each variable individually. Once the most clinically useful variable has been determined, all pairs of variables consisting of this parameter and any of the remaining parameters are tested. Although not rigorously designed to achieve statistically optimized algorithms, this simple method of parameter selection provides valuable insight into how well more complicated statistical algorithms can be expected to perform.

1:3.6.2. Defining Decision Surfaces

We use two methods to define decision surfaces in our diagnostic algorithms. The first, simpler method, is used to develop a preliminary assessment of potential algorithm performance. If promising, more sophisticated methods are used to optimize decision surfaces for individual clinical settings.

1:3.6.2.1: Scatter Plots

A simple method of formulating a decision surface is to plot the model parameters of each individual sample in the defining set. This plot is known as a scatter plot, and is easiest to represent when the number of parameters is two or less. Decision surfaces can then be empirically drawn on this scatter plot, separating it into various regions which correspond to the different categories to be differentiated. Decision surfaces can be defined to maximize any measure of algorithm performance.

Although it is simple to define decision surfaces from scatter plots of the defining data set, the method has a number of drawbacks. By constructing complicated decision surfaces and dividing the scatter plot into many different, non-contiguous regions, it is generally possible to correctly diagnose all samples in the defining set. However, when the algorithm so defined is applied to a second, similar set of data, the performance generally falls drastically. This problem can be minimized by restricting the shape of the decision surfaces and requiring that no non-contiguous regions of the parameter space be accorded the same diagnosis.

A second problem is the clinical interpretation of the diagnosis of samples whose fluorescence parameters fall close to the decision surfaces. Intuitively, we associate more uncertainty with the diagnosis of these samples than that of samples with fluorescence parameters not close to the decision surface. This uncertainty is difficult to quantify, however, with this method.

Perhaps the most important problem with this method of defining decision surfaces is that of optimizing different measures of algorithm performance. Generally, the measure of performance of most clinical interest is the positive predictive value [121]. The predictive value depends on initial likelihood of encountering disease in a given patient population; this is known as the prior probability of disease. For optimal algorithm performance, decision surfaces need to be defined differently for very rare and very common diseases. Unfortunately, customizing the decision surfaces for different clinical settings of the same disease is not easily incorporated in the scatter plot method of defining decision surfaces.

1:3.6.2.2: Discriminant Analysis

Discriminant analysis is a probabilistic method of defining decision surfaces which overcomes these problems [121]. In this procedure, for each classification of disease, probability distributions are calculated for each of the fluorescence parameters from the defining data set. These probability distributions are then used with estimations of the prior probability to develop an expression for the posterior probability for each tissue classification. The posterior probability represents the probability that an unknown sample with measured fluorescence properties belongs to a particular classification. The algorithm then consists of allocating unknown tissue samples to the tissue category for which they have the greatest posterior probability.

1:3.6.3. Clinical Studies and Trials

Throughout this procedure, clinical trials of the diagnostic algorithms under development are pursued. These studies serve three important purposes. First, the hardware for collecting tissue fluorescence spectra *in vivo* and the software for analyzing the resulting data can be tested and modified as necessary. Second, we can attempt to account for any differences between *in vitro* and *in vivo* data within the framework of our histochemical understanding of the basis of tissue fluorescence, ensuring that algorithms developed *in vitro* will ultimately be applicable *in vivo*. Finally, actual clinical

implementation of the algorithms developed through this method can begin, in order to assess the role of these techniques in diagnostic medicine.

The remainder of this thesis describes the implementation of these methods in three clinically relevant situations. In Chapter 3, a spectroscopic diagnostic algorithm is developed for atherosclerosis in t human aorta and coronary artery. Chapter 4 contains a diagnostic algorithm for the presence of colonic dysplasia, while Chapter 5 includes diagnostic algorithms for the presence of premalignant and malignant changes associated with transitional cell carcinoma of the urinary bladder. Finally, in Chapter 6, the important conclusions which can be drawn from this work are summarized, and future experiments are proposed.

1:4: References

1. Robbins SL, Cotran RS, Kumar V, Pathologic Basis of Disease, 3rd ed., WB Saunders Co., Philadelphia, 1984, p. 1.

2. Armstrong P, Wastie ML, Diagnostic Imaging, 2nd ed., Blackwell Scientific Publications, Oxford, 1987, p. 1-11.

3. Matson GB, Weiner MW, MR Spectroscopy *in vivo*: Principles, Animal Studies and Clinical Applications, in Stark DD, Bradley WG, eds, Magnetic Resonance Imaging, The CV Mosby Co., 1988, p. 201-222.

4. Ham AW, Cormack DH, Histology, 8th ed., JB Lippincott Co.. Philadelphia, 1979, p. 3 -32.

5. Richards-Kortum RR, Rava R, Fitzmaurice M, Tong L, Ratliff NB, Kramer JR, Feld MS: A One-Layer Model of Laser Induced Fluorescence for Diagnosis of Disease in Human Tissue: Applications to Atherosclerosis, IEEE Transactions on Biomedical Engineering, 36:1210-21, 1989.

6. Sartori M, Sauerbrey R, Kubodera S, Tittel F, Roberts R, Henry PD, Autofluorescence Maps of Atherosclerotic Human Arteries - A New Technique in Medical Imaging, IEEE Journal of Quantum Electronics, QE-23:1794-97, 1987.

7. Leon MB, Lu DY, Prevosti LG, Macy WW, Smith PD, Granovsky M, Bonner RF, Balaban RS, Human Arterial Surface Fluorescence: Atherosclerotic Plaque Identification and Effects of Laser Atheroma Ablation, JACC 12:94-102, 1988.

8. Laifer LI, O'Brien K, Stetz ML, Gindi GR, Garrand TJ, Deckelbaum LI, Biochemical Basis for the Difference Between Normal and Atherosclerotic Arterial Fluorescence, Circulation, 80:1893-1901, 1989.

9. Alfano RR, Pradhan A, Tang GC, Optical Spectroscopic Diagnosis of Cancer and Normal Breast Tissues, J. Opt. Soc. Am. B, 6:1015-23, 1989.

10. Yuanlong Y, Yanming Y, Fuming L, Yufen L, Paozhen M, Characteristic Autofluorescence for Cancer Diagnosis and its Origin, Lasers in Surgery and Medicine, 7:528-32, 1987.

11. Schulman SG, Fluorescence and Phosphorescence Spectroscopy: Physico-chemical Principles and Practice, 1st ed., Pergamon Press, Oxford, p. vii, 1977.

12. Lansing Taylor D, Waggoner AS, Murphy RF, Lanni F, Birge RR, eds, Applications of Fluorescence in the Biomedical Sciences, Alan R. Liss, New York, 1986.

13. Slater PN, Remote Sensing, Optics and Optical Systems, Addison Wesley, Reading, MA, 1980.

14. Birnbaum M, Laser Excited Fluorescence Techniques in Air Pollution Monitoring, Ch. 5 in, Wehry EL, ed, Modern Fluorescence Spectroscopy, vol. 1, Plenum Press, NY, p. 121-57, 1976.

15. Gaiger J, Hall FF, Laser Applications in the Geosciences, Western Periodicals Co., Hollywood, CA, 1970.

16. Sivak M, Gastroenterologic Endoscopy, WB Saunders Co, Philadelphia, 1987.

17. Uchida Y, Percutaneous Coronary Angioscopy by Means of a Fiber Scope with a Steerable Guidewire, Am Heart J, 117:1153-55, 1989.

18. Anderson PS, Montan S, Svanberg S, Multispectral system for Medical Fluorescence Imaging, IEEE JQE QE23:1798, 1987.

19. Cothren RM, Kittrell C, Hayes GB, Willett RL, Sacks B, Malk EG, Ehmsen RJ, Bott-Silverman C, Kramer JR, Feld MS, Controlled Light Delivery for Laser Angiosurgery, IEEE JQE QE22:4-7, 1986.

20. Puig-Tintore LM, Gonzales-Merlo J, Jou P, Marquez M, Faus R, Treatment of CIN with CO2 Laser Vaporization, Eur J Gynaec Oncol IX:320-23, 1988.

21. Robbins SL, Cotran RS, Kumar V, Pathologic Basis of Disease, WB Saunders Co., Philadelphia, p. 506-19, 1984.

22. Wissler RW, Principles of the Pathogenesis of Atherosclerosis, in Braunwald E, ed, Heart Disease: A Textbook of Cardiovascular Medicine, WB Saunders Co, Philadelphia, p. 1185-99, 1984.

23. Cohn PF, ed, Diagnosis and Therapy of Coronary Artery Disease, Martinus Nijhoff Publishing Co, 1985.

24. Bolli R, Bypass Surgery in Patients with Coronary Artery Disease, Chest, 91:760-64, 1987.

25. Cohen LS, Results of Coronary Bypass Surgery, Ann Rev Med, 38:457-65, 1987.

26. Ratliff NB, Myles JL, Rapidly Progressive Atherosclerosis in Aortocoronary Saphenous Vein Grafts, Arch Pathol Lab Med, 113:772-76, 1989.

27. Lytle BW, Loop FD, Cosgrove DM, Ratliff NB, Easley K, Taylor PC, Long -term (5 to 12 Years) Serial Studies of Internal Mammary Artery and Saphenous Vein Coronary Bypass Grafts, J Thorac Cardiovasc Surg 89:248-58, 1985.

28. Neitzel GF, Barboriak JJ, Pintar K, Qureshi I, Atherosclerosis in Aortocoronary Bypass Grafts. Morphologic Study and Risk Factor analysis 6 to 12 Years After Surgery, Atherosclerosis 6:594-600, 1986.

29. Lie JT, Lawrie CM, Morris GC, Aortocoronary Bypass Saphenous Vein Graft Atherosclerosis, Anatomic Study of 99 Vein Grafts from Normal and Hyperlipoproteinemic Patients Up to 75 Months Postoperatively, Am J Cardiology, 40:906-14, 1977.

30. Atkinson JB, Forman MB, Vaughn WK, Robinowitz M, McAllister HA, Virmani R, Morphologic Changes in Long-term Saphenous Vein Bypass Grafts, Chest 88:341-48, 1985.

31. Stewart RW, Loop FD, Cosgrove DW, Lytle BW, Current Status of Coronary Artery Surgery, Heart Transplantation III:210-19, 1984.

32. Vlietstra RE, Holmes DR Jr, Percutaneous Transluminal Coronary Angioplasty, FA Davis Co., 1987.

33. Baim DS, Ignatius EJ, Use of Percutaneous Transluminal Coronary Angioplasty: Results of a Current Survey, Am J Cardiol, 61:3G-8G, 1988.

34. Talley JD, Hurst JW, King SB III, Douglas JS, Roubin GS, Gruentzig AR, Anderson HV, Weintraub WS, Clinical Outcome Five Years After Attempted Percutaneous Transluminal Coronary Angioplasty in 427 Patients, Circulation, 77:820-29, 1988.

35. Kent KM, Restenosis After Percutaneous Transluminal Coronary Angioplasty, Am J Cardiol, 61:67G-70G, 1988.

36. Hwang MH, Sidhu P, Pacold I, Johnson S, Scanlon PJ, Loeb HS, Progression of Coronary Artery Disease After Percutaneous Transluminal Coronary Angioplasty, Am Heart J, 115:297-301, 1988.

37. Serruys PW, Luijten HE, Beatt KJ, Geuskens R, De Feyter PJ, Van Den Brand M, Reiber JHC, Ten Katen HJ, Van Es GA, Hugenholtz PG, Incidence of Restenosis After Successful Coronary Angioplasty: A Time Related Phenomenon, Circulation, 77:361-71, 1988.

38. Black AJR, Anderson V, Roubin GS, Powelson SW, Douglas JS, King SB III, Repeat Coronary Angioplasty: Correlates of a Second Restenosis, J Am Coll Cardiol, 11:714-8, 1988.

39. Galan KM, Deligonul U, Kern MJ, Chaitman BR, Vandormael MG, Increased Frequency of Restenosis in Patients Continuing to Smoke Cigarettes After Percutaneous Transluminal Coronary Angioplasty, Am J Cardiol 61:260-63, 1988.

40. Austin GE, Lynn M, Hollman J, Laboratory Test Results as Predictors of Recurrent Coronary Artery Stenosis Following Angioplasty, Arch Pathol Lab Med, 111:1158-62, 1987.

41. Potkin BN, Roberts WC, Effects of Percutaneous Transluminal Coronary Angioplasty on Atherosclerotic Plaques and Relation of Plaque Composition and Arterial Size to Outcome, Am J Cardiol, 62:41-50, 1988.

42. Pujadis G, Coronary Angiography, McGraw-Hill, 1980.

43. Abrams HL, Angiography, Brown and Co., Boston, 1971.

44. Uchida Y, Percutaneous Coronary Angioscopy by Means of a Fiber Scope with a Steerable Guidewire, Am Heart J, 117:1153-55, 1989.

45. Nanda NC, Doppler Echocardiography, Igaku-Shoin, New York, 1985.

46. Pohost GM, NMR Evaluation of the Cardiovascular System, in Pohost GM, Higgins CB, Morganroth J, Ritchie JL, Schelbert HR, eds, New Concepts in Cardiac Imaging, GK Hall Medical Publishers, Boston, p. 255-99, 1985.

47. Ellis SG, Roubin GS, King SB III, Douglas JS, Weintraub WS, Thomas RG, Cox WR, Angiographic and Clinical Predictors of Acute Closure after Native Vessel Coronary Angioplasty, Circulation, 77:372-70, 1988.

48. Nigel I, McCabe CH, Sipperly ME, Baim DS, Predictors, Therapeutic Options and Long-Term Outcome of Abrupt Reclosure, Am J Cardiol, 61:61G-66G, 1988.

49. Roubin G, Gruntzig A, The Coronary Artery Bypass Surgery - Angioplasty Interface, Cardiology, 73:269-77, 1986.

50. Marcus ML, Harrison DG, White CW, McPherson DD, Wilson RF, Kerber RE, Assessing the Physiologic Significance of Coronary Obstructions in Patients: Importance of Diffuse Undetected Atherosclerosis, Progress in Cardiovascular Diseases, 31:39-56, 1988.

51. Abela GS, Laser Arterial Recanalization: A Current Perspective, J Am Coll Cardiol, 12:103-5, 1988.

52. Gerrity RG, Loop FD, Golding LA, et al, Arterial Response of Laser Operation for Removal of Atherosclerotic Plaques, J Thorac Cardiovasc Surg, 85:409-21, 1985.

53. Sanborn TA, Laser Angioplasty, What has Been Learned From Experimental Studies and Clinical Trials?, Circulation, 78:769-74, 1988.

54. Litvack F, Grundfest WS, Papaioannou T, Mohr FW, Jakubowski AT, Forrester JS, Role of Laser and Thermal Ablation Devices in the Treatment of Vascular Diseases, Am J Cardiol 61:81G-86G, 1988.

55. Choy DSJ, Stertzer SH, Myler RK, Marco J, Fournial G, Human Coronary Laser Recanalization, Clin Cardiol 7:377-81, 1984.

56. Isner JM, Clarke RH, The Current Status of Lasers in the Treatment of Cardiovascular Disease, IEEE JQE QE20:1406, 1984.

57. Cothren RM, Hayes GB, Kramer JR, Sacks B, Kittrell C, Feld MS, A Multifiber Catheter with an Optical Shield for Laser Angiosurgery, Lasers in the Life Sciences, 1:1, 1986.

58. Kjellstrom BT, Cothren RM, Kramer JR, The Use of Lasers in Vascular and Cardiac Surgery, Acta Chir Scand, 153:493-99, 1987.

59. Lee G, Chan MC, Garcia JM, Pichard AD, Corso PJ, Hannah H III, Reis RL, Mason DT, Effects of Coronary Laser Radiation, in Waller BF, ed, Contemporary Issues in Cardiovascular Pathology, FA Davis Co, Philadelphia, 1988.

60. Cothren R, LAS: A Look form the Laboratory, Plenary Session, SPIE Symposium on Medical Applications of Lasers, Fiber-Optics, and Electro-Optics, Los Angeles CA, January, 1990.

61. Bell RY, Carpenter KLH, Mitchinson MJ, What is the Significance of Ceroid in Human Atherosclerosis?, Arch Pathol Lab Med, 111:1134-40, 1987.

62. American Cancer Society, 1986 Cancer Facts and Figures, American Cancer Society, New York, 1986.

63. Nowell PC, Mechanisms of Tumor Progression, Cancer Research, 46:2203-07, 1986.

64. Muto T, Bussey JR, Morson BC, The Evolution of Cancer of the Colon and Rectum, Cancer, 36:2251-70, 1975.

65. Koss LG, Tumors of the Urinary Bladder, Armed Forces Institute of Pathology, Washington DC, 1974.

66. Gilbertson V, Colon Cancer Screening - the Minnesota Experience, Gastrointest Endosc 26(S):31s-32s, 1980.

67. Williams CB, Price AB, Colon Polyps and Carcinoma, Chapt. 45 in, Sivak M, Gastroenterologic Endoscopy, WB Saunders Co, Philadelphia, p. 921-45, 1987.

68. Crowson TD et al, Colonoscopy: Inefficiency for Early Carcinoma Detection in Patients with Ulcerative Colitis, JAMA, 236:2651-52, 1976.

69. Wallace DMA, Hinkmarsh JR, Webb NJ, Busutt JA, Hargrave TB, Newsome JE, Chisholm GD, The Role of Multiple Mucosal Biopsies in the Management of Patients with Bladder Cancer, Br J Urol, 51:535, 1979.

70. Robbins SL, Cotran RS, Kumar V, Pathologic Basis of Disease, WB Saunders Co., Philadelphia, p. xxx, 1984.

71. Kewenter J, Ahlman H, Hulten L, Cancer Risk in Extensive Ulcerative Colitis, Ann Surg, 188:824-28, 1978.

72. Collins RH Jr, Feldman M, Fortran FS, Colon Cancer, Dysplasia and Surveillance in Patients with Ulcerative Colitis, NEJM, 316"654, 1987.

73. Devroede GJ, Tayler WF, Saver WB, et al, Cancer Risk and Life Expectancy of Children with Ulcerative Colitis, NEJM, 285:17, 1971.

74. Greenstein AJ, Sachar DB, Smith H, et al, Cancer in Universal and Left-sided Ulcerative Colitis: Factors Determining Risk, Gast End 77:290, 1979.

75. Ritchie JK, et al, Prognosis of Carcinoma in Ulcerative Colitis, Gut, 22:752, 1981.

76. Bonnevie O, Binder V, Anthonisen P, Riis P, The Prognosis of Ulcerative Colitis, Scand J Gastroenterol, 9:81-91, 1974.

77. Bauer JJ, Gelernt IM, Salky B, Kreel I, Sexual Dysfunction after Protocolectomy for Inflammatory Bowel Disease, Gastroenterology 78:1138A, 1980.

78. Riddell RH, Hodman H, Ransohoff DF et al, Dysplasia in Inflammatory Bowel Disease: Standardized Classification with Provisional Clinical Applications, Hum Pathol, 14:931, 1983.

79. Lennard-Jones JE, Ritchie JK, Morson BC, Williams CB, Cancer Surveillance in Ulcerative Colitis Experience over 15 Years, Lancet, July 16:149-52, 1983.

80. Rosenstock E, Farmer RG, Petras RE, et al, Surveillance for Colonic Carcinoma in Ulcerative Colitis, Gast End, 89:1342, 1985.

81. Petras RE, Non-Neoplastic Intestinal Disease, in Sterburg SS, ed, Diagnostic Surgical Pathology, New York, p. 993-95, 1989.

82. Robbins SL, Cotran RS, Kumar V, Pathologic Basis of Disease, WB Saunders Co., Philadelphia, p. 1062-80, 1984.

83. Koss LG, Evaluation of Patients with Carcinoma in situ of the Bladder, Pathol Annu, 17:353, 1982.

84. Murphy WM, Diseases of the Urinary Bladder, Urethra, Ureters and Renal Pelvis, in Murphy WM ed, Urological Pathology, WB Saunders Co, Philadelphia, p. 68-73, 1989.

85. Farrow GM, Utz DC, Rife CC, Greene LH, Clinical Observation is 69 Cases of in situ Carcinoma of the Urinary Bladder, Cancer Res, 37:2794, 1977.

86. Farrow GM, Pathologist's Role in Bladder Cancer, Seminars in Oncol 6:198-206, 1979.

87. Badalament RA, Kimmel M, Gay H et al, The Sensitivity of Flow Cytometry Compared with Conventional Cytology in the Detection of Superficial Bladder Carcinoma, Cancer, 59:2078-85, 1987.

88. Wallace DMA, Hindmarsh JR, Webb JN, et al, The Role of Multiple Mucosal Biopsies in the Management of Patients with Bladder Cancer, Brit J Urol, 51:535-40, 1979.

89. Murphy WM, Nagy GK, Rao MK, Soloway MS, Parija GC, Cox CE, Friedel GH, Normal Urothelium in Patients with Bladder Cancer, Cancer, 44:1050, 1979.

90. Soloway MS, Bicknell L, Role of Selected Mucosal Biopsy in the Evaluation of Patients with Bladder Cancer, in Bladder Cancer, Part A: Pathology, Diagnosis and Surgery, Alan R. Liss, New York, p. 275-81, 1984.

91. Paulson DF, Avoiding Complications with Radical Cystectomy in Bladder Cancer, in Bladder Cancer, Part A: Pathology, Diagnosis and Surgery, Alan R. Liss, New York, p. 409-34, 1984

92. Ellis Bell J, Fluorescence: Solution Studies, in Ellis Bell J, ed, Spectroscopy in Biochemistry, Volume I, CRC Press, Boca Raton, Florida, p. 155-94, 1981.

93. Mayevsky A, Chance B, Intracellular Oxidation-Reduction State Measured in situ by a Multi-channel Fiber-optic Surface Fluorometer, Science, 217:537-40, 1982.

94. Ball RY, Carpenter KL, Mitchinson MJ, What is the Significance of Ceroid in Human Atherosclerosis?, Arch Pathol Lab Med, 111:1134-39, 1987.

95. Kittrell C, Wiliet RL, de los Santos-Pacheo C, Ratliff NB, Kramer JR, Malk EG, Feld MS, Diagnosis of Fibrous Atherosclerosis using Fluorescence, Applied Optics, 24:2280-81, 1985.

96. Deckelbaum LI, Lam JK, Cabin HS, Soni Clubb K, Long MB, Discrimination of Normal and Atherosclerotic Aorta by Laser Induced Fluorescence, Lasers in Surgery and Medicine, 7:330-35, 1987.

97. Deckelbaum LI, Laser Induced Fluorescence Spectroscopy, Seminar on Lasers in Biomedical Research, Wellman Laboratories, Mass. General Hospital, Boston, MA, Oct. 24, 1989.

98. Clarke RH, Isner JM, Gauthier T, Nakagawa K, Cerio F, Hanion E, Gaffney E, Rouse E, DeJesus S, Spectroscopic Characterization of Cardiovascular Tissue, Lasers in Surgery and Medicine, 8:45-59, 1988.

99. Gaffney EJ, Clarke RH, Lucas AR, Isner JM, Correlation of Fluorescence Emission with the Plaque Content and Intimal Thickness of Coronary Arteries, Lasers in Surgery and Medicine, 9:215-28, 1989.

100. Alfano RR, Tata DB, Cordero J, Tomashefsky P, Longo FW, Alfano M, Laser Induced Florescence Spectroscopy from Native Cancerous and Normal Tissue, IEEE JQE, QE20:1507-11, 1984.

101. Alfano RR, Tang GC, Pradhan A, Bleich M, Choy DSC, Opher E, Steady State and Time-Resolved Laser Fluorescence from Normal and Tumor Lung and Breast Tissues, J Tumor Marker Oncology, 3:165-74, 1988.

102. Alfano RR, Tang GC, Pradhan A, Lam W, Choy DSC, Opher E, Fluorescence Spectra from Cancerous and Normal Human Breast and Lung Tissues, IEEE JQE, QE23:1806-11, 1987.

103. Ghadially FN, Neish WJP, Porphyrin Fluorescence of Experimentally Produced Squamous Cell Carcinoma, Nature, 185:1124, 1960.

104. Ghadially FN, Red Fluorescence of Experimentally Induced and Human Tumors, J Path Bact, 80: 345-51, 1960.

105. Ghadially FN, Neish WJP, Dawkins HC, Mechanisms Involved in the Production of Red Fluorescence of Human and Experimental Tumors, J Path Bact, 85:77-92, 1963.

106. Harris DM, Werkhaven J, Endogenous Porphyrin Fluorescence in Tumors, Lasers in Surgery and Medicine, 7:467-72, 1987.

107. Montan S, Stromblad LG, Spectral Characterization of Brain Tumors Utilizing Laser-Induced Fluorescence, Lasers in the Life Sciences, 1:275-85, 1987.

108. Yakshe PN, Bonner RF, Patterson R, Leon MB, Fleischer DE, Laser-Induced Fluorescence Spectroscopy: Can it be Used in the Diagnosis and Treatment of Colonic Malignancy?, (Abstract) Am J Gastroenterol, 84:1199, 1989.

109. Kapadia CR, Cutruzzolo FW, O'Brien KM, Stets ML, Enriquez R, Deckelbaum LI, Detection of Adenomatous Transformation of Colonic Mucosa by Fiber-Optic Laser-Induced Fluorescence Spectroscopy, (Abstract) Gastroenterol, 94:A216, 1988.

110. Sundstrom F, Fredriksson K, Montan S, Hafstrom-Bjorkman, Strom J, Laser-Induced Fluorescence from Sound and Carious Tooth Substance: Spectroscopic Studies, Swed Dent J, 9:71-80, 1985.

111. Christian GD, Callis JB, Davidson ER, in Wehry EL, ed, Modern Fluorescence Spectroscopy, Vol. 4, Plenum Press, New York, Ch. 4, 1981.

112. Wolfbeis OS, Leiner M, Mapping of the Total Fluorescence of Human Blood Serum as a New Method for its Characterization, Analytic Chimica Acta, 167:203-15, 1985.

113. Campbell ID, Dwek RA, Biological Spectroscopy, The Benjamin Cummings Publishing Co., Menlo Park, California, p. 7-36, 1984.

114. Jacques SL, Prahl SA, Modeling Optical and Thermal Distributions in Tissue During Laser Irradiation, Lasers in Surgery and Medicine 6:494-503, 1987.

115. Keijzer M, Richards-Kortum RR, Jacques SL, Feld MS, Fluorescence Spectroscopy of Turbid Media: Autofluorescence of the Human Aorta, Applied Optics, 28:4286-92, 1989.

116. Robbins SL, Cotran RS, Kumar V, Pathologic Basis of Disease, WB Saunders Co., Philadelphia, p. 502-546, 1984.

117. Segel IH, Biochemical Calculations, 2nd Ed, John Wiley and Sons, New York, p. 324-52, 1976.

118. Ishimaru I, Wave Propagation and Scattering in Random Media, Vol. I, Academic Press, New York, 1978.

119. Welch AJ, Yoon G, van Gemert MC, Practical Models for Light Distribution in Laser Irradiated Tissue, Lasers in Surgery and Medicine, 6:488-93, 1987.

120. Flock ST, Patterson MS, Wilson BC, Wyman DR, Monte Carlo Modeling of Light Propagation in Highly Scattering Tissues - I: Model Predictions and Comparisons with Diffusion Theory, IEEE Transactions in Biomedical Engineering, 36:1162-68, 1989.

121. Harris EK, Albert A, Multivariate Interpretation of Clinical Laboratory Data, Decker, New York, 1987.

2: Common Experimental and Data Analysis Methods

In applying our method of algorithm development to the three specific clinical conditions detailed in Chapter One, many of the same tissue handling protocols, experimental procedures, and methods of data analysis were followed. This chapter contains a summary of these common methods; experimental results and conclusions are presented individually in Chapters Three, Four and Five.

2.1: Tissue Handling Protocols

All tissues studied in this thesis were human. Tissues were studied both *in vivo*, in the living organism, and *in vitro*, or in the laboratory. In all cases, studies were initially carried out *in vitro*, to determine if fluorescence spectroscopy could be used to differentiate normal and pathologic tissues under easily accessible, controlled conditions. If promising results were obtained in the laboratory, clinical studies were initiated to develop methods of making spectroscopic measurements *in vivo* and to determine if algorithms developed *in vitro* could be applied in the living patient.

Tissues studied *in vitro* were obtained from two sources - whenever possible samples were obtained from surgically resected human organs, in other cases samples were obtained from human cadavers at autopsy. There are several fundamental differences between these tissues and tissue in the living patient. The most important difference is that these tissues studied *in vitro* are no longer alive, because they are no longer perfused. This implies that respiration and metabolism have ceased, and that the degradative processes of autolysis have begun [1].

In all cases, we have attempted to minimize the effects of autolysis so that *in vitro* studies will yield information which is relevant for application in the living patient. As autolysis progresses with time [1], every effort was made to obtain samples for study *in vitro* as quickly as possible following tissue death. In cases where samples were obtained from surgical resections this was usually accomplished within 1 hour of tissue death. When samples were obtained at autopsy this was usually within 24 hours of tissue death. For this reason, surgical samples were considered preferable; however, they were not always obtainable, as in the case of normal aorta. To halt the process of autolysis, upon receipt, samples were immediately frozen and stored at -70° C until use [2].

At the time of study, samples were warmed to room temperature, and were kept moist in a buffered (50 mM TRIS), pH = 7.4, isotonic saline solution (140 mM), in an attempt to mimic the lumen environment *in vivo* as closely as possible.

We have determined that the freezing process does not alter the fluorescence lineshape of human aorta at 476 nm excitation. In addition, following *in vitro* studies, all samples were submitted for histologic analysis; in most cases, only minimal autolytic changes were present. Data from samples displaying severe autolysis were discarded. It should be noted that these autolytic effects were most prominent in gastro-intestinal tissues, and least prominent in arterial tissues, reflecting the different autolytic propensities of these tissues.

2.2: Experimental Methods

Experimental methods of recording tissue fluorescence properties are summarized here. The method of recording fluorescence excitation emission matrices (EEMs), in order to survey the spectroscopic properties of tissue over a wide range of UV and visible excitation and emission wavelengths, is first described. Methods used to measure tissue fluorescence emission spectra at excitation wavelengths indicated from a comparison of the fluorescence EEMs of normal and pathologic tissues are then described. Particular emphasis is given to methods which can be easily adapted for use *in vivo* in real time. Finally, methods of fluorescence microscopy and microspectroscopy, for use in determining the histochemical basis of tissue fluorescence at selected excitation wavelengths, are described

2.2.1: Fluorescence EEMs

A fluorescence EEM is a matrix containing the fluorescence intensity as a function of excitation and emission wavelength. Fluorescence EEMs of arterial tissue were constructed from a series of fluorescence emission spectra collected at excitation wavelengths (λ_{exc}) varying from 250 to 550 nm in 10 nm steps. For each emission spectrum, fluorescence intensities were recorded at 10 nm intervals of emission wavelength (λ_{em}) over the range

$$[\lambda_{exc} + 10\text{ nm}] < \lambda_{em} < [2\lambda_{exc} - 10\text{ nm}] \text{ or } [700\text{ nm}].$$

At each emission wavelength, fluorescence signal was integrated for a 1 s interval. For

gastro-intestinal and urinary bladder tissues, excitation wavelength was varied from 250 - 500 nm in 10 nm steps; emission intensities were recorded in 5 nm intervals of emission wavelength over the range:

$$[\lambda_{exc} + 10\text{ nm}] < \lambda_{em} < [2\lambda_{exc} - 10\text{ nm}] \text{ or } [700\text{ nm}].$$

Emission spectra were collected using a standard spectrofluorimeter. Figure One shows a schematic diagram of the instrument. Excitation light was incident perpendicular to the lumenal surface of the tissue; emission light was collected at a 23° angle with respect to the excitation beam. The instrument was modified to yield an excitation beam size of approximately 2 x 3 mm at the tissue. In these experiments, the spectral resolution of the excitation monochromator was 2 nm FWHM, that of the emission monochromator was 4 nm FWHM.

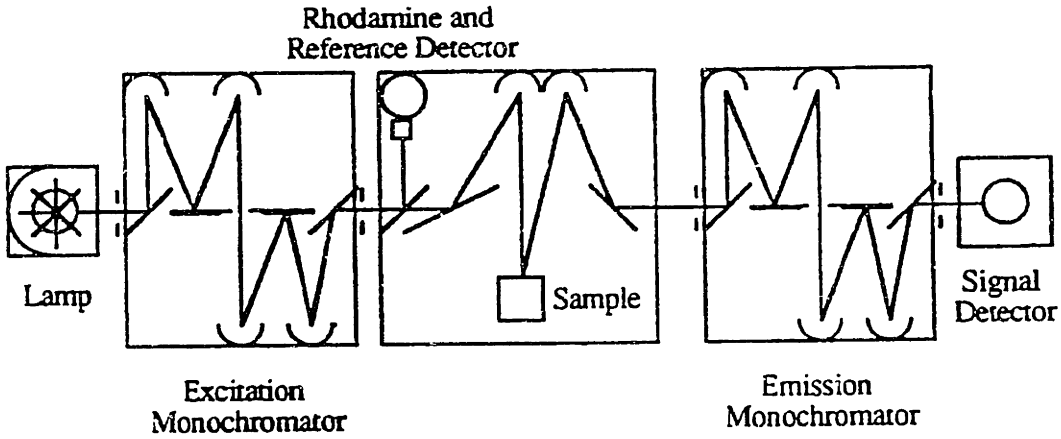

Figure 1: Schematic diagram of the spectrofluorimeter used to record fluorescence EEMs.

The incident intensity varied with excitation wavelength, but was always less than 40 $\mu W/mm^2$. Variations in the incident intensity were corrected for by ratioing the fluorescence emission of the sample to that of a standard 1 cm reference cuvette containing 8 µg/L of Rhodamine B in reagent grade propylene glycol [3]. Total collection of a fluorescence EEM required approximately 1 and 1/2 hours. To minimize the exposure of tissue to excitation light during this procedure, a shutter was employed, so that light was incident on tissue only during the time which fluorescence emission was being recorded. Emission spectra were collected in order of increasing excitation wavelength, with the 250 nm excited spectrum collected first. To monitor for

photobleaching, a 250 nm excited spectrum was recorded again following collection of the EEM. In all cases, deviations between the first and last 250 nm excited spectrum were less than 5%.

To correct for slight day to day variations in the throughput of the system, absolute fluorescence intensities were calibrated daily using a standard fluorescent filter. Fluorescence intensities are reported here in arbitrary units relative to the intensity of this standard. All spectra have been corrected for the non-uniform spectral response of the spectrofluorimeter. These correction curves were obtained by recording the emission spectrum of a calibrated tungsten filament lamp.

EEMs are presented here as fluorescence contour maps, where emission wavelength is on the abscissa, excitation wavelength is on the ordinate, and contour lines connect points of equal fluorescence intensities.

2.2.2: Fluorescence Emission Spectra

2.2.2.1: Fluorimeter

The spectrofluorimeter described above was also used to measure tissue fluorescence emission spectra at excitation wavelengths ranging from 250 - 550 nm. Here, emission spectra are reported with 290, 330, 370 and 476 nm excitation. In all cases, emission intensity was recorded at 1 nm intervals from 10 nm past the excitation line to 580 nm for 290 nm excitation, to 650 nm for 330 excitation, or to 700 nm for 370 and 476 nm excitation. The fluorimeter was used under the conditions reported above, except in some cases the incident beam size was approximately 10 x 3 mm, and in others was approximately 2 x 3 mm. Because of this variation in incident spot size, all data collected with this instrument was normalized to unity at a specified emission wavelength.

It should be pointed out that the collection geometry of the fluorimeter in Fig.1 is not well defined; fluorescent light is collected from a large, ill-defined surface area of the sample. This collection geometry is typical for conventional fluorimeters. In general, this is not a problem for dilute samples, which do not scatter light. However, the fluorescence spectra of turbid samples, such as human tissue, are extremely dependent on the excitation and collection geometry of the detector [4,5]. It has been shown that the contribution of attenuation to the fluorescence spectrum of turbid samples is enhanced as the sample surface area from which fluorescence is collected is increased relative to the area which is illuminated [4,5]. This has two important implications: (1) the contribution

of attenuation to tissue fluorescence spectra can be altered by changing the excitation/collection geometry; and (2) to obtain comparable results with different detection systems requires that the systems have similar, well-defined collection geometries [4].

2.2.2.2: Spectral Catheter

Special systems were developed which could easily be adapted to record and analyze entire tissue fluorescence spectra *in vivo* in real (or near real) time. To allow remote sensing of fluorescence, a spectral catheter containing optical fibers was designed and constructed. In designing this device, because of the above considerations, the geometry of delivery of excitation light and collection of resulting fluorescent light was carefully considered.

The fluorescence signal from turbid samples, such as human tissue, is dependent on this geometry [4, 5]; obtaining reproducible results depends on the control of this geometry. It will be shown in Chapter Three that in arterial tissue, the diagnostically useful information in the fluorescence spectrum is primarily related to the fluorophores; thus, the collection geometry of this catheter was chosen so that attenuation effects in the fluorescence spectrum would be minimized [4,5]. As shown in [4], this consists of a geometry in which tissue fluorescence is collected from only that surface area directly illuminated by excitation light.

Two different systems were used to record tissue fluorescence emission spectra at several selected excitation wavelengths. The first system described was utilized to record spectra at 476 nm excitation. In this system, a continuous wave (CW) argon ion laser was used to provide excitation light, and a scanning monochromator and photo-multiplier tube (PMT) were used to measure the fluorescence intensity as a function of emission wavelength. With this system, fluorescence spectra with good signal to noise ratio (S/N) could be collected in less than a minute[1]. The second system used a pulsed laser system to provide excitation light at 319.9, 369.9 and 435.7 nm; a monochromator and optical multi-channel analyzer (OMA) were used to record an entire fluorescence spectrum within a single pulse of the excitation laser.

---

[1]Here, S/N ratios are given as peak signal divided by peak to peak noise. For the purposes of this thesis 'good' S/N will be used to mean S/N > 20. This value was chosen experimentally - given peak widths typical for tissue, with this S/N, closely overlapping peaks could be fairly well resolved visually.

2.2.2.2.1: 476 nm Excitation

Figure 2 shows a block diagram of the system used *in vitro* to record tissue fluorescence spectra at 476 nm excitation. This system consists of an argon-ion laser, used to provide 476 nm light, an optical fiber laser catheter and a scanning monochromator and photomultiplier tube. The optical fiber laser catheter consists of seven optical fibers, encased in a transparent quartz shield. The central fiber, coupled to the laser, provides a 1 mm diameter spot of excitation light at the surface of the shield. This optical shield was placed in contact with tissue in order to collect fluorescence spectra. Six collection fibers, surrounding the central fiber, are arranged so that each views only the spot illuminated by the central fiber, and are used to collect tissue fluorescence. The distal ends of these fibers are coupled to the entrance slits of the monochromator. The well defined collection geometry of this system represents a substantial improvement over that of typical spectrofluorimeters, in which the collection geometry is not well defined and which record signals from turbid samples that can be significantly distorted by attenuation [4, 5].

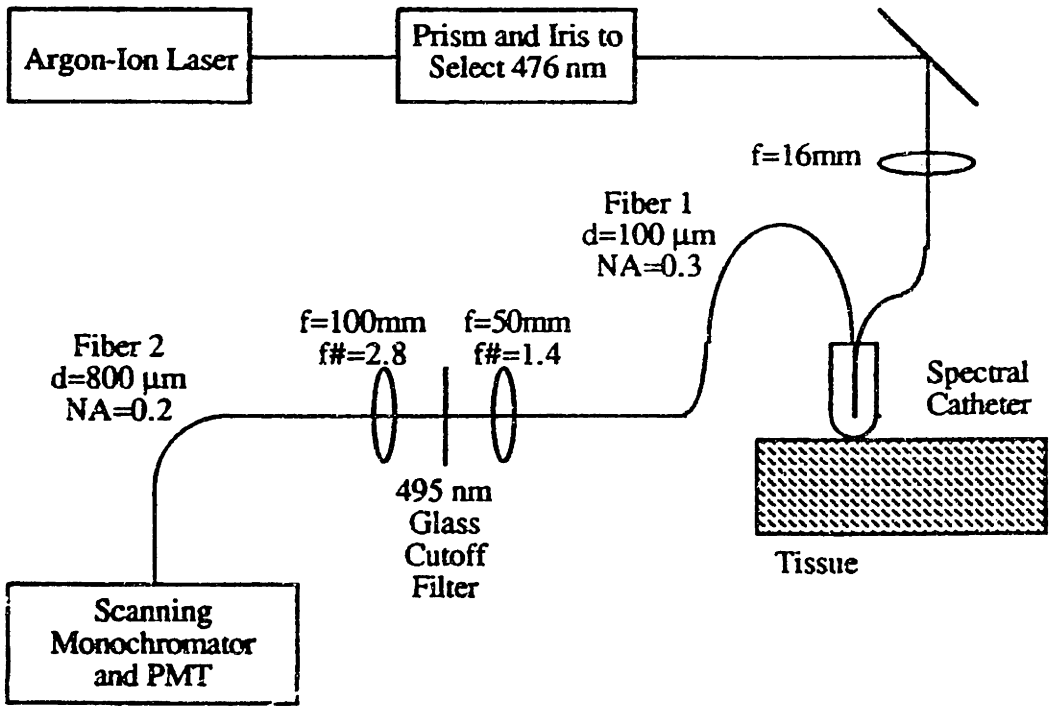

Figure 2: Block diagram of the system used to collect tissue fluorescence spectra of tissue *in vitro* at 476 nm excitation.

Fluorescence emission intensity was recorded at 0.5 nm intervals from 500 - 650 nm. Spectral resolution of the detector was 6 nm FWHM. A time constant of 250 msec was used to record all data. For all spectra obtained *in vitro*, an excitation intensity of 100 $\mu W/mm^2$ was used; data collection time was 40 seconds. Thus, tissue samples were exposed to a fluence of 4 mJ/mm^2 per spectrum recorded. This is well below the value of 80 mJ/mm^2 required to produce significant laser induced alteration of tissue spectral properties at this excitation wavelength [6].

The total throughput of this detection system has been estimated as $5x10^{-7}$; the single greatest loss in signal occurs as fluorescent light enters the spectral catheter. The throughput of the spectral catheter for fluorescent light is $1x10^{-3}$ [7]. Variations in the day to day throughput of the system were corrected for by regularly recording the fluorescence intensity of a calibrated standard. Tissue fluorescence intensities are presented relative to the intensity of this standard. All data has been corrected for the non-uniform spectral response of the detection system using correction curves obtained with a calibrated tungsten filament lamp.

2.2.2.2.2: 320, 370, and 436 nm Excitation

Figure 3 shows a block diagram of the system used *in vitro* to record emission spectra of tissue at 319.9, 369.9, and 435.6 nm excitation. This system consists of a pulsed Nd:YAG laser, an optical fiber catheter used to deliver excitation light to the tissue and collect resulting fluorescence, and an imaging spectrograph and optical multi-channel analyzer used to record fluorescence intensity as a function of emission wavelength.

The Nd:YAG laser provided 8.5 ns pulses of 1064 nm radiation at a repetition of 10 Hz. This light was frequency doubled using KDP crystals to provide 532 nm radiation. The 532 nm light was then used to pump a 1 m long cell filled with H_2 gas at a pressure of 150 psi. Stimulated Raman scattering is a well known technique which can be used to produce co-linear light at a series of wavelengths shifted up and down in frequency from the excitation frequency by an integer multiple of the frequency corresponding to the strongest Raman transition of the gas [8]. The frequency corresponding to the strongest Raman transition of H_2 gas is 4155 cm^{-1}; with 532 nm excitation, the first three anti-Stokes lines are at wavelengths of 435.7, 369.9 and 319.9 nm. Light at any one of these wavelengths was isolated using a Pellin-Broca prism and a 10 nm wide interference filter centered near the wavelength of interest.

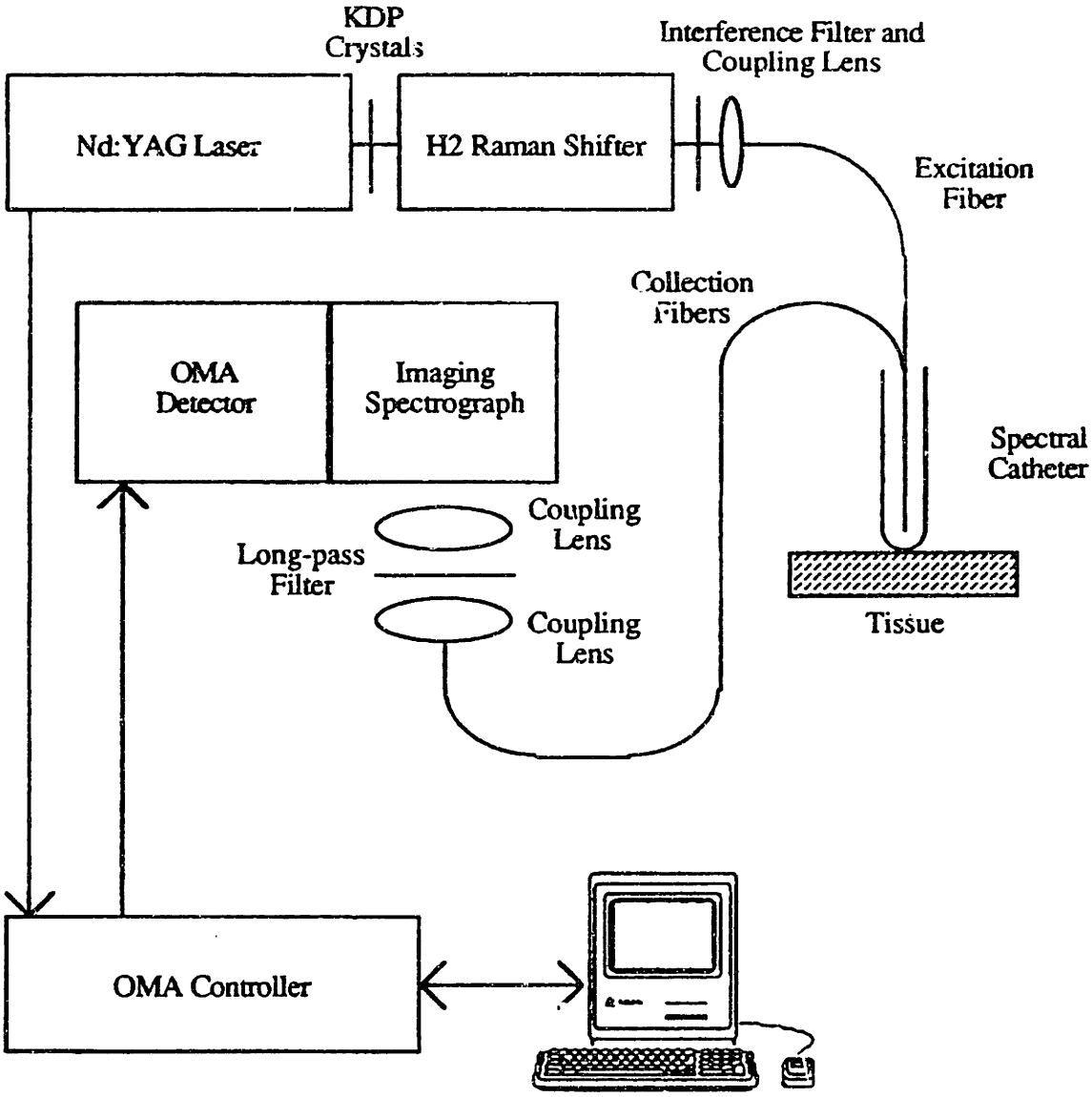

Figure 3: Block diagram of the system used to record fluorescence spectra of tissue *in vitro* at 319.9, 369.9 and 435.7 nm excitation.

This monochromatic excitation light was focused into the central fiber of a 10 fiber, shielded, optical fiber catheter. All fibers had a quartz core, and were capable of transmitting light from 300-700 nm efficiently. The central fiber was used to provide a 1.0 mm diameter illumination spot at the distal tip of the optical shield. This optical shield was placed in contact with tissue in order to collect fluorescence spectra. Tissue fluorescence was collected with the nine optical fibers surrounding the central fiber. These collection fibers were arranged so that each fiber collected fluorescence only from

the surface area of tissue directly illuminated by excitation radiation, providing a well defined collection geometry [4,5].

The proximal tips of the collection fibers were imaged onto the entrance slit of an imaging spectrograph. A long pass cutoff filter with a 50% transmission wavelength 20 nm longer than the excitation wavelength was placed before the entrance slits and was used to reject scattered excitation radiation. This polychromator dispersed the incident light and conducted it to a linear array of 1024 photodiodes. An emission spectrum was formed by reading the diode array following a 0.5 s collection period. During this collection period, the image at the diode array was intensified for 100 ns; intensification was gated off the leading edge of the excitation pulse. To achieve better S/N, a single emission spectrum was formed from the sum of 100 such consecutive accumulations for each sample.

The diode array covered the spectral range from approximately 175 to 820 nm, with a diode spacing corresponding to a spectral spacing of 0.63 nm. The spectral resolution of the system was approximately 3 nm FWHM. The excitation pulse energy, as measured at the distal tip of the catheter, varied slightly with excitation wavelength; at 435.7 nm, the energy was approximately 200 nJ/pulse. In collecting a single spectrum, the tissue was exposed to 500 excitation pulses, corresponding to a total fluence of 0.13 mJ/mm^2 at 435.7 nm. This is well below the threshold of 80 mJ/mm^2 required to produce laser induced alteration of tissue spectral properties at 476 nm excitation [6]. In principle, spectra with similar S/N could be collected more rapidly, in fewer excitation pulses, by increasing the excitation intensity. To ensure that no photobleaching occurred at the excitation wavelengths used in this study, for all tissue samples, two successive spectra were recorded using the parameters described here. In all cases, differences in the first and second spectra were less than 5%.

Variations in the excitation intensity at different excitation wavelengths and in the day to day throughput of the system were corrected for by recording the fluorescence intensity of a calibrated standard every time the excitation wavelength was changed. This standard consisted of a 1 cm cuvette filled with a solution of 8.0 g/L rhodamine B in reagent grade propylene glycol [3]. Tissue fluorescence intensities are presented relative to the intensity of this standard. All data has been corrected for the non-uniform spectral response of the detection system.

2.2.3: Fluorescence Microscopy

In order to establish the basis of tissue autofluorescence at the morphologic level, techniques of fluorescence and light microscopy were used. To establish the morphologic identity of fluorescent structures within tissue, the autofluorescence of tissue frozen sections was observed visually, and documented photographically, with a fluorescence microscope. Serial sections were stained with histochemical stains and viewed through the light microscope to establish the morphologic basis of tissue fluorescence. To measure the fluorescence emission spectra of chromomorphs identified with this method a microspectrofluorimeter was constructed. This fluorimeter could be used to record fluorescence emission spectra of areas of tissue as small as 10 μm x 10 μm. These techniques will be described in more detail here.

2.2.3.1: Photographic

Figure 4 shows a block diagram of a typical, epi-illuminated, fluorescence microscope. Narrow band excitation light is typically provided by a mercury lamp, with an interference filter to select a narrow range of the spectrum. This light is reflected through the objective using a dichroic mirror which reflects all light incident at a 45° angle below a cutoff wavelength slightly longer than the emission wavelength. Tissue fluorescence is collected through the same objective, but since the fluorescence emission occurs at a longer wavelength than the excitation, it is transmitted through the dichroic mirror. A barrier filter or long pass filter with a 50% transmission wavelength slightly longer than the excitation wavelength is also used to more fully reject scattered excitation light. The fluorescent light transmitted through the dichroic mirror and barrier filter is then directed to the eyepieces of the microscope where it can be viewed, or to a trinocular port or camera port where it can be recorded photographically.

This type of fluorescence microscope, or a variation of it, was used to determine the color, intensity, and distribution of fluorescing structures within arterial, gastro-intestinal and urinary bladder tissues. The specific experimental parameters varied in each case, and will be described in detail in Chapters Three, Four and Five.

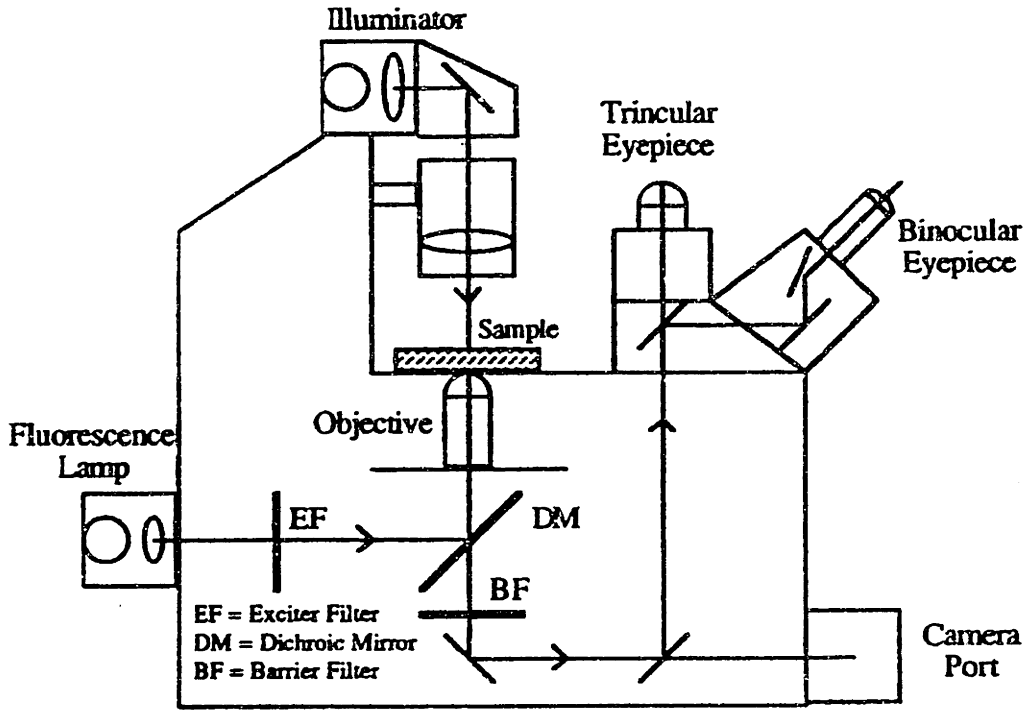

Figure 4: Block diagram of a typical epi-illuminated fluorescence microscope.

2.2.3.1.1: Correlation with Histochemical stains

In order to determine the morphologic identity of the fluorescent structures identified with the fluorescence microscope, serially stained sections were viewed through the light microscope. Two stains were primarily used to achieve this morphologic identity.

2.2.3.1.1.1: Hemotoxylin and Eosin

In cells stained with hemotoxylin and eosin (H&E), basophilic substances stain blue with hemotoxylin, while acidophilic substances stain pink with eosin [1]. In particular, DNA stains blue, while RNA stains pink, giving the nucleus a characteristic purple color [1]. Structural proteins are acidophilic, and appear pink with this stain [1]. Eosinophils also contain granules which stain vividly with eosin [1].

2.2.3.1.1.2: Movat's Pentachrome

Movat's I pentachrome stain consists of five dyes: acid fuchsin, which stains elastic tissues deep purple to black; alcian blue which stains ground substance aqua; saffran, which stains collagen fibers yellow; crocein scarlet red which stains muscle red; and iron hematoxylin, which stains DNA deep blue to purple [9].

2.2.3.2: Spectroscopic

Figure 5 shows a block diagram of the microspectrofluorimeter used to collect emission spectra of tissue chromomorphs. This system consists of an epi-illuminated, inverted fluorescence microscope (Fig 4), which is coupled to a conventional spectrofluorimeter (Fig. 1). Narrow-band excitation light from the fluorimeter is collimated and directed onto the dichroic mirror of the fluorescence microscope. This excitation light is focused onto the sample using the microscope objective. The same objective is used to collect the resulting fluorescence. The sample is imaged at either the binocular or trinocular microscope eyepieces. When the image is directed to the trinocular eyepiece, an 800 μm core, 0.2 NA optical fiber, placed at the conjugate image formed outside this eyepiece, collects the fluorescent light. The distal end of this optical fiber is placed at the entrance slit to the collection monochromator of the spectrofluorimeter, enabling fluorescence intensity to be recorded as a function of emission wavelength. The NA of the optical fiber is greater than the NA of the eyepiece, and matches the NA of the collection monochromator, so maximal collection efficiency is achieved. The double collection monochromator is sufficient to reject scattered excitation light, thus no barrier filter is required.

A magnified real image of the sample is formed within the fluorescence microscope. At this location, an aperture has been added to the fluorescence microscope. The size of this aperture can be varied, controlling the area of the sample from which autofluorescence is collected. By varying this aperture, fluorescence spectra with good S/N were collected from rectangular areas of tissue ranging in size from 100 μm x 100 μm to as small as 10 μm x 10 μm.

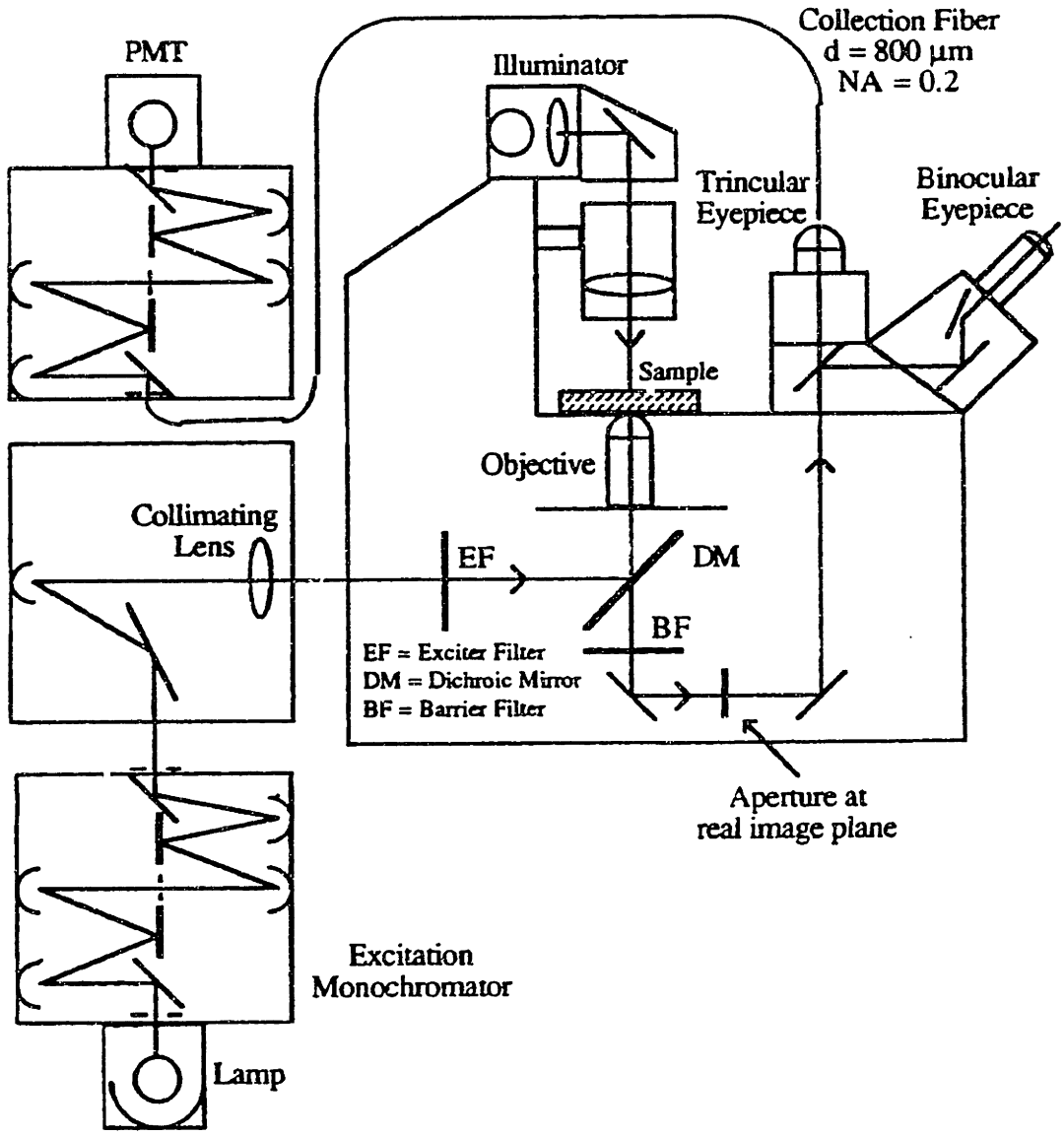

Figure 5: Block diagram of the microspectrofluorimeter.

Although the system was designed so that any excitation wavelength greater than 350 nm could be achieved, it was used here primarily at 370 nm excitation. The dichroic mirror was optimized for 370 nm excitation. At a 45° angle, it reflected 90% of light at 370 nm and below, it transmitted 90% of light at 410 nm and above. The resolution of the excitation source was 10 nm FWHM; the emission resolution was 5 nm FWHM. At 370 nm excitation, fluorescence spectra were collected primarily using a 40X dry objective (0.7 NA) and a 100X oil immersion objective (1.3 NA). The size of the field of view illuminated was 450 µm in diameter with the 40X objective and 180 µm in diameter with the 100X objective. Excitation intensity was 0.38 mW/mm^2 with the 40X objective

and 0.75 mW/mm^2 with the 100X objective. Fluorescence emission was recorded from 400 to 700 nm in 2 nm intervals. Signal was integrated for 1 s at each point. Total time required to obtain a fluorescence emission spectrum was approximately three minutes. This corresponds to a maximum total fluence of 135 mJ/mm^2, greater than that required to produce significant alterations in arterial tissue spectra at 476 nm excitation [6]. Fluorescence photobleaching was monitored for by recording two successive tissue spectra. In all cases, no alterations in the fluorescence lineshape of tissue chromomorphs was observed. However, a decrease in fluorescence intensity was sometimes observed. In most cases, this was 10% or less, but was sometimes as much as 30%. All data obtained with this system has been corrected for background fluorescence of a blank slide and for the non-uniform spectral response of the detection system.

2.3: EEM Analysis Methods

Fluorescence EEMs were recorded to compare the spectroscopic properties of normal and pathologic tissues over a wide range of UV and visible excitation wavelengths, to select those excitation wavelengths which are optimal for differentiating normal and diseased tissues, and to identify the tissue components which contribute to the fluorescence spectrum. A complete physico-chemical understanding of all features of a tissue fluorescence EEM is complicated, as multi-component absorption, scattering and fluorescence all contribute. Here, we present a simple method of analysis for achieving these goals with only simplified references to these processes.

2.3.1: Survey of Differences in Spectroscopic Properties of Normal and Pathologic Tissues

To determine the spectroscopic properties of normal and pathologic tissues from fluorescence EEMs, average EEMs were constructed for a small group of normal and pathologic tissues. A visual comparison of these average EEMs was made to determine whether any differences were present. In addition, the positions and intensities of all local excitation-emission maxima were compared. From these comparisons, excitation regions likely to be useful in discriminating the fluorescence of normal and pathologic tissues were identified. A drawback of this procedure is that it involves a vast amount of data reduction; some subtle differences, useful diagnostically, were not identified with this method.

2.3.2: Identifying Optimal Excitation Bands

A more sensitive method of comparison is to mathematically contrast all the information in the average EEMs of normal and pathologic tissues. One method to achieve this is to calculate the ratio and difference of the average fluorescence EEMs of normal and pathologic tissues. Both the ratio and difference maps can be used to detect differences in the intensity, position or bandwidth of a peak in a tissue EEM. As our results in Chapter Four will demonstrate, the ratio map is more sensitive to small differences in lineshape which are superimposed on backgrounds of similar intensity. The difference map, on the other hand, is particularly useful for detecting small absolute intensity differences in peaks with similar lineshapes.

We use the average ratio and difference maps to choose the optimal excitation wavelengths for diagnosing the presence of disease.[2] The average ratio and difference maps summarize all spectroscopic bands where the fluorescence properties of normal and diseased tissues differ. We wish to obtain the most complete set of diagnostic information with the minimum number of excitation wavelengths. A single excitation wavelength can be represented by a horizontal line on our contour map representations of EEMs. Thus, we can achieve our goal graphically by drawing the minimum number of horizontal lines which intersect (or are in the vicinity of) all local minima and maxima in the average ratio and difference maps. Because these peaks are broad, this can generally be accomplished with a small number of excitation lines.

2.3.3: Identifying Tissue Fluorophores and Attenuators

In general, tissue fluorescence spectra contain contributions from intrinsic fluorescence, absorption, and scattering. It is necessary to separate these effects in order to fully understand and interpret the tissue EEMs in terms of contributions from individual tissue chromophores. Definitive identification of chromophores from tissue EEMs requires a model of tissue fluorescence which incorporates these effects. This is a complicated task, however, preliminary identification of these components can be achieved with a much simpler method of analysis.

---

[2]The ratio or difference map could also be used to choose best emission wavelength(s) in principle. However, in a clinical setting, where obtaining fluorescence spectra in a short amount of time is important, currently, obtaining emission spectra is more practical than obtaining excitation spectra.

For purposes of comparison, we reduced the information in the average tissue EEMs to the positions and intensities of local excitation-emission maxima (peaks) and minima (valleys). This data reduction can also aid in preliminary identification of tissue fluorophores. Each fluorophore within the tissue can be characterized by its excitation-emission maxima. Thus, a simple method of identifying potential tissue fluorophores is to compare excitation/emission peaks in tissue EEMs to those in EEMs of individual tissue constituents as well as those for fluorophores cited in the literature.

Note, that the band positions of potential chromophores need not exactly match the band positions in tissue EEMs. Two effects may shift the observed position of the excitation-emission maxima. Absorption and scattering cause light attenuation; fluorescent light generated within tissue can be attenuated as it travels to the tissue surface where it can be detected. This process of attenuation can alter both the observed location of the excitation/emission maxima and observed lineshape of individual tissue fluorophores in the multi-component tissue EEMs. Similarly, the observed lineshapes and positions of chromophore maxima can be altered in multi-component tissue EEMs when the excitation and emission of individual chromophores closely overlap. For these reasons, identifications made with this method should be considered preliminary.

A similar method can be used to determine the identity of tissue attenuators from EEMs. Attenuation peaks act to produce valleys in the fluorescence emission spectra of optically thick tissue samples [4, 5]. In an EEM of tissue, the effect of an attenuation peak is to create valleys parallel to the excitation and emission wavelength axes, because both exciting radiation and emitted fluorescence are attenuated. Preliminary identification of tissue attenuators can be made by comparing the location of these valleys in tissue EEMs to total reflectance spectra of tissue constituents, absorption spectra of relevant molecules in a library of data which we are in the process of constructing, and a consideration of the available literature.

2.4: General Model of Tissue Fluorescence

In interpreting tissue fluorescence spectra, we wish to extract parameters which are related to the histochemical composition of tissue. Once the histochemical basis of fluorescence has been established for a particular tissue, this can be accomplished using a model which describes the composite fluorescence spectrum of tissue in terms of contributions from individual tissue components. Here, we present a general model of tissue fluorescence which can be applied to describe the UV and visible fluorescence

spectra of tissue given a spectroscopic characterization of individual tissue constituents. In subsequent chapters, this model is modified specifically for application to arterial and gastro-intestinal tissues.

2.4.1: General Features

In describing the fluorescence spectrum of any multi-component, inhomogeneous, turbid material such as human tissue, there are several general features a model must incorporate. These include describing the propagation of excitation and fluorescent light in the tissue in terms of contributions from individual tissue components, the conversion of absorbed light into fluorescent light for each individual tissue component, and the distribution of these components in tissue or tissue geometry.

2.4.1.1: Absorption, scattering, fluorescence

We are concerned primarily with three physical events which can occur as light propagates through tissue. These are elastic scattering, absorption and subsequent fluorescence. It is instructive to consider each of these in terms of molecular energy levels. When electromagnetic radiation is incident on a molecule, it interacts with the bound electron cloud [10]. If the frequency of the electromagnetic radiation is near the frequency corresponding to the energy difference between the ground and first excited electronic states, the molecule can absorb radiation, and make a transition to a vibrational level of the first excited state [10]. This procedure, known as absorption, removes some energy from the incident electromagnetic wave [10]. As discussed in Chapter 1, the excited molecule must somehow return back to the ground state, and can do so non-radiatively by a variety of pathways. However, the molecule can also lose energy via a radiative transition, in which it emits a fluorescence photon at a longer wavelength than the incident radiation [11].

If the frequency of incident electromagnetic radiation is significantly different than that associated with an electronic or vibrational transition, the incident radiation can transfer energy to the molecule, causing the molecular electron cloud to vibrate with respect to the nuclei [10]. These vibrating electrons may be thought of as oscillating electric dipoles, and as such they will reradiate electromagnetic energy at the same frequency as the incident radiation [10]. This emission will propagate out in the characteristic dipole pattern; thus, this process, known as elastic scattering, will change

the direction of propagation, but not the frequency of the incident electromagnetic wave [10].

Although this description is true for an isolated molecule, for an infinite, homogeneous array of small molecules, it is always possible to choose pairs of particles, for which the scattered light interferes destructively in all directions but the direction of the incident light [11]. The net result is that there is no observed scattering from such an array [11]. However, in a solution (one can view tissue as a turbid solution), molecules are always in motion, leading to local variations in concentration (and, thus, in refractive index) [11]. These fluctuations in refractive index lead to incomplete destructive interference for directions other than that of propagation, and scattering is observed [11].

This qualitative description shows that both absorption and scattering are dependent on the molecular energy levels, and that scattering is dependent on molecular geometry and local variations in refractive index. Although complex theories have been constructed to describe these processes in terms of molecular geometry and energy levels [10, 13], here we attempt only to experimentally determine the wavelength dependence of these processes. Thus, we characterize each tissue component by a wavelength dependent scattering and absorption coefficient, $\mu_s(\lambda)$ and $\mu_a(\lambda)$, and a phase function $p(\hat{s},\hat{s}')$ which characterizes the probability of scatter from an initial propagation direction $\hat{s}$, to a final direction of propagation $\hat{s}'$. The first moment of this phase function, g, is the average cosine of the scattering angle [13].

In addition, this qualitative picture shows that the occurrence of fluorescence requires absorption of radiation. Again, complex theories have been derived to describe the dependence of fluorescence on the wavelength of incident radiation and molecular energy levels [12]. However, here, we experimentally characterize the fluorescence properties of tissue components with two parameters, the quantum yield, ϕ, and the fluorescence lineshape $F(\lambda)$. Here, ϕ is a dimensionless parameter which represents the proportion of absorbed energy which is converted to fluorescence energy. The fluorescence lineshape is a normalized lineshape which describes the proportion of energy emitted at any specific wavelength.

In this work, we assume that absorption and scattering are dependent only on wavelength, thus, the same treatment can be used to describe the propagation of excitation and fluorescence radiation in tissue. In our description of tissue emission spectra, we neglect phosphorescence, inelastic scattering, energy transfer, and 'secondary'

fluorescence, or the emission of fluorescence following the reabsorption of a fluorescence photon generated within the tissue. Measurements of the lifetime of arterial tissue fluorescence are consistent with our assumption that phosphorescence is negligible [14]. Furthermore, we have observed no evidence of inelastic scattering processes in arterial, gastro-intestinal or urinary bladder tissues (an emission line separated from the excitation line by a constant energy difference [12]) at any of the excitation wavelengths studied in detail. Our approximate measurements of the tissue quantum yield [15] demonstrate that the intensity of 'secondary' fluorescence is sufficiently small that it can be neglected. In the region of excitation from 250 - 300 nm, we have observed evidence of energy transfer between tryptophan and tyrosine in the fluorescence spectra of arterial tissue [16]. This energy transfer is well known [11], and would have to be included in any model of tissue fluorescence in this excitation region. Here, we concentrate on excitation wavelengths above 300 nm. Finally, any mismatch in refractive index which may occur at the tissue surface has been neglected.

2.4.1.2: Multi-component samples

It is well known that human tissue contains many molecules which interact with UV or visible electromagnetic radiation. A model of tissue fluorescence can easily incorporate contributions from multiple components, by describing each component with five parameters: g, $\mu_s(\lambda)$, $\mu_a(\lambda)$, ϕ, and $F(\lambda)$. Again, energy transfer between these components is neglected.

2.4.1.3: Multi-layer samples

Finally, the distribution of these tissue constituents is inhomogeneous. However, it is well known that many tissues have a layered structure, and that within each layer of tissue, tissue components are distributed more homogeneously. Thus, in this work, inhomogeneities will be approximately incorporated by assuming tissue is composed of multiple layers, within which individual constituents are distributed homogeneously. In these models, the incident beam will always be assumed to be infinite in extent and with direction of propagation parallel to the surface normal. Fluorescence will be collected with an infinitely wide detector, parallel to the tissue surface. Thus, edge effects, which are important with finite excitation and detection [15], can be neglected[3].

---

[3]We have previously demonstrated [4, 7], that for the collection geometry of our optical fiber catheter, at 476 nm excitation in arterial tissue, edge effects can be neglected for excitation spot diameters greater than 100 μm. The excitation spot diameter in our spectral catheter is 1 mm, so this assumption is justified where the tissue absorption and scattering coefficients are similar to that of arterial tissue at 476 nm.

2.4.2: Attenuation of Light

With the considerations discussed above, we now turn to our method of model development. We consider tissue to be composed of layers, which each contain a homogeneous distributions of multiple components. These components can be characterized by five parameters: g, $\mu_s(\lambda)$, $\mu_a(\lambda)$, ϕ, and $F(\lambda)$. In order to utilize these assumptions to derive an expression which describes the composite tissue fluorescence power as a function of emission wavelength, $S(\lambda)$, it is necessary to consider in more detail how we can describe the propagation of light in tissue given the scattering and absorption coefficients and the phase function.

2.4.2.1: Equation of transfer

A consideration of light propagation in biological tissues must include multiple scattering events. Historically, two theories have been developed to describe light propagation in media of this type. The first is analytical theory, in which the starting point is Maxwell's equations [13]. In principle, this method is mathematically rigorous, in that it includes all multiple scattering, diffraction and interference effects. The second method is transport theory [13]. This method utilizes the transport equation to describe the transport of energy in multiple scattering media. It too, can be derived analytically with certain assumptions, the most important of which is that interference and diffraction effects are neglected. Although this method is less rigorous than the analytic method, it has been successfully used to describe the propagation of electro-magnetic radiation in the atmosphere, sea water, and photographic emulsions [13].

We define $I(\mathbf{r},\hat{s})$, the specific intensity, measured in $Wm^{-2}sr^{-1}Hz^{-1}$ to be the average intensity within a unit frequency, within a unit solid angle. The equation of transfer describes the behavior of this function within the multiply scattering medium, and is given by [13]:

$$(1)\ \frac{dI(\mathbf{r},\hat{s})}{ds} = -\mu_{tot}I(\mathbf{r},\hat{s}) + \frac{\mu_{tot}}{4\pi}\int_{4\pi} p(\hat{s},\hat{s}')I(\mathbf{r},\hat{s}')d\omega' + \varepsilon(\mathbf{r},\hat{s})$$

Here, μ_{tot} represents the sum of the absorption and scattering coefficients, and describes the reduction of the incident intensity due to absorption and scattering. In the second term, $p(\hat{s},\hat{s}')$ represents the phase function which describes the scattering from the $\hat{s}$

direction to the $\hat{s}'$ direction. This term describes the change in I due to scattering in and out of the direction and volume of interest. Finally, $\varepsilon(r,\hat{s})$ represents a source term due to emission within the volume ds [13].

In describing tissue fluorescence emission spectra with the equation of transfer, it is necessary to write eq. (1) for the excitation wavelength and for each emission wavelength of interest. For monochromatic excitation, Eq. (1), with $\varepsilon(r,\hat{s}) = 0$, describes the behavior of the incident intensity within the tissue. At emission frequencies, the source term at a given point in space, $\varepsilon(r,\hat{s})$, is proportional to the fluorophore concentration at that point, the excitation intensity at that point, the fluorophore absorption coefficient at the excitation wavelength, the fluorophore quantum yield and the value of the normalized fluorescence lineshape at the emission wavelength of interest (Eq. (2)). The factor of $1/4\pi$ arises because we assume isotropic emission of fluorescence.

$$(2)\ \varepsilon_{\lambda_{em}}(\vec{r},\hat{s}) = \frac{I_{\lambda_{exc}}(\vec{r},\hat{s})\mu_a \Phi F(\lambda_{em})}{4\pi}$$

Although these equations have been written for only a single component, they can easily be generalized to multiple components. With this formulation, the fluorescence emission spectrum of tissue can be calculated. This would simply represent the intensity emanating from the tissue surface as a function of emission wavelength.

With the appropriate initial and boundary conditions, these equations completely describe the propagation of excitation and fluorescent light in tissue, apart from diffraction and interference effects. However, the exact solutions of these equations can be obtained only in a limited number of cases [13]. For a plane parallel geometry, with a collimated incident wave, at the excitation wavelength, eq. (1) can be greatly simplified [13]. However, even in cases where exact solutions can be obtained, the expressions are often complex, and simpler, approximate solutions are more useful [13].

Here, we consider an approximate description of light propagation in tissue. A frequently considered approximation is the diffusion approximation. Here, we utilize an even simpler approximation, that of exponential attenuation of light due to a combined treatment of scattering and absorption. These approximations can be compared to results which would be obtained using the transport equation with Monte Carlo simulations of light propagation in tissue [17, 18].

2.4.2.2: Monte Carlo Simulations

The Monte Carlo method of describing both excitation [17, 19] and fluorescent [15] light propagation in biological tissue has been described in detail previously. Essentially, a Monte Carlo simulation obtains an approximation of the light distribution in tissue by simulating the random walks of many individual photons within tissue. A random number generator is used to sample discrete events from probability distributions of interactions derived from tissue optical properties [17].

Flock and colleagues have shown, that for an infinitely wide collimated excitation source normally incident on a semi-infinite medium, the diffusion approximation to the equation of transfer is increasingly inaccurate as the albedo tends to zero and/or the average cosine of scatter tends to unity [17]. In their calculations, they assumed the phase function was that first used by Henyey and Greenstein [20]. The first moment of this phase function, g, tends to 0 for isotropic scattering and to 1 for forward peaked scattering [17]. The albedo, a', is defined as:

$$(3)\ a' = \frac{(1-g)\mu_s}{(1-g)\mu_s + \mu_a}.$$

The albedo represents the ratio of the scattering cross section to the total cross section for absorption and scattering. For values of albedo (~0.9) and g (~0.9) typical for human tissue in the red region of the spectrum[4] [15], Flock showed that the diffusion approximation of fluence versus depth differed maximally from the results of Monte Carlo simulations by less than 30% [17]. This difference was most pronounced within 50 transport mean free paths of the tissue surface [17]. For values of the albedo and g closer to zero, the agreement of this theory with Monte Carlo calculations is even better [17].

---

[4]The optical properties of human aorta have been measured in the visible, and it has been shown that in this tissue scattering is highly forward peaked, with g approximately varying from 0.73 to 0.92 over the wavelength range 476 - 650 nm [14]. The corresponding albedo varies approximately from 0.7 to 0.9 [14].

Furthermore, Flock showed that the Monte Carlo and diffusion theory results were similar to exponential attenuation of light according to an effective attenuation coefficient, μ_t, given by:

$$(4)\ \mu_t = [3\mu_a(\mu_a + (1-g)\mu_s)]^{1/2}.$$

Again, the assumption of exponential attenuation differed most from the Monte Carlo simulation within 50 transport mean free paths of the tissue surface and for cases where the albedo approached unity and g approached zero. For parameters typical of human tissue in the red region of the spectrum, in this case, maximal deviation was on the order of factor of two at the surface. Further from the tissue surface, exponential attenuation, diffusion theory and Monte Carlo simulations agreed within 10% [17].

2.4.2.3: Exponential Attenuation

Because of its simplicity and its reasonable agreement with transport theory 50 mean free paths within the tissue[5], we initially consider a model of tissue fluorescence in which light is attenuated exponentially, due to a combination of absorption and scattering. Specific equations are developed which describe tissue fluorescence spectra in terms of contributions from individual components. These equations are later applied to fluorescence spectra of arterial and gastro-intestinal tissues in Chapters Three and Four.

2.4.2.3.1: One Layer Model

For the purpose of modeling fluorescence, tissue is represented as a single layer, which is infinitely thick with respect to the penetration depth of the irradiating light. This assumption is most appropriate for excitation wavelengths for which the 1/e penetration depth is less than the thickness of the top layer. In addition, the following assumptions are made:

1. Light is attenuated exponentially in tissue, due to absorption and scattering. In describing this attenuation, scattering and absorption are not treated separately but are considered together as total attenuation, with attenuation coefficient, μ_t.

2. Chromophores are distributed homogeneously in the tissue.

---

[5]In arterial tissue at 476 nm excitation, 50 transport mean free paths corresponds to a distance of less than 50 μm [14].

3. The excitation beam is assumed to be uniform in profile and infinitely wide. Edge effects are neglected.

This last assumption is equivalent to restricting the model to a single dimension, depth into the tissue. The composite tissue fluorescence power arriving at the detector, $S(\lambda_x, \lambda_m)$, which is a function of both the excitation (λ_x) and emission (λ_m) wavelength, can then be written as:

$$(5)\quad S(\lambda_x,\lambda_m) = kP(\lambda_x)\int_0^{\infty} \underbrace{e^{-\mu_t(\lambda_x)z}}_{a}\underbrace{\mu_a(\lambda_x)\frac{\phi(\lambda_x,\lambda_m)}{2}}_{b}\underbrace{e^{-\mu_t(\lambda_m)z}}_{c}dz$$

Due to scattering, the maximum intensity just below the tissue surface may be higher than the incident intensity [17, 18]. This effect is included in Eq. (5) as k, a proportionality factor which depends on the tissue index of refraction and the incident wavelength, and also contains the detector efficiency. $P(\lambda_x)$ denotes the incident excitation power, $\mu_t(\lambda)$ and $\mu_a(\lambda)$, in units of length^{-1}, are the total attenuation and absorption coefficients of the tissue, respectively, $\phi(\lambda_x, \lambda_m)$ is the quantum yield of fluorescence, defined as the total fluorescence energy emitted at λ_m over the total absorbed energy at λ_x, and z is the distance from the irradiated surface.

Eq. (5) has a simple physical interpretation. Term a represents the attenuation of the incident radiation; term b represents the conversion of this light into backward directed fluorescence; and term c represents the attenuation of this net backward directed fluorescence. On average, assuming isotropic emission of fluorescence, the net backward directed fluorescence is half that of the total net fluorescence, resulting in the factor of 2 in term b.

Integrating Eq. (5) yields:

$$(6)\quad S(\lambda_x,\lambda_x) = \frac{kP(\lambda_x)\mu_a(\lambda_x)\frac{\phi(\lambda_x,\lambda_x)}{2}}{(\mu_t(\lambda_x) + \mu_t(\lambda_m))}$$

The quantities $\mu_a\phi$ and μ_t contain contributions from all of the individual tissue chromophores. It is this information which we wish to separate. Thus, a more useful way to write Eq. (6) is to express $\mu_a\phi$ and μ_t as sums over the N chromophores:

$$(7)\quad S(\lambda_x,\lambda_x) = kP(\lambda_x)\frac{\sum_{i=1}^{N} \mu_{ai}(\lambda_x)\frac{\phi_i(\lambda_x,\lambda_x)}{2}}{\sum_{i=1}^{N} (\mu_{ti}(\lambda_x) + \mu_{ti}(\lambda_m))}$$

Equation (7) is the fundamental equation for interpreting tissue fluorescence spectra in situations where exponential attenuation of light can be assumed, and the tissue consists of a single layer in which chromophores are distributed homogeneously. It is applied specifically to the fluorescence of arterial and gastro-intestinal tissues in Chapters Three and Four.

2.4.2.3.2: Two Layer Model

Equations (5-7) can be easily extended for multi-layer tissues, in which chromophores are distributed homogeneously. Here, eqs. (8-13) represent the extension to two layers, the first of thickness l_1, the second infinite in extent. Again, chromophores are distributed homogeneously within each layer.

$$(8)\quad S(\lambda_x,\lambda_m) = kP(\lambda_x)\int_0^{l_1} e^{-\mu_a(\lambda_x)z}\mu_{a1}(\lambda_x)\frac{\phi_1(\lambda_x,\lambda_m)}{2}e^{-\mu_a(\lambda_m)z}dz +$$

$$kP(\lambda_x)e^{-(\mu_a(\lambda_x)+\mu_a(\lambda_m))l_1}\int_{l_1}^{\infty} e^{-\mu_a(\lambda_x)(z-l_1)}\mu_{a2}(\lambda_x)\frac{\phi_2(\lambda_x,\lambda_m)}{2}e^{-\mu_a(\lambda_m)(z-l_1)}dz$$

$$(9)\ S(\lambda_x,\lambda_m) = kP(\lambda_x)\frac{\mu_{a1}(\lambda_x)\frac{\Phi_1(\lambda_x,\lambda_m)}{2}}{(\mu_{a1}(\lambda_x)+\mu_{a1}(\lambda_m))}\left(1 - e^{-(\mu_{a1}(\lambda_x)+\mu_{a1}(\lambda_m))l_1}\right) +$$

$$kP(\lambda_x)e^{-(\mu_{a1}(\lambda_x)+\mu_{a1}(\lambda_m))l_1}\frac{\mu_{a2}(\lambda_x)\frac{\Phi_2(\lambda_x,\lambda_m)}{2}}{(\mu_{a2}(\lambda_x)+\mu_{a2}(\lambda_m))}$$

$$(10)\ S(\lambda_x,\lambda_m) = kP(\lambda_x)\frac{\sum_{i=1}^{N}\mu_{a1i}(\lambda_x)\frac{\Phi_{1i}(\lambda_x,\lambda_m)}{2}}{\sum_{i=1}^{N}(\mu_{a1i}(\lambda_x)+\mu_{a1i}(\lambda_m))}\left(1 - e^{-\sum_{i=1}^{N}(\mu_{a1i}(\lambda_x)+\mu_{a1i}(\lambda_m))l_1}\right) +$$

$$kP(\lambda_x)e^{-\sum_{i=1}^{N}(\mu_{a1i}(\lambda_x)+\mu_{a1i}(\lambda_m))l_1}\frac{\sum_{j=1}^{M}\mu_{a2j}(\lambda_x)\frac{\Phi_{2j}(\lambda_x,\lambda_m)}{2}}{\sum_{j=1}^{M}(\mu_{a2j}(\lambda_x)+\mu_{a2j}(\lambda_m))}$$

These equations can be generalized to any number of tissue layers. As l_1 approaches infinity, it can be seen that eqs. (8-10) reduce to the form of eqs. (5-7), as expected.

2.5: Algorithm Development

In this work, our ultimate goal is to develop methods of extracting parameters from tissue fluorescence spectra which are related to the histochemical composition of tissue and use these parameters to determine whether the sample is normal or pathologic. Here we consider the final step in this process, algorithm development.

We have broken this procedure into two steps. Given the parameters of the fluorescence spectrum, the first step in algorithm development is to determine which parameters should be included in the algorithm. The algorithm should incorporate those parameters which provide useful diagnostic information. Given these parameters, the second step is to determine a decision surface which assigns tissue type as a function of this parameter space. This is accomplished using a defining data set, for which these parameters have been measured and tissue type has been determined by some other independent means, such as histology. The decision surface is drawn so as to maximize

the number of samples in the defining data set correctly classified by the algorithm. These two iterative steps are described in more detail below.

2.5.1: Selection of Parameters for Use in Algorithm

In selecting parameters for inclusion in the algorithm, our goal is to select the minimum number of independent parameters which provide the most accurate diagnostic algorithm. As stated previously, our ultimate goal is an algorithm based on parameters related to the histochemical composition of the tissue. The model of tissue fluorescence described in the previous section provides one method of extracting such parameters from tissue fluorescence spectra. Thus, the parameters included in our ultimate algorithms will be some subset of the parameters of our model of tissue fluorescence.

However, in many cases it is desirable to initially evaluate the potential diagnostic performance of fluorescence spectroscopy before the histochemical basis of tissue fluorescence has been established. In these situations, the parameters of the diagnostic algorithm must be extracted from tissue fluorescence spectra in some empirical way.

Our methods of selecting parameters for inclusion in empirical and model based diagnostic algorithms will be described here.

2.5.1.1: Empirical Algorithms

In defining empirical algorithms, fluorescence intensities at various emission wavelengths were used as algorithm parameters. A fluorescence spectrum of tissue consists of fluorescence intensities recorded at closely spaced emission wavelengths; because the fluorescence lineshapes of biological chromophores are broader than this spacing, many of these data points are not independent. Thus, we attempt to reduce an individual spectrum to a small, independent subset of fluorescence intensities at specific wavelengths and use these as parameters for development of empirical diagnostic algorithms. For most effective algorithm development, this subset of data should contain all independent pieces of information which can be extracted from the spectrum. The model of tissue fluorescence provides a way to achieve this with parameters which have a quantitative interpretation. However, using the average fluorescence emission spectra of normal and pathologic tissues, we can achieve this approximately, where the parameters are fluorescence intensities at various emission wavelengths.

We construct the ratio and difference of the average spectra of normal and pathologic tissue and note the emission wavelengths corresponding to local maxima and minima in these spectra. The fluorescence intensities at these emission wavelengths then form the subset of data from which algorithm parameters are drawn. In principle, if the emission of individual tissue chromophores is well separated, the intensities at these wavelengths are correlated to the products of the concentration and quantum yield (or attenuation coefficient) of individual chromophores. In practice, this separation is rarely complete, and these parameters are only crudely related to the histochemically based parameters of the model.

The subset of these emission wavelengths most useful diagnostically was determined by applying diagnostic algorithms including various combinations of these parameters to the defining data set. First, algorithms based on fluorescence intensity at a single emission wavelength were defined for each of the emission wavelengths corresponding to local maxima and minima in the ratio and difference spectra. These algorithms were defined using the scatter plot method described below; their performance was evaluated for the defining data set. This identified the single emission wavelength most useful diagnostically. Then, in a similar way, the performance of all binary combinations of this emission wavelength and other emission wavelengths within the subset of data were considered. In cases where the performance of a single emission wavelength was not significantly greater than the others, all possible binary combinations were considered. In this way, the binary combination of emission wavelengths most useful diagnostically could be selected. Because this method of algorithm development was used primarily to evaluate the potential of fluorescence diagnostics, more complicated, higher order classification schemes were not considered.

2.5.1.2: Model Based Algorithms

Spectroscopic algorithms based on histochemical features of disease were achieved with parameters extracted from tissue fluorescence spectra utilizing the model of tissue fluorescence described previously. The scatter plot method described below was used to establish which single model parameter was most effective diagnostically with the defining data set. Then, the diagnostic ability of all binary combinations of this model parameter with all other model parameters were evaluated, also using the scatter plot method with the defining data set. This method is most convenient for selecting two model parameters for inclusion in the algorithm.

For clinical application, a more rigorous, statistical method of defining decision surfaces was used. These algorithms were defined utilizing the binary combination of model parameters determined diagnostically most effective with the scatter plot method.

2.5.2: Drawing Decision Surfaces

Once parameters have been selected for inclusion in a diagnostic algorithm, it is necessary to divide this parameter space into regions which correspond to different types of tissue. The surfaces which affect this partition are known as 'decision surfaces'. We have used two methods to define decision surfaces, which we refer to as the scatter plot method and the probability method. Both methods require a defining data set, a data set for which the algorithm parameters have been determined and for each tissue sample, the tissue type has been histologically determined. These methods and their advantages and disadvantages will be described below.

2.5.2.1: Scatter Plot Method

In this method of defining decision surfaces, a scatter plot[6] of the algorithm parameters as a function of tissue type is constructed for the defining data set. This plot is then divided into regions representing the various tissue types. In our method, these decision surfaces are restricted to straight line segments, and are drawn to maximize the number of samples of the defining data set which are correctly classified.

Although an extremely simple and useful method of defining decision surfaces, this method does suffer from several problems. Because it is a graphical method, it is difficult to visualize in more than two dimensions, and is thus difficult to carry out with more than two algorithm parameters. In addition, with this arbitrary method of constructing decision surfaces, interpretation of individual data points which fall on or near the decision surfaces can be difficult. Finally, this method of drawing decision surfaces optimizes algorithm performance for only the proportion of normal and diseased samples found in the defining data set (prior probability). It provides no way to customize the decision surfaces for applications in clinical situations where the occurrence of disease may vary.

---

[6]Scatter plot is used here to refer to a plot of the values of the algorithm parameters for each of the individual samples in the defining dat set. Tissue type is indicated for each sample as well.

2.5.2.2: Probability Method

The wealth of research in medical statistics provides a more sophisticated method of drawing decision surfaces which overcomes these disadvantages [21]. Using the concept of prior and posterior probabilities, we can use statistical distributions of model parameters from the defining data set to calculate the probability of a given tissue type as a function of parameter space. This probability is known as the posterior probability, and is a function of the likelihood of encountering a given tissue type, or the prior probability. Given the posterior probability as a function of parameter space, decision surfaces can then be determined. It can be shown that the total sample misclassification rate is minimized if decision surfaces are drawn to divide parameter space into regions for which the posterior probability for a specific type of tissue is greater than the posterior probability for all other types of tissue [21].

Calculating posterior probability as a function of prior probability and the distributions of the model parameters is accomplished using Bayes rule. Eq. (11) shows the general form of this equation for M model parameters and N types of tissue. Here, the positive integer index i is used to represent tissue type, and model parameters are represented by β_j, where the index j is also a positive integer.

$$(11)\quad P(i|\beta_1,\beta_2,\ldots\beta_M) = \frac{p(i)P(\beta_1,\beta_2,\ldots\beta_M|i)}{\sum_{i=1}^{N} p(i)P(\beta_1,\beta_2,\ldots\beta_M|i)}$$

Here $P(i|\beta_1,\beta_2,\ldots\beta_M)$ represents the posterior probability for tissue type i, or the probability that for a tissue sample with model parameters $(\beta_1,\beta_2,\ldots\beta_M)$ the sample is of tissue type i. p(i) represents the prior probability that the sample is of type i, and can be though of as the incidence of tissue type i. The sum of prior probabilities over tissue type is defined to be unity. The posterior probabilities are similarly normalized by virtue of the denominator in eq. (11). Finally, $P(\beta_1,\beta_2,\ldots\beta_M|i)$ is the probability that given a tissue sample of type i, the model parameters $(\beta_1,\beta_2,\ldots\beta_M)$ will be measured. This probability is calculated from the distributions of model parameters for tissue type i in the defining data set.

With this method, the diagnostic significance of individual data points in parameter space can be easily evaluated. The posterior probability gives the probability that the corresponding tissue sample belongs to any particular tissue category. In addition, decision surfaces can easily be determined for clinical applications in which the incidence of disease, or prior probability varies. Furthermore, this method can be easily implemented for an arbitrary number of independent parameters. Initially, decision surfaces were determined using the probability method for the two parameters judged to have the greatest diagnostic utility with the scatter plot method.

With this summary of common experimental and data analysis methods, we now turn to describing our results for the three clinical conditions of interest.

2.6: References

1. Ham AW, Cormack DH, Histology, 8th ed., JB Lippincott Co., Philadelphia, 1979.

2. Doyle A, Morris CB, Armitage WJ, Cryopreservation of Animal Cells, in Upstream Processes: Equipment and Techniques, Alan R. Liss Inc, p. 1-17 1988.

3. Taylor DG, Demas JN, Light Intensity Measurements I: Large Area Bolometers with μW Sensitivities and Absolute Calibration of the Rhodamine B Quantum Counter, Anal Chem, 51:712-17, 1979.

4. Richards-Kortum RR, Mehta A, Hayes G, Cothren R, Kolubayev T, Kittrell C, Ratliff NB, Kramer JR, Feld MS: Spectral Diagnosis of Atherosclerosis Using an Optical Fiber Laser Catheter, American Heart Journal, 118(2):381, 1989.

5. Keijzer M, Richards-Kortum RR, Jacques SL, Feld MS: Fluorescence Spectroscopy of Turbid Media: Autofluorescence of Human Aorta, Applied Optics, 28:4286-4292, 1989.

6. Chaudhry HW, Richards-Kortum R, Kolubayev T, Kittrell C, Partovi F, Kramer JR, Feld MS: Alteration of Spectral Characteristics of Human Artery Wall due to 476 nm Laser Irradiation, Lasers in Surgery and Medicine, 9:572-580, 1989.

7. Richards-Kortum RR: Understanding Laser Induced Fluorescence Spectra of Human Artery Wall with Applications to Diagnosis of Atherosclerosis, SM Thesis, Massachusetts Institute of Technology, September 1987.

8. Wilke V, Schmidt W, Tunable Coherent Source Covering a Spectral Range from 185-850 nm, Appl Phys 18:177-81, 1979.

9. McManus JFA, Mowry RW, Staining Methods Histologic and Histochemical, Harper and Row, New York, 1960.

10. Hecht E, Zajac A, Optics, Addison-Wesley Publishing, Reading, MA, 1979.

11. Campbell ID, Dwek RA, Biological Spectroscopy, The Benjamin Cummings Publishing Co, Menlo Park, CA, 1984.

12. Schulman SG, Fluorescence and Phosphorescence Spectroscopy: Physico-chemical Principles and Practice, 1st ed., Pergamon Press, Oxford, 1977.

13. Ishimaru A, Wave Propagation and Scattering in Random Media, Academic Press, Orlando, 1978.

14. Baraga JJ, Taroni P, Park YD, An K, Maestri A, Tong LL, Rava RP, Kittrell C, Dasari RR, Feld MS, Ultra Violet Laser Induced Fluorescence of Human Aorta, Spectrochimica Acta 45A:95, 1989

15. Keijzer M, Richards-Kortum RR, Jacques SL, Feld MS, Fluorescence Spectroscopy of Turbid Media: Autofluorescence of the Human Aorta, Applied Optics, 28:4286-92, 1989.

16. Rava RP, Baraga JJ, Richards-Kortum RR, Tong L, Fitzmaurice M, Cowan W, Sivak J, Feld MS, Analysis of Fluorescence and Absorption from Normal and Pathologic Aorta Using Fluorescence Excitation-Emission Matrices, in preparation, 1990.

17. Flock ST, Patterson MS, Wilson BC, Wyman DR, Monte Carlo Modeling of Light Propagation in Highly Scattering Tissues - I: Model Predictions and Comparison with Diffusion Theory, IEEE Transactions on Biomedical Engineering, 36:1162-68, 1989.

18. Welch AJ, Yoon G, van Gemert MJC, Practical Models for Light distributions in Laser Irradiated Tissue, Lasers in Surgery and Medicine 6:488-93, 1987.

19. Keijzer M, Jacques SL, Prahl SA, Welch AJ, Light Distributions in Artery Tissue: Monte Carlo Simulations for Finite-Diameter Laser Beams, Lasers Surg Med 9:148-54, 1989.

20. Henyey LG, Greenstein JL, Diffuse Radiation in the Galaxy, Astrophys J, 93:70-83, 1941.

21. Harris EK, Albert A, Multivariate Interpretation of Clinical Laboratory Data, Decker, New York, 1987.

3: Spectroscopic Diagnosis of Atherosclerosis

3:1. Atherosclerosis

The basic lesion of atherosclerosis is a raised, focal plaque which forms within the intimal layer of the artery [1]. The resulting increase in intimal thickness causes progressive narrowing of the arterial lumen [1]. This narrowing can severely compromise the delivery of oxygen to tissues whose vascular supply originates distal to the site of the atherosclerotic obstruction [1]. Although atherosclerosis affects all muscular and elastic arteries, the consequences of coronary artery atherosclerosis are particularly severe [1]. A frequent complication of this disease is myocardial infarction, responsible for 20-25% of deaths in the United States [1].

This chapter is concerned primarily with the application of fluorescence spectroscopy to the diagnosis and management of coronary artery atherosclerosis. As an introduction, relevant clinical issues in the diagnosis and treatment of CAD will be briefly reviewed. In addition, the etiology and pathogenesis of atherosclerosis will be reviewed; in particular, the chemical and physical changes amenable to study using spectroscopic techniques will be emphasized. A brief summary of literature related to applications of fluorescence spectroscopy in the diagnosis and treatment of atherosclerosis will be presented. Finally, we will present, in detail, our method of developing a histochemically based diagnostic algorithm for atherosclerosis in both muscular and elastic arteries.

3:1.1. Clinical Issues

Symptoms of coronary artery disease (CAD) are those of diminished myocardial oxygen supply [1, 2]. Therapies of CAD are therefore directed towards restoring the balance of myocardial oxygen supply and demand [2]. This is achieved primarily by augmenting myocardial blood flow and thus oxygen supply [2]. The three most commonly used forms of treatment for CAD include medical management, in which drugs are used to relax vascular smooth muscle and increase lumen diameter [2], coronary artery bypass grafting (CABG), in which a venous or arterial bypass is surgically constructed around the atherosclerotic obstruction [3], and percutaneous transluminal coronary angioplasty (PTCA), in which a balloon tipped catheter is advanced to the site of the obstruction and inflated, remodeling the plaque to increase lumen diameter [4].

These methods of treatment have been reviewed in Chapter One. Although it is clear that each has advantages and disadvantages, predicting in advance which method of treatment would be most beneficial to a particular patient with CAD is difficult. Certain measurable risk factors have been associated with the failure of each of these treatments, yet these are insufficient to accurately determine the most appropriate treatment for a particular individual. Studies of the chemical composition of atherosclerotic lesions at autopsy have indicated that the failure of some of these treatments may be related to certain aspects of the histochemical composition of the lesion [5]. Currently, however, no method of diagnosis is available to assess the histochemical composition of atherosclerotic lesions *in vivo*. If such a method were developed, it would potentially facilitate determination of the most appropriate therapy for CAD on an individual basis.

A newer method of treatment for CAD, currently under investigation in many labs, is laser angiosurgery (LAS) [6-9]. LAS utilizes a percutaneously inserted optical fiber catheter to deliver high power laser radiation to the site of an atherosclerotic obstruction, resulting in its ablation [6]. This treatment appears to have some important advantages relative to CABG and PTCA. As a percutaneous technique, it is a less invasive form of therapy than CABG. However, unlike PTCA, LAS results in the removal of atherosclerotic obstructions, leaving behind a smooth vessel wall, which may result in a lower rate of restenosis [7-9]. In addition, this method of plaque removal may allow for the treatment of diffuse atherosclerosis, the significance of which is becoming more apparent [10].

Although LAS promises many potential advantages, there are currently significant problems which must be solved before it can be implemented clinically. A major problem is that of catastrophic vessel perforation [6, 7, 9]. The laser radiation used to vaporize atherosclerotic obstructions is also capable of removal of normal vessel wall, necessitating the use of an appropriate guidance system to ensure that radiation is only delivered to atherosclerotic tissue. Ideally, this guidance system would be capable of establishing the amount of laser energy required to remove the atherosclerotic obstruction without damage to any normal vessel wall. This is the concept of dosimetry, achieved with interactive diagnosis and removal of tissue. As the amount of laser energy required to remove a given volume of plaque varies with plaque composition and morphology [11], the successful guidance system must be capable of determining the chemical composition of the vessel both prior to and following laser ablation.

As discussed in Chapter One, fluorescence spectroscopy provides a potential means of non-invasively assessing the chemical composition of tissue *in vivo* in real time. If applied to arterial tissues, such a method could play an important role in improving the therapies of CAD discussed above. One potential application is the development of a guidance system for laser angiosurgery catheters. In addition, fluorescence techniques may prove useful in the non-invasive determination of arterial histochemistry to predict the most appropriate therapy for CAD.

This chapter summarizes our work to develop such a spectroscopic method to determine the histochemical composition of normal and atherosclerotic vessel wall in muscular and elastic arteries. In developing this method, it is first necessary to consider the morphologic and biochemical composition of normal and atherosclerotic arterial tissues, with special attention to those elements of tissue which will contribute to the spectroscopic signal. To this end, the next section contains a discussion of the morphology, etiology and pathogenesis of atherosclerosis with special emphasis given to those features which can be investigated using spectroscopic techniques.

3:1.2. Pathology of Atherosclerosis

To understand atherosclerosis, it is first necessary to consider the structure of the normal arterial wall.

3:1.2.1. Normal Vessel Wall

Arteries can be divided into three categories based on their size and certain histologic factors. These categories include: large, elastic arteries, such as the aorta, medium sized, muscular arteries, including the coronary arteries, and small arteries [1]. All arteries are comprised of three circumferential layers, the intima, media and adventitia, in order of progression from the vessel lumen [1].

3:1.2.1.1. Aorta

In elastic arteries, such as the aorta, these three layers are well defined. At birth, the intima of these vessels is comprised of only a layer of endothelial cells atop a delicate basement membrane [1]. Throughout life, the intima progressively thickens, accumulating a matrix of connective tissue, predominantly collagen, and some smooth muscle like (myointimal) cells [1]. This process is known as intimal fibroplasia or diffuse intimal thickening [1]. The second layer of the aorta, media, is made up mainly of

concentric layers of elastin fibers, alternating with some layers of smooth muscle cells [1]. The outer layer, adventitia, is comprised of loose connective tissue, in which nerve fibers and some small nutrient vessels are dispersed [1].

3:1.2.1.3. Coronary Artery

The intima of muscular arteries, such as the coronary arteries, resembles that of the elastic arteries [1]. However, the intimal-medial border is more well-defined in muscular arteries; the two layers are separated by the internal elastic lamina (IEL), a discrete, fenestrated, layer of elastic tissue [1]. The media of muscular arteries predominantly contains smooth muscle cells, arranged in concentric layers [1]. Only a few, fine elastic fibers are present. The media is separated from the adventitia by another, less well developed layer of elastic tissue, the external elastic lamina (EEL) [1]. The adventitia is similar to that of elastic arteries, except that is is richer in nerve fibers, largely because autonomic regulation of vessel caliber is important in controlling blood supplied by muscular arteries [1].

3:1.2.2. Atherosclerosis

3:1.2.2.1. Morphology

Atherosclerotic plaques are focal, raised, lesions which protrude into the lumen of the artery [1]. They vary in size from 0.3 to 1.5 cm in diameter, but can sometimes coalesce to form larger masses [1]. Frequently these lesions are white to whitish-yellow in color [1]. Histologically, plaques are generally confined to the intima [1]. There are many methods of classifying atherosclerotic plaques. However, atherosclerotic lesions are very heterogeneous, and it has been difficult to assess the relationship of different classes of lesions to one another [1].

We have utilized the classification scheme recently adopted by the Cleveland Clinic Foundation, which subclassifies atherosclerotic lesions on the basis of their histologic features [12]. Although defined on histologic grounds, the classifications within this scheme can be related roughly to stages in the progression of atherosclerosis. Normal tissue (0) is indicated by an intimal layer constituted primarily of endothelial cells with minimal intimal thickening. Intimal fibroplasia (1), is characterized initially by intimal proliferation of smooth muscle cells and fibroblasts. In well developed intimal fibroplasia, collagen accumulates. An atherosclerotic plaque (2) is indicated when the intima is infiltrated by lipids and foam cells. When the center of the plaque becomes necrotic, the plaque is characterized as atheromatous (3). Both atherosclerotic and

atheromatous plaques can develop significant calcifications, and are then classified as calcified atherosclerotic (4) and calcified atheromatous (5) plaques respectively. Non-calcified (6) and calcified fibrotic/sclerotic lesions (7) are end stage plaques, characterized by intimal sclerosis with loss of lipids and foam cells. The location of the calcification - the fibrous cap or atheromatous core - was noted for all calcified plaques. Figure 1 illustrates the histologic structure of each of these tissue types in the coronary artery.

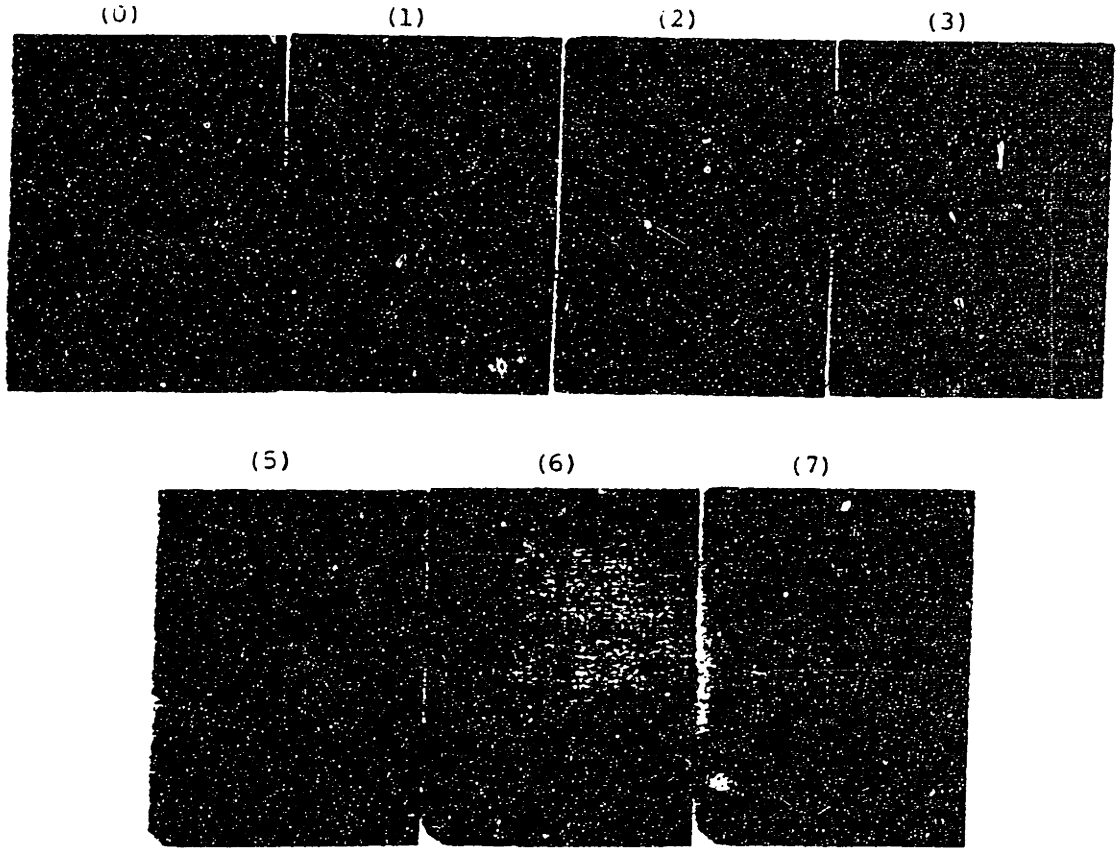

Figure 1: Histologic sections of normal and atherosclerotic coronary artery stained with H&E, illustrating each of our tissue classifications: (0) normal, (1) intimal fibroplasia, (2) atherosclerotic plaque, (3) atheromatous plaque, (4) calcified atherosclerotic plaque, (5) calcified atheromatous plaque, (6) fibrotic/sclerotic plaque, and (7) calcified fibrotic/sclerotic plaque. Classification (4), calcified atherosclerotic plaque is not shown.

The most clinically significant lesions are the atheromatous and calcified atheromatous plaques [1]. In the coronary arteries, the narrowing of the lumen due to these plaques, especially if accompanied by thrombosis, can frequently lead to occlusion, and may be the ultimate event causing myocardial infarction [1]. However, to better understand the importance and inter-relationships of the aforementioned categories of atherosclerosis, it is useful to consider the etiology and pathogenesis of the disease.

3:1.2.2.2. Etiology and Pathogenesis

The etiology and pathogenesis of atherosclerosis are widely studied fields, which have been recently reviewed [13, 14]. Many competing theories have been proposed to describe this process, all of which can account for some of the features of atherosclerosis. It appears unlikely that there is a single, unique pathogenesis of the disease [14]. Here, we will summarize one theory, which invokes the role of hypercholesterolemia [14].

Hypercholesterolemia is a major risk factor for the development of atherosclerosis [1]. Studies in Europe and the United States have shown that correction of hypercholesterolemia will slow the progression and may even cause modest regression of atherosclerosis [14]. All plasma lipoproteins contain cholesterol; however, it is primarily low density lipoproteins (LDL) that are atherogenic [14].

Normally, endothelial cells prevent the deposition of plasma constituents in the intima [1]. However, increased levels of LDLs, focal injury to or a focal increase in the permeability of the endothelial cells can all result in the intimal deposition of LDL [14]. LDL deposited in the intima can be scavenged by macrophages [14]. However, in the presence of myointimal cells, as in intimal fibroplasia, oxidative modification of LDL can occur [14]. The resulting oxidized fatty acids can covalently link to proteins, forming the relatively insoluble pigment, ceroid [14-16]. Ceroid is the term given to autofluorescent material that is insoluble in a variety of organic solvents while retaining the ability to stain with lipid soluble dyes [15]. Oxidized LDLs and ceroids are powerful chemotactic agents, acting to recruit monocytes from the circulating blood stream to the intima [14]. In the presence of oxidized LDLs and ceroid these monocytes can be phenotypically modified, acquiring the properties of macrophages [14]. As these macrophages attempt to scavenge oxidized LDLs and ceroid they are converted into foam cells [14]. This uptake of oxidized LDLs and ceroids results in a decrease in macrophage motility, so that

the resulting foam cells are trapped within the intima [14]. The presence of foam cells is a defining feature of atherosclerosis [12].

Oxidized LDL is also cytotoxic to endothelial cells, and its accumulation in the intima results in damage to the endothelial cell lining [14]. This enhances the intimal migration of more LDL, monocytes and macrophages during early stages of lesion development [14]. As the endothelial cell layer is further disturbed, platelets adhere to the exposed connective tissue matrix or to foam cells themselves [14]. These platelets release platelet factors, which ultimately cause smooth muscle cell proliferation, deposition of extracellular connective tissue (primarily collagen [17]) and the other processes that give rise to the stenotic, advanced lesion [14]. Figure 2 illustrates this complex process of lesion development.

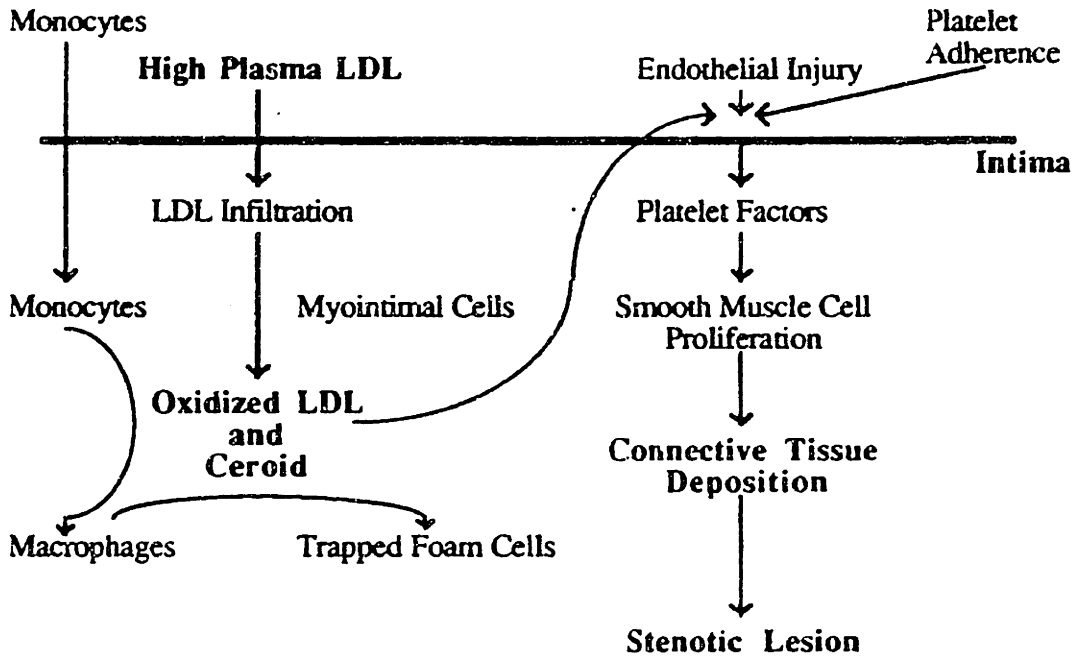

Figure 2: Schematic diagram illustrating the etiology and pathogenesis of atherosclerosis induced by hypercholesterolemia. Adapted from [14].

This explanation of the atherosclerotic process can be used to understand the relationship of our various classifications of atherosclerosis. Intimal fibroplasia (1), although not a normal state, rarely leads to hemodynamically significant obstructions, especially in elastic arteries. However, the presence of myointimal cells in this lesion implies that it may be a precursor to atherosclerosis. Atherosclerotic plaques (2), characterized by the presence of foam cells, represent the initial step in atherosclerosis. Atheromatous plaques (3), characterized by the formation of a necrotic center, represent a

more advanced stage of disease, in which tissue degeneration occurs, because diffusion of oxygen from the lumen can no longer supply the nutritional requirements of the thickened atherosclerotic intima [1].

Fibrotic/sclerotic plaques (6), in which lipids and necrotic tissue have been replaced with collagenous scar tissue, represent lesions in which regression of atherosclerosis has occurred [18]. It is believed that this regression is affected by macrophages, which phagocytize lipids and necrotic debris [18]. This implies that monocytes and macrophages can play several roles in atherosclerosis [14, 18]. Steinberg has suggested that they are important in atherogenesis [14], while other groups have shown that they may be important in regression [18]. The role played by these cells may depend on the activities of macrophages in other processes in the body [18]. For example, the effect of macrophage activators on tumor development depend on the timing of their application in relationship to other activities of the reticulo-endothelial system [18].

In some lesions, extensive calcification develops, either in the fibrous cap or necrotic center of the atheroma. This calcification is an inorganic mixture of calcium and phosphate, primarily carbonate apatite or hydroxy-apatite [19]. These calcifications deposit in a random way in an organic matrix consisting primarily of elastin fibers. In situations where extensive calcification has occurred, some collagen fibers may also be calcified [19]. It appears that calcification begins when calcium ions bind to free carboxyl groups on degenerating or regenerating elastin fibers [19]. Phosphate ions then form small complexes with the bound calcium, providing nucleation sites for further deposition of inorganic apatites [19].

In our discussion of the pathobiology of atherosclerosis, particular attention has been given to the role of oxidized lipoproteins and ceroid and the deposition of the structural proteins, collagen and elastin. Although these substances are intimately involved in the development of atherosclerosis, they have been stressed because they also have been associated with autofluorescence [15, 16, 20-23]. It is known that collagen and elastin from various sources are autofluorescent [20, 21]. This autofluorescence is believed to be associated with crosslinks related to pyridinoline in these structural proteins [20, 21]. Previous studies have reported an excitation maximum between 300 and 350 nm and an emission maximum between 400 and 500 nm for these types of crosslinks [20, 21]. Fluorescent lipofuscin pigments, ceroids, have been observed in many pathologic processes, where their deposition has been correlated with lipid peroxidation

damage [22]. The excitation maxima of these pigments have been reported in the range from 350 - 400 nm, with emission maxima ranging from 430 - 460 nm and 540 - 580 nm [23]. Thus, it appears possible that fluorescence spectroscopy can be used to detect the presence of chemical constituents central to the development and progression of atherosclerosis.

3:1.3. Brief Review of Arterial Fluorescence Literature

Many studies of arterial fluorescence have been carried out to determine if fluorescence spectroscopy can be used to develop a diagnostic algorithm for atherosclerotic plaque [24-31]. A detailed overview of these feasibility studies was presented in Chapter One. They will only be briefly summarized here.

Kittrell and Sartori showed that fluorescence excited at visible wavelengths could be used to differentiate normal aorta from fibrous atherosclerotic plaque [24], and calcified plaque *in vitro*, respectively [25]. Deckelbaum and Leon showed, that using ultra-violet excitation wavelengths, fluorescence spectroscopy could be used to differentiate normal aorta from white fibrous plaques and yellow fatty plaques [26, 28]; Leon noted, with UV excitation, that calcified plaques were more similar to normal tissues in their fluorescence properties. Deckelbaum has suggested that the differentiation of normal and atherosclerotic coronary artery is not as successful with 325 nm excitation as is that of normal and atherosclerotic aorta [28].

Both Clarke and Deckelbaum have attempted to correlate UV excited fluorescence spectra to histochemical composition of tissue. Deckelbaum has shown with chemical extraction studies, that at 325 nm excitation, the fluorescence signal of normal and atherosclerotic aorta can be attributed to the structural proteins collagen and elastin [29]. Clarke has empirically correlated the fluorescence signal at this excitation wavelength to the intimal thickness and the relative proportions of fibrous, fatty, and calcified tissue within coronary artery atherosclerosis [30]. In our laboratory, Baraga has established diagnostic algorithms for the presence of non-calcified and calcified atherosclerosis in human aorta based on fluorescence emission spectra obtained at 308 nm excitation [31]. Following a procedure similar to that detailed in Chapter One, he has shown that this differentiation is due to differences in the contributions of tryptophan, collagen and elastin to the spectra of these tissues [31].

The ultimate goal of most of these studies has been to develop a fluorescence based guidance system for laser angiosurgery catheters. Although the potential of this technique has been demonstrated in [24 - 31], there are many remaining issues which need to be addressed. Many of these relate to the procedure followed in developing fluorescence based algorithms. For example, the choice of excitation wavelength in most of these studies [25 - 30] appears largely to be a function of the laser available in the researcher's laboratory. In developing algorithms at these excitation wavelengths, only the most rudimentary attempts have been made to extract the information contained in the fluorescence spectra about the physico-chemical composition of the tissue [29, 30]. Finally, in developing and evaluating diagnostic algorithms, the wealth of previous work in medical statistics has been neglected [24 - 31]. These issues can be incorporated within the systematic method of algorithm development we have proposed in Chapter One.

Other problems with these works are related to the choice of tissue samples. For example, although most studies have been conducted *in vitro* using cadaver aorta [24-26, 28-31], recent studies have implied that significantly different results are obtained with muscular arteries such as the coronaries [28]. In addition, some workers have focused on only differentiating normal tissue from advanced atherosclerotic lesions and have neglected intimal fibroplasia and atherosclerotic plaques with minimal intimal thickening [26, 28, 29]. Many have not carefully determined tissue type with well defined histologic categories, using instead such terms as yellow plaque, white plaque and whitish-yellow plaque [26-30]. Furthermore, detailed studies of tissue fluorescence have not been conducted in human subjects *in vivo*, to determine whether the results obtained *in vitro* are representative of the clinical situation. Leon has reported some data collected *in vivo*; however, in this study, the presence or absence of atherosclerosis was not determined independently by histology [27].

In this chapter, we will attempt to overcome these problems. We will apply our systematic method to develop an algorithm for coronary artery atherosclerosis which can be applied *in vivo* to several clinical problems. These clinical goals have already been alluded to, but will be briefly described in the next section. Finally, our results will be described in detail.

3:2. Clinical Problems Addressed by this Work

The diagnostic algorithm for coronary atherosclerosis which will be presented in this work was developed with three goals in mind. The first of these was to provide a guidance system for laser angiosurgery catheters which could be applied in real time *in vivo* to determine the histochemical composition of arterial tissue. In describing our results, this goal will be emphasized, as this task is nearest completion. However, the same algorithm has potential applications in two other situations, which will also be described. The first is to utilize fluorescence to determine the chemical composition of clinically symptomatic coronary artery atherosclerosis in order to ascertain the most appropriate form of therapy. The second is to use this method to study the evolving pathobiology of atherosclerosis *in vivo* in a way not before possible.

3:2.1. Guidance System for Laser Angiosurgery Catheters: Requirements of a Diagnostic Algorithm

For fluorescence to be effective as a guidance system for laser angiosurgery in the tortuous coronary arteries, it obviously must allow removal of atherosclerotic tissue while preventing arterial perforation. It is known that ablation of non-calcified atherosclerotic tissues results in removal of a greater volume of tissue for a given laser energy than does ablation of calcified atherosclerotic tissues [11]. Thus, a method of determining the chemical composition of atherosclerotic lesions would prove valuable in tailoring the ablation dosimetry to vaporize the atherosclerotic obstruction with minimal damage to normal tissue. At the very least, to avoid perforation, a fluorescence diagnostic system must be capable of identifying unknown vessel wall as normal, non-calcified plaque or calcified plaque both before and after removal of tissue by laser ablation. Our algorithm will be discussed in terms of these requirements.

We apply our method of algorithm development to both aorta and coronary artery. The feasibility of developing a diagnostic algorithm is first illustrated using aorta, since cadaver samples of this tissue are easy to obtain and work with. The method is then extended to coronary artery *in vitro*. This represents an important step; this work will demonstrate that there are important differences in the fluorescence spectra of elastic and muscular arteries. The algorithms developed *in vitro* for atherosclerosis in these arteries are then applied *in vivo* to ascertain whether modification is necessary for clinical

application. Finally, the integration of this method of diagnosis with a particular laser ablation system is discussed.

3:2.2. Method of Determining Optimal Form of Treatment

In addition to the specific application of guiding laser angiosurgery, it is our belief that fluorescence spectroscopy may ultimately impact on and improve each of the treatments for CAD discussed previously. The efficacy of many therapies of CAD has been correlated to the chemical composition of the atherosclerotic obstruction [5]. Fluorescence spectroscopy may be useful in selecting appropriate therapy, as it promises to provide a method of assessing the chemical composition of plaque *in vivo*. This may ultimately allow accurate prediction of those lesions which are truly ideal candidates for LAS, PTCA, or CABG. In addition, using fluorescence spectroscopy, it may be possible to determine when medical therapy is most appropriate. Supporting this contention is the fact that the presence of the autofluorescent oxidized lipoprotein, ceroid, has been correlated with the formation of irreversible atherosclerotic lesions [15].

Although testing these hypotheses is not the focus of this work, the algorithm developed here provides a means for doing so in clinical studies. Experiments addressing these questions are proposed in Chapter Six.

3:2.3. Method of Studying Pathogenesis and Progression of Disease

Finally, it is our belief that the development of reliable ways to study the histochemical composition of atherosclerotic lesions *in vivo* will facilitate the study of the pathogenesis of atherosclerosis. Currently, there are no reliable methods of assessing the composition of arterial tissue *in vivo*; standard histologic techniques can be used only following removal of tissue at autopsy, or less commonly, at surgery [1]. As there are many controversies in the etiology and pathogenesis of this disease, a method capable of assessing the presence of the histochemical features central to the development of atherosclerosis *in vivo* would be most valuable. In addition, the pathogenesis of restenosis following CABG or PTCA could be studied in with this technique, to determine whether it is similar to the formation of the initial lesion. Although studying the pathogenesis of atherosclerosis is not the focus of this work, the algorithm developed here provides a means for doing so, in the appropriate clinical studies. Experiments addressing this topic are proposed in Chapter Six.

With this introduction, we now focus on the experimental results obtained following our method for developing a spectroscopic algorithm for the diagnosis of atherosclerosis.

3:3. Survey of Arterial Spectroscopic Properties

The purpose of the first step in our procedure is to explore the potential of fluorescence spectroscopy for the differentiation of normal and atherosclerotic arterial tissue, and to determine the excitation wavelengths which are optimal for achieving this differentiation. To address these issues, we surveyed the fluorescence properties of a small group of samples of aorta and coronary artery *in vitro* over a wide range of UV and visible excitation wavelengths. These tissues represent typical examples of elastic and muscular arteries [1].

3:3.1. EEMs of Normal and Atherosclerotic Tissue

This survey was accomplished by recording fluorescence excitation emission matrices (EEMs), using the experimental procedure outlined for arterial tissues in Chapter Two.

3:3.1.1. Aorta

Fluorescence EEMs were recorded from 14 samples of human aorta *in vitro* [32]. Samples of abdominal and thoracic aorta were obtained from 10 human cadavers at autopsy, within 24 hours of death. Upon receipt, samples were snap frozen in liquid nitrogen and isopentane, and were stored at -70°C until study. At the time of study, samples were thawed to room temperature and were kept moist in a buffered (50 mM TRIS), pH 7.4, isotonic, saline (140 mM) solution. Fluorescence EEMs were recorded from grossly observable atherosclerotic lesions and surrounding normal appearing areas. EEMs were recorded from the intimal surface of the tissue, and following collection, the surface area of the tissue studied was marked with india ink.

Samples were then fixed in 4% neutral, buffered formalin and submitted for routine histologic analysis. Samples were classified according to the aforementioned classification scheme of the Cleveland Clinic Foundation [12], by a single pathologist. Of the 14 samples studied, seven displayed (1) intimal fibroplasia, one was classified as

(2) atherosclerotic plaque, two as (3) atheromatous plaque, and four as (5) calcified atheromatous plaque. The calcified plaques were noted to be extremely advanced lesions.

The EEMs of these tissues provide a complete characterization of their UV and visible spectroscopic properties. Our ultimate goal in analyzing this data is to determine whether there are significant differences in the fluorescence properties of normal and atherosclerotic tissues, and to determine at which excitation wavelengths these differences are diagnostically useful. Ideally, we would like to compare the fluorescence properties of normal tissue with those of each stage in the progression of atherosclerosis. In developing a guidance system for LAS catheters, at a minimum, we wish to use fluorescence to differentiate non-atherosclerotic vessel wall, non-calcified plaques and calcified plaques. Here, because of the relatively small number of samples of aorta studied using this method, we have attempted to achieve only the latter goal.

To this end, average EEMs were constructed for each of the following tissue categories: (0,1) non-atherosclerotic, (2,3) non-calcified plaque and (4,5) calcified plaque. These are shown as fluorescence contour maps in Figure 3, where contour lines connect points of equal fluorescence intensity. The general features of the UV and visible fluorescence of each of these types of tissue are similar. Seven peaks are present at or near (280, 330 nm), (330, 380 nm), (350, 460 nm), (370, 590 nm), (470, 530 nm), (470, 550 nm), and (470, 590 nm). Many of these peaks are separated by valleys which run parallel to the excitation and emission axes. In particular, valleys can be noted at 420 nm, 540, and 580 nm. The fluorescence intensity, location and lineshape of each of these peaks was different for the three types of tissue. However, the differences in location and lineshape were more subtle than the differences in intensity. The fluorescence intensity of each of these peaks is summarized as a function of tissue type in Table 1. In addition, Table 1 includes a potential assignment of the morphologic or molecular basis of each of these peaks. These assignments are based on results presented in Section 3:4.3, and are discussed in detail later.

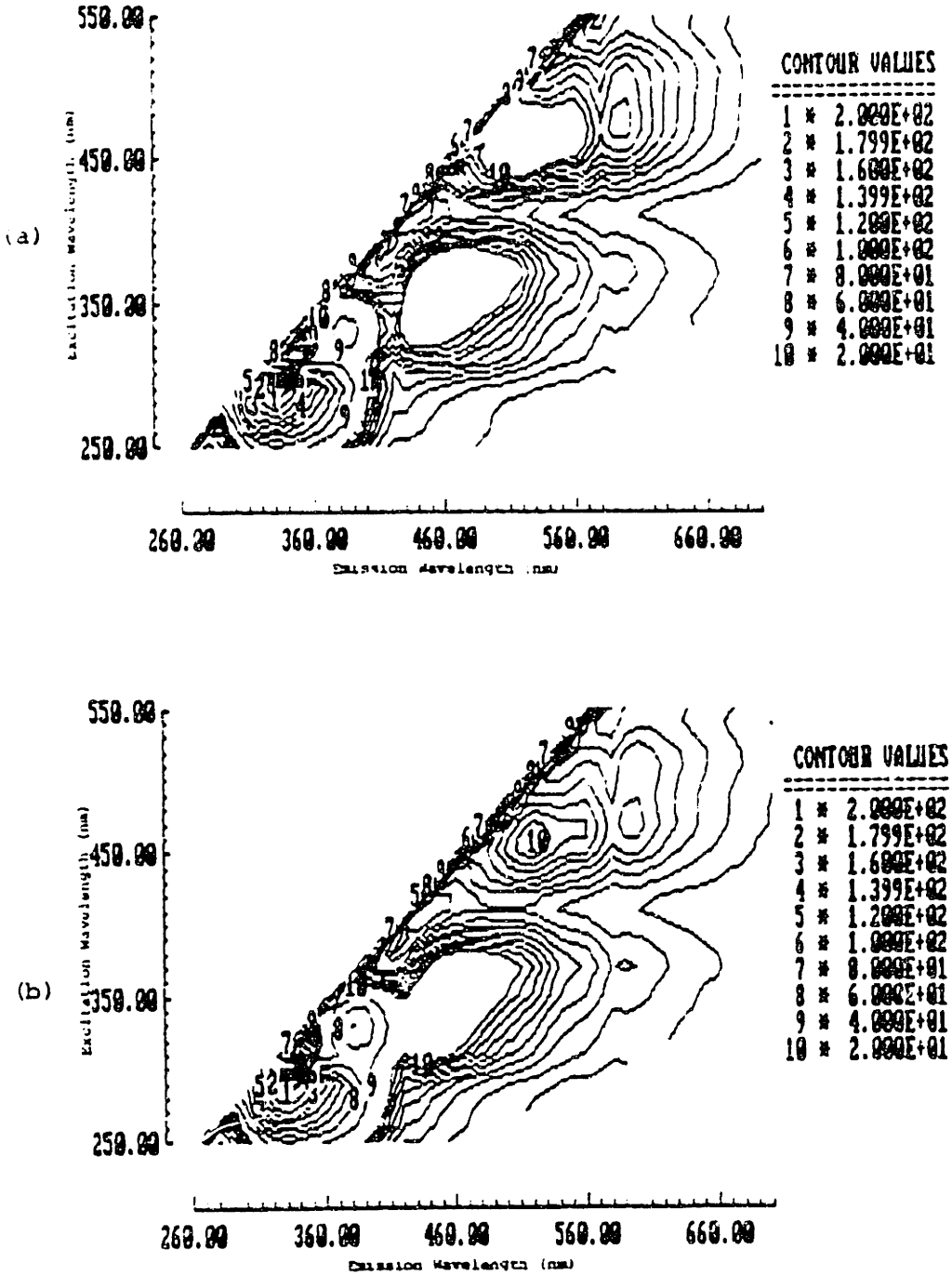

Figure 3: Contour map representations of the average fluorescence EEMs of: (a) (0,1) non-atherosclerotic aorta, (b) (2,3) non-calcified plaque and (c) (4,5) calcified plaque. Two sets of linearly spaced contour lines are shown; ten from 200.0 to 20.0 and nine from 18.0 to 2.0, where fluorescence intensity is given in arbitrary units relative to the fluorescence intensity of a standard. Ten contours are labeled as per the figure legend. The same set of arbitrary units is maintained for all EEMs shown in this thesis.

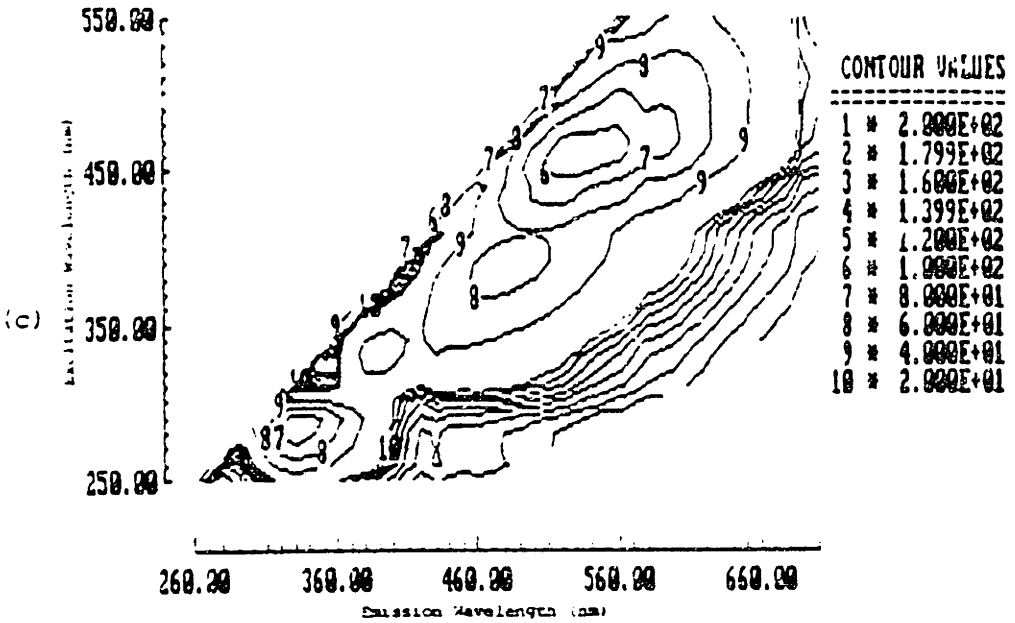

Figure 3 (cont.).

Table 1: Excitation emission maxima in the average fluorescence EEMs of human aorta.

Approximate Excitation-Emission Maximum	Peak Fluorescence Intensity from Average Fluorescence EEM (Arbitrary Units)			Potential Fluorophore/ Chromomorph (Table 4)
	Non-Athero-sclerotic (0,1)	Non-Calcified Plaque (2,3)	Calcified Plaque (4,5)	
(290, 330 nm)	200	200	80	Tryptophan
(330, 380 nm)	40	80	40	Collagen Fibers
(350, 460 nm)	20	20	60	Elastin Fibers Ceroid
(370, 590 nm)	10	6	20	Elastin Fibers Ceroid
(470, 530 nm)	30	20	100	Elastin Fibers Collagen
(470, 550 nm)	20	18	100	Elastin Fibers Collagen Fibers Ceroid
(470, 590 nm)	18	14	80	Elastin Fibers Collagen Fibers Ceroid

Although the general features of the fluorescence contour maps of these three types of tissue are similar, there are many differences in the absolute and relative intensities of the various excitation emission maxima. The peak near (290, 330 nm) is

similar in intensity in normal and non-calcified plaques; however, it is approximately a factor of two less intense in calcified plaques. The peak near (330, 380 nm) is of similar intensity in normal tissues and calcified plaques; in non-calcified plaques it is roughly two times more intensely fluorescent. The peak near (350, 460 nm) is approximately three times more intensely fluorescent in calcified plaques that in non-calcified tissues. That at (370, 590 nm) is least intense in non-calcified plaques, and most intense in calcified plaques. Finally, there are three peaks at 470 nm excitation and 530, 550 and 590 nm emission. These are most intense in the calcified plaques, with the 530 and 550 nm emission maxima being relatively the highest maxima. The fluorescence intensity of these peaks is lowest in non-calcified plaques; here again, the peaks at 530 and 550 nm have relatively greater fluorescence intensity than that at 590 nm. In contrast, the 530 nm peak is more intense than either of the subsidiary maxima in non-atherosclerotic tissue. The valleys at 420, 540 and 580 nm are most prominent in the EEMs of non-atherosclerotic tissues and non-calcified plaques.

3.3.1.2. Coronary Artery

Fluorescence EEMs were recorded from 20 samples of coronary artery *in vitro* using the method described in Chapter Two for arterial tissue. Tissue samples were obtained surgically during heart transplants from 10 recipient hearts. After removal of the heart, the first several centimeters of the main branches of the coronary arteries were blunt dissected. Intact arteries were then frozen in liquid nitrogen and isopentane and stored at -70°C. Before study, samples were thawed to room temperature; during all experiments samples were kept moist with a buffered (TRIS 50 mM), pH 7.4, 140 mM saline solution. The artery was opened, and spectra were obtained from the intimal surface. EEMs were recorded from grossly visible atherosclerotic lesions and from surrounding normal appearing areas. Following study, the intimal areas sampled spectroscopically were marked with india ink. Samples were fixed in 4% formalin and submitted for routine histologic analysis. A single pathologist classified all samples according to the classification scheme presented earlier in this chapter [12].

Of the 20 samples, one was classified as (0) normal, four as (1) intimal fibroplasia, two as (2) atherosclerotic plaque, one as (4) atheromatous plaque, three as (5) calcified atherosclerotic plaque, seven as (6) calcified atheromatous plaque and two as (7) calcified fibrotic/sclerotic plaque. Average EEMs were calculated for non-atherosclerotic samples of coronary artery belonging to categories (0) and (1), non-calcified plaques

including categories (2) and (3), and calcified plaques including samples from categories (4), (5) and (7). These average EEMs are shown as fluorescence contour maps in Fig. 4.

Again, the fluorescence EEMs of each tissue type contain similar features: four broad excitation-emission maxima, located near (290, 330 nm), (330, 380 nm), (340, 440 nm), and (450, 520 nm). These peaks are separated by valleys parallel to the excitation and emission axes at 420 nm. More subtle valleys are also appreciable at 540 nm. Although the general features of these fluorescence EEMs are similar, many differences can be appreciated in the fluorescence intensity, location and lineshape of these peaks. To summarize this information and facilitate comparison, these fluorescence EEMs have been characterized by the approximate position and intensity of all local excitation-emission maxima in Table 2. This comparison neglects the small shifts in the positions of these maxima and the fluorescence lineshapes of the associated peaks. In addition, Table 2 includes a potential assignment of the morphologic or molecular basis of each of these peaks. These assignments are based on results presented in Section 3:4.3, and are discussed in detail later.

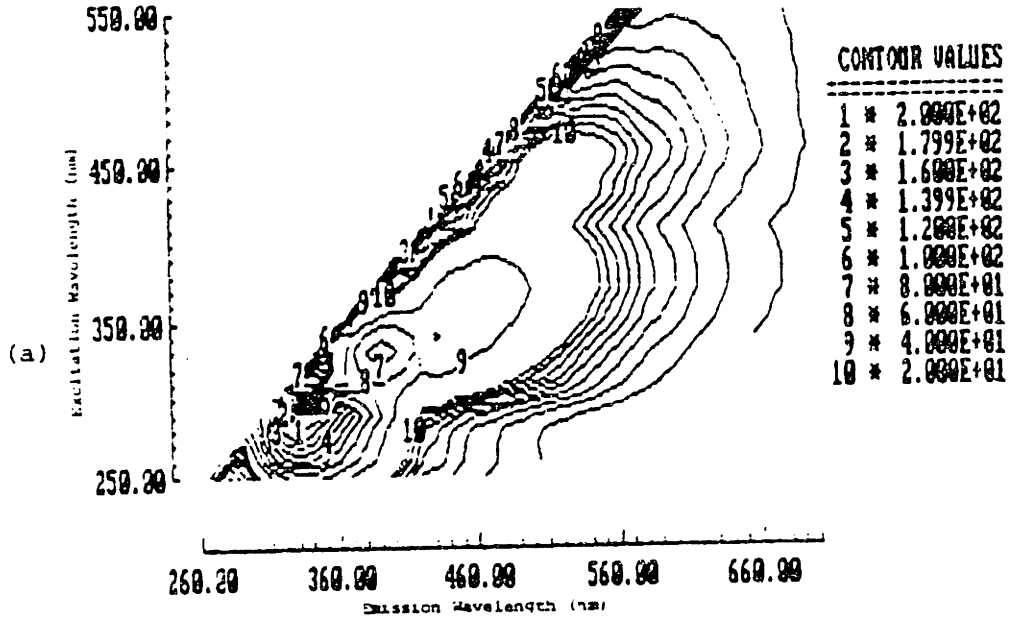

Figure 4: Average fluorescence contour maps of (0,1) non-atherosclerotic coronary artery, (2,3) non-calcified plaque, and (4,5,7) calcified plaque. Two sets of linearly spaced contour lines are shown; ten from 200.0 to 20.0 and nine from 18.0 to 2.0 units, where fluorescence intensity is given in arbitrary units relative to the fluorescence intensity of a standard. The ten contours are labeled as per the figure legend. The same set of arbitrary units is maintained for all EEMs shown in this thesis.

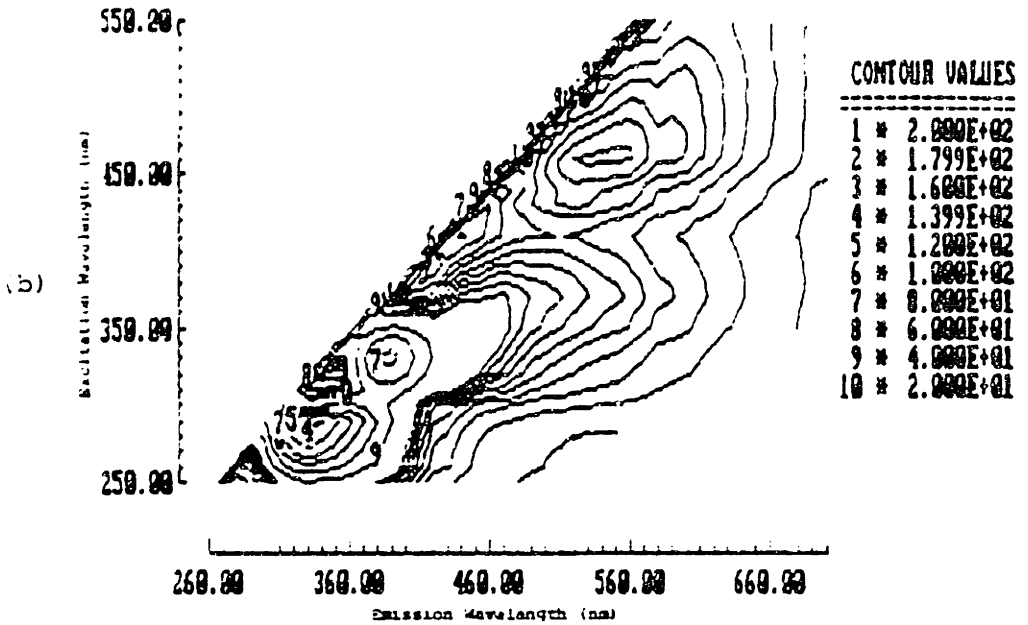

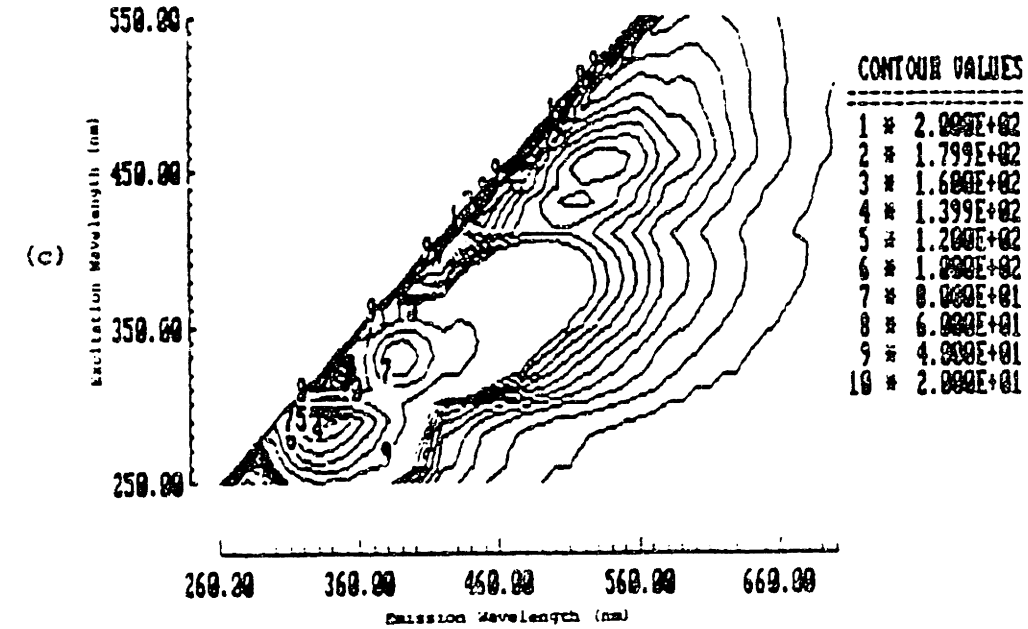

Figure 4 (cont.)

Table 2: Excitation Emission Maxima in the Average Fluorescence EEMs of Coronary Artery

Approximate Excitation-Emission Maximum	Fluorescence Intensity (Arbitrary Units)			Potential Chromophore/ Chromomorph (Table 4)
	Non-Atherosclerotic Tissue (0, 1)	Non-Calcified Plaque (2, 3)	Calcified Plaque (4, 5)	
(290, 330 nm)	200	140	140	Tryptophan
(330, 380 nm)	80	80	80	Collagen Fibers
(340, 440 nm)	60	20	40	Elastin Fibers Ceroid
(460, 520 nm)	20	18	20	Elastin Fibers Collagen Fibers Ceroid

From Table 2, it is evident that, for a given peak, the fluorescence intensity varied with tissue type; for example, the (450, 520 nm) peak was more intense in non-atherosclerotic tissues than in other types of tissue. The (290, 330 nm) peak was more intense in non-atherosclerotic tissues than in other types of tissue. The peak at (340, 440 nm) was slightly more intense in non-atherosclerotic tissues. In addition, although each type of tissue contained four peaks in generally similar locations, there were slight shifts in the exact location of the maxima, as well as slight differences in peak width or fluorescence lineshape. For example, visual inspection of Figure 4 shows that the peak near (450, 520 nm) is shifted to longer excitation and emission wavelengths in the fluorescence EEMs of all types of atherosclerotic tissue.

Thus, based on this limited number of samples, it can be concluded that the fluorescence properties of normal and atherosclerotic artery differ; in fact, the fluorescence properties of lesions with different composition are different. It should also be noted that there are many differences in the fluorescence EEMs of muscular and elastic arteries. Diagnostic algorithms for atherosclerosis, based on fluorescence spectroscopy, will, as a result, have to be tailored depending on the ultimate target.

3:3.2. Choice of Optimal Excitation Wavelength

Based on the differences observed in a visual inspection of the fluorescence contour maps of a limited number of normal and atherosclerotic arterial tissues, it is clear that it may be possible to differentiate normal arterial tissue and several types of atherosclerotic lesions using fluorescence spectroscopy. Thus, further study, to exploit these differences in a diagnostic algorithm for atherosclerosis was undertaken. In this process, the primary goal was the development of a guidance system for laser angiosurgery catheters. As discussed earlier, this application requires, at a minimum, the discrimination of normal tissue, non-calcified and calcified plaque. The first step in our process of algorithm development is the selection of excitation wavelengths at which this discrimination can best be achieved. We have utilized the fluorescence EEMs to select these wavelengths in both aorta and the coronary arteries.

The following procedures were used to compare the average fluorescence EEMs of normal, non-calcified and calcified plaques. First we compare the fluorescence intensities of the excitation emission maxima to determine which of the corresponding excitation wavelengths is most sensitive to the presence of various types of disease. Then, for more detail, we compare the diagnostic efficiency of all wavelengths using the ratio and difference of the average fluorescence EEMs.

3:3.2.1. Aorta

An examination of Table 1 shows that at any of the excitation maxima - 290, 330, 350, 370, and 470 nm - there are observable differences in the average intensities of the fluorescence emission maxima of normal and atherosclerotic human aorta. At either 370 or 470 nm excitation, these average intensities are different for normal tissue, non-calcified plaque and calcified plaque. These differences are greatest at 470 nm excitation.

This simple analysis, however, is not sensitive to differences in the precise location of excitation emission maxima, or to differences in fluorescence lineshape, such as the bandwidth of a peak. A simple method of detecting these types of differences, described in detail in Chapter Two, is to calculate the ratio and difference of the average fluorescence EEMs of the various subgroups of tissue. In ratio EEMs presented in this chapter, the EEMs of atherosclerotic tissue were always divided by the EEM of non-atherosclerotic tissue. In difference EEMs, the EEM of non-atherosclerotic tissue was always subtracted from that of atherosclerotic tissues. A simple interpretation of these

comparison EEMs is to regard all local maxima as regions where atherosclerotic tissues exhibit greater fluorescence intensity or unique fluorescence bands, and local minima as regions where normal tissues exhibited greater fluorescence intensity or unique fluorescence bands.

Figure 5 shows the difference of the average fluorescence EEMs of non-calcified plaques and non-atherosclerotic tissue and calcified plaques and non-atherosclerotic tissue. There are five peaks in the contour map of the difference of the average EEMs of non-calcified plaques and non-atherosclerotic tissues, at (330, 380 nm), (380, 460 nm), (470, 520 nm), (470, 560 nm) and (470, 600 nm); again, these peaks are separated by valleys parallel to the excitation and emission axes at 420, 540 and 580 nm. The largest of these is at (330, 380 nm). There are three peaks in the corresponding contour map for calcified plaque at (290, 330 nm), (390, 460 nm), and at (450, 540 nm), separated by valleys at 420, 540 and 580 nm. The largest of these is the (450, 540 nm) peak.

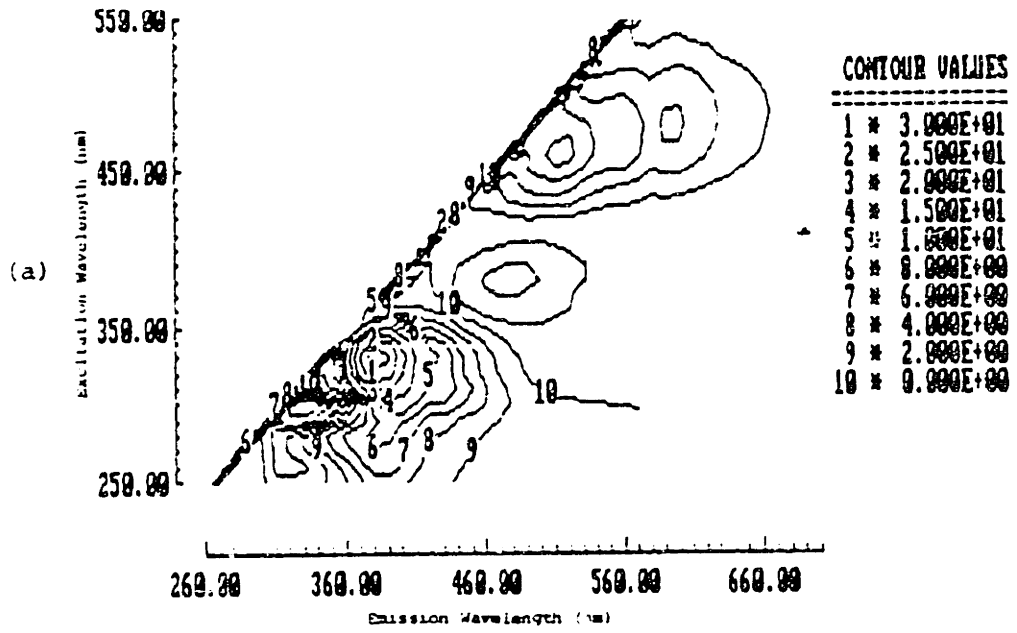

Figure Five: Contour map representations of the difference of the average fluorescence EEMs of (a) non-calcified plaque and (b) calcified plaque and non-atherosclerotic tissue. In (a), 15 contours are shown; five spaced linearly from 30 to 10 units, and ten spaced linearly from 8 to -10 units. In (b), 10 linearly spaced contours are shown from -100 to 80 units, where fluorescence intensity is given in arbitrary units relative to a standard. Ten contours are labeled in each, as per the figure legend.

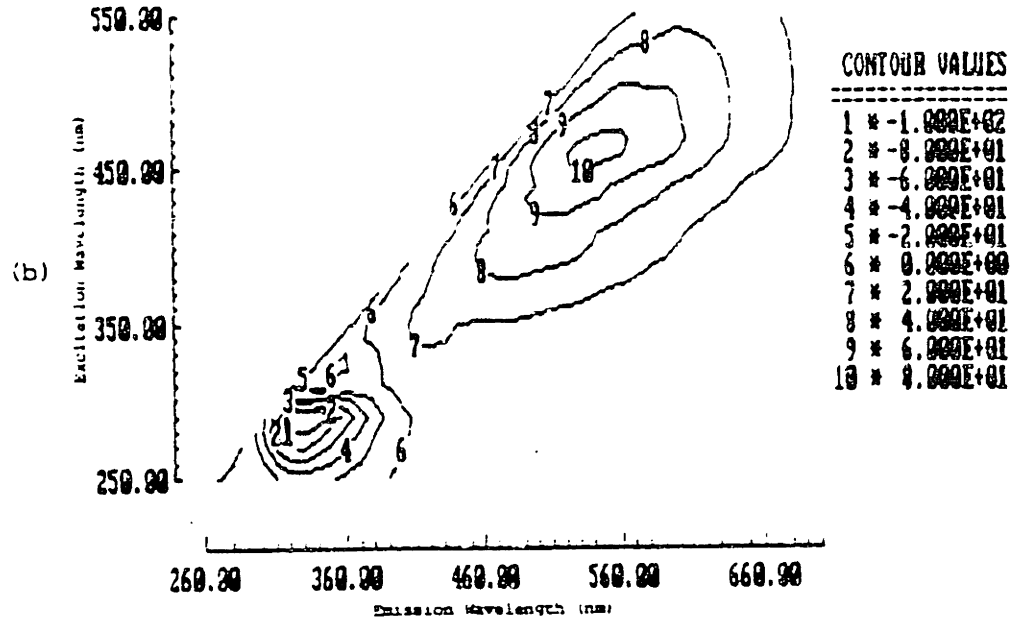

Figure 5 (cont.):

These peaks correspond to the differences in peak intensity highlighted in Table 1; however, the shifts in the location of the excitation-emission maxima in the difference maps indicate that, in addition to differences in the intensities of the excitation-emission maxima, the peak position and lineshape are also sensitive to the presence of disease.

Figure 6 shows a contour map representation of the ratio of the average fluorescence EEMs of non-calcified and calcified plaques to non-atherosclerotic aorta. Four peaks are discernible in the ratio of the non-calcified plaque to non-atherosclerotic aorta at (330, 380 nm), (390, 490 nm), (470, 560 nm) and (310, 420 nm). The first three of these peaks correspond to the differences highlighted in both Table 1 and the difference map. Five broad peaks are discernible in the contour map representing the ratio of the average EEM of calcified plaque to that of non-atherosclerotic aorta. These are at (290, 350 nm), (330, 360 nm), (340, 450 nm), (470, 570 nm) and (470, 610 nm), and again represent differences already highlighted in Table 1 and the difference map. In addition, in both these ratio maps a broad peak parallel to the emission axis is present at 420 nm.

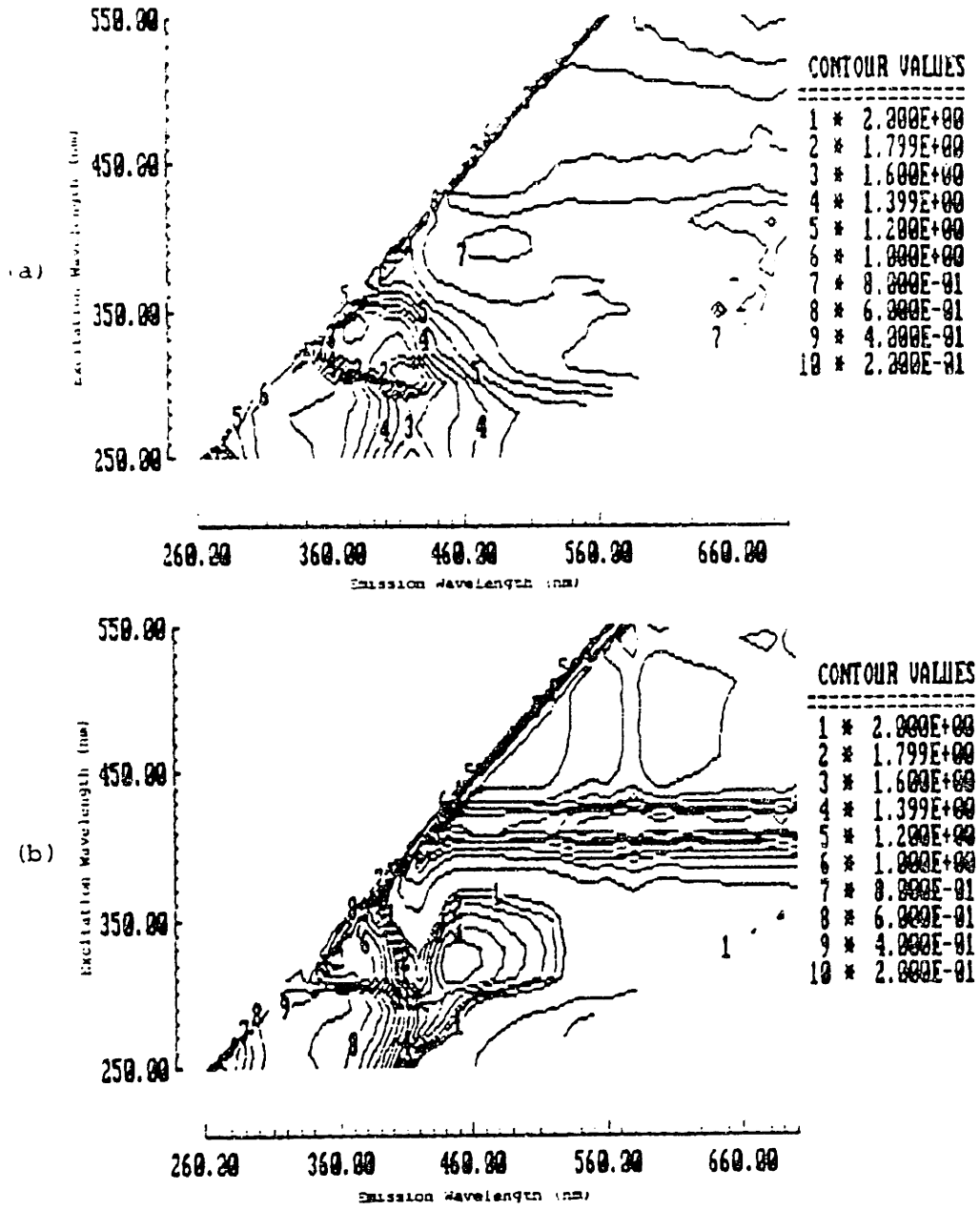

Figure 6: Contour map representations of the ratio of the average fluorescence EEMs of (a) non-calcified plaque and (b) calcified plaque to non-atherosclerotic aorta. Twenty linearly spaced contours are shown from 0.1 to 2.0; alternate contours are labeled 1 - 10. In (b) an additional 8 linearly spaced contours are shown from 3 to 10.

Thus, the ratio and difference maps provide a complete characterization of the differences in the fluorescence properties of normal and pathologic tissues. As discussed in Chapter Two, the location and value of local maxima and minima provide a means of characterizing these differences. Each local maxima or minima in these comparison maps can be thought of simply as representing a portion of the spectrum sensitive to the

presence of disease. In selecting excitation wavelengths to accomplish the diagnosis of disease, the most complete amount of information can be obtained by selecting excitation wavelengths which sample all regions sensitive to pathology.

Obviously, to record data in or near real time, it is useful to limit the number of excitation wavelengths to a minimum. A single excitation wavelength can be represented on a fluorescence contour map as a horizontal line parallel to the emission wavelength axis. Thus, a graphical analysis of the ratio and difference maps provides a method of selecting the minimal number of excitation wavelengths which can be used to completely characterize all histochemically distinct differences in the fluorescence properties of normal and pathologic tissues. This analysis consist simply of drawing the minimum number of horizontal lines which intersect all the separate peaks in the ratio and difference maps.

Figure 7 indicates that this can be accomplished in aorta with only three excitation lines: 310, 350 and 470 nm ± 10 nm. These excitation wavelengths were selected on the basis of empirical comparisons; however, it will be shown later that these wavelengths sample chromophores which are intimately related to the pathobiology of atherosclerosis.

(a)

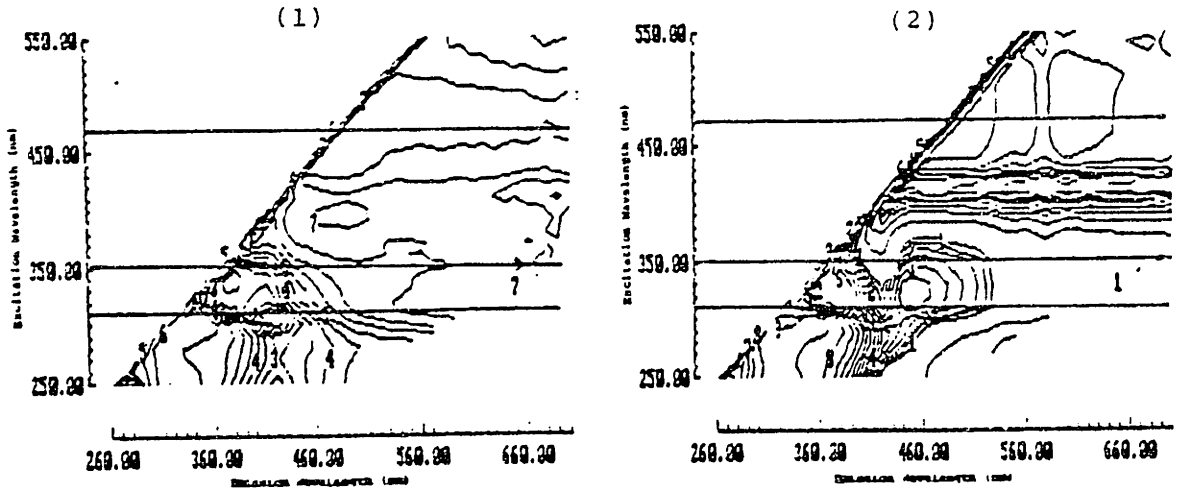

Figure 7: contour maps of the (A) ratio and (B) difference of the average fluorescence EEMs of (1) non-calcified plaque and (2) calcified plaque and non-atherosclerotic aorta. The three horizontal lines at excitation wavelengths of 310, 350 and 470 nm indicate the three excitation lines which sample all local maxima and minima in the ratio and difference maps.

(b)

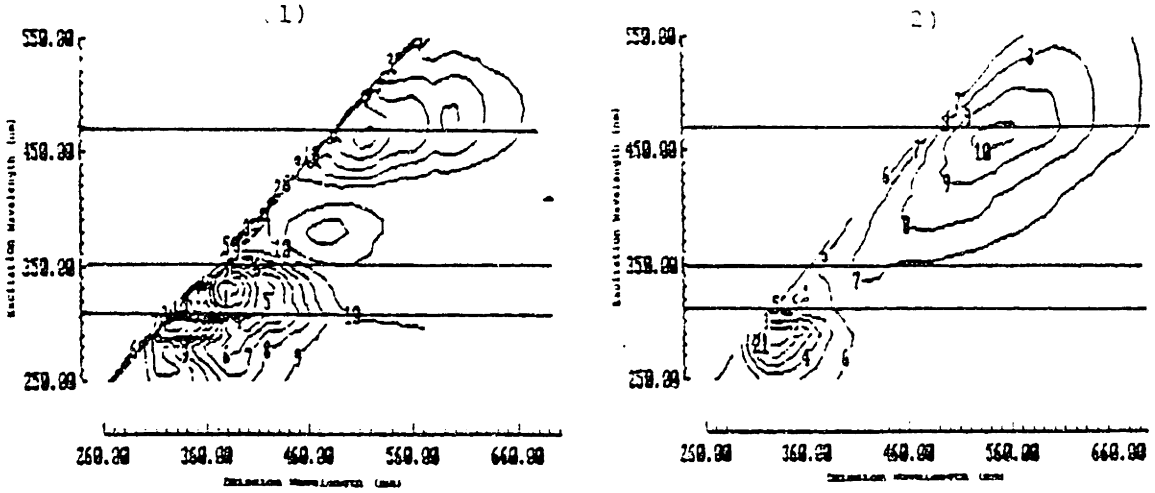

Figure 7 (cont.):

3:3.2.2. Coronary Artery

In a similar way, the excitation wavelengths most sensitive to the presence of coronary artery atherosclerosis can be selected. An examination of Table 2 shows that the excitation emission maxima at (290, 330 nm), (340, 440 nm) and (450, 520 nm) all exhibit a higher fluorescence intensity in non-atherosclerotic tissues than in calcified or non-calcified plaques. The fluorescence intensity of the peak at (330, 380 nm), on the other hand, is relatively constant in these types of coronary artery. This simple characterization indicates that there are differences in the fluorescence emission intensity at three of the excitation wavelengths corresponding to excitation maxima: 290, 340, and 450 nm. These differences are greatest at 290 and 450 nm excitation. Again, this simple analysis, however, is not sensitive to differences in the precise location of excitation emission maxima, or to differences in fluorescence lineshape, such as the bandwidth of a peak. To assess these differences, the ratio and difference of the average fluorescence EEMs of the various subgroups of tissue were calculated.

Figure 8 shows contour map representations of the difference of the average non-atherosclerotic tissue EEM and the average EEMs of non-calcified and non-calcified

plaques. Both difference maps exhibit maxima at three locations: (290, 330 nm), (360, 460 nm) and (440, 510 nm). The largest absolute difference in both types of plaque is at (290, 330 nm). Smaller differences in absolute fluorescence intensity can be observed at (360, 460 nm) and (440, 510 nm). These correspond roughly to the differences observed from a comparison of the fluorescence intensities of the three peaks at (290, 330 nm), (340, 440 nm) and (450, 520 nm), summarized in Table 2. The slight shift in the positions of the excitation emission maxima in the difference maps indicate that there are differences in the exact position and lineshape of the four peaks observed in the average fluorescence EEMs of tissue.

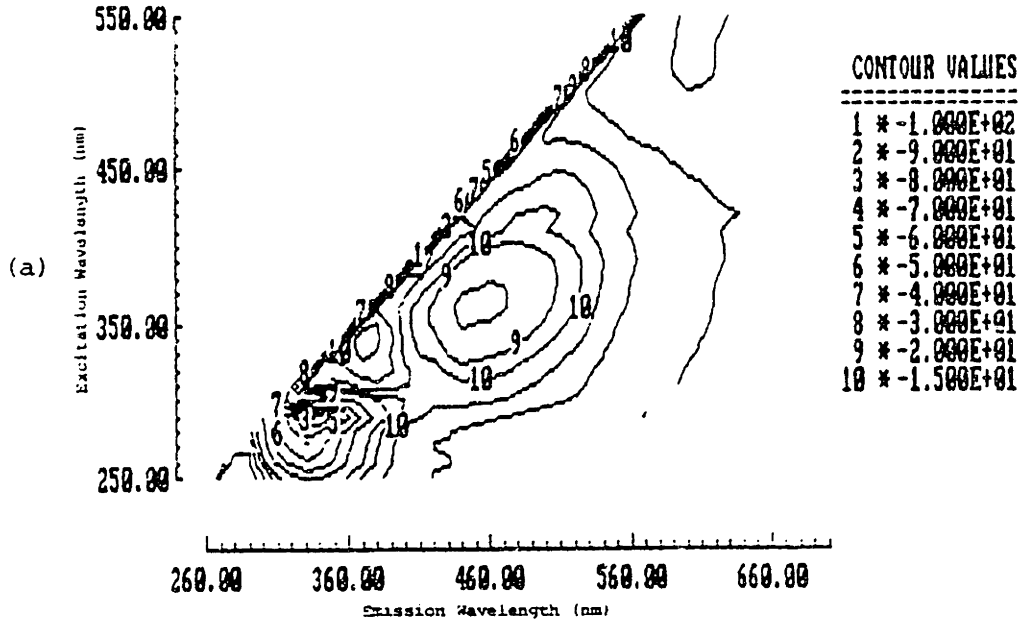

Figure 8: Contour map representations of the difference of the average fluorescence EEMs of non-atherosclerotic tissue and (a) non-calcified plaque and (b) calcified plaque. Two sets of linearly spaced contours are shown; nine from -100 to -20 units and six from -15 to 10 units. The same set of arbitrary units is maintained for all EEMs in this thesis. Ten contours are labeled as per the figure legend.

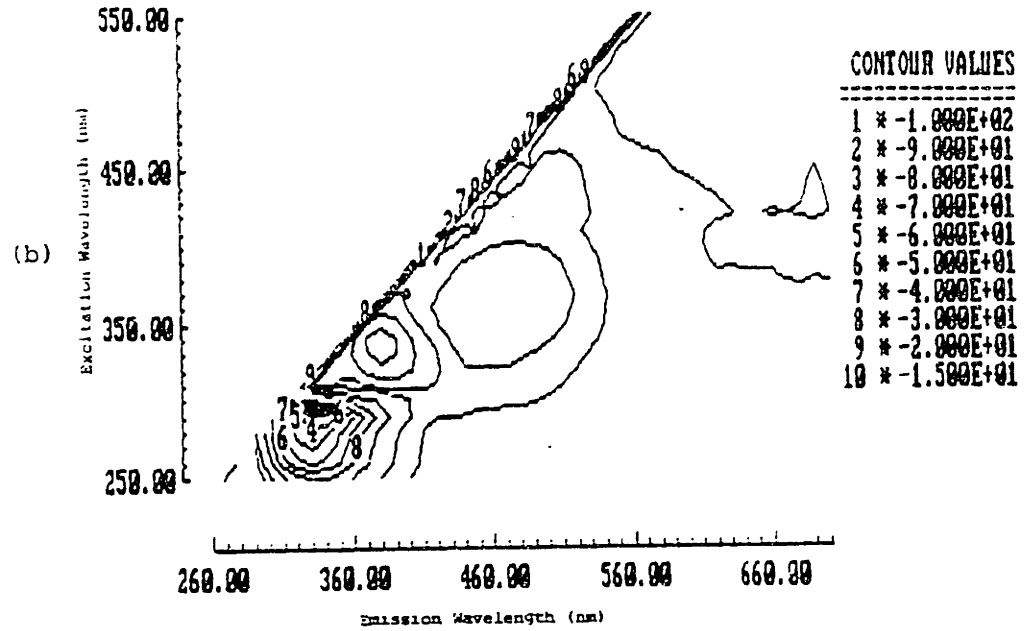

Figure 8 (cont.):

Figure 9 shows the contour map representations of the ratio of the average EEMs of non-calcified plaque and calcified plaque to the average non-atherosclerotic EEM. In these ratio maps, four peaks can be appreciated with excitation- emission maxima at (280, 380 nm), (340, 380 nm), (400, 460 nm) and (550, 610 nm). Again, these differences are similar to the differences described in the absolute intensities of the excitation emission maxima in the average EEMs of each tissue type, as summarized in Table 2.

The greatest relative difference in fluorescence intensity of normal and pathologic tissue is observed at (550, 610 nm); here the fluorescence intensity of atherosclerotic tissue is greater than that of normal tissue. However, this corresponds to a region of tissue in which the absolute fluorescence intensities are small. The fluorescence intensity of atherosclerotic tissues is less than that of non-atherosclerotic tissues, maximally less at (280, 380 nm) and (400, 460 nm). The fluorescence intensity of these tissues is roughly the same at (330, 380 nm); however, this location represents a local maximum of 1.0 in the ratio contour maps.

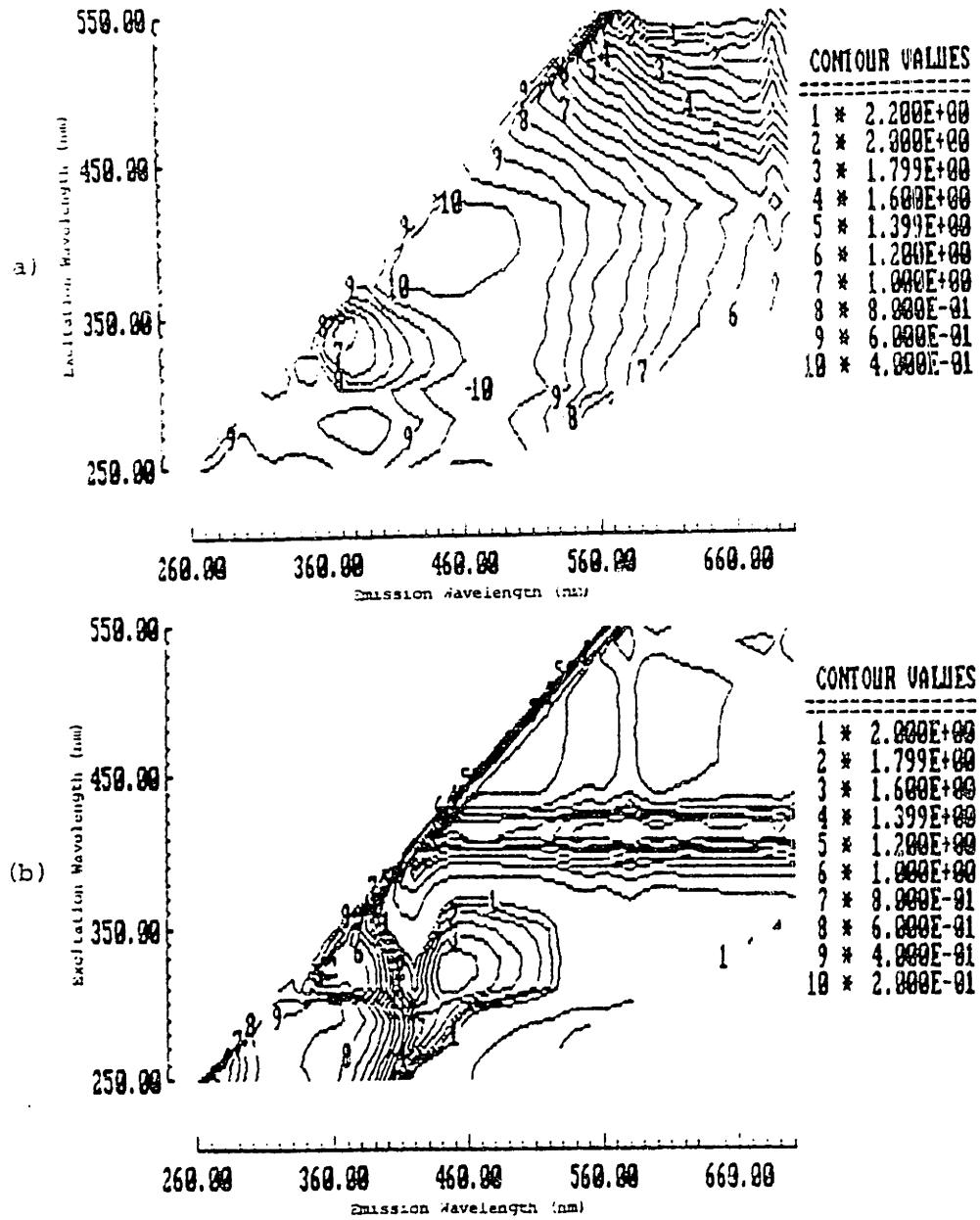

Figure 9: Contour map representation of the ratio of the average fluorescence EEMs of (a) non-calcified plaque and (b) calcified plaque to that the average EEM of non-atherosclerotic coronary artery. Twenty linearly spaced contours are shown from 2.2 to .2; alternate contours are labeled 1 - 10.

The ratio and difference maps provide a measure of the differences in the fluorescence properties of normal and non-calcified and calcified plaques. As discussed above, the location and value of local maxima and minima provide a means of characterizing these differences. Figure 10 shows, that for normal and atherosclerotic coronary artery, all local minima and maxima in the ratio maps can be sampled with only three excitation wavelengths at 310, 350 and 450 ± 10 nm. These excitation

wavelengths were selected on the basis of empirical comparisons; however, it will be shown later that these wavelengths sample chromophores which are intimately related to the pathobiology of atherosclerosis. Interestingly, although there were significant differences in the fluorescence EEMs of non-atherosclerotic and atherosclerotic elastic and muscular arteries, the same excitation wavelengths can be used to diagnose the presence of atherosclerosis in these types of arteries.

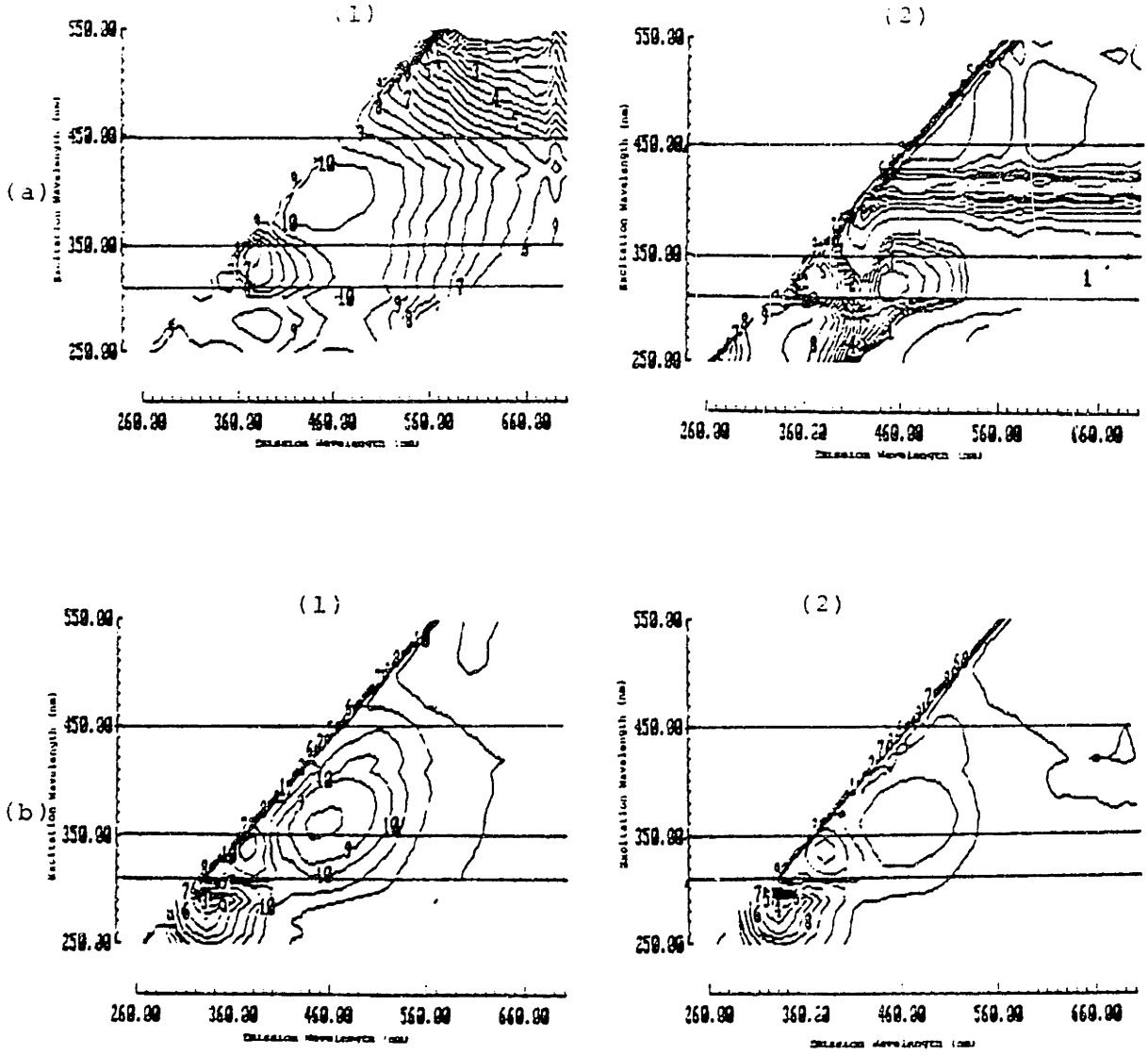

Figure 10: The (A) ratio and (B) difference of the average EEMs of (1) non-calcified plaque and (2) calcified plaque to non-atherosclerotic coronary artery. The three horizontal lines drawn at 310, 350 and 450 nm represent excitation lines which intersect all local maxima and minima in these maps. Thus, these represent excitation wavelengths which sample all possible histochemical differences in normal and pathologic coronary artery in the UV and visible region of the spectrum.

3:4. 476 nm Excitation

Based on the results of the EEM study, three excitation wavelength regions were identified at which the emission spectra of non-atherosclerotic and atherosclerotic muscular and elastic arteries were most different. These three excitation regions were chosen because they sampled all regions of the UV and visible portion of the spectrum at which the emission of these tissues differs. Thus, all of the diagnostic information in a fluorescence EEM can be obtained with three emission spectra excited in these regions.

In choosing a single excitation wavelength region for detailed development of a diagnostic algorithm, several factors should be considered, including:

1. the ease of generation of the excitation wavelength, from a consideration of available laser sources;

2. the penetration depth of the excitation wavelength in normal and atherosclerotic artery. In particular, in developing guidance systems for laser angiosurgery, the relationship of the penetration depth of the excitation wavelength and the ablating radiation needs to be considered. For effective control of ablation, the penetration depth of the excitation wavelength should be greater than that of the ablation wavelength.

3. The relationship of the chromophores sampled with the particular wavelength to the pathobiology af atherosclerosis should be considered, and

4. the relative size of the emission intensity at particular excitation wavelength should be examined for signal to noise (S/N) considerations.

Based on these considerations, and the results of previous studies conducted in our laboratory [24], the 450-470 nm excitation region was selected for further in depth studies. In particular, 476 nm excitation was chosen, as it can be easily obtained from an argon-ion laser. The penetration depth of this wavelength in normal human aorta is approximately 300 μm [33]. This is greater than the intimal thickness of normal muscular and elastic arteries and is also greater than the typical intimal thickness in intimal fibroplasia and many early atherosclerotic plaques, implying that with this excitation wavelength both structural and histochemical information can be extracted from the resulting emission spectra. Many groups use UV or IR wavelengths for ablation of

atherosclerotic plaque, and the penetration depth of wavelengths in these regions is significantly less than 300 μm [34]. Also the amount of tissue which can be reliably removed by ablation at these wavelengths is less than 300 μm [34]. The chromophores which are sampled by this excitation wavelength have been shown to be intimately related to the pathobiology of atherosclerosis [35]. Finally, although the emission intensities of arterial spectra excited in the visible portion of the spectrum are less than those excited in the far UV region, spectra with reasonable S/N have been obtained with 476 nm excitation *in vivo* in near real time [36].

At 476 nm excitation, the spectroscopic properties of normal vessel wall and the various stages in the progression of atherosclerosis were characterized in detail. From this characterization, a model of tissue fluorescence was developed. The parameters of this model were then utilized to develop diagnostic algorithms for the presence of atherosclerosis in muscular and elastic arteries. The results of these studies will be presented here.

Samples of thoracic and abdominal aorta were obtained from human cadavers at autopsy, within 24 hours of expiration. Samples of the first 5-10 mm of the major coronary arteries were obtained at surgery from recipient hearts during heart transplants. Upon receipt, all samples were snap frozen in liquid nitrogen and isopentane and stored at -70°C until study.

At the time of the experiment, tissues were thawed to room temperature, and were kept moist in a buffered (TRIS 50 mM), pH 7.4, 140 mM solution of saline. At the time of study, the artery was opened, and fluorescence spectra were recorded from the intimal surface of the artery. 476 nm LIF spectra were recorded from all discrete observable plaques and surrounding normal appearing regions using the spectral catheter system described in Chapter Two. Following spectral analysis, the intimal area sampled by fluorescence was marked with india ink, the sample was fixed in 4% formalin, and submitted for histologic analysis. All samples were classified according to the scheme presented earlier by a single pathologist [12].

Spectra were obtained from 148 separate sites in aorta from 30 cadaver sources. Spectra were recorded from 82 sites of coronary artery from 15 patients. Table 3 provides a summary of the histologic classification of these tissues. Data presented in the remainder of this report is from these sample sets.

Spectra at this excitation wavelength were obtained using the spectral catheter system described in Chapter Two. This system was chosen for several reasons. The first is that, unlike the conventional spectrofluorimeter used to collect tissue EEMs, it provides a well defined excitation and collection geometry [33, 37]. It has been shown that the contributions of attenuation to the fluorescence spectra of turbid materials such as human tissue are governed in part by the excitation and collection geometries. Thus, a well defined collection geometry is required for meaningful comparisons of data obtained with different fluorimeters. The catheter system described in Chapter Two also provides a collection geometry with a fixed distance between the surface of the tissue and the detector, so calibrated fluorescence intensity information can be reliably recorded. Finally, this system can be used to collect data *in vivo* with minor modifications [36].

Table 3: Summary of histologic classifications of 148 samples of human aorta and 82 samples of human coronary artery.

Tissue Classification	# Samples of Aorta	# Samples of Coronary Artery
(0) Normal	16	5
(1) Intimal Fibroplasia	58	34
(2) Atherosclerotic Plaque	25	15
(3) Atheromatous Plaque	11	1
(4) Calcified Atherosclerotic Plaque	10	0
(5) Calcified Atheromatous Plaque	14	18
(6) Fibrotic/Sclerotic Plaque	7	0
(7) Calcified Fibrotic/Sclerotic Plaque	0	8

3:4.1. Typical Data

3:4.1.1. Aorta

Figure 11 shows characteristic spectra of normal human aorta (0), and two types of plaque: atherosclerotic plaque (2),and calcified atheromatous plaque (5). Each of these spectra contains similar features; three peaks are present near 520, 560 and 600 nm, two valleys occur at 540 and 580 nm. Although generally similar, there are several differences in the fluorescence spectra of these tissues. The peak fluorescence intensity of the normal aorta is greater than that of both plaques; with the calcified plaque having a slightly greater peak fluorescence intensity than that of the non-calcified plaque. The

relative intensities of the peaks also varies. The 520 nm peak is the most intense peak in the normal tissue spectrum; however, in the spectrum of non-calcified plaque, the 550 nm peak is roughly the same intensity as that of the 520 nm peak, and in the calcified plaque, the 550 nm peak is the most intense peak. Finally, the valleys at 540 and 580 nm appear more prominent in the fluorescence spectrum of the normal tissue. Although spectra are presented here from three individual samples, these trends were observed in the fluorescence of most samples of normal aorta and non-calcified and calcified plaques.

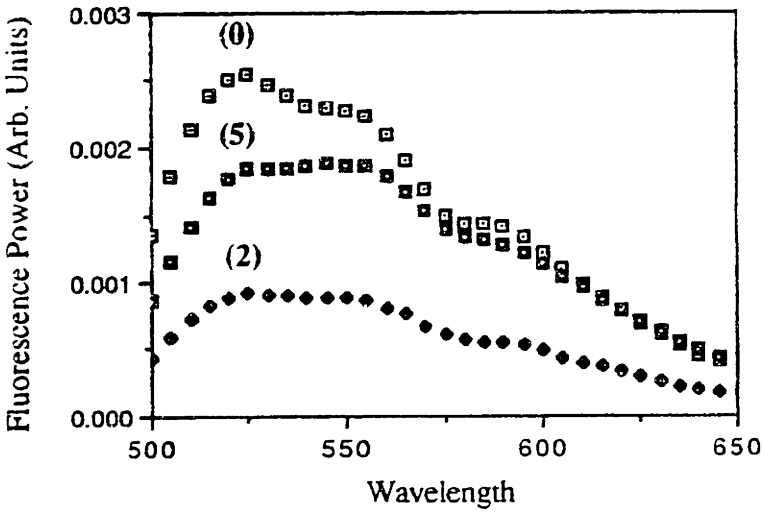

Figure 11: Representative 476 nm excited laser induced fluorescence spectra of human aorta. Typical data is shown for (0) normal tissue, (2) an atherosclerotic plaque, and (5) a calcified atheromatous plaque. Fluorescence power is given in arbitrary units, but the same set of arbitrary units is maintained throughout this chapter for data obtained with the spectral catheter system described in Chapter Two.

These features are similar to those observed in the fluorescence EEMs of normal and atherosclerotic aorta at 470 nm excitation (Fig. 3 and Table 1). There, emission maxima were present at 530, 550 and 590 nm with more prominent valleys at 540 and 580 nm than in Fig. 11. It will be later demonstrated that these valleys are due to attenuation of oxy-hemoglobin, and are more prominent in spectra collected with systems that have the collection geometry of the conventional fluorimeter used to record the EEMs [37].

The differences in the fluorescence lineshape of normal and atherosclerotic aorta are similar in both Figs. 3 and 11. In both, the 550 nm emission peak is more intense

relative to the 530 nm peak in atherosclerotic tissues, particularly in calcified plaques. The fluorescence intensity of normal tissue is more intense than that of non-calcified plaques at 470 nm excitation both in the EEMs and in Fig. 11. However, the fluorescence intensity of calcified plaques was greater than normal tissue at 470 nm excitation in the EEMs. Figure 11 shows that, typically, with the catheter system, the fluorescence intensity of normal tissues is slightly greater than that of calcified plaques tissues at 476 nm excitation. As discussed in more detail later, this difference is likely due to the fact that the fluorescence EEMs of calcified plaques were collected from extremely advanced calcified lesions in which the fibrous cap had calcified. An EEM of a more typical lesion, histologically similar to those examined with the catheter system, showed similar intensity differences as in Fig. 11.

3.4.1.2. Coronary Artery

Figure 12 shows representative spectra of three samples of human coronary artery obtained at 476 nm excitation using the catheter system described in Chapter Two. Spectra are shown for individual samples of (0) normal artery, (2) atherosclerotic plaque and (5) calcified atheromatous plaque. Fluorescence power is reported here in the same set of arbitrary units as that of Fig. 11.

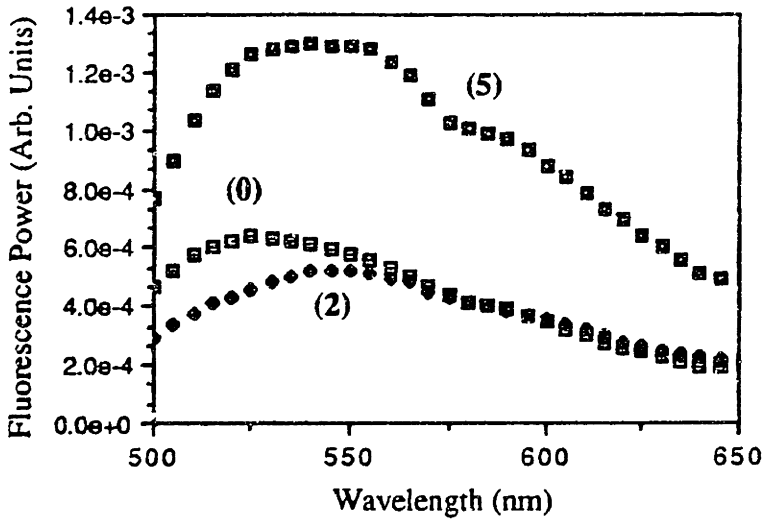

Figure 12: Typical 476 nm laser excited fluorescence spectra of (0) normal coronary artery, (2) atherosclerotic plaque and (5) calcified atheromatous plaque. Fluorescence power is reported here in the same arbitrary units as Fig. 11.

Again, the general features of these three spectra are similar, with fluorescence peaks present at or near 520, 550 and 600 nm, and valleys at or near 540 and 580 nm. Differences were observed in the peak and relative fluorescence intensities of normal and atherosclerotic tissues. In coronary artery, the peak fluorescence intensity of normal artery is higher than that of non-calcified plaque; however, the peak fluorescence intensity of the calcified plaque was greater than that of normal tissue. The 520 nm peak was the most intensely fluorescent peak in the spectrum of normal tissue, however; the 550 nm peak was the most intense in the spectra of atherosclerotic tissues. For coronary artery, the valleys at 540 and 580 nm were slightly more pronounced in the fluorescence spectrum of normal tissues. Although spectra are presented here from three individual samples, these trends were observed in general in the fluorescence of normal aorta and non-calcified and calcified plaques.

These features are again similar to those observed in the EEMs of non-atherosclerotic and atherosclerotic coronary artery (Fig. 4 and Table 2). In general, the valleys at 540 and 580 nm were much less pronounced in the EEMs of muscular arteries; thus, Table 2 reported only a single excitation emission maximum in this excitation region at (450, 520 nm). However, as pointed out earlier, this maximum was shifted to longer emission wavelengths in atherosclerotic tissues. This is also seen in Fig. 12, where the peak emission wavelength of non-calcified and calcified plaques is at approximately 560 nm. Again, in both the EEMs and in Fig. 12, the peak intensity of non-calcified plaques is slightly less than that of normal tissues at 470 nm excitation. The fluorescence EEMs indicate that the fluorescence intensity of calcified plaques is also slightly less than that of normal tissues at 470 nm excitation. This is not in agreement with Fig. 12; however, many of the calcified plaques from which EEMs were recorded were only minimally calcified. As discussed later, this is most likely the source of this discrepancy.

Thus, at 476 nm excitation, the fluorescence spectra of normal and pathologic aorta and coronary artery share the same general features. As noted in the EEM study, at 476 nm excitation, there are significant differences in the fluorescence properties of normal and atherosclerotic muscular and elastic arteries. However, both the absolute fluorescence intensity and the relative intensities of the peaks and valleys appear to vary between normal tissues, non-calcified plaques and calcified plaques in these arteries, suggesting that the chemical differences in these tissues can be sampled using 476 nm excited fluorescence spectroscopy. The remainder of this chapter focuses on developing methods to extract this chemical information from the fluorescence spectra and applying it

to the diagnosis of atherosclerosis. The differences observed in the fluorescence spectra of aorta and coronary artery suggest that algorithms will need to be developed separately for muscular and elastic arteries.

3:4.2. Empirical Algorithms

The simplest method of algorithm development, in fact, does not require developing a method to extract chemical information from the fluorescence spectra. The empirical comparison of the typical spectra shown in Figs. 11 and 12 suggests several parameters of these spectra that might have diagnostic utility. For example, in aorta, the peak fluorescence intensity of normal tissues is greater than that of atherosclerotic tissues. A simple diagnostic algorithm might then consist of comparing the absolute fluorescence intensity of the 520 nm peak, I(520). Similarly, the relative intensities of the 520 and 550 nm peaks or the 600 nm peak and the 580 nm valley might also be utilized.

3:4.2.1. Aorta

We have explored the performance of such empirical algorithms using the data set of 148 samples of aorta. Figure 13 provides a graphical representation of the most successful, that based on I(520). This figure shows the fluorescence intensity of the 520 nm peak as a function of sample type for all 148 samples. On average, I(520) is greater for non-atherosclerotic tissues than for atherosclerotic tissues. A simple algorithm represented by the straight line at I(520) = .011 separates most non-atherosclerotic tissues (0,1), from atherosclerotic tissues (2-6). This algorithm correctly diagnoses 77% of the 148 samples; however, its performance is particularly poor for calcified tissue (5,6), achieving a correct diagnosis in only 52% of the cases. Figure 11 illustrates the reason for this, the peak fluorescence intensity of calcified plaques is more similar to that of normal tissues than is that of non-calcified plaques.

The performance of this simple algorithm is encouraging; it indicates that fluorescence spectroscopy does provide diagnostically useful information. However, although simple, this method of algorithm development completely neglects the wealth of information about the chemical and physical characteristics of the tissue contained in the fluorescence spectra. As stressed earlier, it is likely that a method of obtaining this information in real time *in vivo* will be useful in improving therapies of CAD. Extraction of this information may also improve the performance of diagnostic algorithms for atherosclerosis based on fluorescence spectroscopy. The remainder of this chapter

focuses on developing a model of tissue fluorescence and applying this model to data from the previously described sample sets in order to extract this type of physicochemical information and utilize it diagnostically to detect atherosclerosis.

Figure 13: Empirical diagnostic algorithm for the detection of atherosclerosis in human artery. The fluorescence intensity at 520 nm is plotted versus sample type for 148 samples of human aorta. The straight line at I(520) = 0.11 indicates the decision surface; points above this line are diagnosed as non-atherosclerotic, while points below the line represent atherosclerotic samples. The algorithm correctly diagnoses 77% of all samples; however, only 52% of calcified plaques are correctly diagnosed with this algorithm.

3:4.3. Morphologic/Biochemical Basis of Fluorescence

The groundwork for developing a model of tissue fluorescence has been developed previously. In Chapter Two, we derived a general equation which described the fluorescence of single and multi-layer tissues in terms of contributions from individual constituents which could contribute to the fluorescence spectrum through attenuation or fluorescence. This equation, shown below for tissues comprised of a single, optically thick layer, provides the basis by which we will extract physicochemical information from tissue fluorescence spectra.

$$(1)\ S(\lambda_x,\lambda_m) = kP(\lambda_x)\frac{\sum_{i=1}^{N} \mu_{ai}(\lambda_x)\frac{\phi_i(\lambda_x,\lambda_m)}{2}}{\sum_{i=1}^{N} (\mu_{ti}(\lambda_x) + \mu_{ti}(\lambda_m))}$$

The symbols used here are defined in detail in Chapter Two, basically, μ_i represents contributions of absorption or attenuation from individual tissue constituents, and ϕ_i represents the same for fluorescence. Our procedure will be to fit tissue spectra to eq. (1), where the individual fluorescence and attenuation contributions from each tissue component will be varied to minimize the sum of the squares of differences between the experimental and calculated spectra. These parameters are related to the chemical composition of the tissue. In this chapter, we will interpret the diagnostic implications of these parameters for atherosclerosis in muscular and elastic arteries.

In order to accomplish this task, we must first identify which components of arterial tissue contribute to the fluorescence spectrum. This requires identification of the individual moieties in tissue which attenuate light or fluoresce and determination of their spectral characteristics. This identification can be made at several levels, for example, the precise chemical structures which are responsible for attenuation or fluorescence (chromophores) can be determined. Another approach is to identify tissue constituents which fluoresce and/or attenuate based on their morphologic characteristics (chromomorphs).

The most fruitful approach depends on the ultimate application of the diagnostic algorithm. As our primary goal is to obtain histochemical information about atherosclerotic lesions *in vivo* in real time using fluorescence spectroscopy, we have approached this identification from a morphologic point of view. We have utilized 476 nm excited fluorescence microscopy to identify the fluorescent morphologic structures within aorta and coronary artery.

This identification, which will be described in the following section, allowed for two important steps to be taken. Knowledge of the morphologic identity and localization of individual fluorescing chromomorphs allowed us to manipulate tissue samples in order to separately record the fluorescence and attenuation lineshapes of chromomorphs which both attenuate light and fluoresce. Furthermore, using these techniques and reflectance spectroscopy, identification of chromomorphs which simply attenuate was completed, and attenuation lineshapes were obtained. These studies provide the basis for application of Eq. (1) to 476 nm excited fluorescence spectra of arterial tissue.

Furthermore, based on this identification of chromomorphs contributing to spectra excited with 476 nm light, we were able to utilize fluorescence EEMs in order to identify

most of the chromomorphs contributing to the fluorescence spectra of these tissues over a wider range of UV and visible wavelengths. In some cases, this coupled information allowed us to make a molecular identification of the chromophores.

3:4.3.1. Aorta

The morphologic, and in some cases, the biochemical identity of fluorescing constituents of aorta have been established in the UV and visible regions of the spectrum. At 476 nm excitation, fluorescence microscopy was utilized to morphologically identify these constituents. These identifications were then used to identify the morphologic basis of peaks in the fluorescence EEMs near 476 nm excitation.

3:4.3.1.1. 476 nm Excitation

3:4.3.1.1.1. Fluorescence Photo-Microscopy[1]

The morphologic basis of human aorta autofluorescence at 476 nm excitation has been established using fluorescence microscopy and has been reported in detail previously [35]. The relevant results of this study will be summarized here. A standard fluorescence microscope was adapted for 476 nm epi-illumination from an argon-ion laser. The fluorescence of 4 μm thick unstained frozen sections of human cadaver aorta was observed using long pass filters with 50% transmission at: 515, 530, 570, 590 and 610 nm. Excitation intensities varied from 0.3 - 2.6 mW/mm^2. Fluorescence was observed visually, and documented photographically. In all cases morphologic identity of fluorescing structures was determined by comparing the autofluorescence of unstained section to light microscopy of serial sections stained with hemotoxylin and eosin (H&E), Movat's pentachrome and oil red O stains. The various barrier filters were used to characterize the peak emission wavelength and approximate bandwidth of fluorescent peaks emanating from the various chromomorphs. Autofluorescence was characterized for 16 samples of human aorta from 9 patients. Samples were classified according to histologic type; one sample was classified as normal, five as displaying intimal fibroplasia, six as non-calcified plaque and four as calcified plaque on the basis of H&E morphology.

---

[1]The results described in this section are largely the work of collaborators at the Cleveland Clinic Foundation, primarily Dr. Maryann Fitzmaurice and Dr. George Bordagaray. Their contributions are gratefully acknowledged.

In normal arteries the observed autofluorescence was attributed to the structural proteins, collagen and elastin. The majority of the intima in normal aorta was not fluorescent. The media, however, contained thick intensely fluorescent fibers arranged in parallel arrays which corresponded to elastin fibers on Movat stains. Also in the media were thinner, less intensely fluorescent fibers which corresponded to collagen fibers on Movat stains. The fluorescence of the adventitia was intermediate in intensity between that of the intima and media, and was due to loosely arranged connective tissue fibers. Although the collagen fibers appeared less intensely fluorescent, the color of elastin and collagen autofluorescence was similar with all barrier filters from 515 to 590 nm. No structural protein autofluorescence was observed in normal tissues with the 610 nm barrier filter. In intimal fibroplasia, the autofluorescence of the intima was increased, sometimes approaching the fluorescence intensity of the media. This fluorescence corresponded to the presence of densely packed collagen fibers on Movat stains.

In the intima of non-calcified plaques, there was a moderately intense band of autofluorescence associated with the fibrous cap, which corresponded to densely packed collagen fibers on Movat stains. The color of this autofluorescence was similar to that of the structural protein fluorescence associated with normal aorta. When an atheromatous core was present, its autofluorescence was extremely heterogeneous, and was characterized by intensely fluorescent deposits, either solid or ring-shaped, seen against a non-fluorescent background. The autofluorescence of these deposits corresponded to large extra-cellular lipid deposits in the atheroma core on oil red O stains. These fluorescent deposits were most abundant at the border between the atheroma core and the adjacent fibrous cap, and appeared to increase in amount with the severity of the plaque. With the 515 nm barrier filter, these fluorescence deposits appeared yellow in color. As the wavelength of the barrier filter was increased, the fluorescence intensity of these deposits decreased, but not to the same extent as did the structural protein fluorescence. Further studies showed that these deposits were resistant to extraction with typical lipid solvents, thus they possessed all the properties of ceroid, an oxidation product of lipoproteins [15], and were identified as such [38]. In atherosclerotic plaques, the fluorescence characteristics of the media remained essentially unchanged from that of normal arteries, unless the atherosclerotic lesion extended to involve the media.

The autofluorescence of calcified plaques was generally similar to that of non-calcified plaques. Some of the fluorescent deposits in the atheromatous core of these plaques corresponded to discrete calcified deposits on H&E stains. The fluorescence of

these deposits was yellow in color, and frequently visible even with the 610 nm barrier filter.

3.4.3.1.1.2. EEMs

These results suggest that in normal aorta, two arterial constituents contribute to the fluorescence spectrum: the structural proteins collagen and elastin. A preliminary survey of their fluorescence properties under the fluorescence microscope indicates that, with 476 nm excitation, the fluorescence properties of these proteins are similar, with a peak fluorescence near the green region of the spectrum (510-520), and fluorescence intensity decreasing with increasing wavelength, not extending past 610 nm. In atherosclerotic plaques, these proteins also contribute to the fluorescence spectrum; however, the fluorescence of ceroid, peaking near the yellow region of the spectrum (550-560 nm), is also important [35].

This can be used to interpret the visible region of the EEMs and the typical fluorescence spectra obtained at 476 nm excitation presented earlier. In both the EEMs of aorta and the spectra in Fig. 11, at 470 nm excitation, three distinct peaks are present at 520, 550 and 590 nm emission. These results suggest that the 520 nm peak is due to the emission of collagen and elastin fibers, and the 550 nm peak is due to the emission of ceroid. The 550 nm peak was observed to be relatively more intense than the 520 nm peak in atherosclerotic plaques, consistent with our observation of increased ceroid in these tissues. In addition, the 520 nm peak is most intense in the fluorescence EEMs of normal tissues. This is consistent with our observation that the fluorescence intensity of elastin fibers is greater than that of collagen fibers. The media of aorta is primarily comprised of elastin, and the primary fluorescent structure in the intima is collagen. As the intimal thickness increases, in atherosclerosis, the relative contribution of the media (elastin fibers) decreases, and the fluorescence intensity at 520 nm decreases.

Although this interpretation is consistent with our data, it cannot account for two features of the fluorescence EEMs at 470 nm excitation. The origin of the fluorescent peak at 590 nm emission is unclear in all tissues. In normal tissues, where no ceroid was observed, the origin of the 550 nm peak is also unclear. These peaks can be explained by considering the effects of attenuation of emitted fluorescence light. As described in Chapter Two, attenuation acts to create valleys in the fluorescence EEMs which run parallel to the excitation and emission axes. Figure 14 shows a typical total reflectance spectrum of normal human aorta obtained with a conventional absorption

spectrophotometer equipped with an integrating sphere. Valleys in the total reflectance spectrum indicate peaks in attenuation, and are present at 420, 540 and 580 nm. An examination of Fig. 3 shows that these match the positions of the valleys in the EEMs at 420 nm, 540 nm and 580 nm; similar attenuation valleys are also present in the emission spectra of Fig. 11 at 540 and 580 nm. The attenuation peaks in Fig. 14 are consistent with the attenuation of oxy-hemoglobin [33,.37, 39]. Thus, the origin of the valleys in the fluorescence spectra at 420, 540 and 580 nm is oxy-hemoglobin attenuation.

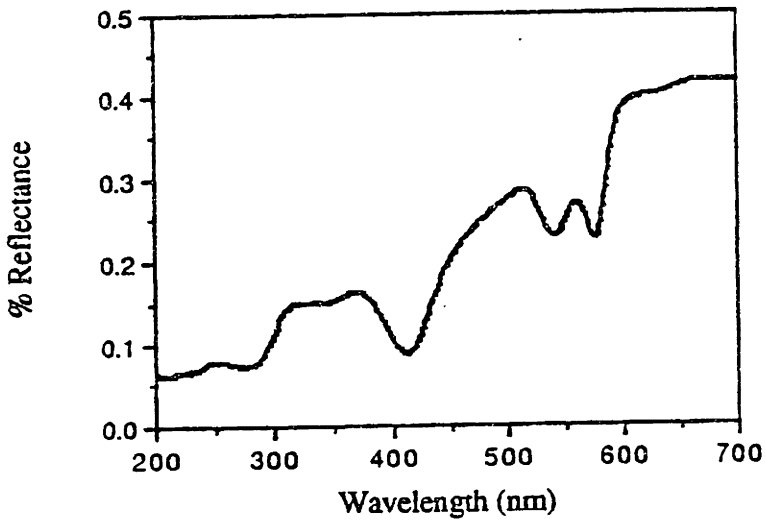

Figure 14: Typical total reflectance spectrum of a normal human aorta. Valleys in this spectrum indicate peaks in attenuation, and are located at 420, 540 and 580 nm. These are consistent with the attenuation of oxy-hemoglobin.

3:4.3.1.2. General - EEMs

This simple interpretation of the morphologic basis of the fluorescence EEMs of aorta at 470 nm excitation provides a basis for interpreting the entire EEM in morphologic terms. At 470 nm excitation, several layers of normal and atherosclerotic aorta contain only a single chromomorph: for example, media contains only elastin fibers, while fibrous cap contains primarily collagen fibers, and necrotic core contains mainly ceroid. Thus, recording EEMs of 50 μm sections of these tissue layers provides a method of characterizing the UV and visible spectroscopic properties of these chromomorphs. In the near UV and visible regions of the spectrum, sections of this thickness are optically

thin, so that the effects of attenuation will be minimal [33]. EEMs of these samples are shown in Figure 15. In interpreting this data, it must be kept in mind that at excitation wavelengths other than 470 nm, these layers of tissue may contain more than a single chromomorph.

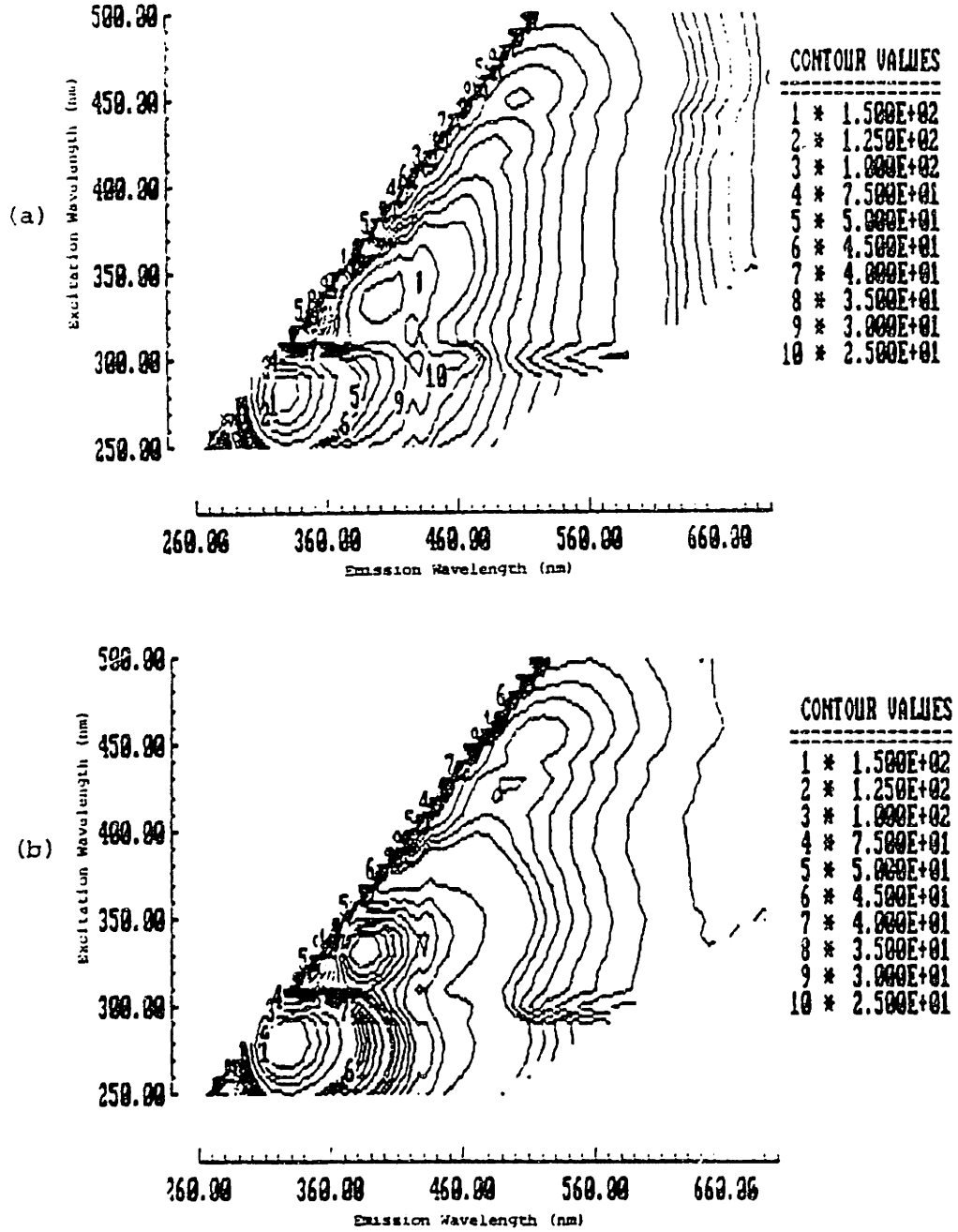

Figure 15: Fluorescence EEMs of 50 μm thick unstained frozen section of (a) media, (b) fibrous cap, and (c) necrotic core. In (a) and (b), four sets of linearly spaced contours are shown, five from 150 - 50 units, six from 45 - 20 units, nine from 18 to 2 units, and seven from 1.75 - 0.25 units. In (c), similarly spaced contours are shown from only from 10 - 0.25 units. All samples were from human cadaver aorta.

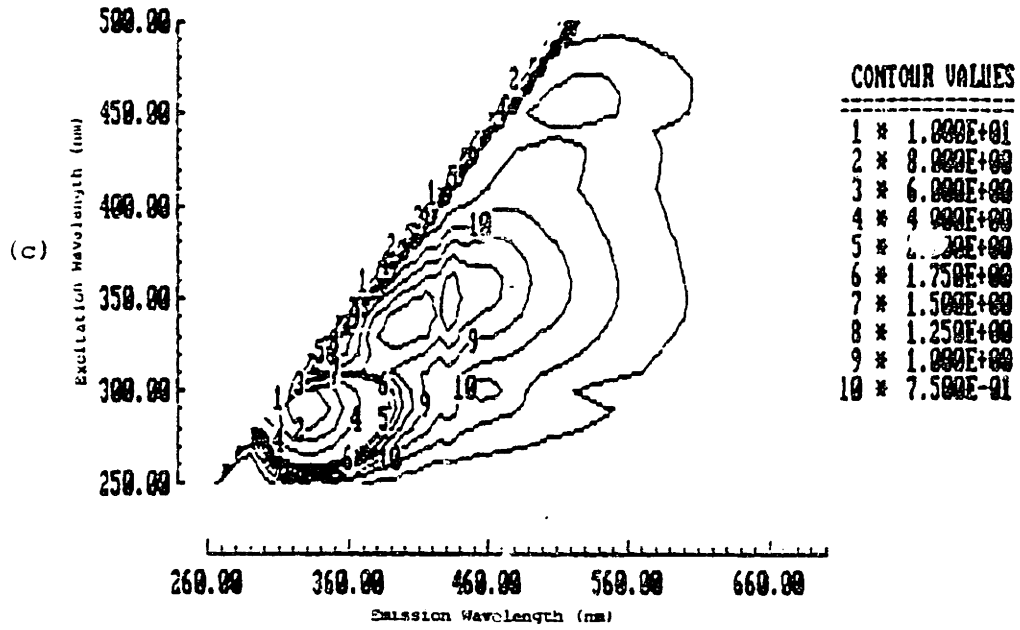

Figure 15 (cont.).

The fluorescence EEM of media is shown in Fig. 15(a), and is characterized by excitation-emission maxima at (280, 330 nm), (330, 380 nm), (350, 440 nm), (420, 480 nm), and (460, 520 nm). That of fibrous cap, in Fig. 15(b), shows maxima at (280, 330 nm), (330, 380 nm), (350, 440 nm), and (450, 520 nm). That of necrotic core has maxima at (280, 330 nm), (350, 400 nm), (350, 460 nm), (420, 480 nm), and (450, 520 nm) and (450, 560 nm). The fluorescence intensities of these maxima are characterized in Table 4.

At 470 nm excitation, again, the EEM of media is due to the fluorescence of elastin fibers, that of fibrous cap is due to contributions from collagen fibers and that of necrotic core due to contributions from ceroid. At 470 nm excitation, these results are consistent with our previous observations through the fluorescence microscope at 476 nm excitation [35]. The collagen and elastin contributions are similar, peaking near 520 nm, except the fluorescence of collagen fibers is relatively less intense than that of elastin fibers. Although these structural proteins have similar fluorescence lineshapes near 450 nm excitation, at other excitation wavelengths their fluorescence properties differ. The 470 nm excited fluorescence of ceroid (necrotic core) has peaks near 520 and 560 nm.

Table 4: Fluorescence excitation-emission maxima in optically thin sections of media, fibrous cap and necrotic core form normal and atherosclerotic human cadaver aorta.

Excitation Emission Maximum	Fluorescence Intensity		
	Media	Fibrous Cap	Necrotic Core
(280, 330 nm)	150	150	8
(330, 380 nm)	30	40	-
(340, 440 nm)	30	14	1.5
(350, 460 nm)	-	-	1.25
(420, 480 nm)	14	1.75	.5
(450, 520 nm)	12	1.5	.5
(450, 560 nm)	-	-	.25

As stated earlier, at other excitation wavelengths, the fluorescence EEMs of these layers may contain contributions from more than one chromomorph. In fact, each contains a strongly fluorescent peak at (280, 330 nm). This is likely due to fluorescence from the aromatic amino acid, tryptophan, which a has a fluorescence maximum near this region [40]. Neither collagen nor elastin contains tryptophan [41], and thus in this region of the spectrum, the emission is due to proteins other than collagen or elastin.

A comparison of the fluorescence EEMs of media and fibrous cap to that of pure powdered bovine collagen and elastin (Fig. 16) indicates that the chromophores associated with these proteins fluoresce over the entire visible region of the spectrum. In collagen, peaks are present at (280, 310 nm), (260, 380 nm), (330, 380 nm) and (450, 520 nm); the most intense peak is at (330, 380 nm). In elastin, peaks are present at (340, 440 nm), (420, 480 nm) and (450, 520 nm). Each of these peaks has relatively similar fluorescence intensity. These peaks are similar in location and relative intensity to those observed in the near UV and visible regions of the fluorescence EEMs of media and fibrous cap. This similarity indicates, that over most of the UV and visible regions of the spectrum, the fluorescence EEMs of media and fibrous cap contain contributions from a single chromomorph, elastin fibers and collagen fibers, respectively.

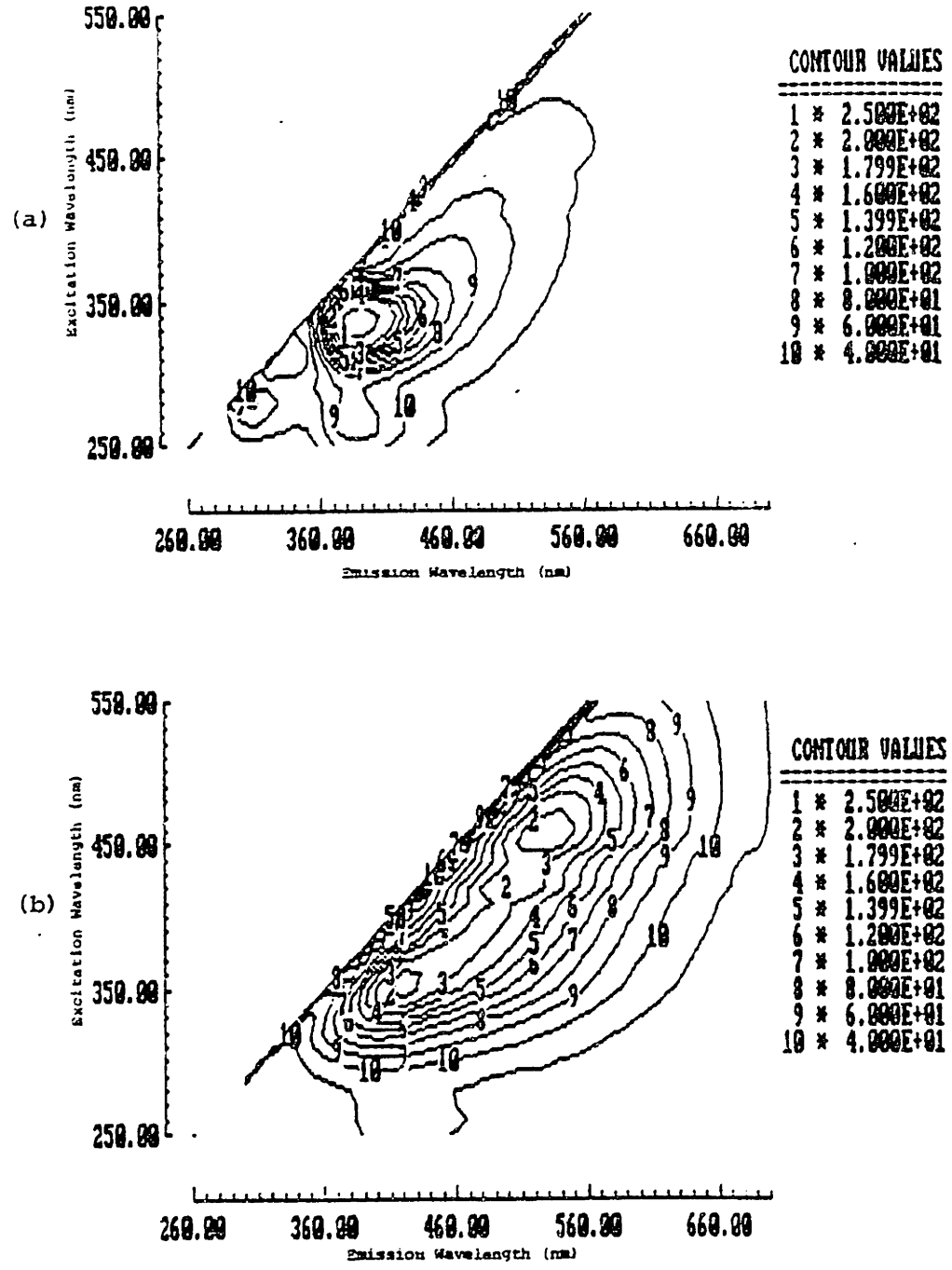

Figure 16: Contour map representations of the fluorescence EEMs of powdered bovine (a) collagen and (b) elastin.

These results suggest interpretations for the morphologic basis of the peaks characterized in the fluorescence EEMs of aorta in Fig. 3 and Table 1. These interpretations are based on a comparison of Tables 1 and 4. Note that the positions of the excitation-emission maxima in Table 4 do not exactly match those in Table 1. This is because the attenuation of oxy-hemoglobin at 420, 540 and 580 nm can act to significantly alter the observed excitation-emission maxima of the individual tissue chromophores. The largest peaks in the EEMs of normal and atherosclerotic aorta at (290, 330 nm) is due to the emission of tryptophan. The peak at (330, 380 nm) is due to collagen fluorescence. The peaks near (360, 460 nm) and (370, 590 nm) are likely due to a combination of emission from elastin fibers and ceroid. The emission peak at (470, 530 nm) is due to a combination of emission from collagen and elastin fibers, while those peaks at (470, 550 nm) and (470, 590 nm) are due to the emission of these structural proteins and ceroid.

This interpretation is consistent with the pathobiology of atherosclerosis: the peak at (330, 380 nm) due to the emission of collagen fibers is more intense in non-calcified plaques, where significant deposition of intimal collagen occurs [1, 17]. The contribution of collagen at this location is somewhat decreased in calcified plaques, consistent with the observation that elastin fibers calcify more readily than collagen fibers [18].

The peaks at (350, 460 nm) and (370, 590 nm) are less intense in the EEMs of non-calcified plaque. These peaks are due to the contributions of elastin, which we expect to decrease in atherosclerotic plaques as the intimal thickness increases and the contributions of the elastin rich media to the overall fluorescence spectrum decrease, and ceroid which we expect to increase as the severity of the lesion increases [1, 14]. The emission of elastin fibers is likely to dominate, as the relative intensity of media emission (elastin fibers) is much greater than necrotic core emission (ceroid) in this region of the spectrum. This is in fact what is observed - the fluorescence intensity of non-calcified plaque is less than normal tissue in this region. On the other hand, the fluorescence intensity of the severely calcified plaques is greater than that of normal tissues, likely reflecting two effects: significant ceroid deposition and extensive calcification of degenerating and regenerating elastin fibers [1, 18].

The peak at (470, 530 nm) is due to the emission of both collagen fibers and elastin fibers. As the emission of media (elastin fibers) is much greater than fibrous cap (collagen fibers) in this region, the intensity of this peak can be though of simply as the

ratio of fluorescent elastin fibers to collagen fibers. This peak is higher in normal tissue than in non-calcified plaque, consistent with the composition of these tissues - the intima of normal tissue is quite thin and much of the spectrum is due to contributions of the elastic media. The fibrous cap of non-calcified plaques is much thicker, and composed primarily of collagen, thus the intensity of this peak is reduced in these tissues. Calcified plaque on the other hand, contains a much greater component of calcified elastin in the intima [18], thus this peak is greater in intensity than that of non-calcified tissues.

Finally, the peak at (460, 550 nm) is due to the emission of structural proteins and ceroid. These peaks are more intense relative to the (470, 530 nm) peak in non-calcified and especially calcified plaques, reflecting the increased ceroid content of these tissues. The peak at (470, 590 nm) is also due to the emission of these same chromophores, but its relative intensity is strongly influenced by hemoglobin attenuation, and it is thus difficult to interpret within this framework. The morphologic basis of the lower intensity of tryptophan fluorescence in calcified plaques is unknown at this time.

3:4.3.2. Coronary

3:4.3.2.1. 476 nm Excitation

3:4.3.2.1.1. Fluorescence Photo-Microscopy

Similar studies were conducted of coronary artery autofluorescence using the fluorescence microscope described earlier with 476 nm argon-ion laser excitation [35]. The autofluorescence of normal coronary arteries differed dramatically from that of normal aorta in two ways. A bright, thick line of fluorescence was observed in the intima of normal coronary arteries, at the border of the intima and media, which corresponded to the internal elastic lamina on Movat stains. Similarly, the external elastic lamina was autofluorescent, although less so than the internal elastic lamina. Secondly, the media of coronary arteries exhibited much less intense fluorescence than that of the aorta. The weak fluorescence present corresponded to rare elastic fibers within the media of these muscular arteries on Movat stains. Again, this structural protein fluorescence appeared green in color with the 515 nm barrier filter, and decreased in intensity with increasing barrier filter wavelength.

The autofluorescence of coronary artery intimal fibroplasia and atherosclerosis was similar to that observed in aorta. The fluorescence of the internal elastic lamina,

when present, was often discontinuous in the region of the plaque. This corresponded to disruption of the internal elastic lamina on Movat stains.

3:4.3.2.1.2. EEMs

Again, these observations are consistent with our observations at 470 nm excitation in the fluorescence EEMs of coronary artery (Fig. 4) and the data obtained with the spectral catheter at 476 nm excitation presented in Fig. 12. These results suggest that the 520 nm peak is due to emission of collagen and elastin fibers and that the 550 hm peak is due to ceroid. Again, the shallow valleys at 540 and 580 nm are due to oxy-hemoglobin attenuation. The relative increase in the size of the 550 nm peak in non-calcified and calcified atherosclerotic plaques is due to the increased ceroid content of these tissues. In normal coronary artery, the 520 nm peak is due primarily to the fluorescence of elastin in the IEL. In non-calcified plaques, the 520 nm peak is primarily due to collagen fibers in the fibrous cap. As the fluorescence intensity of collagen fibers is less than that of elastin fibers this peak is less intense in the non-calcified plaque. In calcified plaque, this peak is due both to the emission of collagen fibers in the fibrous cap and calcified elastin fibers [17, 18]. The absolute intensity of this peak depends on the extent of calcification - in the EEMs of minimally calcified tissues, this peak is relatively less intense than in that of more extensively calcified plaque in Fig. 12.

3:4.3.2.2. General - EEMs

These fluorescence EEMs of aorta chromomorphs in Fig. 15 can also be used to interpret the morphologic identity of the peaks given in the coronary artery EEMs. The peak at (330, 380 nm) is due to the emission of collagen fibers, and is slightly more intense in the fluorescence EEMs of non-calcified plaque. This is consistent with the intimal composition of these tissues, which are particularly rich in collagen [1, 17]. The peak at (340, 440 nm) is due to the emission of both elastin fibers and ceroid. Again, the contribution of elastin fibers likely dominates as the fluorescence intensity in the EEM of media (elastin fibers) is much greater than that of necrotic core (ceroid) in this region of the spectrum. This peak is less intense in the fluorescence EEM of non-calcified plaques than in non-atherosclerotic tissues. Although these non-calcified plaques contain increased ceroid, the relative contribution of the IEL is decreased as it degenerates and becomes further away from the lumen due to intimal thickening. The intensity of this peak is slightly increased in the minimally calcified plaques in coronary artery primarily due to ceroid and the calcification of degenerating and regenerating elastin fibers [18].

Using the identifications presented above, the most general form of eq.(1) (See Sec. 3:4.3) including all of these moieties is:

$$(2)\ S(476,\lambda_m) = kP(476)\left[\frac{\mu_{aSP}(476)\frac{\phi_{SP}(476,\lambda_m)}{2} + \mu_{aCe}(476)\frac{\phi_{Ce}(476,\lambda_m)}{2} + \mu_{aHb}(476)\frac{\phi_{Hb}(476,\lambda_m)}{2}}{(\mu_{tSP}(476)+\mu_{tSP}(\lambda_m)) + (\mu_{tCe}(476)+\mu_{tCe}(\lambda_m)) + (\mu_{tHb}(476)+\mu_{tHb}(\lambda_m))}\right]$$

A knowledge of the chemical properties of these chromophores and the physical structure of arterial tissue allows us to simplify Eq. (2). First, the quantum efficiency of hemoglobin for fluorescence is negligible. Second, fluorescence microscopy shows that ceroid is present as small discrete deposits near the central necrotic region of plaques. The implications of this can be most easily seen if we write eq. (2) as:

$$(3)\ S(476,\lambda_m) = kP(476)\left\{\left[\frac{\mu_{aSP}(476)\frac{\phi_{SP}(476,\lambda_m)}{2}}{(\mu_{tSP}(476)+\mu_{tSP}(\lambda_m)) + (\mu_{tCe}(476)+\mu_{tCe}(\lambda_m)) + (\mu_{tHb}(476)+\mu_{tHb}(\lambda_m))}\right] + \left[\frac{\mu_{aCe}(476)\frac{\phi_{Ce}(476,\lambda_m)}{2}}{(\mu_{tSP}(476)+\mu_{tSP}(\lambda_m)) + (\mu_{tCe}(476)+\mu_{tCe}(\lambda_m)) + (\mu_{tHb}(476)+\mu_{tHb}(\lambda_m))}\right]\right\}$$

The localization of ceroid implies that the attenuation of structural protein fluorescence by ceroid is small; therefore, the ceroid attenuation terms can be neglected in the denominator of the first term in eq. (3). Although the effects of ceroid attenuation can be neglected for structural protein fluorescence, they are important for ceroid fluorescence. We include these effects in an approximate way. The ceroid attenuation terms in the denominator of the second term in eq. (3) are neglected, but the ceroid fluorescence term in the numerator is replaced with an effective ceroid fluorescence lineshape. This lineshape is approximated as the intrinsic fluorescence lineshape divided by a normalized ceroid attenuation lineshape. Eq. (3) can be rewritten to reflect these considerations as:

The morphologic basis of the peaks at 470 nm excitation have been interpreted above. The morphologic basis of the decrease in tryptophan fluorescence in atherosclerotic plaque is not known at this time.

3:4.4. Model of Tissue Fluorescence

The requirements for a model of tissue fluorescence were discussed in detail in Chapter Two. In Chapter Two, assuming exponential attenuation of light, expressions wer developed for tissue fluorescence for tissue comprised of one and two layers containing homogeneous distributions of fluorophores and attenuators. Here, we will concentrate on the application of these expressions to arterial tissue.

As noted earlier, applying these equations to a specific tissue requires a knowledge of the identity of tissue constituents which fluoresce and/or attenuate light, as well as determination of their spectroscopic properties. The previous section presented results of experiments designed to identify tissue constituents which fluoresce. In summary, 476 nm laser induced fluorescence microscopy of normal aorta and coronary artery and the types of atherosclerotic plaques described previously has shown that the important fluorophores are the structural proteins, collagen and elastin, and ceroid. In normal tissue, fluorophores in or associated with the structural proteins (SP), collagen and elastin, are important. Fluorescence contributions from collagen and elastin are not treated separately below, as these compounds have identical fluorescence lineshapes with 476 nm excitation. In atherosclerotic tissue, ceroid (Ce) contributes to the fluorescence in addition to the structural proteins. Ceroid is a morphologic term used to denote substances which (i) stain like a lipid, (ii) are not dissolved by usual lipid solvents, and (iii) fluoresce in the visible when excited by UV light. Ceroid is a complex of protein associated with oxidized lipids [42] and its exact identity is unknown. The attenuation effects of these moieties must also be included within the model of tissue fluorescence. In addition, absorption spectroscopy indicates that hemoglobin (Hb) is an important attenuator [43, 34] in normal and atherosclerotic tissues.

3:4.4.1. Exponential Attenuation, One-Layer Model

With these identifications, the general expressions for tissue fluorescence can be written expressly for application to arterial tissues. As the moieties which contribute to tissue fluorescence are the same in both muscular and elastic arteries, one expression can be used to describe the fluorescence spectra of both types of artery. We proceed here to develop the one layer model of tissue fluorescence for arterial tissue.

$$(4)\ S(476,\lambda_m) = kP(476)\left[\frac{\left(\mu_{aSP}(476)\frac{\phi_{SP}(476,\lambda_m)}{2} + \left[\frac{\mu_{aCe}(476)}{\left(\frac{(\mu_{tCe}(476)+\mu_{tCe}(\lambda_m))}{\mu_{tCe}(476)+\mu_{tCeMax}}\right)}\right]\frac{\phi_{Ce}(476,\lambda_m)}{2}\right)}{\{(\mu_{tSP}(476)+\mu_{tSP}(\lambda_m))+(\mu_{tCe}(476)+\mu_{tCe}(\lambda_m))+(\mu_{tHb}(476)+\mu_{tHb}(\lambda_m))\}}\right]$$

In eq. (4) μ_{tCeMax} is the maximum ceroid attenuation coefficient over the emission wavelength range. As discussed above, the modulation of ceroid fluorescence by ceroid attenuation is included by dividing the ceroid fluorescence by a normalized ceroid attenuation lineshape. This represents a relaxation of the assumption that ceroid is distributed homogeneously, in order to better model the physical situation. This approximation allows the ceroid fluorescence lineshape to be extracted from bulk samples (samples thick with respect to the penetration depth of the excitation light), eliminating difficulties which would be associated with obtaining an unattenuated ceroid fluorescence lineshape.

Eq. (4) can be simplified further if the fluorescence and attenuation lineshapes are normalized to yield:

$$(5)\ S(476,\lambda_m) = kP(476)\left[\frac{\{\beta_{SP}(476)F_{SP}(476,\lambda_m)+\beta_{Ce}(476)F_{Ce}(476,\lambda_m)\}}{\{x_{SP}(476)A_{SP}(476,\lambda_m)+x_{Hb}(476)A_{Hb}(476,\lambda_m)\}}\right]$$

where

$$(6)\quad \beta(476) = \frac{\mu_a(476)\phi_{Max}}{2}$$

$$F(476,\lambda_m) = \frac{\phi(476,\lambda_m)}{\phi_{Max}}$$

$$x(476) = \mu_t(476) + \mu_{tMax}$$

$$A(476,\lambda_m) = \frac{\mu_t(476)+\mu_t(\lambda_m)}{\mu_t(476)+\mu_{tMax}}$$

$$\beta' = \frac{\mu_a(476)\phi_{Max}}{2}$$

$$F' = \left(\frac{\phi(476,\lambda_m)}{\left[\frac{\mu_t(476)+\mu_t(\lambda_m)}{\mu_t(476)+\mu_{tMax}}\right]}\right)\left[\frac{1}{\phi_{Max}}\right] = \frac{\phi(476,\lambda_m)}{\phi_{Max}}$$

In Eq. (6), ϕ_{Max} and μ_{rMax} are the maximum quantum yield and attenuation coefficient over the emission wavelength range, respectively. F represents a normalized intrinsic fluorescence lineshape and A represents a normalized round trip attenuation lineshape. As μ is proportional to the chromophore concentration, both β and x are proportional to the chromophore concentration. In addition, β is proportional to the fluorescence quantum yield at the peak emission wavelength. Thus, changes in β can reflect either changes in the chromophore concentration or quantum yield.

In our treatment of ceroid, ϕ is replaced by ϕ'; ϕ' represents an effective quantum yield for the net ceroid fluorescence which has been modulated by ceroid absorption. Thus, β'_{Ce} is proportional to the ceroid concentration and its maximum effective quantum yield. F_{Ce} is the normalized fluorescence lineshape from a sample thic' compared to the penetration depth of 476 nm radiation.

Eq. (5) is the key equation to understanding the fluorescence from artery wall. It shows that the fluorescence from both the structural proteins and ceroid are modulated by attenuation of the structural proteins and hemoglobin. Ceroid fluorescence is also modulated by ceroid attenuation. In the following section we will extract the lineshapes needed to utilize Eq. (5) with fluorescence spectra of optically thick tissues.

3:4.4.1.1. Aorta

In order to fix the lineshapes in Eq. (5), several simple one-layer arterial tissue systems were studied, as opposed to studying the optical properties of pure chromophores. The advantage of this approach is that it intrinsically includes the effects of scattering in the tissue. In addition, this method allows us to investigate endogenous chromophores in their natural environment, avoiding possible effects due to extraction. Precise identification of the chromophores on a molecular level is not required, and therefore our identification of the chromophores as structural proteins and ceroid should not be considered rigorous at the molecular level. These one layer tissue systems to be described were derived from samples of human cadaver aorta. Fluorescence spectra of these tissues at 476 nm excitation were recorded using the spectral catheter system described in Chapter Two. As the spectra of elastic and muscular arteries contain contributions from the same constituents at 476 nm excitation, these results should be applicable to both types of arteries. Aorta was selected rather than coronary artery

because the individual layers of tissue could be separated more easily using techniques of blunt dissection.

The first system utilized a single optically thick section of media, blunt dissected from a sample of normal aorta. A fluorescence spectrum of the bulk tissue was recorded, yielding $S(476, \lambda_m)$, and is shown in Fig. 17. The 476 nm excited fluorescence lineshape of media is found to be identical to that of powdered bovine collagen and elastin [43]. In addition, the fluorescence spectrum of this section of media did not exhibit valleys at 540 and 580 nm, which have been attributed to the presence of hemoglobin. Thus, it can be assumed that the important chromophores in this system are limited to structural proteins. Eq. (5) simplifies to

$$(7)\ S(476,\lambda_m) = kP(476)\frac{\beta_{SP}(476)F_{SP}(476,\lambda_m)}{x_{SP}(476)A_{SP}(476,\lambda_m)}$$

A fluorescence spectrum was then obtained from a 10 μm section of normal media directly providing an unattenuated structural protein emission, as

$$(8)\ S_{Thin}(476,\lambda_m) = kP(476)\beta_{SP}(476)F_{SP}(476,\lambda_m)dz$$

where dz is the sample thickness. $\beta_{SP}(476)F_{SP}(476)dz$ is also shown in Fig. 17. Thus, $x_{SP}(476)A_{SP}(476, \lambda_m)$ can be extracted, and is shown in Fig. 18.

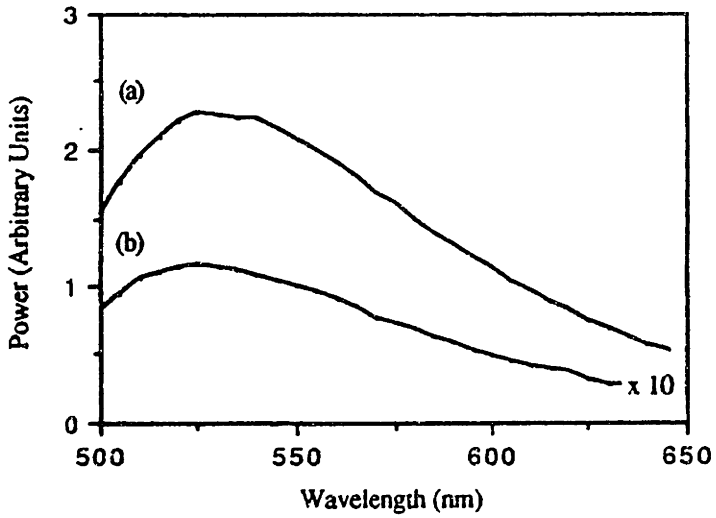

Figure 17: (A) Fluorescence spectrum of optically thick media excited with 476 nm radiation. (B) Fluorescence spectrum of 10 μm thick section of media. For scaling purposes, the spectrum of the thin section is shown multiplied by a factor of 10.

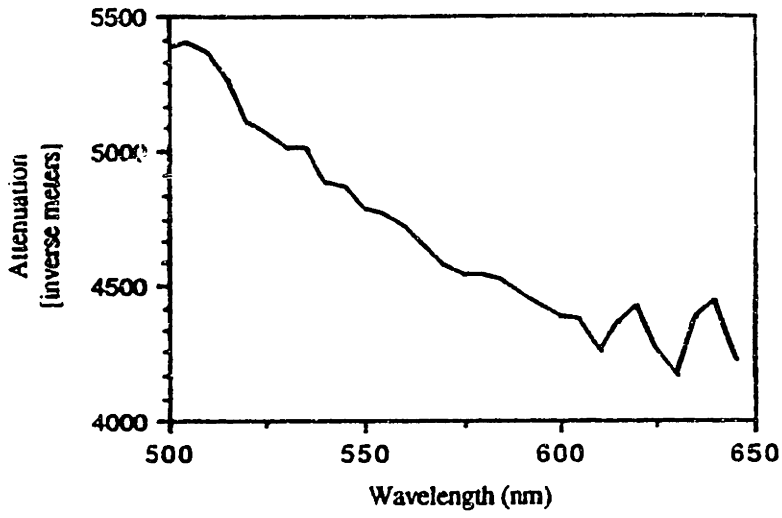

Figure 18: Attenuation spectrum of structural protein.

The next step was to obtain the hemoglobin attenuation lineshape, $x_{Hb}(476)A_{Hb}(476,\lambda_m)$. It has been shown that the hemoglobin content of tissue can be increased by exposing the tissue to hemolysed blood [44, 45]. We exploited this fact to extract the hemoglobin attenuation lineshape. The same thick section of media used above was exposed to hemolysed blood and a fluorescence spectrum of the bulk tissue was recorded. As hemoglobin is now an important chromophore Eq.(4) takes the form

$$(9)\ S(476,\lambda_m) = \frac{kP(476)\beta_{SP}(476)F_{SP}(476,\lambda_m)}{\{x_{SP}(476)A_{SP}(476,\lambda_m) + x_{Hb}(476)A_{Hb}(476,\lambda_m)\}}$$

Since F_{SP} and A_{SP} are known, A_{Hb} can be extracted directly. Several A_{Hb} curves were obtained for different concentrations (x_{Hb}) of hemoglobin corresponding to those typically observed in tissue *in vitro*, as judged by the depth of the valleys in the fluorescence spectrum at 540 and 580 nm. These curves were averaged, yielding the curve shown in Fig. 19. Up to a constant background, the shape of this attenuation curve is nearly identical to that of oxy-hemoglobin absorption [39].

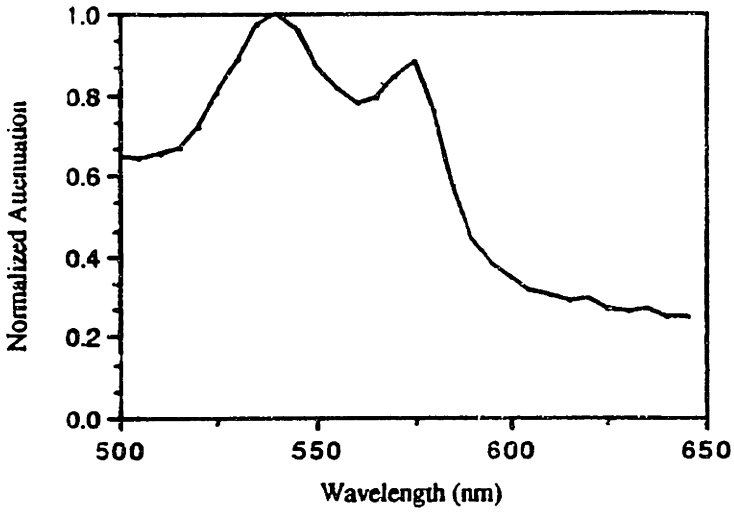

Figure 19: Attenuation spectrum of oxy-hemoglobin.

The only remaining lineshape in Eq. (4) is F_{Ce}. F_{Ce} was measured directly from bulk necrotic core which was blunt dissected from specimens of fatty plaque. The localization of ceroid in the necrotic core permits this approach. The average lineshape from several samples is shown in Fig. 20.

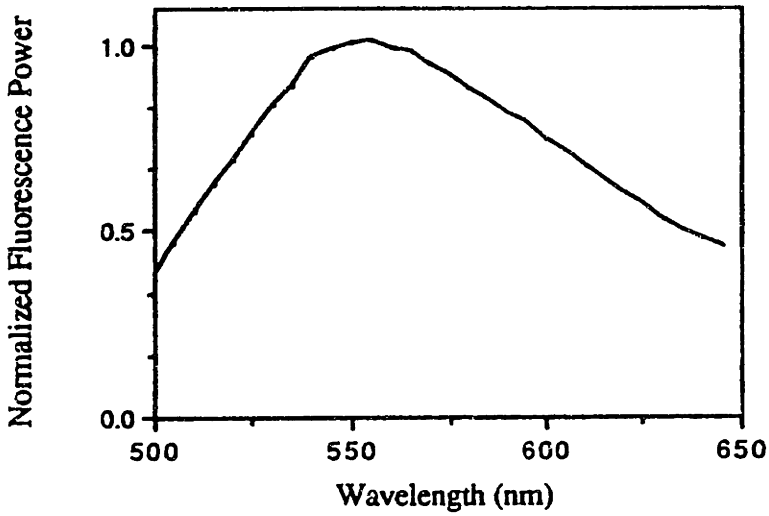

Figure 20: Normalized fluorescence spectrum of bulk necrotic core.

Having determined the relevant lineshapes in Eq. (4), F_{SP}, F_{Ce}, A_{SP} and A_{Hb}, the experimental LIF spectra from bulk tissue can now be modeled. The parameters in the model are β_{SP}, β'_{Ce} and x_{Hb}, and are restricted to values greater than zero. The value obtained for x_{SP} of media is held as constant. Maintaining a constant value of x_{SP} is equivalent to assuming that the structural protein attenuation is approximately constant in different tissues, and does not appear to affect the goodness-of-fit. It is not inconsistent to allow β_{SP} to vary while holding x_{SP} constant, as β_{SP} depends on the quantum yields, absorption coefficients and concentrations of both collagen and elastin, while x_{SP} depends on the attenuation coefficients and concentrations.

With these restrictions, data from the 148 samples of aorta were then fit to eq. (4). In fitting the data, the parameters were varied in order to minimize chi-square, the square of the difference between the experimental and calculated fluorescence signal divided by the standard deviation. Typical fits to data are shown in Fig. 21 for several different tissue types. The goodness of fit of the model to the data was judged by calculating the probability that a value of chi-square found in the calculation should occur by chance rather than due to an inappropriate model. This probability was calculated using an incomplete gamma function. In general, a probability less than 0.1 for many samples would indicate that the model was a poor representation of the system. Typically, values of this probability for our data were found to be greater than 0.9. This shows that the model provides an adequate representation of arterial LIF spectra.

Scatter plots for each of the parameters, β_{SP}, β'_{Ce} and x_{Hb}, for all samples are shown in Figs. 22, 23, and 24, respectively. Table 5 lists averages and standard deviations for β_{SP}, β'_{Ce} and x_{Hb} for each of the classifications as well as some additional combinations of these classifications. A two-sided students t test was used to compare the parameters β_{SP} and β'_{Ce} for several different tissue classifications [46]. β_{SP} of (0,1) was significantly higher than that for pathologic tissues, (2,3), (4,5), with $p < .01$. β'_{Ce} for calcified tissues, (4,5), was significantly higher than that of other tissues: (0,1), with $p < .01$, (2,3), with $p < .10$. Interestingly, the values of β_{SP} for (0) and (1) were not found to be significantly different, while the values of β'_{Ce} were ($p < .10$).

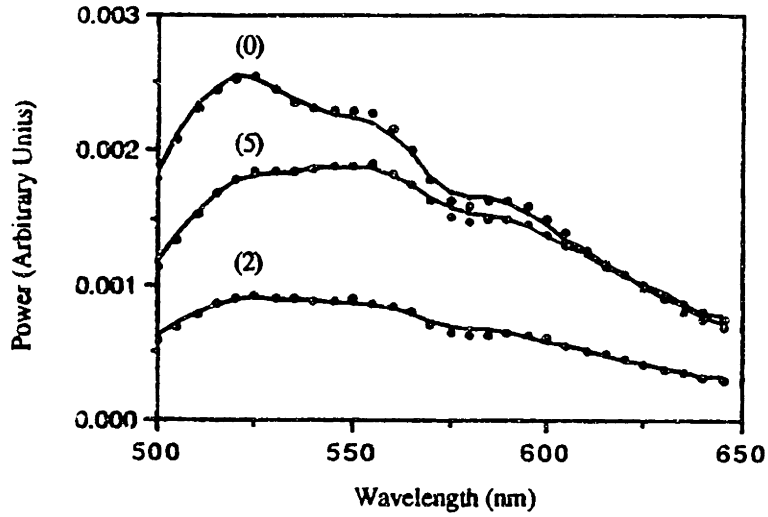

Figure 21: Comparison of typical fluorescence spectra (•) to model calculation (-) for (0) normal tissue, ßSP = 17.01, ß'Ce = 1.04, xHb = 2089; (2) atherosclerotic plaque, ßSP = 4.66, ß'Ce = 1.04, xHb = 1283; and (5) calcified atheromatous plaque, ßSP = 7.8, ß'Ce = 4.28, xHb = 1312.

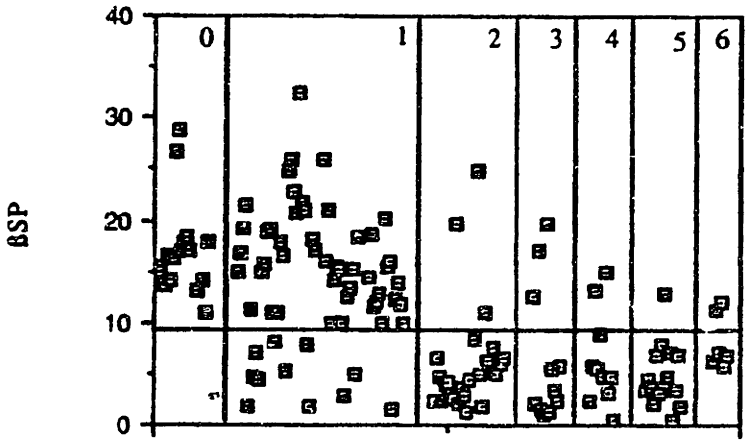

Figure 22: Scatter plot of ßSP versus sample type. The horizontal division at ßSP = 9.0 represents a diagnostic algorithm which maximizes the correct classification of normal and pathologic tissues.

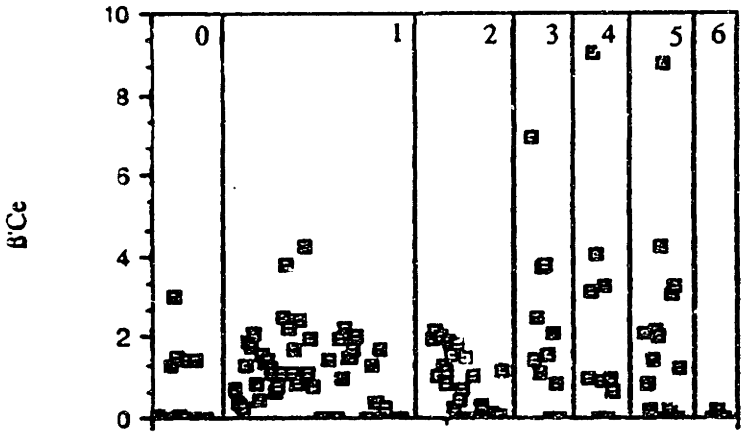

Figure 23: Scatter plot of $ß'_{Ce}$ versus sample type.

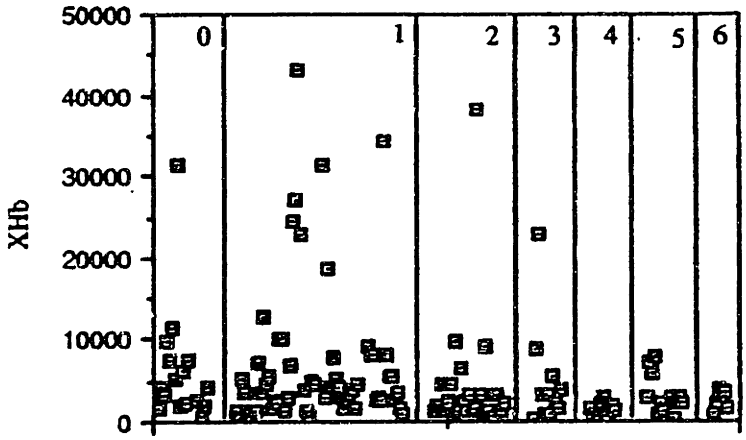

Figure 24: Scatter plot of x_{Hb} versus sample type.

Table 5: Average values of model parameters ± standard deviations for 148 samples of human aorta.

Sample Classification	Average ßSP ± Standard Deviation	Average ß'Ce ± Standard Deviation	Average xHb ± Standard Deviation
(0)	16.95 ± 4.66	0.55 ± 0.91	6370 ± 7362
(1)	14.28 ± 6.53	1.04 ± 0.96	7316 ± 9021
(2)	5.90 ± 5.71	0.88 ± 0.78	2555 ± 1075
(3)	6.41 ± 6.14	1.95 ± 1.95	4261 ± 7480
(4)	6.35 ± 4.35	2.30 ± 2.77	4871 ± 6412
(5)	4.94 ± 3.11	2.11 ± 2.31	1395 ± 980
(6)	8.03 ± 2.50	0.03 ± 0.08	2781 ± 2515
(0,1)	14.86 ± 6.25	0.94 ± 0.96	6934 ± 8610
(2,3)	6.13 ± 5.79	1.26 ± 1.40	3888± 6637
(4,5)	5.53 ± 3.77	2.19 ± 2.46	3216 ± 4915

The average values and standard deviations of these parameters are illustrated graphically versus tissue type for disease free tissue (0,1), non-calcified plaques (2,3) and calcified plaques (4,5) in Fig. 25.

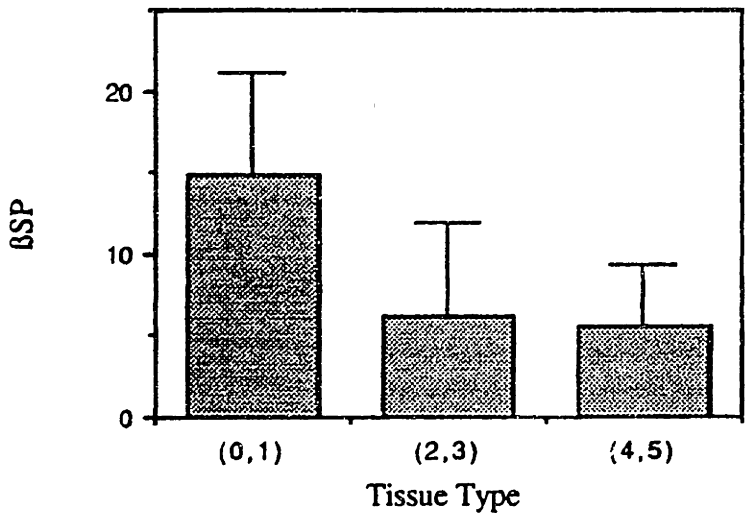

Figure 25: Graphical representation of the average values and standard deviations of (a) ßSP, (b) ß'Ce, and (c) xHb for 158 samples of human aorta. Averages are shown for (0,1) disease free tissue, (2,3) non-calcified plaques and (4,5) calcified plaques.

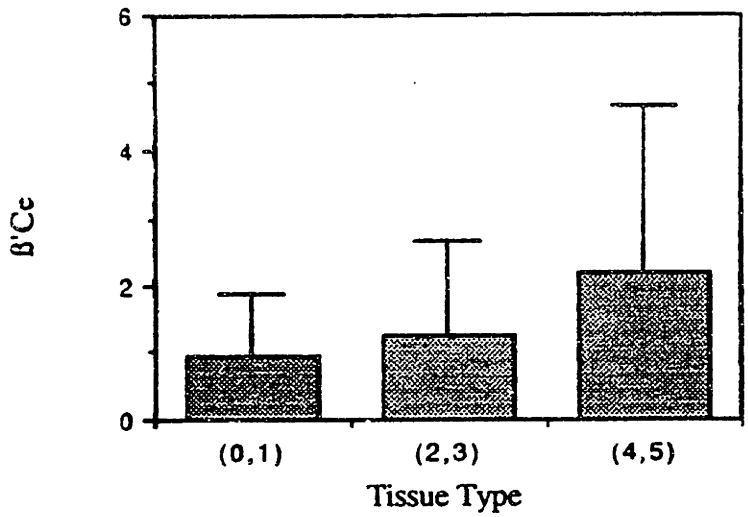

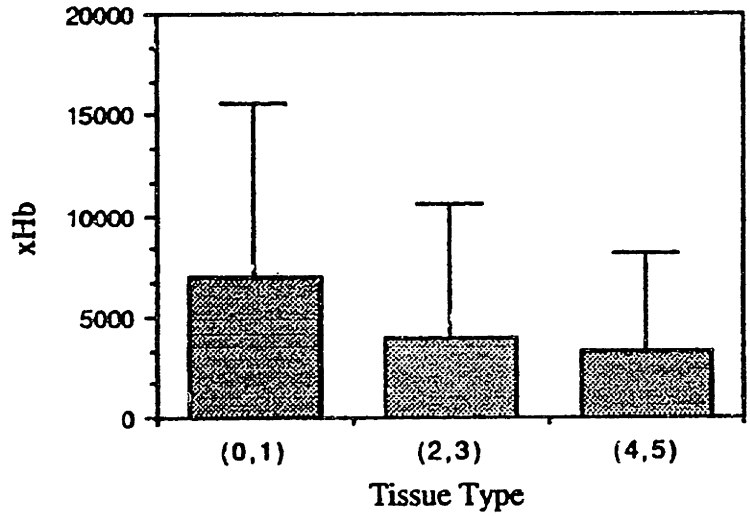

Figure 25 (cont.).

As shown in Eq. (5) the parameters of the model, β and x, are directly proportional to the absorption and attenuation coefficients, respectively, and thus provide a link to the chemical composition of the tissue. As these coefficients are linearly related to the chromophore concentration, β and x are proportional to the chromophore concentration. This linear relationship is only strictly valid for tissue systems in which the three assumptions in Chapter Two are reasonable. The assumption of homogeneous distribution of chromophores is not rigorously true for multi-layered tissues in which the intimal thickness is less than the 1/e penetration depth of 476 nm light in tissue. In applying a one layer model to a two layer system we calculate some average value of β

and x. These average values can vary, ranging from β and x of layer two to that of layer one as the intimal thickness increases.

When measuring absolute fluorescence intensities, the information obtained is a combination of intrinsic fluorescence and attenuation. For example, a low value of absolute intensity can be due to either reduced intrinsic fluorescence or to increased attenuation. To obtain chemical information, it is necessary to separate these processes. In our model, the changing attenuation is due to the presence or absence of hemoglobin, as represented by the parameter x_{Hb}. As shown in Fig. 24, on average x_{Hb} is higher for normal tissues. The distribution of values, however, overlaps widely with other tissue types. The usefulness of extracting x_{Hb} lies in our ability to separate the effects of fluorescence and attenuation. In addition, *in vivo* studies of arterial fluorescence have demonstrated that *in vitro* tissues may contain different concentrations of hemoglobin [44, 45]. Preliminary *in vivo* measurements indicate that hemoglobin is not an important attenuator in normal tissue but is important in calcified plaques. Thus, the model, in separating fluorescence and attenuation effects, provides a method of connecting *in vivo* and *in vitro* data.

A non-zero β'_{Ce} indicates the presence of ceroid. Ceroid has been correlated with the presence of extensive atherosclerosis [43]. Figure 23 and Table 5 show the data are consistent with this; the average value of β'_{Ce} is higher for pathologic specimens and appears to increase with the severity the disease. Calcified plaques were associated with a particularly high value of β'_{Ce}. This is consistent with observations made with a fluorescence microscope indicating ceroid deposits are often localized adjacent to calcified areas of tissue. It is interesting to note, that in fibrotic/sclerotic specimens (6), the amount of ceroid is negligible, reflecting the pathology of this tissue type. Detecting the presence of sub-surface ceroid fluorescence utilizing surface excitation is an important observation. Previous studies have utilized transverse sections which would be impractical *in vivo* [42]. The model provides a method of assessing ceroid content of tissues *in vivo*.

Interpretation of the parameter β_{SP} is complicated by the fact that β_{SP} contains contributions from both collagen and elastin. Preliminary results indicate that the fluorescence quantum efficiency of elastin fibers is higher than that of collagen fibers with 476 nm excitation, although the band shapes are identical. It is possible therefore, that a high value of β_{SP} indicates a high ratio of fluorescent elastin fiber concentration to collagen fiber concentration. Since the media consists mainly of elastin, and the intima

mainly collagen, the effective ratio of these concentrations, reflected by our one-layer value of β_{SP}, decreases as the intimal thickness increases. As shown in Table 5, β_{SP} is highest for normal tissue, is slightly lower for intimal fibroplasia, and is significantly lower for pathologic specimens.

Although the discussion above holds for comparing general classes of tissue, there are other important effects which also can influence β_{SP}. For example, in specimens displaying intimal fibroplasia there is no significant correlation of β_{SP} to intimal thickness. This is likely related to the varying chemical structure of the intima as intimal fibroplasia develops. Initially, the intima is mostly cellular, but becomes collagenous with increasing intimal thickness. These higher concentrations of collagen can also lead to higher β_{SP} values. In addition, it is known that the collagen structure can vary with tissue type and the presence or absence of atherosclerosis [47]. Different collagens do not necessarily have the same quantum yield, and this factor may further affect β_{SP}.

3:4.4.1.2. Coronary Artery

As the chromophores contained within muscular and elastic arteries appear to be the same at 476 nm excitation, in modeling the fluorescence spectra of coronary artery, we again utilized Eq. (4). The fluorescence and attenuation lineshapes determined for aorta were assumed to be applicable to coronary artery. Again, the parameters in the model are β_{SP}, β'_{Ce} and x_{Hb}, and are restricted to values greater than zero. The value obtained for x_{SP} was held held constant, as that of media for aorta. With these restrictions, the model, represented by Eq. (4), was used to fit data from 82 samples of human coronary artery. The same fitting procedures described previously for aorta were used.

Figure 26 shows that the quality of typical fits to data from coronary artery are equal to that obtained with aorta, validating our use of Eq. (4) and the fluorescence and attenuation lineshapes. Figures 27, 28 and 29 show scatter diagrams indicating the values of β_{SP}, β'_{Ce} and x_{Hb} for each of the 82 samples, as a function of histologically determined sample type. The average values and standard deviations of these parameters are given in Table 6 as a function of tissue type. Averages and standard deviations are also shown for non-atherosclerotic tissues (0,1), non-calcified plaques (2,3) and calcified plaques (4,5,7). The values of these parameters should be compared to those of aorta, given for aorta in Table 5. The average values and standard deviations of these

parameters are illustrated graphically versus tissue type for non-atherosclerotic tissue (0,1), non-calcified plaques (2,3) and calcified plaques (4,5,7) in Fig. 30.

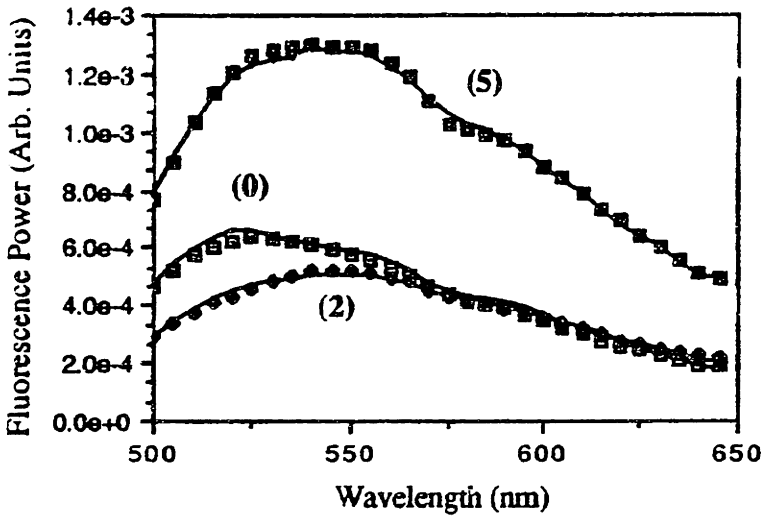

Figure 26: Comparison of the typical fluorescence spectra (•) to model calculation (-) for (0) normal tissue, β_{SP}=4.16, β'_{Ce}=0.03, x_{Hb}=1606; (2) atherosclerotic plaque, β_{SP}=1.65, β'_{Ce}=1.26, x_{Hb}=592; and (5) calcified atheromatous plaque, β_{SP}=4.99, β'_{Ce}=2.61, x_{Hb}=761.

Table 6: Average values of model parameters ± standard deviations for 82 samples of human coronary artery.

Sample Classification	Average ßSP ± Standard Deviation	Average ß'Ce ± Standard Deviation	Average xHb ± Standard Deviation
(0)	3.46 ± 1.37	0.33 ± 0.37	1437 ± 869
(1)	3.80 ± 1.68	0.21 ± 0.20	1456 ± 1427
(2)	2.14 ± 2.44	0.82 ± 0.27	511 ± 730
(3)	1.39	1.01	171
(5)	4.30 ± 3.61	2.76 ± 2.96	737 ± 704
(7)	6.96 ± 3.62		205 ± 202
(0,1)	3.70 ± 2.66	0.22 ± 0.23	1452 ± 1368
(2,3)	2.09 ± 2.37	0.84 ± 0.27	489 ± 711
(4,5,7)	5.12 ± 3.82	2.37 ± 2.60	574 ± 645

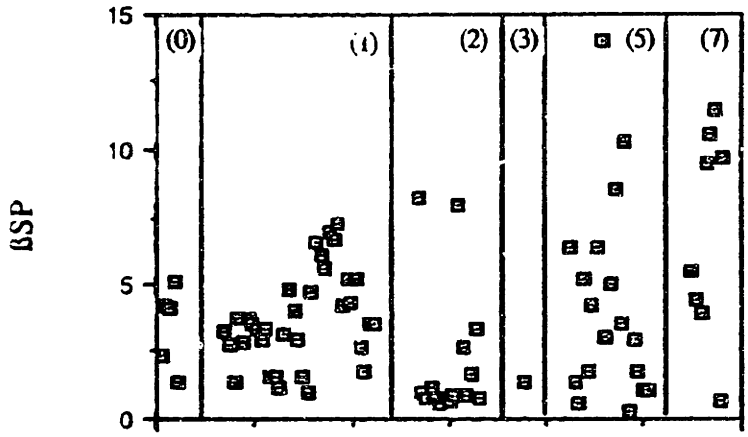

Figure 27: Scatter plot of ßSP versus sample type for 82 samples of human coronary artery.

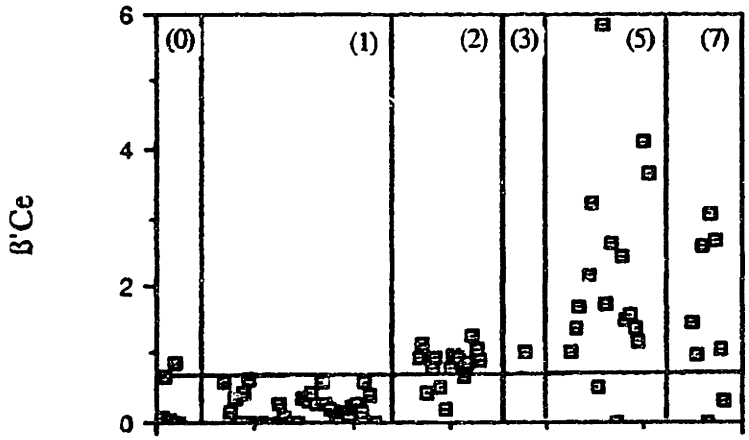

Figure 28: Scatter plot of ß'Ce versus sample type for 82 samples of human coronary artery.

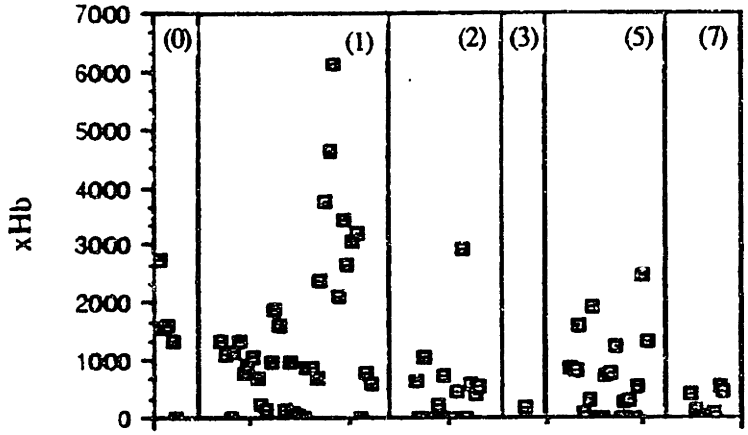

Figure 29: Scatter plot of x_{Hb} versus sample type for 82 samples of human coronary artery.

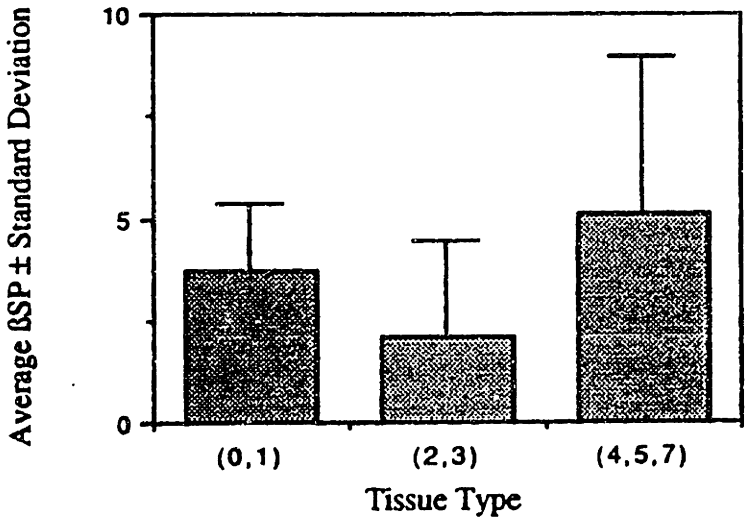

Figure 30: Graphical representation of the average values and standard deviations of (a) ßSP, (b) ß'Ce, and (c) x_{Hb} for 82 samples of human coronary artery. Averages are shown for (0,1) disease free tissue, (2,3) non-calcified plaques and (4,5,7) calcified plaques.

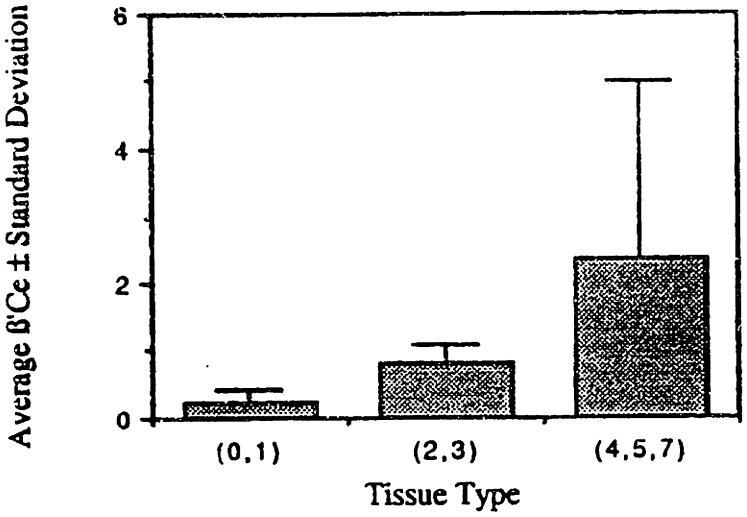

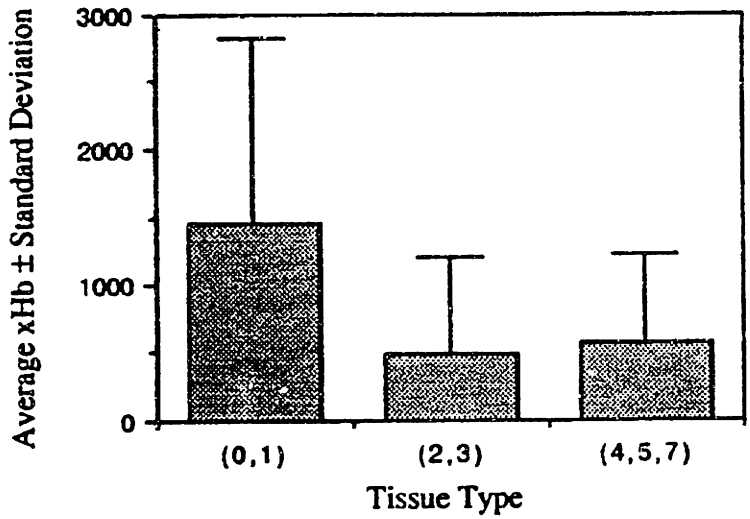

Figure 30 (cont.).

Again, the model parameters, β and x, are directly proportional to the absorption and attenuation coefficients, respectively, and thus provide a link to the chemical composition of the tissue. As these coefficients are linearly related to the chromophore concentration, β and x are proportional to the concentration. This interpretation is only strictly valid for tissues in which the three assumptions made in Chapter Two are valid.

Basically, the interpretation of β'_{Ce} and x_{Hb} are the same for coronary artery as aorta. The absolute and relative values of β'_{Ce} in elastic and muscular arteries are similar, except that there is relatively less ceroid in the non-atherosclerotic muscular arteries as compared to elastic arteries. In both elastic and muscular arteries, normal tissues on average contain more oxy-hemoglobin than atherosclerotic tissues. However, there is relatively less oxy-hemoglobin in coronary arteries than aorta. This is likely due to the different origin of these samples - aorta was obtained from cadavers while coronary artery was obtained from surgical samples. In general, these surgical samples are exposed to far less hemolysed blood, and thus take up less hemoglobin than the samples obtained from cadaver tissue [44].

Because of the different composition of media in muscular arteries, the interpretation of β_{SP} in these tissues is different. In normal tissues, β_{SP} is due primarily to the emission of elastic fibers in the IEL. As non-calcified atherosclerotic plaque develops, the IEL degenerates and intimal thickness increases. Thus the overall contribution if the IEL to the fluorescence spectrum decreases. Although collagen fibers which deposit in the thickening intima also contribute to β_{SP}, their fluorescence intensity is relatively less than that of elastin fibers so β_{SP} decreases in non-calcified plaque. In calcified plaque, β_{SP} contains contributions from both densely packed collagen fibers and calcified elastin fibers. The fluorescence of these calcified elastin fibers contribute to β_{SP}, causing it to rise.

This analysis of β_{SP} in calcified plaques suggests that β_{SP} should be greater in those calcified plaques in which the fibrous cap is calcified than in those in which the necrotic core is calcified. When the fibrous cap is calcified, the calcified elastin fibers are closer to the intimal surface of the tissue, and therefore contribute relatively more to the fluorescence spectrum. Of the 26 calcified plaques studied in coronary artery, the fibrous cap was the site of calcification in 11, and the necrotic core was calcified in 15. Of the 11 samples in which the fibrous cap was calcified, 10 were calcified fibrotic/sclerotic plaques. The 15 samples with a calcified necrotic core were either calcified atherosclerotic or calcified atheromatous plaques. The average value $\pm$ standard deviation of β_{SP} for the calcified plaques in which the fibrous cap was calcified was 7.37 ± 3.78, that of those calcified in the core was lower, 3.47 ± 2.89. When compared in a two-sided student's t-test, these means were significantly different ($p < .005$). It is interesting to note that the average value of β_{SP} for those samples calcified in the core is slightly greater than that of non-calcified atherosclerotic samples, but still less than that of non-

atherosclerotic samples. The average values of β'_{Ce} did not differ significantly with the site of calcification.

This interpretation of β_{SP} in calcified plaques helps to clarify one previously noted discrepancy in the trends observed in β_{SP} in aorta and coronary artery. In aorta, β_{SP} of calcified plaques was less than that of non-atherosclerotic tissues on average. The opposite trend was observed in coronary artery. This can be explained by the fact that, while few of the 24 calcified aortic plaques studied with the catheter system were extensively calcified in the fibrous cap, many of the calcified plaques from coronary artery studied with the catheter system were extensively calcified in the fibrous cap (11 of 26). Those calcified plaques calcified in the fibrous cap consistently displayed higher values of β_{SP} than those calcified in the core.

Furthermore, this interpretation of β_{SP} can help clarify a discrepancy noted earlier in the relative intensity of the peak at (460, 520 nm) in the EEMs of non-atherosclerotic tissues and calcified plaques in both aorta and coronary artery. In the EEMs of aorta, this peak was more intense for calcified plaques than for non-atherosclerotic tissues. However, of the calcified aortic plaques for which EEMs were recorded, many (3 of 4) were extensively calcified in the fibrous cap. Thus, the peak at (460, 520 nm), which has been attributed to elastin fiber fluorescence, exhibited greater fluorescence intensity. In coronary arteries, a different trend was noted; the peak at (460, 520 nm) was of roughly the same intensity in the EEMs of non-atherosclerotic tissues and calcified plaques. However, of the 12 calcified plaques from which EEMs were recorded, only 3 were calcified in the fibrous cap. In all cases, those calcified plaques calcified in the fibrous cap exhibited a relatively more intense fluorescence maximum at (460, 520 nm).

3:4.5. Model Based Algorithms

We have demonstrated that the model parameters contain chemical information about tissue composition which is related to the presence of pathology in the tissue. The challenge in obtaining a clinically useful diagnostic algorithm is to find criteria which separate normal and pathologic tissue, despite the wide variance in the distributions of these parameters. For the purposes of this discussion, intimal fibroplasia is considered non-atherosclerotic. In the context of atherosclerosis this is justified, since intimal fibroplasia alone is rarely hemodynamically significant.

Here, we consider two methods of algorithm development. The first and simplest is based on scatter plots of model parameters versus sample type. Decision surfaces separating various types of disease-free and diseased tissue are drawn in order to maximize the number of samples correctly classified. This method has the advantage of being simple, and it allows the performance of model based algorithms to be easily evaluated. However, as will be discussed, this method suffers from some significant problems. Our second method of algorithm development, which is based on posterior probabilities overcomes these disadvantages, and is also presented here. As significant differences were observed in the average values of the model parameters for aorta and coronary artery, these methods are carried out individually for muscular and elastic arteries. Emphasis was given to algorithms for coronary artery atherosclerosis, as an important goal of this research is to develop methods for improving the diagnosis and treatment of CAD.

3:4.5.1. Aorta

In the aorta, the model parameters of non-atherosclerotic tissue differed significantly from those of non-calcified and calcified plaques. The parameters of non-calcified and calcified plaques also differed; however, the overlap in the distributions of parameters for these tissues was greater. Thus, although a diagnostic algorithm differentiating these three types of tissue is desirable, using 476 nm laser induced fluorescence, a more attainable goal is a diagnostic algorithm which identifies atherosclerotic tissues. In the next two sections, algorithms defined from scatter plots and a consideration of posterior probabilities are presented which indicate the presence of atherosclerosis with a high degree of accuracy.

3:4.5.1.1. Scatter Plot Method

A consideration of Figure 22 shows that a simple criterion, $\beta_{SP} > 9.0$ indicating a non-pathologic (0,1) specimen and $\beta_{SP} < 9.0$ indicating pathology (2,3,4,5,6), provides a fairly accurate diagnostic algorithm for atherosclerosis. This algorithm correctly diagnoses the presence or absence of atherosclerosis in 84% of the 148 samples shown. This criterion, and others discussed below, were chosen to maximize the percentage of samples in which the presence or absence of atherosclerosis was correctly diagnosed. The β_{SP} algorithm should be compared to a simple empirical diagnostic utilizing the intensity at 520 nm (Fig. 13). This empirical algorithm is chosen because this

wavelength corresponds to the fluorescence maximum observed for collagen and elastin, and thus should be related to β_{SP}. The empirical algorithm correctly diagnoses 77% of the samples; however, it is particularly poor for calcified tissue (4,5), achieving a correct diagnosis in only 52% of the cases. The improvement in diagnosing calcified tissues in the model (88% correct) is largely due to the ability of the model to separate the effects of ceroid in β'_{Ce} and those of collagen/elastin in β_{SP}. Neither β'_{Ce} nor x_{Hb} alone were found to be useful in diagnosing tissue type.

A better way to evaluate the efficacy of any algorithm is to test its sensitivity, specificity and positive predictive value as defined in Eq. (10).

(10)
sensitivity = no. of true positives/total no. of diseased samples

specificity = no. of true negatives/total no. of normal samples

positive predictive value = no. of true positives/total no. of positives

Here, positives refer to those samples diagnosed spectroscopically as having disease (2, 3, 4, 5, 6). True positives denote spectroscopic positives actually displaying disease, whereas, true negatives denote spectroscopic negatives which are actually normal [46]. In general, sensitivity measures the ability of the algorithm to detect disease, while specificity determines its ability to detect normal samples. The sensitivity, specificity and positive predictive value of the empirical algorithm shown in Fig. 13 are 69%, 85% and 82%, respectively, which improved to 84%, 85% and 84% for the algorithm shown for β_{SP} in Fig. 22. The improvement in sensitivity reflects the ability of the β_{SP} algorithm to diagnose calcified samples.

In order to achieve more effective diagnosis, a binary classification scheme should be considered. Fig. 31 shows a plot of β'_{Ce} vs β_{SP} for all classifications except intimal fibroplasia. We initially limit our consideration to these tissue categories in order that the sensitivity and specificity of binary schemes with respect to normal tissue (0), and normal and intimal fibroplasia (0,1) can be separately evaluated. The decision surface indicated by the divisions in Fig. 31 correctly diagnoses 98% of the samples. The sensitivity of this algorithm to detect disease is 97%, while its specificity is 100%. The positive predictive value of this scheme is 100%.

Fig. 32 shows a plot of β'_{Ce} vs β_{SP} which includes the intimal fibroplasia samples. The divisions in this plot indicate a different decision surface for classification of tissue type than that in Fig. 31. This surface correctly diagnoses 88% of the samples.

In this case, the sensitivity of the scheme is 91%, while its specificity is 85%. This decision surface has a positive predictive value of 85%. The poorer performance of the binary scheme when intimal fibroplasia is included reflects the fact that intimal fibroplasia is an initial step in the formation of atherosclerosis [14]. Thus, this tissue type is more difficult to differentiate from samples displaying well developed atherosclerotic plaques. Yet, the success of this model for diagnosing disease must be considered impressive.

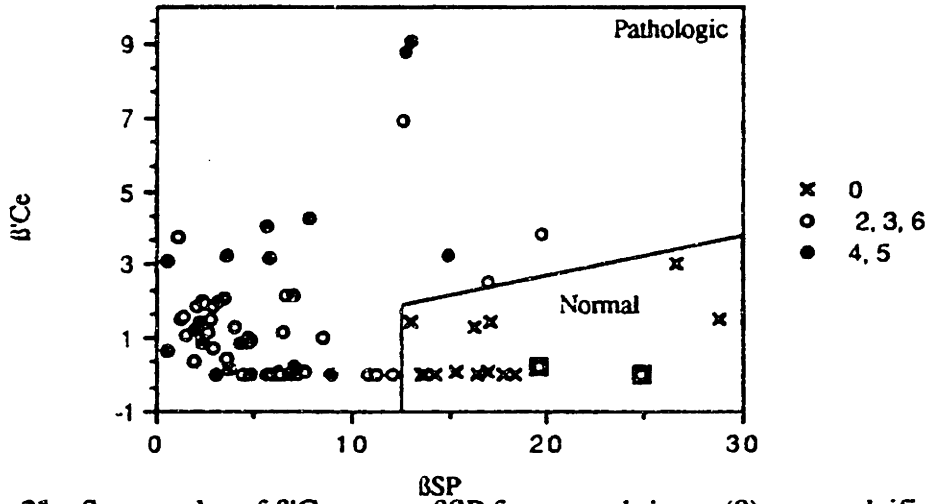

Figure 31: Scatter plot of ß'Ce versus ßSP for normal tissue (0), non-calcified plaques (2,3,6) and calcified plaques (4,5). The decision surface indicated by the divisions represents a diagnostic algorithm which maximizes correct identification of normal and pathologic tissues.

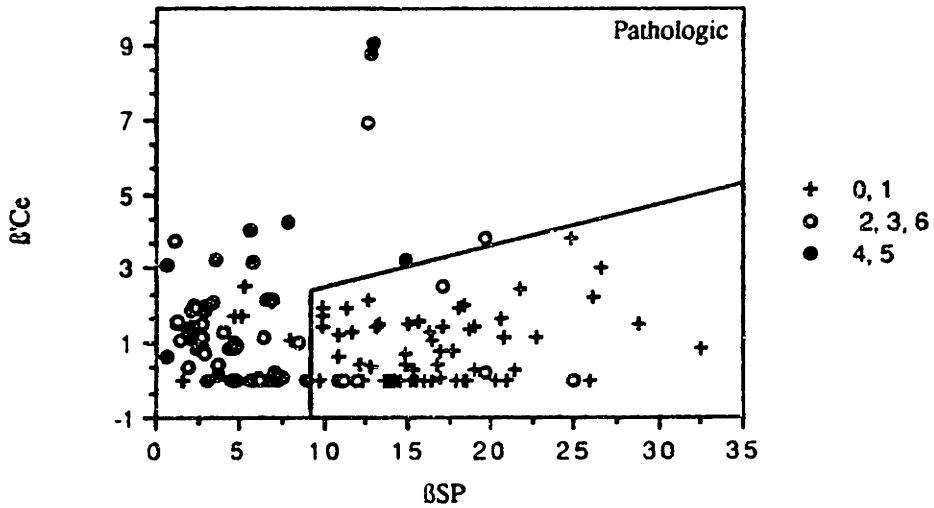

Figure 32: Scatter plot of ß'Ce versus ßSP for normal tissue and tissues displaying intimal fibroplasia (0,1), non-calcified plaques (2,3,6) and calcified plaques (4,5). The decision surface (different than that of Fig. 31) indicated by the divisions represents an algorithm which maximizes correct identification of normal and pathologic tissues.

The decision surfaces discussed above were drawn to maximize the percentage of correctly diagnosed samples. However, for certain applications it might be more advantageous to define other decision surfaces which increase a specific measure of algorithm performance such as sensitivity, specificity or predictive value. For example, a diagnostic algorithm to control laser ablation of atherosclerosis should maximize specificity and negative predictive value in order to avoid perforation of the artery wall. The discrete data presented in Figs. 22 and 31-32 can make it difficult to determine the best diagnostic criteria based on the model parameters.

For this reason it is instructive to consider probability distributions for each of the parameters. For simplicity, these have been modeled as normal distributions truncated at $\beta = 0$ [48]. This distribution is useful to describe concentrations in many chemical and biological systems [48]. The form of this distribution is given by:

$$(11)\quad \frac{\frac{1}{\sqrt{2\pi}\sigma}\exp\left[\frac{-(\beta-m)^2}{2\sigma^2}\right]}{\left[1-\frac{1}{\sqrt{2\pi}}\int_{-\infty}^{\frac{m}{\sigma}}\exp\left[\frac{-t^2}{2}\right]dt\right]}$$

Here, m and σ no longer refer to the mean and standard deviation of the truncated distribution. These quantities can be easily evaluated and expressions for them can be found in [48]. In applying this form of distribution to the data, m and σ were varied, in an iterative fashion, until the mean and variance of the truncated distribution were within 1% of those for the data. Fibrotic/sclerotic samples have been excluded from this discussion because of the small sample number.

Figure 33 shows truncated normal distributions for β_{SP}. These distributions were not greatly different from histograms of the data given in Fig. 22, and can therefore be considered reasonable approximations. Using the same decision surface as in Fig. 22, the sensitivity, specificity and positive predictive value were assessed using the area under the distribution. These quantities were found to be 79%, 82% and 90%, respectively, close to those values calculated from Fig. 22.

A representation of the truncated normal probability distributions for the binary classification scheme of β'_{Ce} vs β_{SP} is shown in Fig. 34 as a contour plot. The decision

surface is that of Fig. 32. Similar to the method used for the single truncated normal distribution for β_{SP}, the sensitivity, specificity and positive predictive value were found to be 82%, 82%, and 88%.

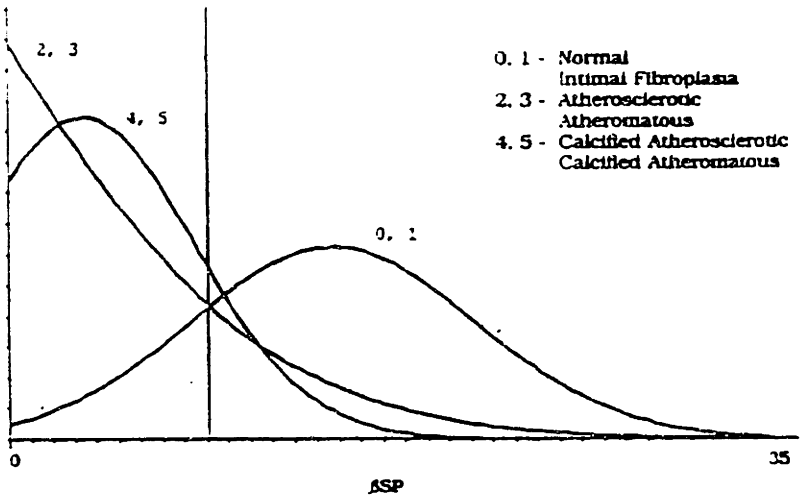

Figure 33: Truncated normal distribution for ßSP for (0,1) non-atherosclerotic tissues, (2,3) non-calcified plaques and (4,5) calcified plaques. Note that fibrotic/sclerotic samples were not included in forming these distributions because of the small number of samples studied. Values of m and σ (Eq. (11) are as follows: (0,1) m = 14.7, σ = 6.5; (2,3) m = -14.3, σ = 12.6; and (4,5) m = 3.4, σ = 5.1.

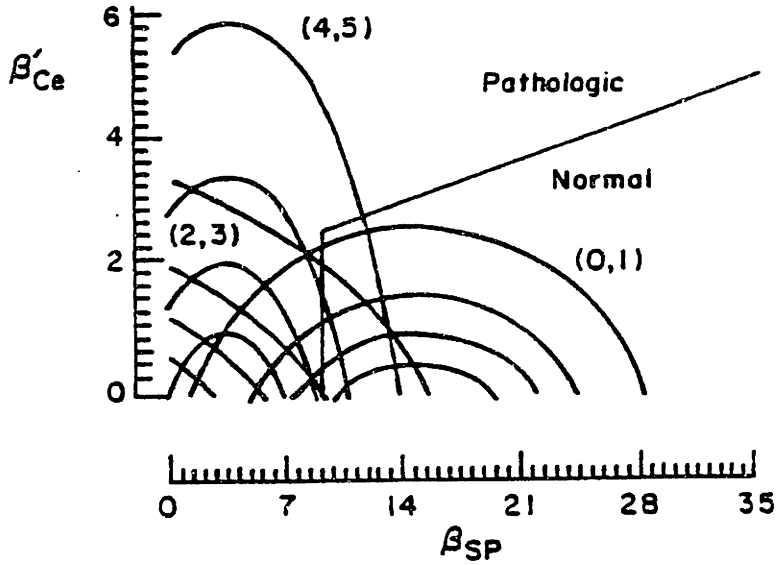

Figure 34: Truncated normal probability distributions of ß'Ce versus ßSP for non-atherosclerotic tissues (0,1), non-calcified (2,3) and calcified plaques (4,5). Note that fibrotic/sclerotic samples (6) were not included in these distributions because of the small number of samples studied. Values of m and σ (Eq. (11)) are as follows: (0,1) m = -2.38, σ = 202; (2,3) m = -4.0, σ = 2.9; and (4,5) m = -6.5, σ = 5.0. Contour lines are drawn at values of 0.8, 0.6, 0.4 and 0.2 times the maximum probability for each of the classifications. Maximum probabilities are: (0,1), 0.053, (2,3), 0.082, and (4,5), 0.037.

Figures 33 and 34 provide the requisite information for defining algorithms for diagnosis of disease to achieve particular values for sensitivity, specificity and positive predictive value. As will be shown in a following section, they also provide the basis for developing diagnostic algorithms which are based on posterior probabilities.

3:4.5.2. Coronary

3:4.5.2.1. Scatter Plot Method

An examination of Figs. 27-29 shows that the model parameters have diagnostic significance for coronary artery as well. In contrast to aorta; however, where the single most useful diagnostic parameter was β_{SP}, for coronary artery, Figure 28 shows that β'_{Ce} is the single most useful parameter diagnostically. The straight line at $\beta'_{Ce} = 0.7$ separates tissues above it as atherosclerotic and those below it as disease free. This simple algorithm correctly classifies 89% of the 82 samples; its performance is poorest for non-calcified plaques, only 75% of these 16 samples are correctly classified. The specificity, sensitivity and predictive value of this algorithm for detecting atherosclerosis are 97%, 81% and 97% respectively.

The algorithm based on β'_{Ce} is poorest for detecting non-calcified plaques; however, examination of Figure 27 shows that β_{SP} is lowest for non-calcified plaques, suggesting that a better diagnostic algorithm might result from a combination of these two parameters. Figure 35 illustrates such an algorithm; shown is a plot of β_{Sp} vs β'_{Ce} for all tissue samples, grouped as (0,1) non-atherosclerotic, (2,3) non-calcified plaque and (4,5) calcified plaque. The three straight lines drawn on this plot represent decision surfaces, separating non-atherosclerotic tissues, non-calcified plaques and calcified plaques. The decision surfaces were drawn in order to minimize the sample misclassification rate.

The bold decision surface represented by two straight lines correctly classifies tissue as normal or atherosclerotic in 96% of cases studied. The third straight line separates non-calcified plaques from calcified plaques. This diagnostic algorithm correctly classifies 92% of the 82 samples as normal, non-calcified plaque or calcified plaque. Table 7 provides a more complete analysis of the performance of this algorithm. Sensitivity is calculated separately for the pathologic categories ((2-5), (2,3) and (4,5). Positive predictive value was calculated separately for three tissue categories: (2-5), (2,3) and (4,5), according to Eq. (10). The algorithm for diagnosing the presence of

atherosclerosis (2,7) was most accurate; the specificity, sensitivity and positive predictive value were greater than that for the corresponding algorithm for atherosclerosis in aorta. The performance of the algorithm which subclassified atherosclerotic lesions as calcified or non-calcified was slightly lower, but still quite good. As Table 7 indicates, this algorithm was detected calcified plaque more accurately than non-calcified plaque.

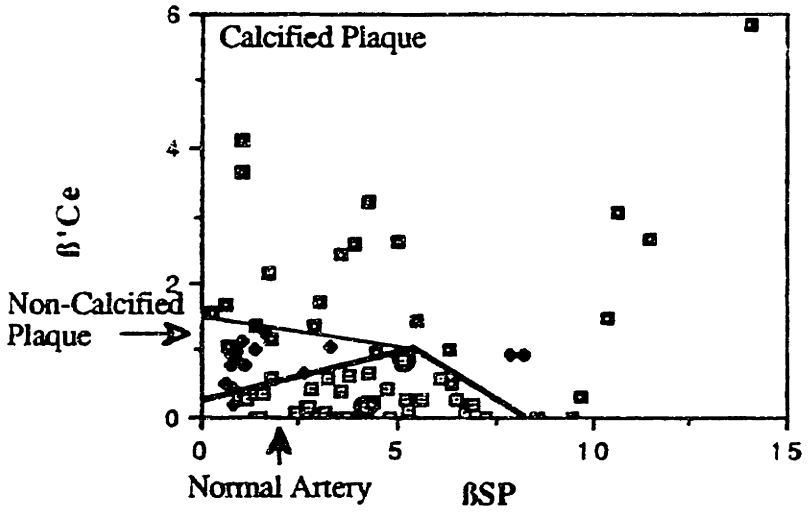

Figure 35: Binary scatter plot showing ß'Ce as a function of ßSP for all 82 samples. Samples have been grouped according to histologic classification as (0,1) disease free tissues, (2,3) non-calcified plaques and (4,5,7) calcified plaques. The three solid lines represent decision surfaces which diagnostically separate tissues as either disease free, non-calcified plaque or calcified plaque.

Table 7: Performance of diagnostic algorithm for coronary atherosclerosis illustrated in Figure 35.

Tissue Classification	Specificity	Sensitivity	Predictive Value
(2-7)	97%	95%	97%
(2,3)	97%	81%	81%
(4,5,7)	97%	88%	92%

Clearly, the method we have used to evaluate the performance of the algorithm depends on the location of the decision surface. The decision surface in Figure 35 was drawn in order to minimize the sample misclassification rate. This algorithm is applicable (optimal in terms of misclassification rate) for other data sets only if two conditions are

met: 1) the values of β_{SP} and β'_{Ce} for the sample set presented here are representative of coronary artery samples in general, and 2) the relative proportions of normal tissue, non-calcified plaque and calcified plaque in our sample set (2:1:1) are similar to those likely to be encountered during application of the algorithm.

One method of judging the representativeness of our sample data set is to apply the algorithm of Figure 35 prospectively to a second, similarly proportioned, data set and evaluate the performance of the algorithm. This is not included here; however, Chapter 6 discusses future experiments to address this issue.

The effectiveness of the algorithm can then be extrapolated to data sets which are comprised of largely different proportions of normal and diseased tissues using Eq. (12), which expresses the predictive value in another form, as a function of sensitivity (SE), specificity (SP) and the prior probability (p) of encountering disease [49].

$$(12)\quad PV_- = \frac{(1-p)SP}{(1-p)SP + p(1-SE)}$$

$$PV_+ = \frac{pSE}{pSE + (1-p)(1-SP)}$$

Here, p represents the prior probability of disease, or proportion of the samples to classify which actually (or are likely) to contain disease. By varying p, the prior probability of disease, we can estimate the performance of this algorithm for other data sets with different fractions of normal tissue, non-calcified and calcified plaques.

Figure 36 shows a plot of the positive predictive value for a given tissue category as a function of prior probability of that category. Three different tissue categories are shown: (2-7) all plaques, (2,3) non-calcified plaques and (4,5,7) calcified plaques. This figure illustrates that the predictive value of the algorithm shown in Figure 35 depends strongly on the prior probability, with predictive value increasing as prior probability increases. This is not a surprising result, it is more difficult to accurately diagnose rare diseases than common ones. It is interesting that the form of these curves are so similar for the three different sample sets; the difference in performance of the algorithm shown in Fig. 35 for non-calcified and calcified plaques appears to be only a function of the different prior probabilities of these data sets. The positive predictive values of our data set are indicated by arrows at prior probabilities of p(2,3) = .2, p(4,5,7) = .32 and p(2-7) = .52.

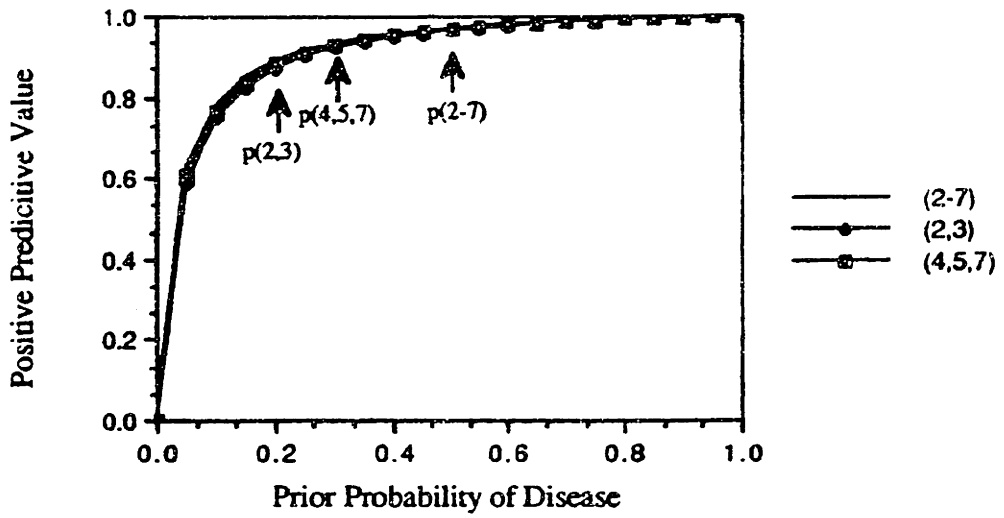

Figure 36: Positive predictive value as a function of prior probability of disease for (2-7) all plaques, (2,3) non-calcified plaques and (4,5,7) calcified plaques.

The positive predictive value gives the probability that a diagnosis of disease based on the algorithm is correct. This curve essentially puts limits on how rare a disease can be detected with the algorithm defined in Figure 35. The positive predictive value is quite high over a large range of prior probabilities, however drops sharply below $p = 0.1$. The positive predictive value for identifying atherosclerosis reaches 0.5 at a prior probability of .067. Here, the positive predictive value is only 50%; essentially, in assigning tissue type as either normal or atherosclerotic we could do as well by chance. For assigning tissue type as either normal, non-calcified plaque or calcified plaque, the predictive value of our algorithm must be greater than 0.33 for its performance to be better than chance. The minimum prior probability at which this condition is met for both non-calcified and calcified plaques is .03.

In developing a diagnostic algorithm to control laser angiosurgery catheters, perhaps a more important quantity is the negative predictive value, which is the probability that a specimen is actually disease free if it is classified as so according to the algorithm. The negative predictive value is also given in Eq. (12). Figure 37 shows the negative predictive value as a function of the prior probability of encountering diseased tissue (2-7). The negative predictive value decreases as the probability of encountering disease increases. Again, this is not a surprising result; it is difficult to accurately rule out the presence of disease in a population of patients at very high risk. From this curve we

can place upper limits on the utility of the algorithm shown in Figure 35. The algorithm is better than chance only when the negative predictive value is greater than 50%, or the prior probability of encountering disease is less than 94%. Using this algorithm to guide laser angioplasty may place even tighter restrictions on this upper limit.

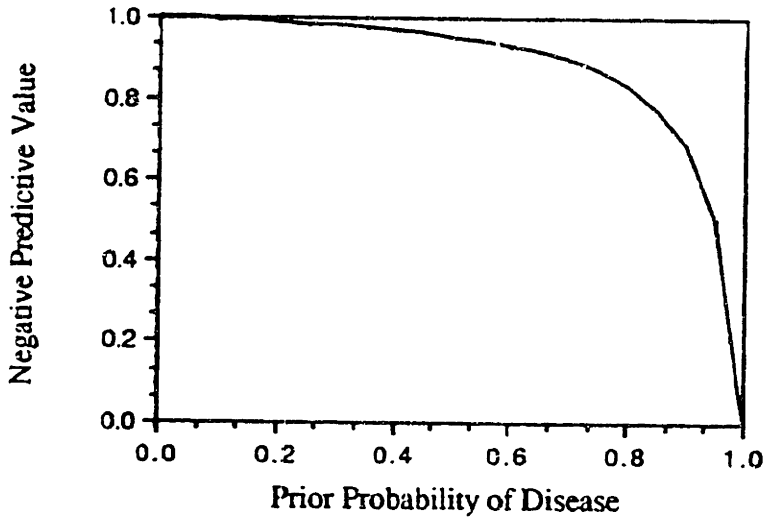

Figure 37: Negative predictive value as a function of the prior probability of disease

This method of estimating algorithm performance for data sets with different prior probabilities has one drawback which must be pointed out. The decision surfaces shown in Figure 35 are optimized in terms of minimizing the total sample misclassification rate for only one set of prior probabilities, that of our data set used in defining the algorithm. Although its performance can be evaluated for other values of p, its performance will not be optimal. Thus, perhaps we could achieve better algorithm performance at prior probabilities lower than .03; however, the decision surface would have to be redefined in terms of this lower prior probability.

The method of analysis presented thus far has reduced the continuous variables $ß_{SP}$ and $ß'_{Ce}$ to a trichotimized decision of sample type. This procedure, although simple, has an additional serious drawback. This substantial reduction of information makes it difficult to interpret the meaning of a given value of $ß_{SP}$ and $ß'_{Ce}$ for an unknown sample. As an example of this difficulty, consider the two circled points in Figure 35. The first has $ß_{SP}$=5.2, $ß'_{Ce}$=0.8, the second $ß_{SP}$=4.2, $ß'_{Ce}$=.03. The algorithm presented in Figure 35 classifies each sample correctly as normal; however,

intuitively, we place more confidence in the classification of the point which lies furthest from the line representing the decision surface. Ideally, given a value of β_{SP} and β'_{Ce} we would like to calculate the probability that the unknown sample belongs to each of the possible tissue categories; this is known as the posterior probability.

3:4.5.2.2. Probability Method

Here, we use statistical techniques to develop a diagnostic algorithm based on such posterior probabilities, overcoming the two most serious drawbacks of the previously presented method. This algorithm can be optimized for any sample set for which the relative proportions of normal and diseased tissue (prior probabilities) are known.

This method is based on the statistical distributions of β_{SP} and β'_{Ce} for normal tissues (0,1), non-calcified plaques (2,3) and calcified plaques (4,5). We assume here that these follow the truncated normal distribution (Eq. 11), which can be characterized in terms of two parameters, m and σ, which are related to the mean and standard deviation of the data set [48]. Figures 38 and 39 show a comparison of a measured histogram and the calculated truncated normal distributions for β_{SP} and β'_{Ce} for each of the three categories of tissue type. In all cases, there is reasonable agreement between the experimentally measured and calculated distributions.

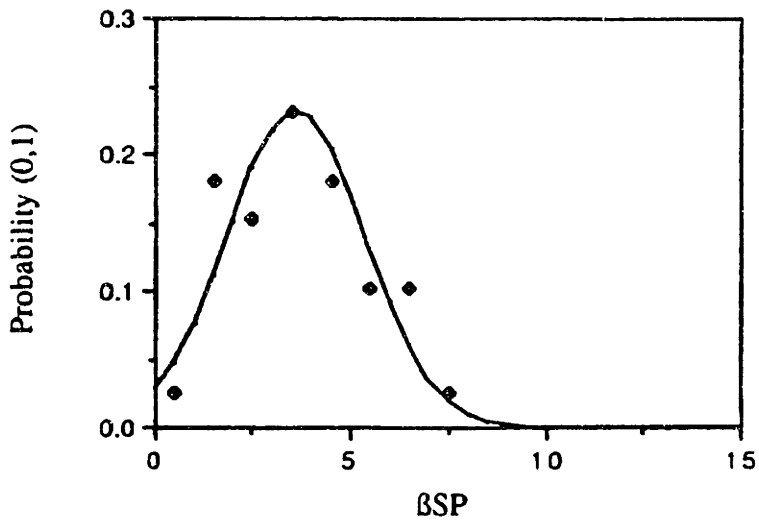

Figure 38: Comparison of histograms of ßSP and calculated truncated normal distributions for disease free tissues (0,1), non-calcified plaques (2,3) and calcified plaques (4,5).

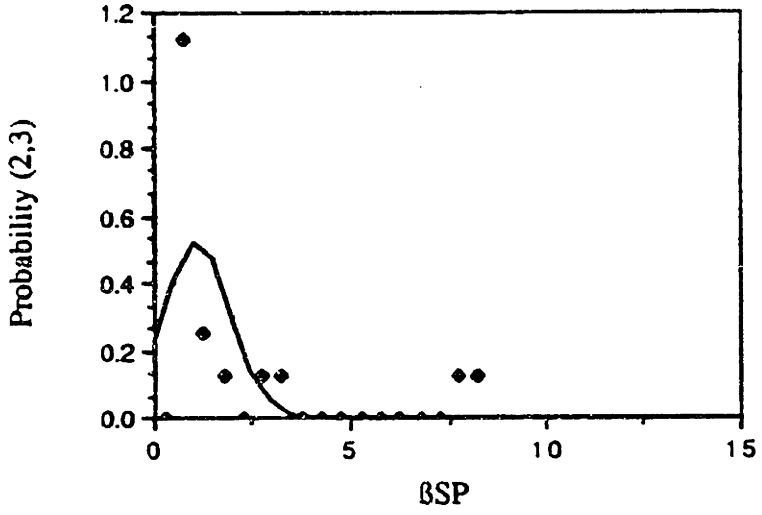

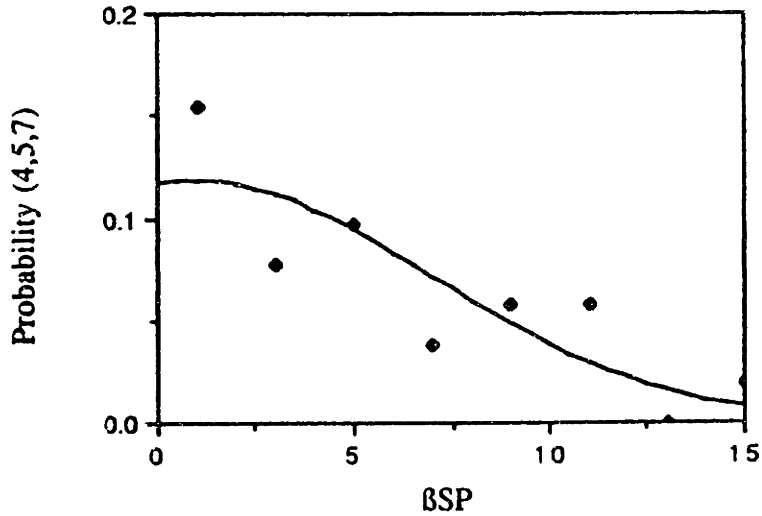

Figure 38 (cont.).

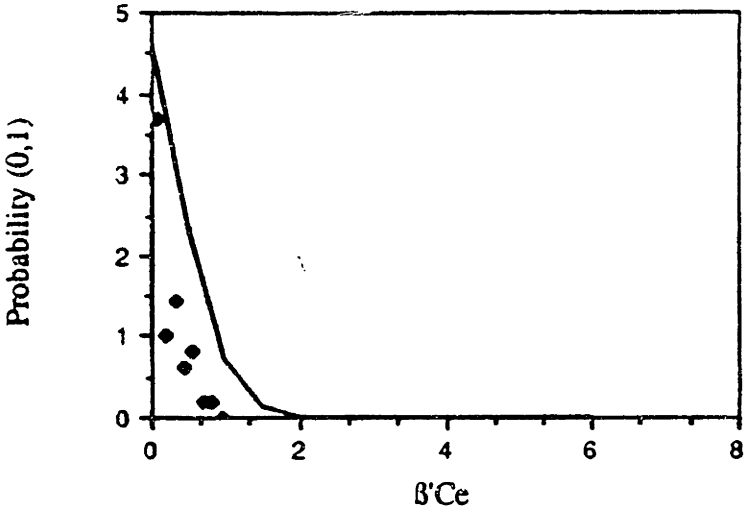

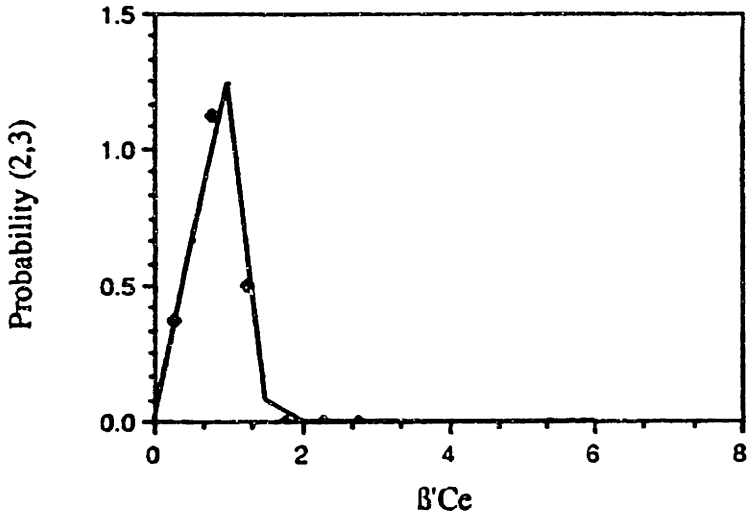

Figure 39: Comparison of histograms of ß'Ce and calculated truncated normal distributions for disease free tissues (0,1), non-calcified plaques (2,3) and (4,5,7) calcified plaques.

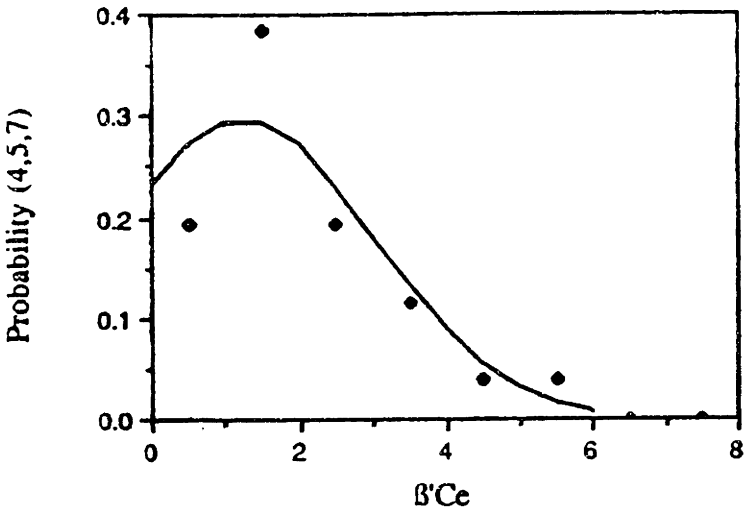

Figure 39 (cont.).

As β_{Sp} and β'_{Ce} are independent parameters, these distributions can be used to calculate the probability that a tissue sample known to belong to a particular category will exhibit fluorescence parameters (β_{Sp}, β'_{Ce}). This probability is given as

$$(13)\quad P(\beta_{SP},\dot{\beta}_{Ce}|(0,1)) = P(\beta_{SP}|(0,1))P(\dot{\beta}_{Ce}|(0,1))$$

These joint probability distributions can be used to calculate the probability that an unknown sample with measured (β_{SP}, β'_{Ce}) is of a particular sample type (posterior probability). The posterior probabilities can be calculated from Eq. (13) using Bayes rule (Eq. (14)), if the relative frequency of that particular sample type in the data set (prior probability) is known (or can be estimated).

$$(14)\quad P((0,1)|\beta_{SP},\dot{\beta}_{Ce}) = \frac{p(0,1)P(\beta_{SP},\dot{\beta}_{Ce}|(0,1))}{\left\{p(0,1)P(\beta_{SP},\dot{\beta}_{Ce}|(0,1)) + p(2,3)P(\beta_{SP},\dot{\beta}_{Ce}|(2,3)) + p(4,5,7)P(\beta_{SP},\dot{\beta}_{Ce}|(4,5,7))\right\}}$$

Equation (14) provides the basis for an optimal classification algorithm. Classifying the sample type of unknown samples as that for which the posterior probability is the highest results in a classification scheme which minimizes the rate of misclassification [49].

We illustrate this method assuming the prior probabilities of our sample data set. Figure 40 shows joint probability distributions $P(\beta_{SP},\beta'_{Ce} \mid (0,1))$, $P(\beta_{SP},\beta'_{Ce} \mid (2,3))$, and $P(\beta_{SP},\beta'_{Ce} \mid (4,5))$. Again, these represent the probability that a sample belonging to one of these categories will exhibit a given value of β_{SP} and β'_{Ce}.

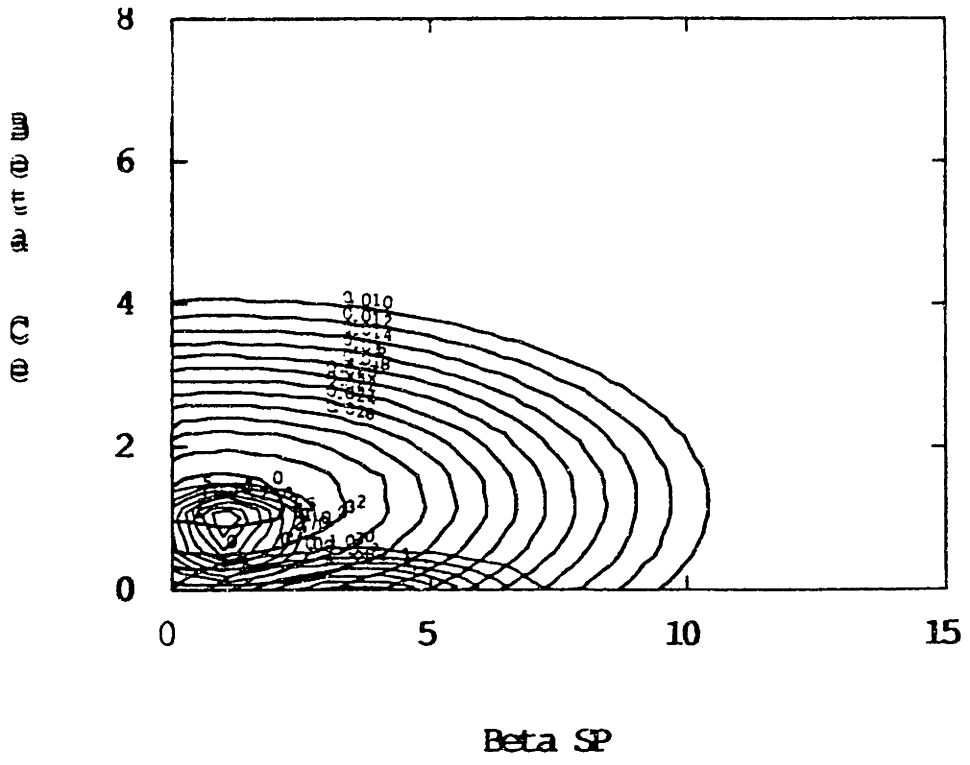

Figure 40: Joint probability distributions $P(\beta_{SP},\beta'_{Ce} \mid (0,1))$, $P(\beta_{SP},\beta'_{Ce} \mid (2,3))$, and $P(\beta_{SP},\beta'_{Ce} \mid (4,5,7))$. These distributions were calculated according to Eq. (15) using the truncated normal distributions of Figs. 38 and 39.

For classifying the sample type of an unknown sample given its fluorescence parameters, the more meaningful quantities are the posterior probabilities, $P((0,1) \mid \beta_{SP},\beta'_{Ce})$, $P((2,3) \mid \beta_{SP},\beta'_{Ce})$, $P((4,5) \mid \beta_{SP},\beta'_{Ce})$. These are shown in Figure 41 for prior probabilities of our data set: P(0,1) =.48, P(2,3) =.2, P(4,5) =.32. The bold lines on this figure represent the decision surfaces based on classifying unknown samples as the sample type for which the posterior probability is highest. These are compared to the algorithm represented by the straight lines in Fig. 35 in Fig. 42. The decision surfaces in these two figures are remarkably similar, except that in Fig. 35, decision surfaces were restricted to straight line segments. This statistically optimized algorithm was applied to data from the 82 samples presented earlier; its performance is summarized in Table 8.

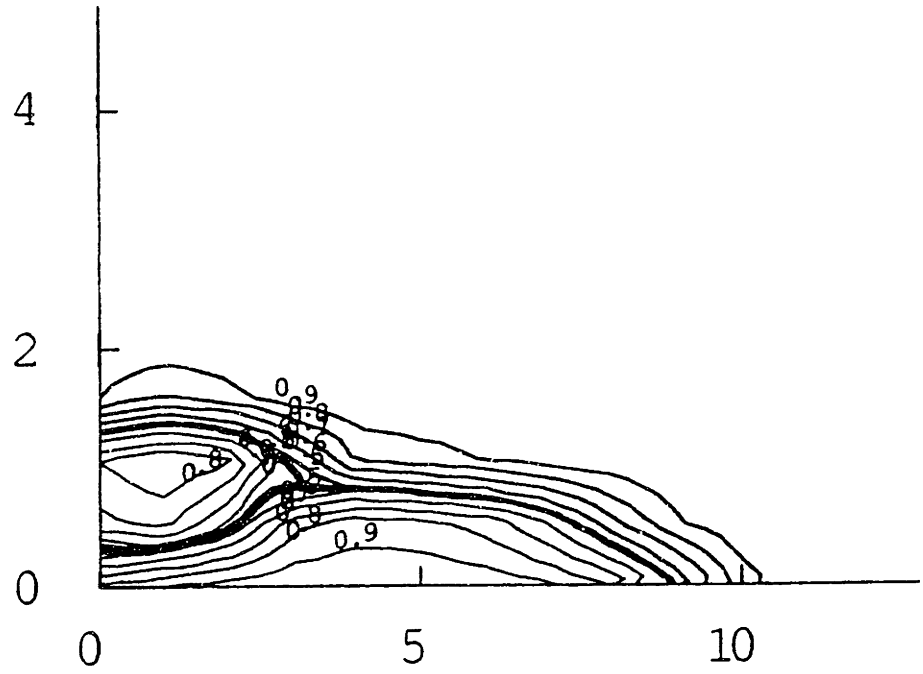

Figure 41: Posterior probability distributions for the prior probabilities of our data set: (0.48:0.2:0.32). The bold lines on this figure represent the diagnostic algorithm based on allocating unknown samples to the category for which the posterior probability is highest.

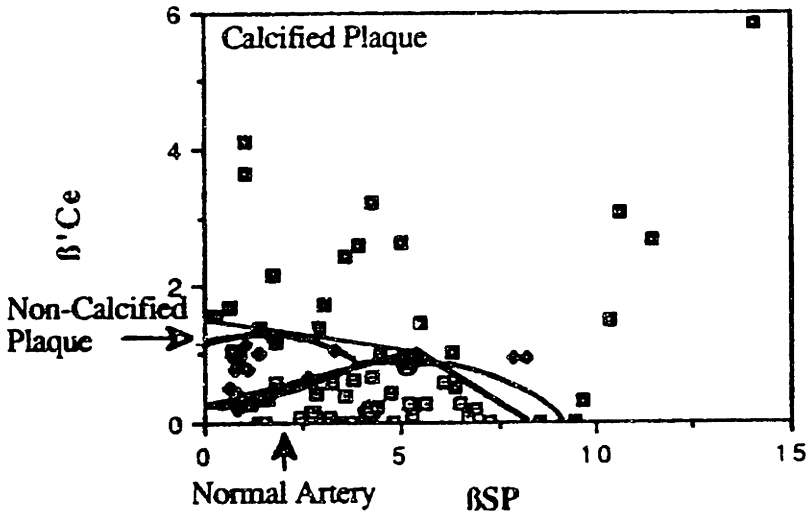

Figure 42: Comparison of the empirically derived decision surface of Fig. 35 and the statistically derived decision surface of Fig. 41.

Table 8: Performance of statistically derived diagnostic algorithm shown in Figure 41.

Tissue Classification	Specificity	Sensitivity	Positive Predictive Value
(2-7)	97%	93%	98%
(2,3)	94%	81%	76%
(4,5,7)	96%	81%	91%

This method of algorithm development also allows us to interpret the meaning of data points which fall on or near the decision surfaces, such as the two circled in Figure 35. It was stated previously, that intuitively we associate less confidence with our ability to make a diagnosis about the point closer to the decision surface. Figure 41 provides a method of quantifying this uncertainty. The point furthest from the decision surface has a 90% probability of being disease free, that near the decision surface has only a 60% probability of being disease free.

Another advantage of the statistically developed algorithm is its ability to be easily optimized for other data sets with different prior probabilities via Eq. (14). This allows us to determine under what conditions the algorithm will be most useful. Figure 43 shows how the diagnostic algorithm itself, which is represented by a decision surface in (β_{SP},β'_{Ce}) space, shifts as a function of prior probability. Decision surfaces are shown for four different sets of prior probabilities: that of our initial sample set, (0.48:0.20:0.32), and three others, (0.8:0.1:0.1), (0.1:0.8:0.1) and (0.1:0.1:0.8).

Figures 36 and 37 predicted that, given the specificity and sensitivity of our algorithm, the decision surfaces would shift significantly for values of the prior probability below 0.1. Figure 43 shows that this is true; the decision surfaces for prior probabilities of (0.8:0.1:0.1) and (0.1:0.8:0.1) are significantly different than that for our data set. These surfaces shift in a predictable way, however. As indicated in Fig. 43, as the prior probability for a particular tissue type increases (decreases) the area bounded by the decision surfaces for that type of tissue increases (decreases). This is simply a consequence of the fact that the probability distributions in (β_{SP}, β'_{Ce}) space overlap for these tissue types. As the relative proportion of one tissue type increases, in order to maximize the number of samples correctly classified, the decision surface must change.

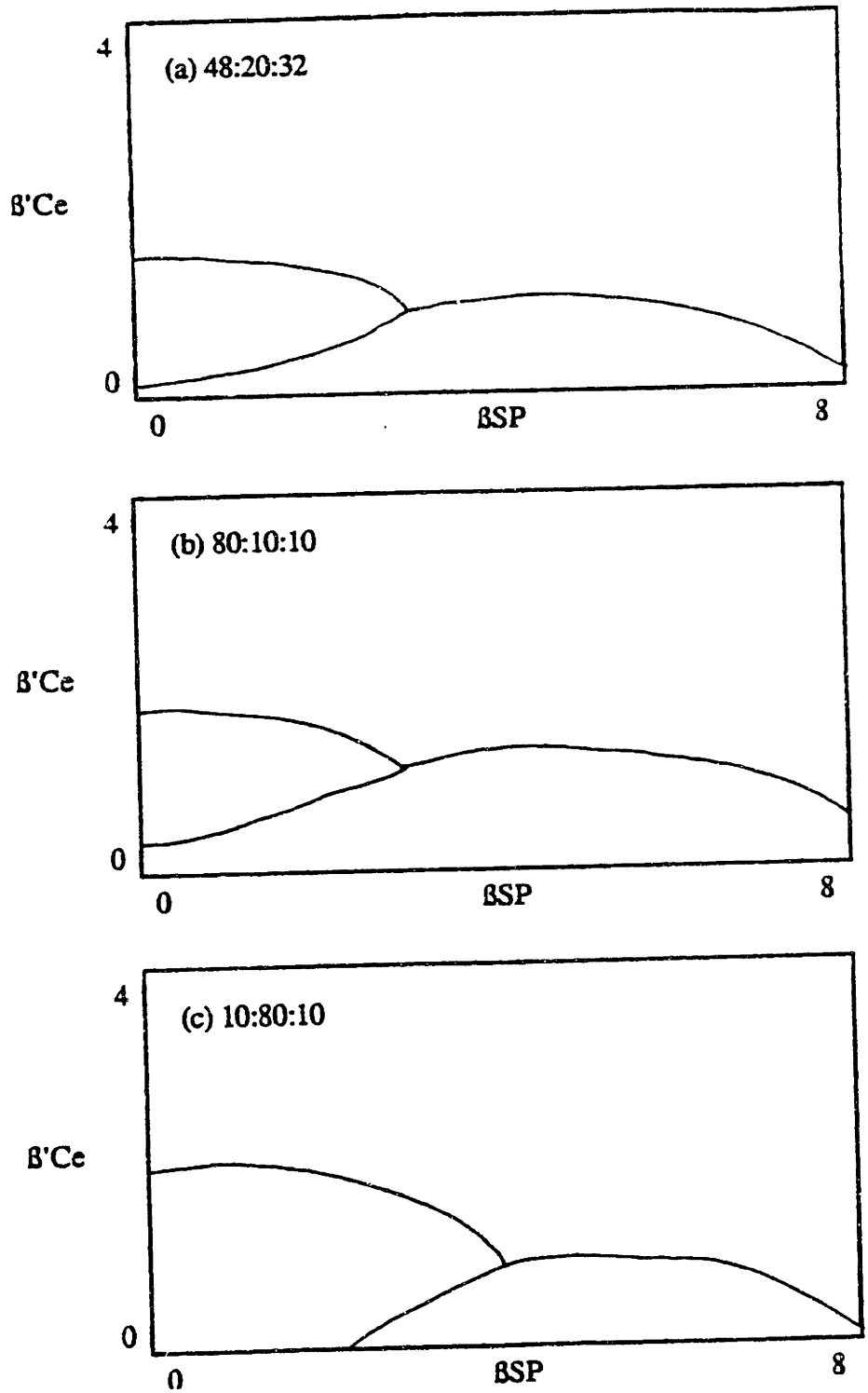

Figure 43: Decision surfaces for three different prior probabilities: that of our data set(0.48:0.2:0.32), (0.8:0.1:0.1), and (0.1:0.8:0.1). Decision surfaces were derived using the statistical method described in the text.

3:4.6. *In vivo* Studies of Arterial Fluorescence[2]

Several studies of the 476 nm excited fluorescence properties of human aorta and coronary artery have been carried out *in vivo*. The goals of these studies were three fold: 1) to show that fluorescence spectra of vascular tissues could be recorded *in vivo* in near real time, 2) to determine whether there were any grossly observable difference in the fluorescence properties of these arteries *in vivo* and *in vitro* and 3) to determine whether the model of tissue fluorescence developed *in vitro* could be used to extract diagnostically meaningful information about the presence of atherosclerosis *in vivo*. These studies have been described in detail elsewhere [50, 51], and will only be briefly summarized here.

476 nm excited fluorescence spectra have been collected from the intimal surface of human aorta in seven patients [50]. Figure 44 indicates the experimental setup used to record these spectra. Spectra were obtained *in vivo* during coronary bypass operations in seven patients. In these experiments, spectra were collected from the intimal surface of the aorta opposite the arteriotomy site. Spectra were obtained *in vivo* during aortic valve replacement operations in four patients. In these experiments, spectra of many intimal sites were obtained under direct visualization. In all cases, tissue type was determined by gross examination as normal, non-calcified plaque or calcified plaque.

Figure 45 shows typical spectra of normal aortic intima, non-calcified and calcified atherosclerotic plaque obtained from a single patient. This data has several important implications. First, spectra with reasonably good signal to noise were obtained in a short period of time, ~10 s. Second, the features of these spectra generally resemble those obtained *in vitro*. Three peaks are present at 520, 550 and 600 nm, with intervening valleys at 540 and 580 nm. The peak fluorescence intensity of normal tissue is higher than that of atherosclerotic tissues, and that of calcified plaques is higher than that of non-calcified plaques. However, there are some important differences. The valleys at 540 and 580 nm are barely observable in the spectra of the normal and non-calcified plaques, in fact significant valleys were never observed in the spectra of these tissue types in any patients.

---

[2]The studies of arterial fluorescence *in vivo* are largely the work of collaborators at MIT and the Cleveland Clinic Foundation, including Rim Cothren, Mike Otteson, and Young Park. Their contributions are gratefully acknowledged.

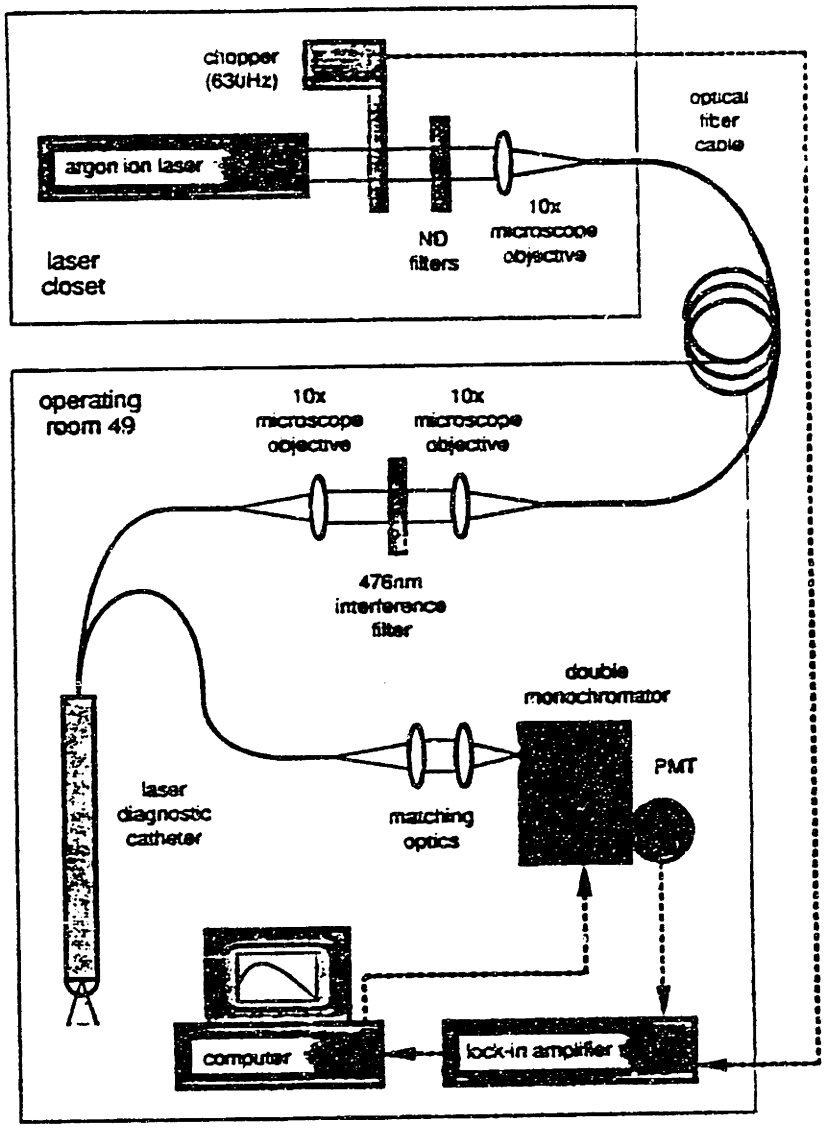

Figure 44: Block diagram of the system used to record 476 nm LIF spectra of human aorta *in vivo* during open heart surgery.

As it has been established that these valleys are due to the reabsorption of oxy-hemoglobin [43], this indicates that there are differences in the oxy-hemoglobin content of vascular tissues *in vivo* and *in vitro*. It has been demonstrated that the presence of oxy-hemoglobin in cadaveric normal aorta and non-calcified atherosclerotic plaque is due primarily to the diffusion of oxy-hemoglobin from the hemolysed blood during the time

between death and procurement of tissue at autopsy [50]. Fortunately, our diagnostic algorithm does not depend on this parameter, so the consequences of this difference are minimal.

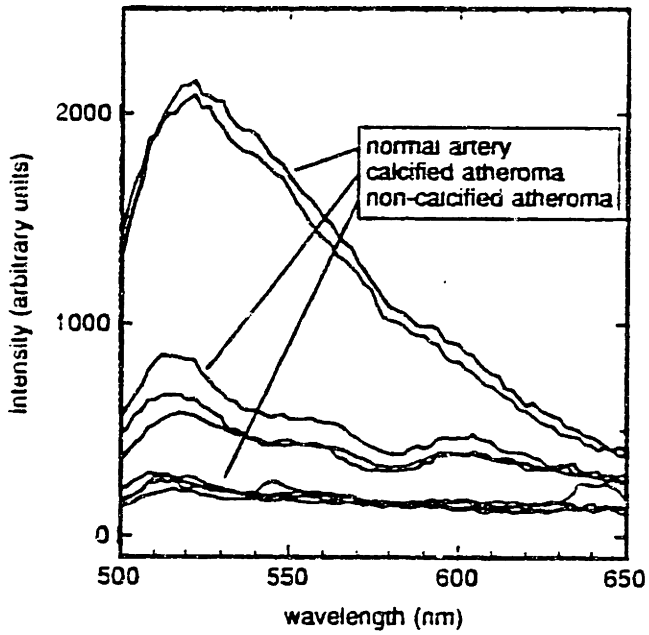

Figure 45: Typical spectra of normal human aorta, non-calcified plaque and calcified plaque obtained *in vivo*.

Subsequently, the system shown in Figure 44 was improved so that 476 nm excited LIF spectra could be recorded from a 1.5 mm area with a resolution of 20 pixels. With the system shown in Figure 46, spectroscopic images of the interior of arteries can be recorded in 12 seconds. This system was used to record fluorescence images of the interior of seven coronary arteries with severe atherosclerotic narrowings at the time of CABG. In all cases, images were obtained of a relatively disease free portion of the intimal surface of the artery opposite the arteriotomy site. Following this, the multi-fiber catheter was advanced to the obstruction and several spectroscopic images were recorded. In between the acquisition of each image, the catheter was withdrawn from the obstruction, rotated slightly, and readvanced to the site of the obstruction. In all cases, the presence and nature of a lesion was documented using white light angioscopy.

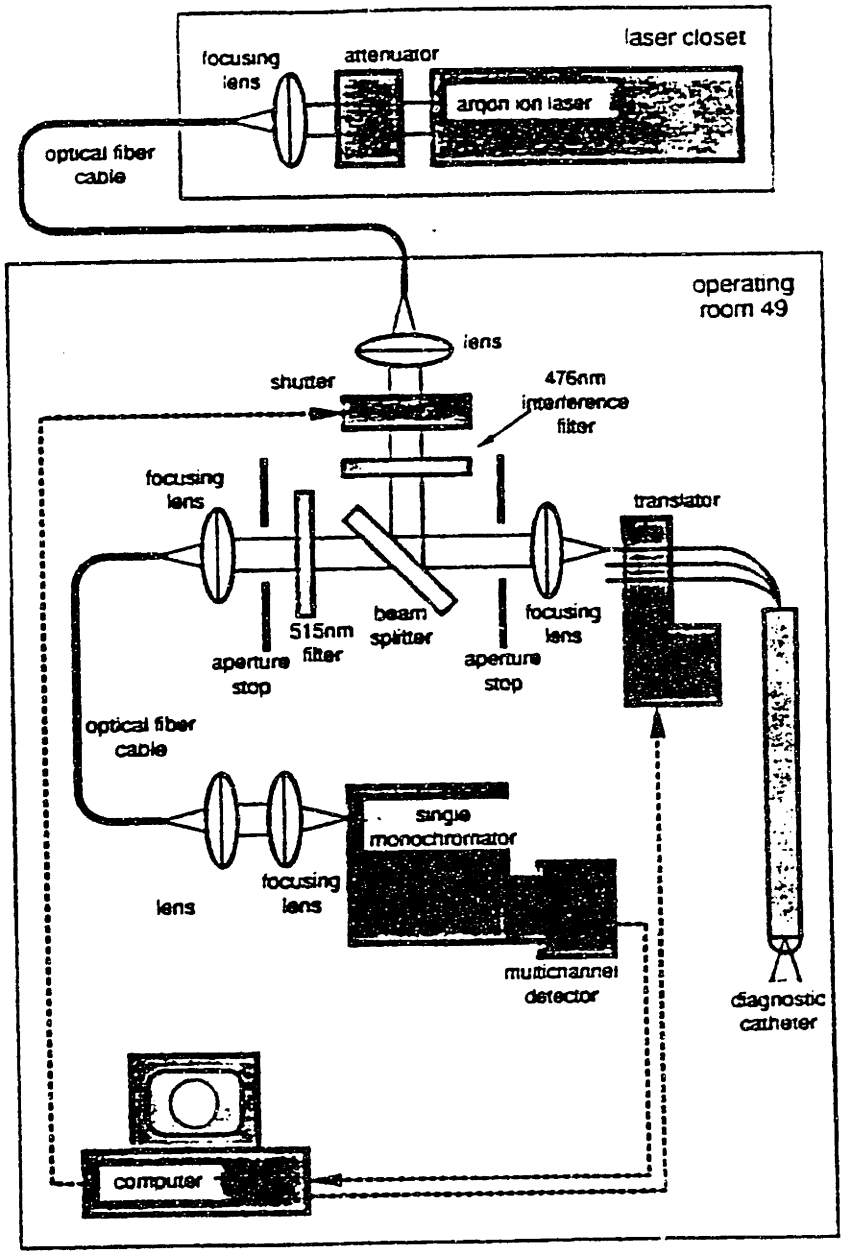

Figure 46: Block diagram of the system used to record 20 pixel spectroscopic images of the interior of human coronary arteries *in vivo*.

Following acquisition of the image, data was analyzed using the model of tissue fluorescence developed *in vitro*. Spectra corresponding to each pixel were fit to the one-layer model of arterial fluorescence described in this chapter. The parameters β_{SP} and β'_{Ce} were extracted from the spectra. Tissue type was assigned based on the decision

algorithm shown in Fig. 35. A plot of tissue type vs. pixel position was then constructed and compared to the angioscopic data collected *in vivo*.

Figure 47 shows a typical spectroscopic image obtained using this method. The top plot shows the individual spectra as a function of pixel position, the bottom plot shows the extracted model parameters and χ^2, the sum of the squares of the differences between the experimental and calculated spectra. Tissue type is indicated by the shading of the pixel. The image obtained with the white light angioscope was not inconsistent with this diagnosis.

This data has two important implications. It shows that the model of arterial tissue fluorescence developed *in vitro* can be used to adequately describe data collected *in vivo* form muscular arteries. In addition, it shows that the values of these parameters can be used to diagnose the condition of the artery wall in a way that roughly corresponds to an independent angioscopic diagnosis.

The most significant shortcoming of this experiment is that no independent histologic assessment of tissue type can be made to determine whether the spectroscopic diagnosis is in fact accurate. An experiment designed to overcome this problem is now underway. In this study, the system described in Figure 46 will be used to record spectroscopic images of vascular tissue during a procedure in which some vascular tissue will be removed, such as abdominal aortic aneurysm repair, femoral-popliteal bypass grafting, brachial artery repair and arteriovenous fistula formation in dialysis patients. Spectroscopic images of tissue will be recorded *in vivo* in the manner described previously. Tissue will then be removed and submitted for standard histologic analysis to confirm whether the spectroscopic diagnosis is in accord with the actual tissue type.

This chapter has summarized our results to date in developing a spectroscopic diagnostic algorithm for the presence of atherosclerosis in muscular and elastic arteries based on the methods outlined in Chapter One. The conclusions which can be drawn from these studies, and future experiments required to achieve our ultimate goals are presented in Chapter Six.

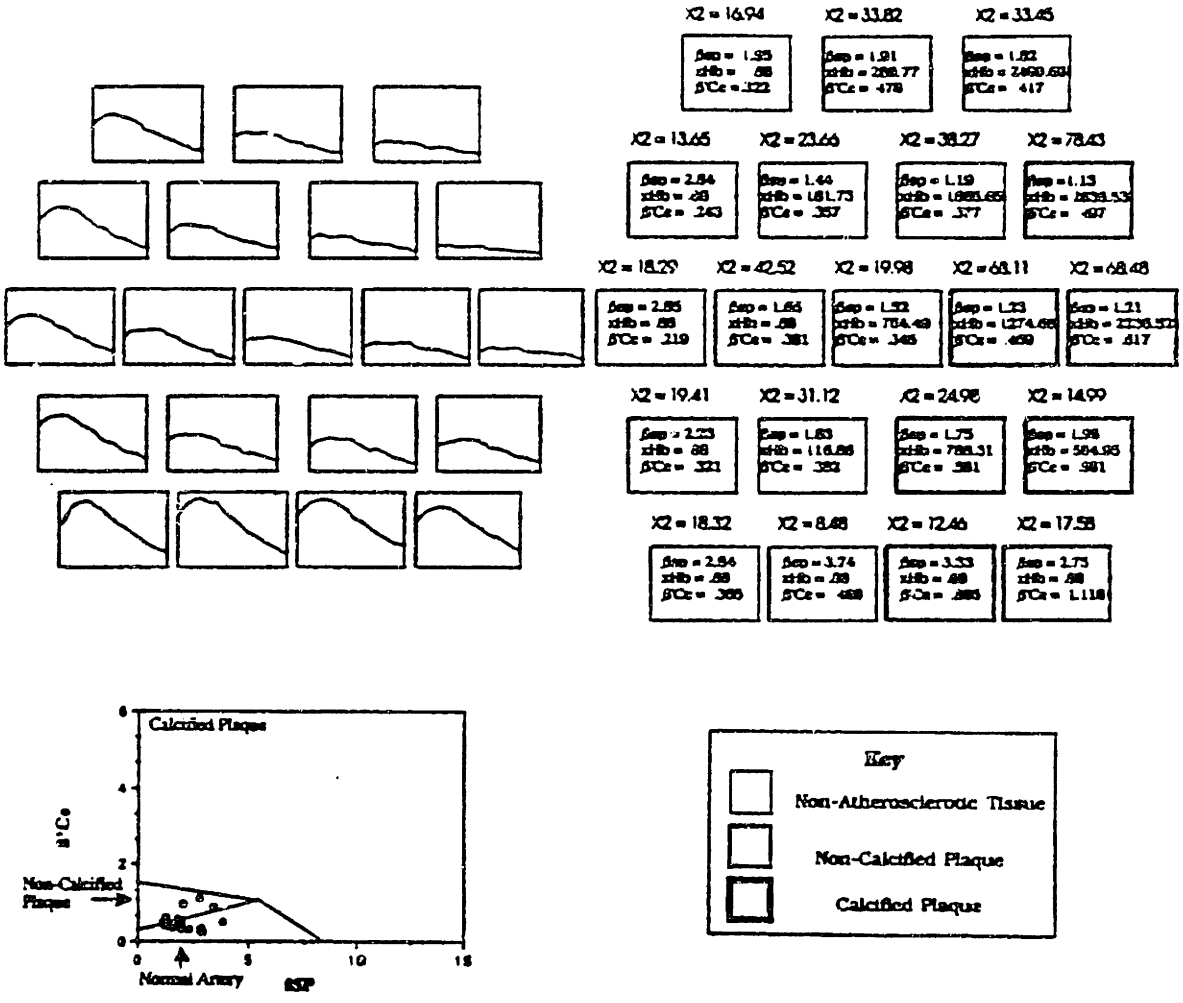

Figure 47: Spectroscopic images of the interior of human coronary artery obtained *in vivo* using the system diagramed in Figure 46.

3:5. References

1. Robbins SL, Cotran RS, Kumar V, Pathologic Basis of Disease, WB Saunders Co, Philadelphia, p. 502-46, 1984.

2. Cohn PF, ed, Diagnosis and Therapy of Coronary Artery Disease, Martinus Nijhoff Publishing Co, 1985.

3. Cohen LS, Results of Coronary Bypass Surgery, Ann Rev Med, 38:457-65, 1987.

4. Vlietstra RE, Holmes DR Jr, Percutaneous Transluminal Coronary Angioplasty, FA Davis Co, 1987.

5. Potkin BN, Roberts WC, Effects of Percutaneous Transluminal Coronary Angioplasty on Atherosclerotic Plaques and Relation of Plaque Composition and Arterial Size to Outcome, Am J Cardiol, 62:41-50, 1988.

6. Litvack F, Grundfest WS, Papaioannou T, Mohr FW, Jakubowski AT, Forrester JS, Role of Laser and Thermal Ablation Devices in the Treatment of Vascular Diseases, Am J Cardiol, 61:81G-86G, 1988.

7. Abela GS, Laser Arterial Recanalization: A Current Perspective, J Am Coll Cardiol, 12:103-5, 1988.

8. Gerrity RG, Loop FD, Golding LA, et al, Arterial Response of Laser Operation for Removal of Atherosclerotic Plaques, J Thorac Cardiovasc Surg, 85:409-21, 1985.

9. Sanborn TA, Laser Angioplasty, What has Been Learned from Experimental Studies and Clinical Trials?, Circulation, 78:769-74, 1988.

10. Marcus ML, Harrison DG, White CW, McPherson DD, Wilson RF, Kerber RE, Assessing the Physiologic Significance of Coronary Obstructions in Patients: Importance of Diffuse Undetected Atherosclerosis, Progress in Cardiovascular Diseases, 31:39-56, 1988.

11. Izatt JA, Albagli D, Itzkan I, Feld MS, Pulsed Laser Ablation of Calcified Tissue: Physical Mechanisms and Fundamental Parameters, Proc. of SPIE O/E Laser, in press, 1990.

12. Personal communication, M. Fitzmaurice, MD, Department of Pathology, Cleveland Clinic Foundation, Cleveland, OH, 1989.

13. Moore S, ed, Vascular Injury and Atherosclerosis, Marcel Dekker, New York, 1981.

14. Steinberg DS, Metabolism of Lipoproteins and Their Role in the Pathogenesis of Atherosclerosis, Atherosclerosis Reviews 18:1-23, Raven Press Ltd, New York, 1988.

15. Ball RY, Carpenter KLH, Mitchinson MJ, What is the Significance of Ceroid in Human Atherosclerosis, Arch Pathol Lab Med, 111:1134-40, 1987.

16. Wolman M, Lipid Pigments (Chromolipids): Their Origin, Nature and Significance, Pathobiol Ann, 10:253-67, 1980.

17. Smith EB, Acid Glycosaminoglycans, Collagen and Elastin Content of Normal Artery, Fatty Streaks, and Plaques, in Wagner WD, Clarkson TB, ed, Arterial Mesenchyme and Arteriosclerosis, Plenum Press, New York, p. 125-39, 1974.

18. Gaton E, Wolman H, Macrophage Activation in the Prevention or Regression of Atherosclerosis, in Wolman M, ed, The Healing and Scarring of Atherosclerosis, Plenum Press, New York, P. 15-36, 1981.

19. Yu S, Calcification Processes in Atherosclerosis, in Wagner WD, Clarkson TB, ed, Arterial Mesenchyme and Arteriosclerosis, Plenum Press, New York, p. 403-25, 1974

20. Fujimoto D, Akiba K, Nakamura N, Isolation and Characterization of a Fluorescent Material in Bovine Achilles Tendon Collagen, Biochem Biophys Res Comm, 76:1124-29, 1977.

21. Deyl Z, Macek K, Adam M, Cikova V, Studies on the Chemical Nature of Elastin Fluorescence, Biochimica et Biophysica Acta, 625:248-54, 1980.

22. Chio KS, Keiss U, Fletcher B, Tappel AL, Peroxidation of Subcellular Organelles: Formation of Lipofuscinlike Fluorescent Pigments, Science, 166:1535, 1969.

23. Sohal RS, Assay of Lipofuscin/Ceroid Pigment *in vivo* During Aging, Methods in Enzymology, 105:484-87, 1984.

24. Kittrell C, Willet RL, de los Santos-Pacheo C, Ratliff NB, Kramer JR, Malk EG, Feld MS, Diagnosis of Fibrous Atherosclerosis using Fluorescence, Applied Optics, 24:2280-81, 1985.

25. Sartori M, Sauerbrey R, Kubodera S, Tittel F, Roberts R, Henry PD, Autofluorescence Maps of Atherosclerotic Human Arteries - A New Technique in Medical Imaging, IEEE Journal of Quantum Electronics, QE-23:1794-97, 1987.

26. Deckelbaum LI, Lam JK, Cabin HS, Soni Clubb K, Long MB, Discrimination of Normal and Atherosclerotic Aorta by Laser Induced Fluorescence, Lasers in Surgery and Medicine, 7:330-35, 1987.

27. Leon MB, Lu DY, Prevosti LG, Macy WW, Smith PD, Granovsky M, Bonner RF, Balaban RS, Human Arterial Surface Fluorescence: Atherosclerotic Plaque Identification and Effects of Laser Atheroma Ablation, JACC 12:94-102, 1988.

28. Deckelbaum LI, Laser Induced Fluorescence Spectroscopy, Seminar on Lasers in Biomedical Research, Wellman Laboratories, Mass. General Hospital, Boston, MA, Oct. 24, 1989

29. Laifer LI, O'Brien K, Stetz ML, Gindi GR, Garrand TJ, Deckelbaum LI, Biochemical Basis for the Difference Between Normal and Atherosclerotic Arterial Fluorescence, Circulation, 80:1893-1901, 1989.

30. Clarke RH, Isner JM, Gauthier T, Nakagawa K, Cerio F, Hanion E, Gaffney E, Rouse E, DeJesus S, Spectroscopic Characterization of Cardiovascular Tissue, Lasers in Surgery and Medicine, 8:45-59, 1988.

31. Baraga JJ, Ultra-Violet Laser Induced Fluorescence Spectroscopy of Normal and Atherosclerotic Human Artery Wall, MS Thesis, MIT, Dept. of Physics, December, 1989.

32. Cowan WC, Fluorescence Contour Mapping of Human Aorta, BS Thesis, MIT, Dept. of Physics, May, 1988.

33. Keijzer M, Richards-Kortum R, Jacques SL, Feld MS, Fluorescence Spectroscopy of Turbid Media: Autofluorescence of Human Aorta, Applied Optics, 28:4286-92, 1989.

34. Izatt JA, Albagli D, Rava RP, Itzkan I, Feld MS, Wavelength Study of Pulsed Laser Ablation of Calcified Tissues, in preparation, 1990.

35. Fitzmaurice M, Bordagaray G, Engelmann G, Richards-Kortum R, Kolubayev T, Feld MS, Ratliff NB, Kramer JR, Argon Ion Laser Induced Autofluorescence in Normal and Atherosclerotic Aorta and Coronary Artery: Morphologic Studies, American Heart Journal, 118:1028, 1989.

36. Cothren RM, Kolubayev T, Kjellstrom BT, Richards-Kortum RR, Healey B, Ratliff N, Engelmann G, Loop F, Kramer JR, Kittrell C, Feld MS, Argon Ion Laser Induced Tissue Fluorescence: Clinical Spectroscopic Studies, 1988 Proceedings of the SPIE Symposium on Medical Applications of Lasers, Fiber Optics, and Electro-Optics..

37. Richards-Kortum R, Mehta A, Hayes G, Cothren R, Kolubayev T, Kittrell C, Ratliff NB, Kramer JR, Feld MS, Spectral Diagnosis of Atherosclerosis Using an Optical Fiber Laser Catheter, Am Heart Journal 118:381-91, 1989.

38. Verbundt RJAM, Cothren RM, Fitzmaurice M, Ratliff NB, Kittrell C, Taroni P, Baraga JJ, Feld MS, Kramer JR, UV Laser Induced Auto-Fluorescence of Ceroid Deposits and Other Structures in Atherosclerotic Plaques as a Potential Diagnostic for Laser Angiosurgery, submitted, Am Heart J, 1990.

39. Van Assendelft OW, Spectrophotometry of Haemoglobin Derivatives, Royal Van-Gorcum Ltd., 1970.

40. Campbell ID, Dwek RA, Biological Spectroscopy, The Benjamin Cummings Publishing Co, Menlo Park, CA, 1984.

41. Stryer L, Connective Tissue Proteins: Collagen, Elastin and Proteoglycans, Chapter 9 in Biochemistry, WH Freeman And Co., San Francisco, p. 185-204, 1981.

42. Mitchinson MJ, Hotherall DC, Brooks PN, DeBurbure CY, The Distribution of Ceroid in Human Atherosclerosis, J Pathol 45:177, 1985.

43. Richards-Kortum R, Understanding Laser Induced Fluorescence of Human Artery Wall with Applications to Diagnosis of Atherosclerosis, SM Thesis, Dept. of Physics, Massachusetts Institute of Technology, Cambridge, MA, 1987.

44. Cothren RM, Kolubayev T, Kjellstrom BJ, Richards-Kortum RR, Healy B, Ratliff NB, Engelmann G, Loop F, Kramer JR, Kittrell C, Feld MS, Argon Ion Laser Induced Fluorescence: Clinical Spectroscopic Studies, in Proc. SPIE Symp Med Appl Lasers, Fiber Optics, Electro-Optics, 1988.

45. Gijsbers GHM, Breederveld D, Van Gemert MJC, Boon TA, Langelaar J, Rettschnick RPH, *In Vivo* Fluorescence Excitation and Emission Spectra of Hematoporphyrin Derivative, Laser Life Sci 1:29, 1986.

46. Bourke GJ, Daly LE, McGilvray J, Interpretation and Uses of Medical Statistics, Blackwell, Oxford, 1985.

47. Shekhonin BV, Domogatsky SP, Idelson GL, Koteliansky VE, Rukosuev VS, Relative Distribution of Fibronectin and Type I, III, IV, V Collagens in Normal and Atherosclerotic Intima of Human Arteries, Atherosclerosis, 9:67, 1987.

48. Johnson NL, Kotz S, Distributions in Statistics, Houghton Mifflin, Boston, MA, 1970.

49. Harris EK, Albert A, Multivariate Interpretation of Clinical Laboratory Data, Decker, New York, 1987.

50. Kolubayev T, Kjellstrom T, Cothren RM, Richards-Kortum RR, Healy B, Ratliff NB, Engelmann G, Loop F, Kramer JR, Kittrell C, Feld MS, Argon Ion Laser Induced Tissue Fluorescence: Clinical Spectroscopic Studies, presented at SPIE Symposium on Medical Applications of Lasers, Fiber Optics, and Electro-Optics, Los Angeles, January, 1988.

51. Cothren R, *In Vivo* Mapping of Human Atherosclerotic Lesions Using LIF Spectroscopy, presented at SPIE Symposium on Lasers in Medicine, Snowbird UT, January, 1989.

4: Spectroscopic Identification of Dysplasia in the Gastro-Intestinal Tract

This chapter is devoted to the problem of developing a spectroscopic diagnostic algorithm for colo-rectal dysplasia, a histologic precursor to colo-rectal carcinoma. If detected, colonic dysplasia implies an individual is at higher risk for the development of colon cancer. Depending on the setting, colonic dysplasia can be treated, either by local removal of dysplastic tissue or by total colectomy. Thus, through vigorous screening programs it should be possible to significantly reduce the incidence of colon cancer. Current methods of screening are capable only of detecting certain forms of dysplasia which are accompanied by alterations in the gross architecture of the mucosa. Potentially, fluorescence spectroscopy could provide a means of detecting dysplasia based on chemical and histologic changes, greatly improving the utility of such screening methods.

The relationship of dysplasia to carcinoma in the gastro-intestinal tract will first be reviewed; the pathology of these conditions and their clinical relevance will be emphasized. A review of the small literature describing attempts to utilize fluorescence to diagnose colonic dysplasia will be given. Our approach to this problem will then be presented. The specific clinical applications of this work will be described and model tissue systems used to study dysplastic colon *in vivo* and *in vitro* will be detailed. Our initial results in these studies will be discussed, with particular emphasis given to their implications for achieving our ultimate clinical goal.

4:1: Colonic Neoplasia and Dysplasia

4:1.1: Clinical Issues

Colo-rectal cancer was responsible for approximately 60,000 deaths in the United States in 1986, second only to lung cancer [1]. Early detection of colo-rectal carcinoma greatly facilitates achieving curative surgical therapy. Table 1 shows that the 5-year survival rate associated with colo-rectal carcinoma decreases dramatically for increasingly invasive disease [2]. These statistics suggest that improving methods of early detection of carcinoma could play an important role in decreasing the mortality associated with colo-rectal carcinoma.

Table 1: Classification of carcinoma of the colon and its prognostic significance. Adapted from [3].

% 5-Year Survival	Stage of Neoplasm
100.0	Limited to mucosa
66.6	Extending into muscularis propria but not penetrating through it, uninvolved nodes
53.9	Through entire wall, uninvolved nodes
42.8	Limited to the wall, involved nodes
22.4	Through entire wall, involved nodes

There is evidence to suggest that, in the general population, mos. colo-rectal carcinomas develop from precursor benign colonic neoplasms [3]. It has been shown that excision of benign colonic neoplasms can reduce the ultimate incidence of colo-rectal carcinoma [4]. This suggests that developing techniques to detect early colonic neoplasia would provide a method of reducing both incidence and mortality of colo-rectal carcinoma. Indeed, such screening methods would be beneficial; in the United States, currently the cumulative lifetime probability of developing colon cancer is roughly 6%, the corresponding probability of dying from colon cancer is 3% [5].

The symptoms of colonic neoplasia can include rectal bleeding, changes in bowel habits, anemia due to chronic bleeding, vague abdominal pain and, in some cases, intestinal obstruction [3, 6]. However, colo-rectal neoplasia can be present for a considerable time before symptoms develop [3]. When present, they are often indicative of advanced, malignant disease. As a result, the presence of symptoms cannot be used to screen effectively for colonic neoplasia, and many attempts have been made to develop methods for detecting neoplasms at an earlier, more curable, stage.

Several quite simple and effective methods for detecting individuals with colo-rectal neoplasia exist [7, 8]. The American Cancer Society recommends that individuals over the age of 40 receive regular screening for the disease by digital rectal examination, guaiac stool examination for occult blood and procto-sigmoidoscopy [1]. Guaiac stool examination consists of performing a colorimetric chemical reaction with a small stool sample to test for the presence of small amounts of hemoglobin undetectable visually [8]. The positive predictive value of this test for colo-rectal neoplasia is almost 50%; however,

4:1.2: Pathogenesis of Colo-Rectal Cancer

To understand the pathogenesis of colo-rectal cancer, it is first necessary to consider the structure and function of the normal colon.

4:1.2.1: Normal Colon: Structure and Function

The colon in man is not essential for life, functioning mainly as a storage and absorptive organ [3]. Its main absorptive function is to resorb water; however, it also has a secretory function, secreting mucin into the lumen [12]. The colon is a layered organ, and absorption and secretion occur across the epithelial layer, the mucosa. These layers are depicted in Figure 1.

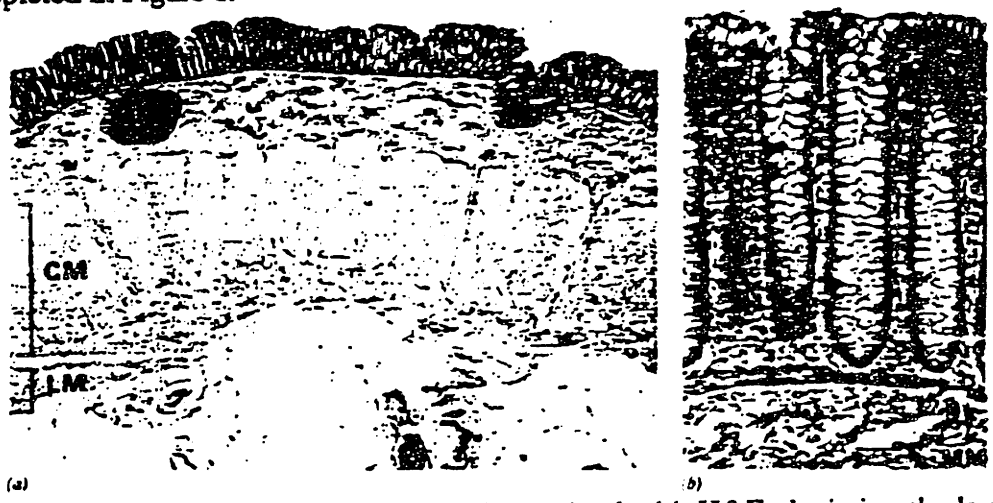

Figure 1: Histologic section of normal colon stained with H&E, depicting the layers of the bowel. In (a) the inner circular layer of muscle is labeled CM, and the outer, longitudinal layer is labeled LM. In (b) the muscularis mucosa is labeled MM. Adapted from [14].

The mucosa consists of tubular crypts, lined by absorptive cells and mucin containing goblet cells [12]. The lamina propria is a delicate connective tissue, found within the mucosa, between the crypts [13]. The lamina propria is vascularized, and a host of inflammatory cells are regularly found within it [3, 13]. These include plasma cells, lymphocytes, and occasionally mast cells, eosinophils and histiocytes [13]. Lymphocytes and histiocytes are more prominent in the superficial aspects of the lamina propria [5, 13]. The mucosa is situated atop a thin layer of smooth muscle, known as the muscularis mucosa [14]. Beneath this layer of tissue is the submucosa, a layer of connective tissue, containing mostly collagen and some small vascular structures [14]. The bulk of the bowel wall is made up of two layers of smooth muscle, the inner and outer muscularis propria [12]. The inner muscularis propria is made up circularly

in 35-50% of known cancer patients, the stool guaiac test is falsely negative [5]. In procto-sigmoidoscopy, a rigid fiber optic endoscope is used to visualize the interior of the rectum and sigmoid colon with reflected white light. This procedure is effective for detection of only 25-50% of colo-rectal neoplasms, the proportion of all colo-rectal neoplasms found in the rectum or distal sigmoid colon [5, 7].

In a symptomatic patient, or one in which an aforementioned screening procedure has indicated the possible presence of neoplasia, more extensive diagnostic studies must be carried out [9]. These include contrast radiographic studies [10], to visualize the lumen of the colon, and colonoscopy [11], in which a flexible fiber optic endoscope is used to visualize the entire lumen of the colon with reflected white light. Both these screening methods detect the presence of neoplasia based on alterations it produces in the architecture or gross morphology of the bowel wall. Comparison of colonoscopy and double contrast barium enema in patients with polyps has shown a 90% specificity of endoscopy and a 70% specificity of barium enema for the detection of lesions 7 mm or more in diameter [11]. Diagnosis of smaller lesions is extremely difficult on barium enema, while endoscopy likely misses 20-30% of 2-5 mm diameter polyps, particularly when attention is focused on removal of larger lesions [11]. Although these techniques can identify very small colonic neoplasms based on gross architectural changes, they cannot be used to differentiate benign neoplasms from malignancies. As the therapeutic and prognostic implications of these lesions are very different, it is necessary to investigate the microscopic histology of neoplasms detected with these techniques [6]. This is usually accomplished with colonoscopically directed biopsy [11].

These more extensive screening methods detect early disease more effectively than the simpler methods described above; thus, it has been suggested that they be used more widely to screen for the presence of disease in asymptomatic patients [5, 6]. It is generally accepted that contrast radiographic studies to visualize the lumen of the colon are too expensive for wide spread screening of colo-rectal carcinoma [6]. Colonoscopy, on the other hand, has been suggested as a wide scale method of screening for colo-rectal carcinoma in individuals over the age of 50. However, more studies are needed to evaluate the cost/benefit ratio of this procedure [5].

To understand the strengths and limitations of these screening and diagnostic methods in various clinical settings, it is necessary to consider what is known about the pathogenesis of colo-rectal cancer in more detail.

arranged fibers of smooth muscle cells. The outer muscularis propria consists of longitudinally arranged smooth muscle fibers. These smooth muscle fibers provide peristaltic contractions within the large intestine. The adventitia, made up of loose connective tissue, is the outer layer of the colon. Nests of ganglion cells, providing the innervation of the colon, are found within the submucosa and between the circular and longitudinal muscle layers [3].

4:1.2.2: Colo-Rectal Carcinoma

Almost all cancers in the large intestine are carcinomas, cancers of epithelial cell origin. 95% of these are adeno-carcinomas, so classified because they demonstrate microscopically a glandular growth pattern [3]. About 75% of colo-rectal carcinomas are located in the rectum, recto-sigmoid or sigmoid colon. The remainder are fairly even distributed throughout the colon [3].

All colo-rectal carcinomas begin as in situ lesions, confined to the mucosal layer of the bowel [3]. If not discovered and treated, they eventually invade adjacent layers, and metastasize, primarily through lymphatics and blood vessels [3]. Upon discovery, most colo-rectal carcinomas have one of two gross morphologies, depending on their location in the colon. Carcinomas of the left, or ascending, colon tend to grow in an annular encircling fashion, producing constriction of the bowel and the early symptoms of obstruction [3]. Lesions of the right colon tend to grow as polypoid masses that extend along the cecum and the ascending colon. Because these lesions occur near the cecum, obstruction of the bowel due to carcinoma of the right colon is uncommon [3].

Early lesions of the left side begin as small elevated lesions, which extend circumferentially to encircle the bowel wall [3]. The neoplasm tends to remain superficial for a long time; however, eventually the deeper layers of the wall are slowly invaded. Cancers in the right colon also begin as small elevated lesions, but progressively assume a polypoid appearance. They frequently become large, irregular, bulky masses, which protrude into the lumen. These lesions eventually penetrate the wall of the colon as well [3]. For both types of lesions, in general, there is a sharp division between the carcinoma and the adjacent normal bowel wall [6].

The microscopic characteristics of right and left sided colonic carcinomas are similar. Most are adeno-carcinomas, many of which secrete mucin [3]. Usually, the adenocarcinoma of the bowel is well to moderately differentiated [6]. The most common cells found within the carcinoma are columnar and goblet cells [6]. Malignant cells are

characterized by anaplasia, pleomorphism, hyperchromatic nuclei, disproportionately large nuclei, large numbers of mitoses, and occasional atypical mitotic figures [3]. The carcinoma elicits a host inflammatory reaction; most inflammatory cells present within the carcinoma are T lymphocytes [15]. Some colon carcinomas have been noted to contain large numbers of eosinophils [15]. The presence of eosinophils has been shown to be of prognostic significance [15]. In one study, the proportion (3 of 15, 20%) of carcinomas with > 10 eosinophils/mm^2 that had metastases was significantly less ($p = 0.01$) than the proportion (8 of 11, 73%) of carcinomas with < 10 eosinophils/mm^2 that had metastases [15]. In addition, the concentration of eosinophils was noted to be significantly lower in the tumor margins in tumors with > 10 eosinophils/mm^2.

In addition, connective tissue proliferation, or tumor desmoplasia is present, most prominently at the tumor border [6]. There is usually good correspondence between the gross and microscopic tumor margins [6]. The edge of the tumor may also demonstrate pre-malignant neoplastic changes or hyperplastic changes [6].

4:1.2.3: Adenoma-Carcinoma Sequence

Even more common than colonic carcinoma are benign neoplasms of the colon. The great majority of these are epithelial polyps, present in as many as 20-50% of older adults [3, 6]. Many of these polyps are hyperplastic, not truly regarded as neoplasms, as they are believed to represent benign controlled proliferations of mucosa [3]. However, a certain portion of epithelial polyps are true neoplasms [3]. These are referred to as adenomatous polyps, and are important because they are recognized as a precursor to the development of colo-rectal adenocarcinoma [3, 6, 16]. About 90% of epithelial polyps are hyperplastic; however, they rarely cause symptoms of colonic neoplasia and are of little clinical concern, and thus account for only 15-20% of epithelial polyps surgically removed [3]. The remainder of epithelial polyps are adenomas, and are subclassified into three types based on their microscopic histologic features.

Tubular adenomas account for about 75% of all adenomatous polyps [3]. They are found in 30-35% of older adults [6], mainly in the left colon [3,6]. Most tubular adenomas do not produce symptoms [6]. Macroscopically, these adenomas have slender stalks with slightly enlarged tips; the heads range in size from a few mm in diameter to more than several cm [3]. Microscopically, the center of the polyp consists of a central core of vascularized fibrous tissue that arises in the submucosa [3]. The stalk is covered with normal colonic mucosa, but the head of the polyp contains a thickened mucosa with

poorly differentiated or dysplastic epithelial cells [3]. Here, the mucosa appears crowded, and the number of cells and glands per unit area is increased [6]. There is little connective tissue between glands in the neoplastic mucosa [3]. The nuclear to cytoplasm ratio of the neoplastic cells is increased, and nuclei contain an abundance of chromatin [3, 6]. Mitotic figures are more numerous and sometimes atypical in these cells [3].

A true tubular adenoma is a benign lesion, and no epithelial cells penetrate the fibrovascular core [3]. Tubular adenomas less than 1 cm in diameter have a 1% chance of containing a focus of cancer, which in many instances has not penetrated the muscularis mucosa [3]. In those lesions 1-2 cm in diameter, the risk of cancer rises to 5-10% [3].

The least common of adenomatous polyps are villous adenomas, which represent 10-15% of all adenomas [3]. Villous adenomas are most likely to be symptomatic, frequently causing rectal bleeding [3]; however, these lesions are often quite soft and cannot be palpated on digital rectal exam [6]. Villous adenomas are most common in the left colon, and are more clustered in the recto-sigmoid colon than are tubular adenomas [3]. They range in size from less than 1 cm to 8-10 cm in diameter [3]. Unlike tubular adenomas, they do not have a well defined stalk, but are broad slightly lobular lesions [3, 6]. Histologically, villous adenomas are characterized by broad, finger-like papillae covered by adenomatous epithelium occupying at least 50% of the adenoma [3, 6]. The residual portion of the polyps often histologically resembles tubular adenomas [3]. The villous proportion of the adenoma correlates almost linearly with the size of the adenoma [3]. Each papilla consists of a fibrovascular core with a covering of dysplastic epithelial cells [3]. About 10% of villous adenomas harbor carcinoma in situ, frank invasive carcinoma is present in about 25-40% of villous adenomas [3].

Tubulovillous adenomas are adenomatous polyps with both tubular and villous components [3]. By definition, the villous portion of a tubulovillous adenoma ranges from 25-50% [3]. These lesions are most common in the left colon, distributed similarly to tubular adenomas, and range in size from .5 to 5 cm in diameter [3]. Most tubulovillous adenomas have a stalk and cannot be macroscopically differentiated from tubular adenomas [3].

Thus, the significance of an epithelial polyp depends on its microscopic features. Hyperplastic polyps are not believed to have malignant potential [6]. On the other hand, all adenomatous polyps are true neoplasms and have malignant potential [3]. This malignant potential increases both with the size and the villous proportion of the adenoma

[3, 6]. There is much evidence to suggest that epithelial polyps are directly related to the formation of colo-rectal adenocarcinoma [3]. This process is viewed by many as a biologic sequence, beginning with benign controlled hyperplasia, then passing progressively through the stages of uncontrolled growth as a tubular and then as a villous adenoma, culminating with the development of carcinoma [3]. This process has been termed the adenoma-carcinoma sequence [16].

By comparing the incidence rates of adenomatous polyps and colo-rectal carcinoma, it is clear that not all adenomatous polyps become malignant during the normal life span of an individual [6]. Furthermore, there is some evidence to suggest that not all colo-rectal cancers arise in pre-existing polyps, arising instead in flat colonic mucosa [6, 17].

However, because of their association with colo-rectal carcinoma, it is currently recommended that all polyps be removed by polypectomy at endoscopy. Experienced endoscopists cannot reliably differentiate between hyperplastic polyps and the various categories of adenomatous polyps [18]. Therefore, after removal, it is important to histologically document the degree of cellular atypia present in the lesion. If no carcinoma is found within the polyp, then further treatment consists of follow up endoscopy at one year. The incidence of repeat polyp formation is about 30% [6]. If an area of carcinoma is found, the therapeutic approach depends on its extent. For carcinoma in situ, in which the malignant cells are confined to the mucosa, polypectomy is sufficient [6]. Focal carcinoma, in which the malignant cells have invaded the muscularis mucosa, but not the stalk of the polyp, is associated with a very slight risk of lymph node metastasis, and again polypectomy is regarded as appropriate therapy [6]. However, in cases where the carcinoma had invaded the stalk of the polyp, the possibility of lymph node metastasis is high enough to justify formal bowel resection [6]. The standard treatment for adenomatous polyps is polypectomy at colonoscopy [6, 11]. In all cases, repeat endoscopy is performed 1 year later [6].

Thus, in the general population, epithelial polyps provide a method of detecting individuals at greater risk for developing colo-rectal carcinoma. By screening for this condition with sigmoidoscopy and colonoscopy, it is possible to remove colonic neoplasms in a pre-malignant stage, thus reducing the ultimate incidence of carcinoma.

4:1.2.4: Dysplasia and Mucosal Ulcerative Colitis

Because colonoscopy relies on largely architectural changes to identify potentially neoplastic mucosa for biopsy, it is less sensitive in clinical situations wherein neoplastic changes are flat, or the normal architecture of the non-neoplastic mucosa has been disrupted. Mucosal ulcerative colitis is a clinically relevant example of this type of situation [3].

Mucosal ulcerative colitis (MUC) is a recurrent ulcero-inflammatory disorder, affecting the mucosa of the rectum and colon [3]. Symptomatically, the disease is characterized by attacks of bloody, mucoid diarrhea, accompanied by crampy, lower abdominal pain [3]. In the United Sates, the incidence of this disease is between 4 and 6 per 100,000 population [3]. Patients with MUC have a much greater risk of developing carcinoma of the large bowel than does the general population [3, 19]. The estimated risk varies somewhat, but cumulative rates as high as 60% at 30 years have been reported, ten times as high as that for the general population [19-22]. Because of this dramatically increased risk of developing carcinoma, prophylactic colectomy with colostomy or continent pouch has been advocated for all patients with extensive long-standing MUC [23, 24]. However, this surgery is not without risk. The death rate for elective colectomy is low, but deaths do occur. Removal of the rectum can result in sexual dysfunction in both men and women [25]. Many patients, particularly those without severe, chronic symptoms of MUC, find it difficult to accept surgery as a means of preventing cancer [24].

Although the risk of ultimately developing colo-rectal carcinoma in long-standing MUC patients is high, it is by no means a certain outcome. Thus, a screening method capable of identifying those MUC patients at most risk for the development of carcinoma would be helpful in assessing the need for colectomy for an individual MUC patient. If an effective screening method could be developed, then colectomy could be safely restricted to the proportion of MUC patients who will ultimately develop cancer, and the remaining patients could be spared this extreme procedure.

A consideration of the pathology of MUC and associated carcinoma suggests that an effective screening method might be developed based on the pre-malignant neoplastic changes (dysplasia) which are known to precede the development of carcinoma in MUC.

Ulcerative colitis begins in the rectal mucosa and spreads continuously throughout the remainder of the colon [3]. Acute and chronic phases of MUC are recognized [3]. In

acute MUC, the mucosa shows the typical signs of inflammation: edema, hyperemia, and a prominent infiltrate of inflammatory cells, including neutrophils, lymphocytes, plasma cells and occasional mast cells [3]. Small focal hemorrhages may develop in the mucosa during the acute phase [3]. These may ultimately give rise to small ulcerations of the mucosa [3]. In some cases, these small ulcers can enlarge and coalesce, virtually destroying the mucosa. Small remaining pieces of edematous mucosa remaining are referred to as pseudopolyps [3]. Mucosal degeneration is often followed by mucosal repair, and in chronic MUC, the fibrosis associated with repair may lead to shortening of the bowel and thickening of the bowel wall [3].

In some cases, cytologic abnormalities are present in the inflamed epithelium, pseudopolyps, or even in uninflamed mucosa, distant from the site of active disease [3]. Microscopically, these abnormalities are quite similar to those associated with neoplasia and can include nuclear hyperchromasia, and an increased nuclear to cytoplasm ratio, increased mitoses and abnormal mitotic figures [3]. These abnormalities vary in severity, and are described as low and high grade dysplasia, or overt carcinoma [3]. It is known that the incidence of colonic carcinoma is particularly high in MUC patients with epithelial dysplasia [26]. Therefore, it has been suggested that the development of carcinoma in patients with MUC also can be viewed as a biologic sequence, beginning with the hyperplasia of repair, progressing in some cases through low and high grade dysplasia, and in some cases culminating in the formation of carcinoma [27].

The similarity of this process to the adenoma-carcinoma sequence suggests that perhaps similar colonoscopic screening methods could be used to detect the pre-malignant changes of dysplasia, or carcinoma in situ in MUC patients. However, the architectural changes associated with adenomatous polyp formation are not present in the dysplastic epithelium of MUC. In addition, the inflammation process in this disease significantly disrupts the normal architecture of the colonic mucosa. These two factors make it considerably more difficult to recognize dysplastic mucosa in MUC through the colonoscope [11]. Thus, current screening programs for dysplasia and CIS in MUC consist of regular colonoscopic examination supplemented by selected mucosal biopsy [11, 20, 28]. If pre-malignant or malignant changes are found, based on the likelihood of developing colo-rectal carcinoma, the physician recommends colectomy.

Surveillance colonoscopy with biopsy has a number of limitations, the most important of which is that participation does not guarantee that the presence of a lethal cancer will be detected [20]. In one series, carcinoma developed in 13 of 186 patients

with a history of disease for ten years or more despite regular colonoscopic surveillance [29]. A major contributing factor to these surveillance failures is the fact that carcinoma and dysplasia do not often cause grossly observable lesions at endoscopy. This coupled with the fact that dysplasia and carcinoma foci can be very small, can lead to tremendous sampling error [28, 30, 31].

Thus, because of limitations in current methods of screening for colo-rectal dysplasia, the ideal result, the prevention of cancer and restriction of operations to patients with demonstrated precancer, has not been realized. Spectroscopic diagnosis of dysplasia has the potential to reduce the sampling error associated with colonoscopy and biopsy, both through better direction of biopsy placement and by allowing the entire surface area of the colon to be screened for dysplasia. This will be of immense practical value in the management of patients with MUC.

4:1.3: Review of GI Tissue Fluorescence Literature

Preliminary results have suggested that, *in vitro*, the fluorescence properties of normal and neoplastic human colon are significantly different. Kapadia has shown that, with 325 nm excitation, an empirical analysis of fluorescence emission spectra can be used to differentiate normal tissue and hyperplastic polyps from adenomatous polyps with an overall accuracy rate of 92% *in vitro* [32]. Yakshe has shown that UV excited fluorescence emission spectra of normal and cancerous human colon obtained *in vitro* are significantly different in the emission region 375-645 nm [33]. With 325 or 337 nm excitation, they reported that the fluorescence spectra of normal colonic mucosa consisted of a broad peak between 400 and 450 nm. The fluorescence spectra of homogeneous epithelial tumors showed a weak peak at 450 nm, while tumors with significant desmoplasia or muscle invasion demonstrated a more intense peak at 400 nm. Based on the differences observed in the fluorescence spectra of architecturally different cancers, they suggested variations in colonic fluorescence spectra are likely due to differences in tissue architecture.

Fluorescence spectroscopy may thus provide a method of improving current screening methods for colonic dysplasia and CIS. These preliminary results suggest that fluorescence can detect some of the changes which accompany neoplastic transformation in the colon. In addition, it has been demonstrated that currently existing endoscopes can be modified, to obtain both reflected white light images of the colon and images based on tissue fluorescence [34]. In particular, if fluorescence spectroscopy could be used to

detect pre-malignant changes based on their histologic and biochemical features, it potentially could greatly enhance the use of screening colonoscopy, which currently relies largely on architectural changes to detect neoplastic transformations.

The combination of fluorescence with traditional colonoscopy could be greatly beneficial in the detection of colonic neoplasia. In the general population, it could potentially allow endoscopists to screen for flat dysplasia and possibly eliminate the need for biopsy in evaluating the significance of epithelial polyps. More significantly, in MUC patients, the technique could be greatly useful in improving screening methods for dysplasia and CIS, reducing the sampling error associated with colonoscopically directed biopsy, by allowing the entire surface area of the colon to be screened, and either better directing biopsy placement or ultimately eliminating of the need for biopsy.

4:2: Clinical Problems Addressed by This Work

4:2.1: Ultimate Goal: Flat Dysplasia in Ulcerative Colitis

This chapter presents basic spectroscopic studies of normal and neoplastic colon, designed to achieve an algorithm capable of detecting colonic dysplasia or CIS based on its histologic or biochemical features. As discussed in the previous section, a significant application of this algorithm would be to improve screening methods for dysplasia and CIS in MUC patients. Our work will be discussed primarily in terms of achieving this objective.

4:2.2: Model Systems Used to Achieve Ultimate Goal

In order to achieve this goal, it is necessary to obtain samples of normal and neoplastic colon for study both *in vitro* and *in vivo*. Obviously, in obtaining these samples, patient care cannot be compromised. We have selected three model systems in which this can be accomplished. The first model system, familial adenomatous polyposis, allows the study of neoplastic and normal colon *in vitro*. The second system, sporadic adenomatous polyps, allows the study of normal and neoplastic colon *in vivo*. The third system, MUC, was used to study dysplastic and non-neoplastic colon in this disease both *in vivo* and *in vitro*. These systems and the rationale for selecting them will be described in more detail here. Their relationship to achieving our final goal is shown schematically in Fig. 2.

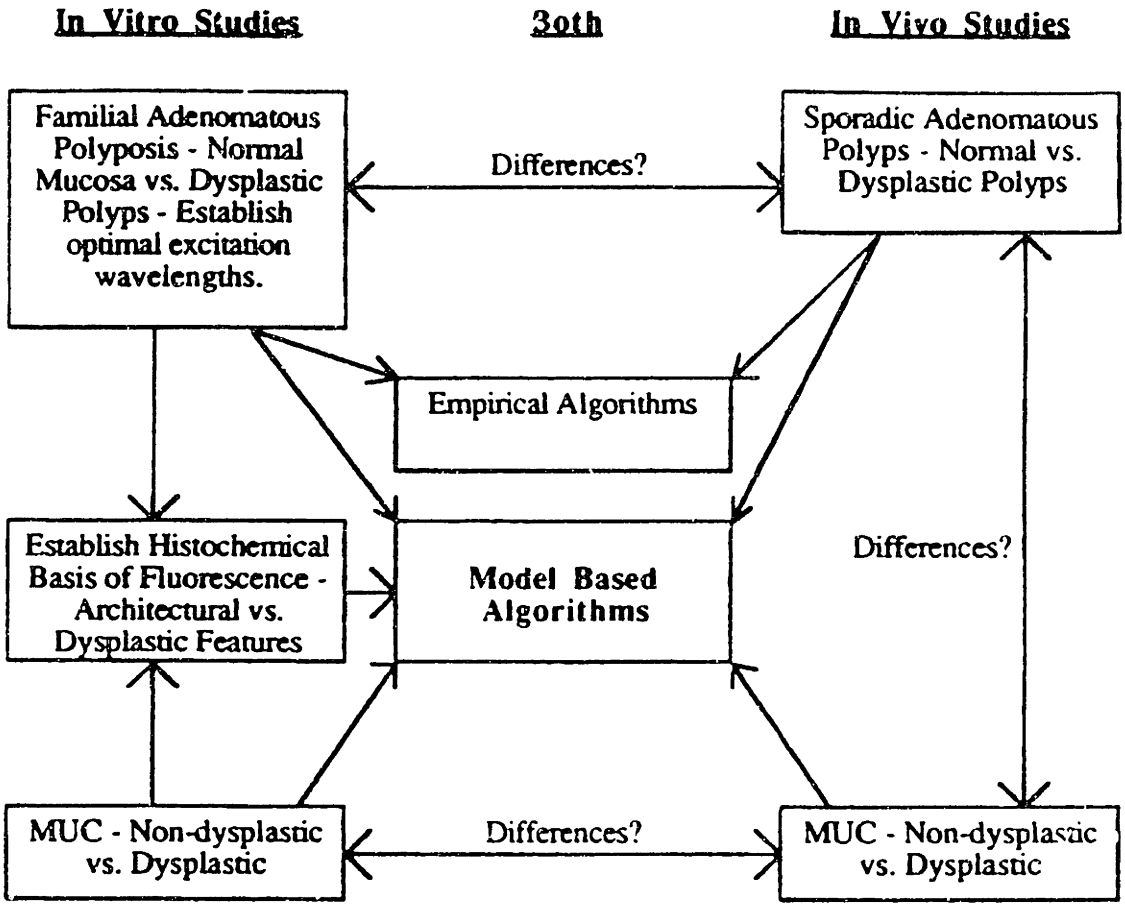

Figure 2: Model systems of normal and dysplastic colon studied *in vitro* and *in vivo* to develop a spectroscopic diagnostic algorithm for dysplasia in MUC.

4:2.2.1: *In Vitro*: Polyposis Model

Our ultimate goal is to use fluorescence spectroscopy to differentiate flat dysplastic mucosa from non-dysplastic mucosa in the face of MUC. However, as has been noted previously, non-dysplastic MUC is an extremely heterogeneous tissue. In addition, obtaining samples of flat dysplastic mucosa is a difficult problem, largely because of problems in recognizing this tissue with current screening methods. Therefore, in approaching our ultimate goal, we first studied a simpler problem - that of using fluorescence spectroscopy to differentiate neoplastic epithelial polyps from normal colon *in vitro*. In studying this model system our hope was to establish the fluorescence properties which characterize normal colon and neoplastic epithelial polyps, determine the histologic and chemical basis of this fluorescence, and assess how accurately

fluorescence based algorithms could be used to differentiate these tissues. These goals were accomplished following the methods outlined in Chapter One.

Only two choices of specimens exist for *in vitro* studies of adenomatous polyps: colectomy specimens from patients with sporadic adenomas or patients with familial adenomatous polyposis, a genetic disorder in which the colon is covered with hundreds of tubular adenomatous polyps [3]. Colectomy specimens from patients with sporadic adenomas cannot be studied without compromising patient care because every adenoma in such specimens is examined histologically to rule out carcinoma. However, colectomy specimens from adenomatous polyposis patients can be studied without compromising patient care because the polyps are too numerous for each adenoma to be studied histologically. Therefore, we have chosen familial adenomatous polyposis as our *in vitro* model. In terms of our ultimate goal, this model is a particularly good choice for study, as the dysplasia associated with tubular adenomas in familial adenomatous polyposis is histologically indistinguishable from that associated with dysplasia in MUC [35].

A limitation of this model is that paired adenomatous and normal tissues from the same patient cannot always be obtained. Frequently in familial polyposis, the surface of the colon is completely covered with adenomatous polyps. Whenever possible, we have attempted to obtain matched adenomatous and normal colon samples; however, in some cases samples of normal colon were obtained from resection specimens of patients with colonic adenocarcinoma or diverticular disease.

4:2.2.2: *In Vivo*: Adenomatous Polyp Model

Because our ultimate application of this technique will be carried out *in vivo*, our second model system was one in which the fluorescence properties of neoplastic and normal colon could be studied *in vivo*. The goals of this study were twofold: 1) to show that fluorescence spectra of colon with good S/N could be collected *in vivo* during colonoscopy in a reasonably short amount of time, and 2) to determine if there are any differences in the fluorescence spectra of these tissues *in vivo* and *in vitro*.

In this case, fluorescence spectra of sporadic adenomatous polyps were selected as a model system as they could be studied without compromising patient care, and paired normal controls could be obtained in every case. During colonoscopy, fluorescence emission spectra were collected from epithelial polyps and surrounding normal appearing areas of colonic mucosa in patients with a history of sporadic colonic polyps. Following

collection of spectra, polyps were removed in the usual fashion and submitted for histologic analysis. Biopsies were obtained from normal appearing areas of tissue and also submitted for histology.

Again, in terms of our ultimate goal, this model is a particularly good choice for study, as the dysplasia associated with sporadic adenomas is histologically indistinguishable from that associated with dysplasia in MUC [35].

4:2.2.3: *In Vitro* Ulcerative Colitis

Finally, studies of non-dysplastic tissue from resection specimens of patients with ulcerative colitis were carried out. The goal of these studies was to determine how the fluorescence properties of normal colonic mucosa differed from that of non-dysplastic MUC. This represents an important step, due to the extreme variability of the mucosal architecture in MUC.

In addition, it will also be necessary to determine how the fluorescence properties of flat dysplasia differ from those of adenomatous epithelial polyps. A preliminary assessment of this can be achieved by studying the histologic basis of the fluorescence of adenomatous polyps, to differentiate fluorescence associated with architectural structures such as connective tissue from that of dysplastic structures such as cytologically abnormal epithelial cells. However, in the end, the fluorescence properties of specimens of dysplastic MUC must be studied. Although these studies are not a part of this thesis, a plan for them will be presented in Chapter Six of this work. In addition, a plan for studying the fluorescence of dysplastic and non-dysplastic MUC *in vivo* will be detailed in Chapter Six.

With this introduction, we now turn to a discussion of our experimental results. Again, the procedures developed in Chapter One were applied to these model systems in an attempt to develop a diagnostic algorithm for dysplasia in MUC.

4:3: Survey of Spectroscopic Properties of Colon

The first step in our procedure is to compare the UV and visible fluorescence properties of normal and pathologic tissues to select excitation wavelengths optimal for the differentiation of these tissues. We again utilize fluorescence EEMs to achieve this goal. Results are presented here from *in vitro* studies of normal colon and adenomatous polyps as well as non-dysplastic MUC.

4:3.1: Fluorescence EEMs

4:3.1.1: Familial Adenomatous Polyposis

As a model of dysplasia accessible for *in vitro* studies, adenomatous polyps were obtained from resection specimens of patients with familial adenomatous polyposis. All adenomas studied were less than 5 mm in greatest cross dimension and most were 1-2 mm. Normal controls were obtained from uninvolved areas in resection specimens from patients with familial adenomatous polyposis, colonic adenocarcinoma or diverticular disease.

Full thickness samples of colon were snap frozen in liquid nitrogen and isopentane and stored at -70 ° C until study. The specimens were thawed at room temperature, kept moist with 140 mM buffered saline, pH 7.4, and mounted in a quartz cuvette for spectroscopic studies. Following study, the tissues were fixed in 4% formalin solution, paraffin embedded, cut into 4 μm thick sections, and stained with hematoxylin and eosin. The resultant slides were examined by a single gastrointestinal pathologist to verify that control tissues were histologically normal and that polyps selected macroscopically were adenomas.

Fluorescence EEMs were recorded for 15 colonic specimens (4 normal, 11 adenomas) from 8 patients; three of the normal samples were matched controls from patients with familial adenomatous polyposis, one was from a patient with colonic carcinoma or diverticular disease. EEMs were recorded using the method described for gastro-intestinal tissue in Chapter Two.

A complete characterization of the UV and visible fluorescence properties of normal and adenomatous colon tissue is presented in Figs. 3 and 4. Figure 3 shows a contour map representation of the average fluorescence EEM of four normal samples; Fig. 4 shows the same for an average of 11 adenomatous samples. Although fluorescence intensity is reported in arbitrary units, the same scale of units is used for both figures so meaningful intensity comparisons can be made between the two.

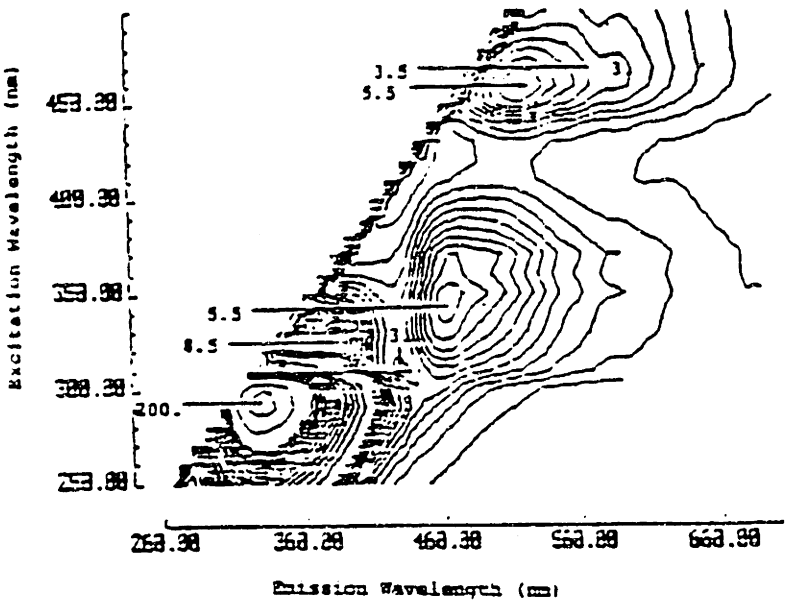

Figure 3: Average EEM of four normal human colon samples. Three sets of linearly spaced contours are shown: twenty from .5 to 10 units; eighteen from 15 to 100 units; and two from 150 to 200 units. Although fluorescence intensities are given in arbitrary units, the same scale of units is maintained throughout the paper.

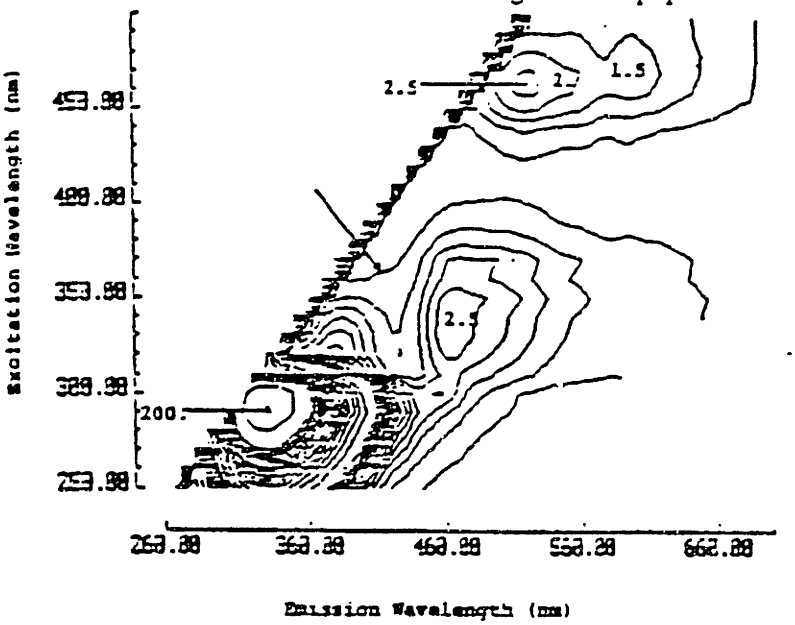

Figure 4: Average EEM of 11 adenomatous samples. Three sets of linearly spaced contours are shown: twenty from .5 to 10 units; eighteen from 15 to 100 units; and two from 150 to 200 units. Although fluorescence intensities are given in arbitrary units, the same scale of units is maintained throughout the paper.

Table 2 summarizes the excitation and emission maxima of the fluorescence peaks in the average fluorescence EEMs of normal and adenomatous tissues. Fluorescence intensities are given for each peak in our scale of arbitrary units. Both tissue types exhibit an intense fluorescence peak at $(\lambda_{exc}, \lambda_{em}) = (290, 330$ nm), which is similar in

lineshape and intensity. Both tissues also exhibit peaks of similar lineshape at or near (345, 465 nm), (460, 520 nm), (465, 555 nm) and (470, 595 nm). However, at each of these peaks, the fluorescence intensity of normal tissue is approximately twice that of adenomatous tissue. These peaks are separated by valleys which run parallel to the excitation and emission axes at 420, 540 and 580 nm. As will be shown later, these are due to attenuation of oxy-hemoglobin. In addition, the average EEM of normal tissue shows two unique peaks at (325, 385 nm) and (315, 430 nm).

Table 2: Excitation-Emission Maxima in the EEMs of Normal and Adenomatous Colon Tissue

(λ_{exc}, λ_{em}) Maxima	Fluorescence Intensity (Arbitrary Units)		Potential Fluorophore[a] (See Table 9)
	Normal	Adenoma	
(290, 330 nm)	200	200	Tryptophan
(325, 385 nm)	8.5	---	Pyridoxal 5'-phosphate, Collagen I, Collagen III
(315, 430 nm)	3.0	---	4-pyridoxic acid
(345, 465 nm)	5.5	2.5	NADH, NADPH
(460, 520 nm)	5.5	2.5	Pyridoxal 5'-phosphate, Elastin
(465, 555 nm)	3.5	2.0	Pyridoxal 5'-phosphate, Elastin
(470, 595 nm)	3.0	1.5	Pyridoxal 5'-phosphate, Elastin

[a] Where potential fluorophores are assigned to a protein, assignments refer to fluorophores associated with the protein.

These differences are highlighted in Figs. 5 and 6, which show contour maps of the ratio and difference of the average EEMs, respectively. Both the ratio and difference maps can be used to detect differences in the intensity, position or bandwidth of a peak in a tissue EEM. However, as our results will demonstrate, the ratio map is more sensitive to small differences in lineshape which are superimposed on backgrounds of similar

intensity. The difference map, on the other hand, is particularly useful for detecting small absolute intensity differences in peaks with similar lineshapes.

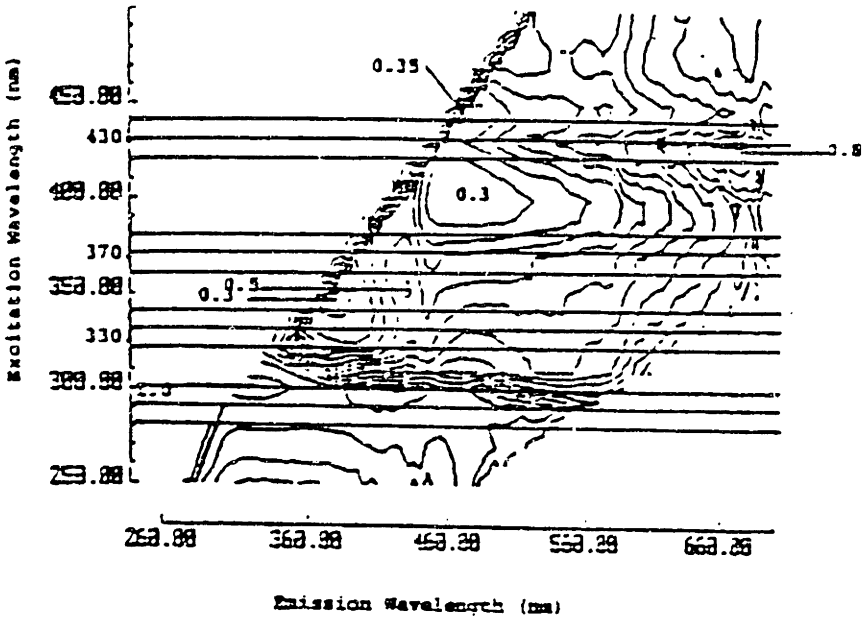

Figure 5: Ratio of the average normal EEM and the average adenomatous EEM, where the normal EEM has been divided by the average adenomatous EEM. Twenty contours are spaced linearly from 0.05 to 1.0. As discussed in the text, the 20 nm wide horizontal bands centered at λ_{exc} = 290, 330, 370 and 430 nm indicate optimal excitation regions for differentiating the fluorescence spectra of normal and adenomatous tissues.

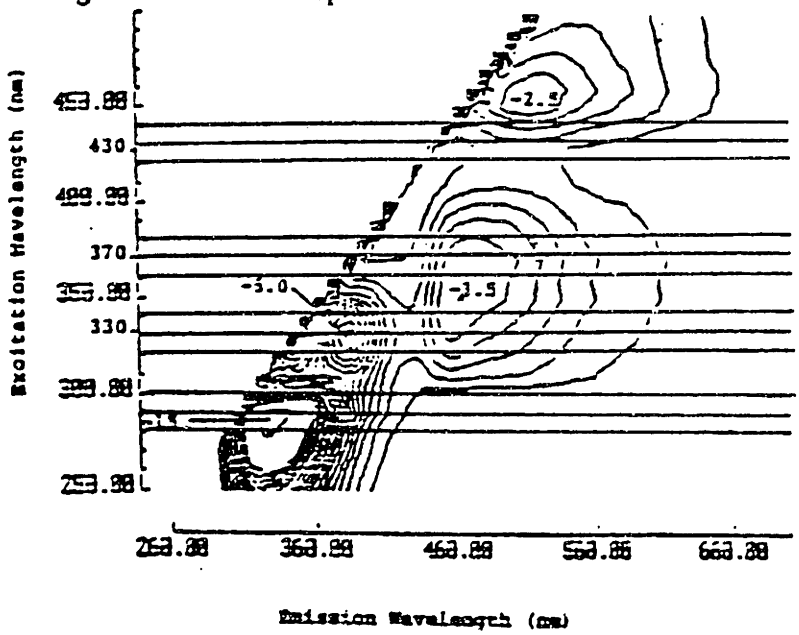

Figure 6: The average difference EEM, where the average adenomatous EEM has been subtracted from the average normal EEM. Two sets of linearly spaced contours are shown: nineteen from -1 to -10 units; and one at -15 units, in the same scale of units used in Figs. 1 and 2. As discussed in the text, the 20 nm wide horizontal bands centered at λ_{exc} = 290, 330, 370 and 430 nm indicate optimal excitation regions for differentiating the fluorescence spectra of normal and adenomatous tissues.

Figure 5 shows the ratio of the average adenomatous fluorescence EEM to that of the average normal fluorescence EEM. Table 3 summarizes the local excitation-emission maxima and minima found in Fig. 5. Although the fluorescence intensity of normal tissue is greater than that of adenomatous tissue for nearly all wavelengths, local maxima can be regarded as regions where adenomatous tissue exhibits additional fluorescence bands, whereas local minima represent regions where normal tissue exhibits additional fluorescence bands. As noted from a comparison of Figs. 3 and 4, normal tissues exhibit a unique fluorescence peak near (345, 385 nm) which is shown nicely in the ratio of the EEMs as a local minimum of 0.3. In the visible region, it was noted that both tissues exhibited peaks in similar locations, with normal tissues having approximately twice the fluorescence intensity of adenomatous tissues. This is reflected in the ratio map as minima at approximately 0.4 in the visible region ((400, 480 nm) and (440, 480 nm)).

Table 3: Local Minima and Maxima in Ratio of Average Fluorescence EEMs of Normal and Adenomatous Colon Tissue

(λexc, λem)	Maxima or Minima	Ratio	Potential Fluorophore[a] (See Table 9)
(345, 385 nm)	Min	0.3	Pyridoxal 5'-phosphate, Collagen I, Collagen III
(350, 430 nm)	Max	0.5	Pyridoxic acid lactone
(400, 480 nm)	Min	0.3	Pyridoxal 5'-phosphate, NADH, NADPH
(440, 480 nm)	Min	0.35	Pyridoxal 5'-phosphate, Elastin
(430, 600 nm)	Max	0.55	Porphyrins
(430, 670 nm)	Max	0.8	Porphyrins

[a] Where potential fluorophores are assigned to a protein, assignments refer to fluorophores associated with the protein.

The ability of the ratio map to detect small changes on top of similar intense backgrounds is demonstrated in Fig. 5. The maximum at (350, 430 nm) in the ratio map was barely visible as an apparent shoulder at (370, 420 nm) in the average adenomatous

map (arrow in Fig. 4). Also, two additional maxima not detected by comparison of the average maps are present in the ratio map at (430, 600 nm) and (430, 670 nm).

Figure 6 shows the difference of the average EEMs, where the normal has been subtracted from the adenomatous. Table 4 summarizes the local excitation-emission minima in Fig. 6. Again, maxima represent bands where adenomatous tissues show additional fluorescence and minima represent bands where normal tissues show additional fluorescence.

Table 4: Local Minima and Maxima in Difference of Average Fluorescence EEMs of Normal and Adenomatous Colon Tissue

(λ_{exc}, λ_{em}) Maxima	**Maxima or Minima**	**Difference** (Arbitrary Units)	**Potential Fluorophore[a]** (See Table 9)
(285, 330 nm)	Min	-15.0	Tryptophan
(330, 385 nm)	Min	-5.0	Pyridoxal 5'-phosphate, Collagen I, Collagen III
(350, 470 nm)	Min	-3.5	NADH NADPH
(460, 515 nm)	Min	-2.5	Pyridoxal 5'-phosphate, Elastin

Although the largest local minimum in the difference map is located at (285, 330 nm), it represents only a small fractional change in the corresponding peak, which was approximately 200 (in arbitrary units) in the average maps of normal and adenomatous tissues. Thus, it was not a prominent feature of the ratio map. This demonstrates that the difference map is most useful for detecting small changes in the absolute intensities of peaks with similar positions and lineshapes.

An additional minimum is present at (330, 385 nm), which corresponds to the unique peak in the average normal tissue map at this location. Again, the peaks noted in Figs. 3 and 4 at (350, 470 nm) and (460, 520 nm) in the average maps, which were approximately two times as intense in normal as adenomatous tissue, are represented by two minima located at (370, 480 nm) and (460, 515 nm) in the difference map. The unique shoulder at (370, 420 nm) in the average adenomatous map is a fairly minor

feature of the difference map, represented by a local maximum at (390, 420 nm). The maxima noted at (430, 600 nm) and (430, 670 nm) in the ratio map are not present in the difference map.

The average ratio and difference maps (Figs. 5 and 6), were used to choose the optimal excitation wavelengths for diagnosing the presence of adenoma in human colon tissue.[1] These maps summarize all spectroscopic bands where the fluorescence properties of normal and adenomatous tissues differ. We wish to obtain the most complete set of diagnostic information with the minimum number of excitation wavelengths. A single excitation wavelength can be represented by a horizontal line on our contour map representations of EEMs. Thus, we can achieve our goal graphically by drawing the minimum number of horizontal lines which intersect all local minima and maxima in Figs. 5 and 6.

In general, these peaks are broad, and can be thought of simply as arising from a single chromophore or chromomorph. Optimal excitation wavelengths then need only to intersect each region associated with a local maximum or minimum in these maps. Where possible, it is desirable for the excitation wavelength to cross the exact local maximum or minimum; however, the number of excitation wavelengths can be reduced if this requirement is slightly relaxed. With these considerations, we see that, as illustrated in Figs. 5 and 6, all local maxima and minima can be sampled with only four excitation lines at 290, 330, 350 and 430 nm.

Thus, the spectroscopic properties of normal colon tissue and colonic adenoma are significantly different over a wide range of UV and visible wavelengths. The optimal excitation wavelengths for differentiating normal and adenomatous colon lie in the regions given by: 290, 330, 370, 430 nm (each ± 10 nm). In this thesis, we will concentrate on the regions at 330, 370, and 430 nm.

4:3.1.2: Mucosal Ulcerative Colitis

Samples of non-dysplastic MUC were studied *in vitro* to establish the differences in the UV and visible fluorescence properties of normal colon and non-dysplastic MUC.

---

[1]The ratio or difference map could also be used to choose best emission wavelength(s) in principle. However, in a clinical setting, where obtaining fluorescence spectra in a short amount of time is important, obtaining emission spectra is more practical than obtaining excitation spectra.

Samples of colon displaying MUC were obtained from resection specimens of patients with the disease.

Full thickness samples of colon were snap frozen in liquid nitrogen and isopentane and stored at -70 ^{o} C until study. The specimens were thawed at room temperature, kept moist with 140 mM buffered saline, pH 7.4, and mounted in a quartz cuvette for spectroscopic studies. Following study, the tissues were fixed in 4% formaldehyde solution, paraffin embedded, cut into 4 μm thick sections, and stained with hematoxylin and eosin. The resultant slides were examined by a single gastrointestinal pathologist to verify the absence of dysplasia. Non-dysplastic MUC samples were further subclassified into the following categories based on the histologic features of the sample: chronic, inactive MUC, active MUC with psuedopolyps and active MUC without pseudopolyps.

Fluorescence EEMs were recorded for 8 specimens of non-dysplastic colon from two patients. Four specimens from two patients were classified as chronic, inactive MUC, two samples from one patient were classified as active MUC with pseudopolyps and two samples from one patient were classified as active MUC without pseudopolyps. EEMs were recorded using the method described for gastro-intestinal tissue in Chapter Two. Average fluorescence EEMs were constructed for each tissue category.

A complete characterization of the UV and visible fluorescence properties of non-dysplastic colon with MUC is presented in Figs. 7, 8 and 9. Figure 7 shows a contour map representation of the average fluorescence EEM of chronic, inactive MUC; Figs. 8 and 9 show the same for an average of the active samples with and without pseudopolyps respectively. Although fluorescence intensity is reported in arbitrary units, the same scale of units is used for all EEMs so meaningful comparisons of absolute fluorescence intensities can be made. It should be noted that extreme intra-patient variability was observed in these EEMs of non-dysplastic MUC. This is consistent with the variable architecture of this disease. It implies that, because of the small number of samples studied, the results presented here should be regarded as preliminary.

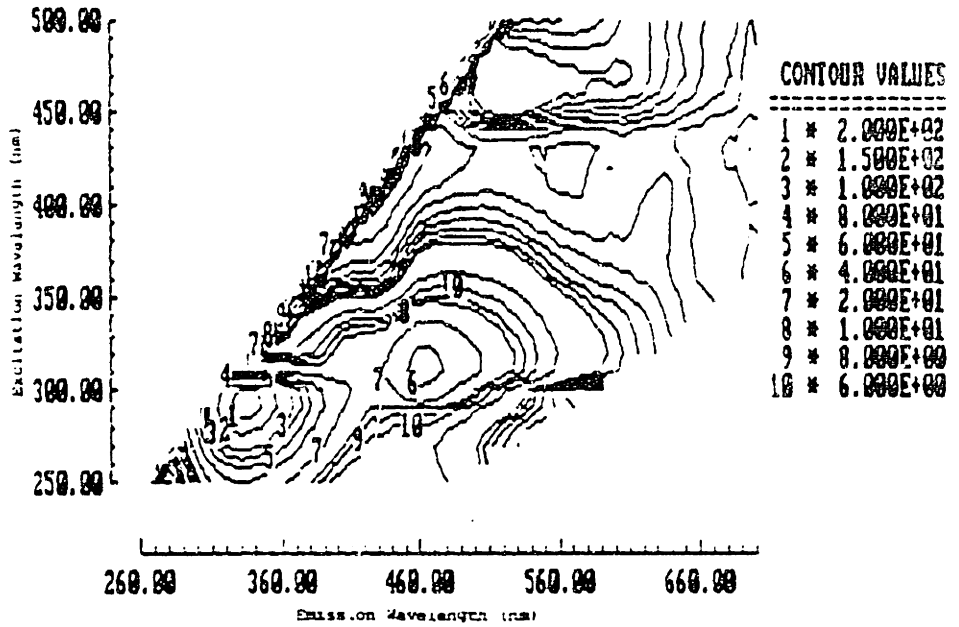

Figure 7: Average fluorescence EEM of four samples of chronic, inactive MUC from 2 patients. Three sets of linearly spaced contours are shown: one at 0.125 units, seven from 0.25 to 1.75 units, four from 2.0 to 8.0 units; six from 10.0 to 100.0 units; and two from 150.0 to 200.0 units.

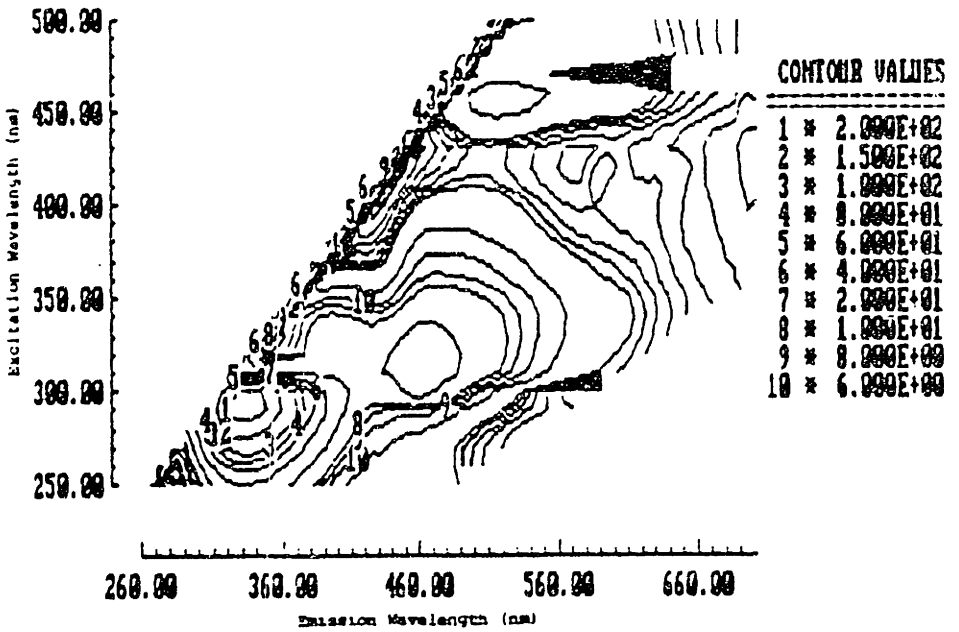

Figure 8: Average fluorescence EEM of two samples of active MUC with psuedopolyps from 1 patient. Three sets of linearly spaced contours are shown: one at 0.125 units, seven from 0.25 to 1.75 units, four from 2.0 to 8.0 units; six from 10.0 to 100.0 units; and two from 150.0 to 200.0 units.

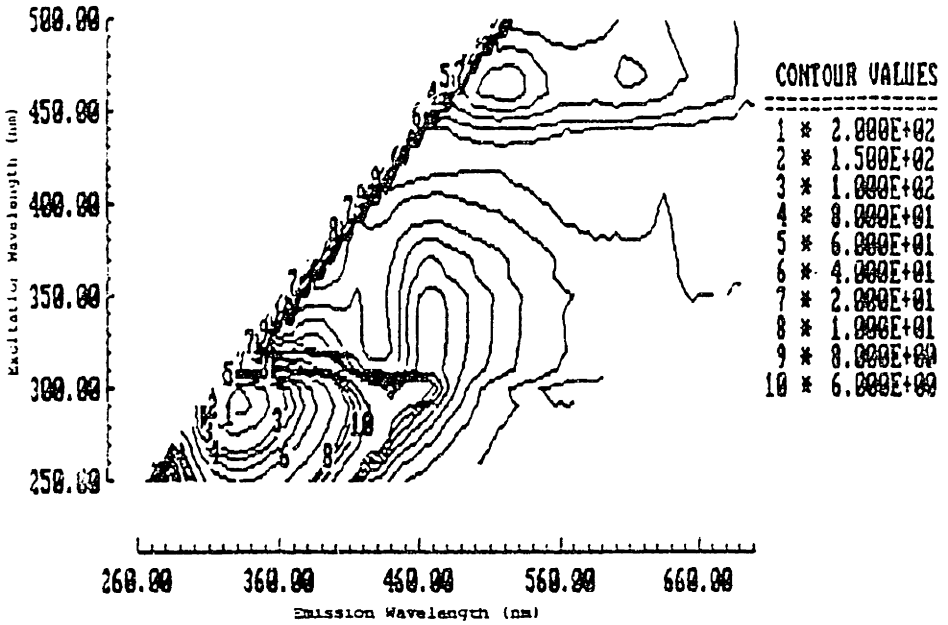

Figure 9: Average fluorescence EEM of two samples of active MUC without pseudopolyps from 1 patients. Three sets of linearly spaced contours are shown: one at 0.125 units, seven from 0.25 to 1.75 units, four from 2.0 to 8.0 units; six from 10.0 to 100.0 units; and two from 150.0 to 200.0 units.

In general, the features of the fluorescence EEMs of all types of MUC studied are similar to the previously reported fluorescence properties of normal colon. Table 5 summarizes the location and average intensity of excitation emission maxima in Figs 7-9. The location of excitation-emission maxima were similar in all types of MUC to that of normal colon. However, in the visible region of the spectrum, the fluorescence intensity of non-dysplastic MUC was significantly different than that of normal tissue.

In all cases, MUC tissues showed an intensely fluorescent excitation emission maximum at (290, 330 nm). The fluorescence intensity of this peak was similar to that of normal and dysplastic colon for all types of MUC investigated. Normal colon exhibited a fluorescence excitation-emission maximum near (325, 385 nm); samples of MUC colon did not exhibit a discernible fluorescence peak at this location. Active MUC without pseudopolyps displayed an excitation-emission maximum near (315, 430 nm) of similar intensity to that observed in normal colon. At (325, 465 nm) all types of MUC tissue investigated exhibited a fluorescence excitation emission maximum. The intensity of this peak was an order of magnitude higher in chronic, inactive MUC and active MUC with pseudopolyps than in active MUC without pseudopolyps and normal and adenomatous colon. The fluorescence EEMs of all types of MUC tissue displayed three peaks near 460 nm excitation. The fluorescence intensity of these peaks in chronic, inactive MUC were similar to those of normal colon, while those of active MUC were even less intense than

the corresponding peaks in adenomatous colon. Finally, the valleys at 420, 540 and 580 nm, due to oxy-hemoglobin attenuation, are much more significant in the fluorescence EEMs of active MUC. This is consistent with the hemorrhagic features of this disease.

Table 5: Excitation-emission maxima in the fluorescence EEMs of non-dysplastic MUC.

$(\lambda_{exc}, \lambda_{em})$ Maxima	Fluorescence Intensity (Arbitrary Units)			Potential Chromophore/ Chromomorph (See Table 9)
	Chronic Inactive	Active No Pseudo-Polyps	Active Pseudopolyps	
(290, 330 nm)	200	200	200	Tryptophan
(315, 430 nm)	---	4.0	---	4-pyridoxic acid
(325, 465 nm)	20	1.5	40	NADH, NADPH
(460, 520 nm)	4.0	1.25	1.75	Pyridoxal 5'-phosphate, Elastin
(465, 555 nm)	2.0	0.75	1.75	Pyridoxal 5'-phosphate, Elastin
(470, 595 nm)	2.0	1.0	1.75	Pyridoxal 5'-phosphate, Elastin

4:3.2: Choice of Optimal Excitation Wavelengths

Thus, the EEMs of normal colon, adenomatous colon and non-dysplastic MUC are significantly different over the visible portion of the spectrum. In a previous section, we demonstrated that 290, 330, 370 and 430 ± 10 nm were optimal excitation wavelengths for differentiating normal colon and adenomatous polyps. Our ultimate goal is to develop a spectroscopic diagnostic algorithm for differentiating dysplastic and non-dysplastic colon in the context of MUC. The differences observed in the fluorescence properties of normal colon and non-dysplastic colon with MUC obviously impact on our choice of excitation wavelength to achieve this goal. In order to completely answer this question, EEMs need to be recorded from dysplastic MUC and directly compared to non-dysplastic MUC. However, as stated earlier, here we assume that the fluorescence properties of adenomatous polyps will be the same as those of dysplastic colon in MUC,

in an attempt to draw some preliminary conclusions about the impact of this data on our choice of optimal excitation wavelength.

Figure 10 shows contour map representations of the ratio of the average EEM of adenomatous polyps (Fig. 4) to that of the EEMs of non-dysplastic MUC, presented in Figs. 7-9. This should be compared to the ratio of the average adenomatous polyps to the average EEM of normal colon (Fig. 5). A consideration of Fig. 10 shows that nearly all local maxima and minima in these ratio maps can be sampled by the same four excitation wavelength regions used to distinguish normal and adenomatous colon, namely 290, 330, 370, and 430 ± 10 nm.

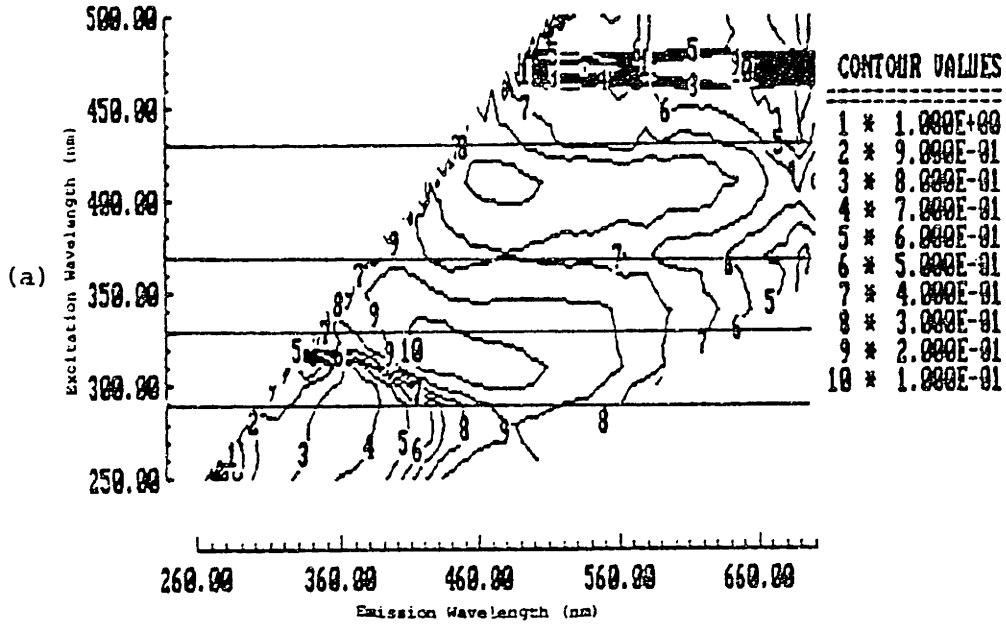

Figure 10: Ratio of the average EEM of adenomatous colon to (a) chronic, inactive MUC, (b) active MUC with psuedopolyps, and (c) active MUC without psuedopolyps. In (a) and (b) ten linearly spaced contours are shown from 0.1 to 1.0 units, while in (c) two sets of linearly spaced contours are shown, nine from 5.0 to 1.0 units, and one at 0.75 units. The horizontal lines at 290, 330, 370 and 430 nm indicate optimal excitation wavelengths for the differentiation of adenomatous colon and non-dysplastic colon with MUC.

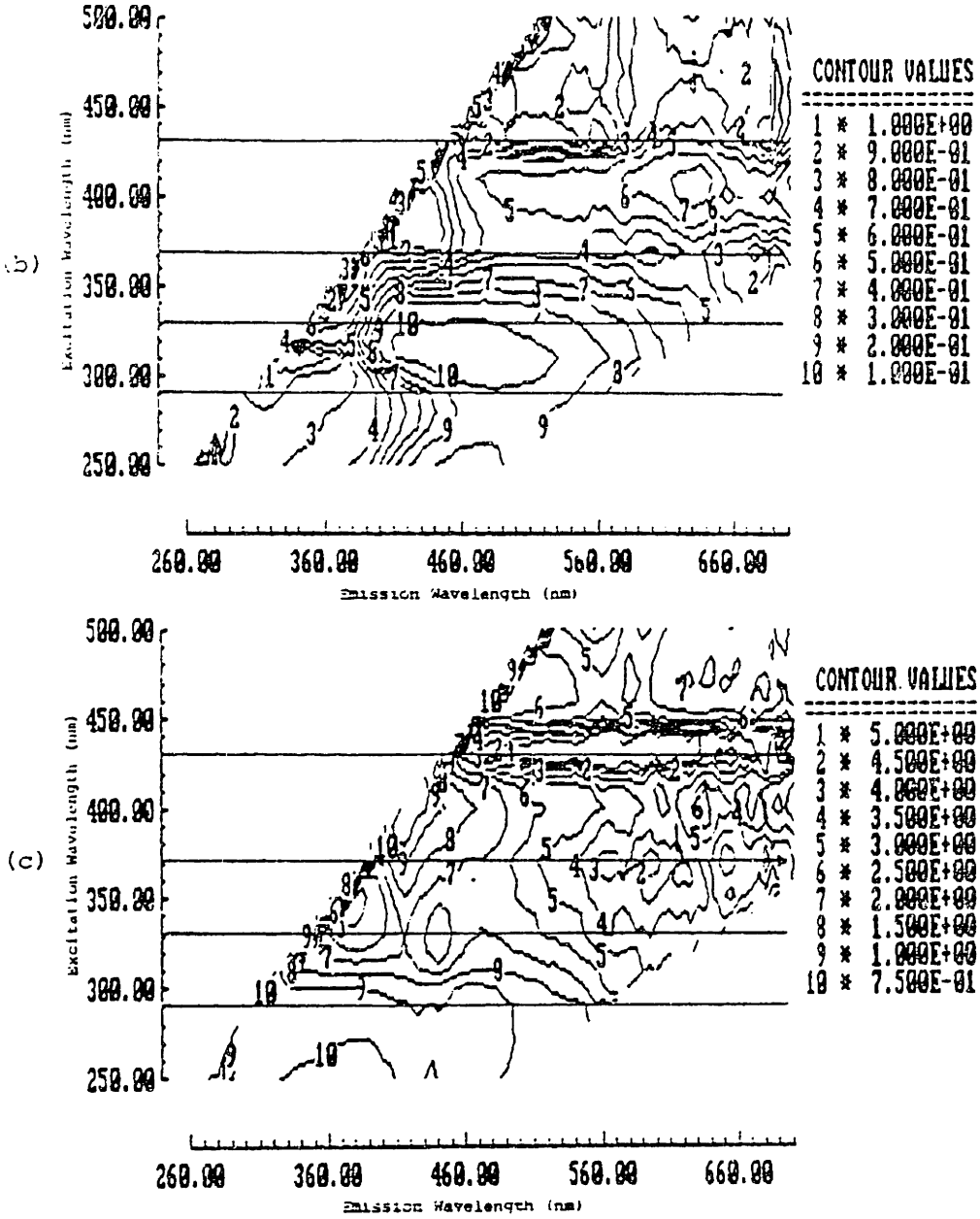

Figure 10 (cont.):

4:4: Empirical Diagnostic Algorithms

In the previous section, we demonstrated how average EEMs of normal and adenomatous tissues could be used to identify optimal excitation wavelengths for differentiating these tissues. In this section, we take the next step in our procedure; that of developing an empirical diagnostic algorithm which can be used to classify a particular sample as normal or adenomatous based on its individual fluorescence properties.

Our ultimate goal, as described in Chapter One, is to develop a diagnostic algorithm based on a histochemical interpretation of tissue fluorescence spectra. We have utilized EEMs to show that chromophores contributing differently to the spectra of normal colon and colonic adenoma can be sampled utilizing only three excitation wavelengths. Analyzing emission spectra at these excitation wavelengths in terms of individual chromophores obviously requires that we understand the identity and nature of these chromophores. Although this is our ultimate goal, first, lacking definitive information on chromophore identity, we evaluate the performance of fluorescence diagnostics at these three excitation wavelengths utilizing empirical diagnostic algorithms. This simplification allows us to easily evaluate whether any single excitation region is most effective diagnostically. If so, then further studies, to determine the histochemical basis of tissue fluorescence, can be carried out first at this excitation wavelength.

4:4.1: *In vitro* Polyposis Model at Three Excitation Wavelengths

Two methods were used to record fluorescence emission spectra of normal and adenomatous colon *in vitro* at excitation wavelengths within the excitation regions indicated by the fluorescence EEMs. The first was to use the same conventional spectrofluorimeter used to measure fluorescence EEMs. This method is described in detail in Chapter Two. The second method, also described in Chapter Two, utilized a fiber optic catheter to deliver excitation light to tissue and collect resulting fluorescence. The primary advantages of this system are twofold - unlike the conventional fluorimeter it provides a well defined excitation/collection geometry [36, 37], and it can, with minimal modifications, be used to collect tissue fluorescence spectra *in vivo*. Despite its drawbacks, the conventional fluorimeter was initially used because of its availability and simplicity. Results obtained with both systems are presented here to illustrate the advantages of each.

Data were collected *in vitro* using familial adenomatous polyposis polyps obtained at resection as a model of colonic dysplasia. Normal controls were obtained from the uninvolved areas of colon from resection specimens of patients with familial adenomatous polyposis, diverticular disease or colonic adenocarcinoma. Full thickness samples of colon were snap frozen in liquid nitrogen and isopentane and stored at -70 ^{o} C until study. The specimens were thawed at room temperature, kept moist with 140 mM buffered saline, pH 7.4. For studies with the fluorimeter, samples were mounted in a quartz cuvette. Following study, the tissues were fixed in 4% formalin solution, paraffin

embedded, cut into 4 μm thick sections, and stained with hematoxylin and eosin. The resultant slides were examined by a single gastrointestinal pathologist to verify the presence or absence of adenoma.

Using the conventional fluorimeter, fluorescence emission spectra at three excitation wavelengths (330, 370, 470 nm) were collected from 38 colonic specimens (15 normal, 23 adenomas) from 18 patients; eight of the normal samples were matched controls from patients with familial adenomatous polyposis, the remaining seven were from patients with colonic carcinoma or diverticular disease. 470 nm excitation was chosen rather than 430 nm excitation as it corresponded to a maximum in the tissue excitation spectrum. With the fluorimeter, several excitation spot sizes were used, so a consistent measurement of absolute fluorescence intensity was not obtained; therefore, spectra obtained with this instrument were normalized to one at the wavelength corresponding to the peak emission intensity of normal colon. Using the optical fiber catheter, at three excitation wavelengths (319.9, 369.9, 435.7 nm) fluorescence emission spectra were collected from 26 colonic specimens (11 normals, 15 adenomas) from approximately 10 patients. With this system, accurate measurements of absolute fluorescence intensities were obtained; fluorescence intensities are reported here in arbitrary units relative to a standard, as described in Chapter Two.

In all cases, the same method was used to define and evaluate empirical diagnostic algorithms for the presence of adenoma. This method utilizes scatter plots of fluorescence intensities at various wavelengths, and is detailed in Chapter Two. Briefly, it consists of comparing the fluorescence intensity of all normal and adenomatous samples at one or two emission wavelengths in a one or two-dimensional scatter plot. Diagnostic algorithms are defined from these plots by using straight line segments to divide the plot into regions classified as normal or adenoma; these decision surfaces are drawn in order to maximize the number of samples correctly classified. The emission wavelengths where the fluorescence intensities of normal and adenomatous tissues are most different are those corresponding to local maxima and minima in the ratio and difference of the average fluorescence emission spectra of normal and adenomatous colon. In principle, if the emission of individual tissue chromophores is well separated, the intensities at the emission wavelengths identified with this method are correlated to the concentration and quantum yield of individual chromophores. Thus, the empirical algorithms presented here are crudely related to the biochemically based algorithms we hope to ultimately achieve.

Here, at 370 nm excitation wavelength, for each detection system, we present the average spectra of normal and adenomatous tissues, the ratio and difference of these average spectra, and the most effective one or two dimensional classification scheme. The average spectra of normal colon and adenomatous polyps are presented for the other two excitation regions; however, because the histochemical basis of fluorescence at these excitation wavelengths has not been studied, an analysis of this data is not presented.

4:4.1.1: Fluorimeter data

Figure 11 shows the average emission spectrum of the 15 normal samples, and a similar average for the 23 adenomas obtained with 370 nm excitation. The spectra of individual tissue samples were normalized to 1 at 470 nm before averaging. In the average normal tissue spectrum two broad peaks are found at 470 and 490 nm. In addition, valleys are present near 420, 540 and 580 nm. In the average spectrum of adenomatous tissue, broad peaks are found at 450, 470 and 500 nm, with valleys at 420, 540 and 580 nm. These valleys are slightly deeper in the fluorescence spectrum of adenoma. In addition, the shoulder at 450 nm appears to be unique to adenoma. In seven of the adenomas, a distinct peak was observed near 445 nm, in the remaining sixteen, smaller shoulders at this wavelength were observed. None of the normal samples exhibited a distinct peak at this wavelength. Finally, the position of the second largest maximum is near 490 nm in the spectrum of normal tissue and appears to be slightly shifted toward longer wavelengths (500 nm) in the adenoma spectrum.

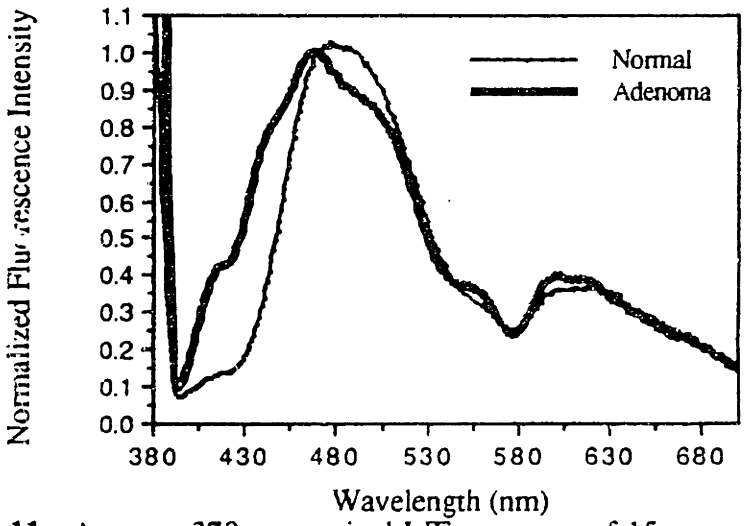

Figure 11: Average 370 nm excited LIF spectrum of 15 normal colon samples (solid line) and 23 adenomatous colon samples (bold line).

The variation in individual tissue spectra was assessed by calculating the standard deviation from the mean of the 15 normal samples and the 23 adenomas. At all wavelengths, the standard deviation of the normal samples was less than 25% of the peak fluorescence intensity. For the subset of normal samples which were matched controls from familial adenomatous polyposis patients, this variation was smaller; at all wavelengths, the standard deviation was less than 15% of the peak fluorescence intensity. However, no significant differences were observed in the average spectra of matched normal controls and other normal samples. A larger variation was observed in the adenomas; at all wavelengths, the standard deviation was less than 55% of the peak fluorescence intensity; it was greatest at 445 nm.

The ratio of the average 370 nm excited spectra of normal and adenomatous tissue was calculated by dividing the average adenomatous spectrum by the average normal spectrum (Fig. 12). In the ratio spectrum in Fig. 11, peaks (ratio >1) indicate regions in which adenomatous tissues exhibit a higher fluorescence intensity relative to that at 470 nm than normal tissue. Valleys (ratio < 1) indicate regions where normal tissues exhibit a higher fluorescence intensity relative to that at 470 nm than adenomatous tissue. The largest peak is found at 422 nm; two smaller peaks are present at 559 and 601 nm. Valleys are present at 480 nm, 530 nm, 580 nm and 634 nm.

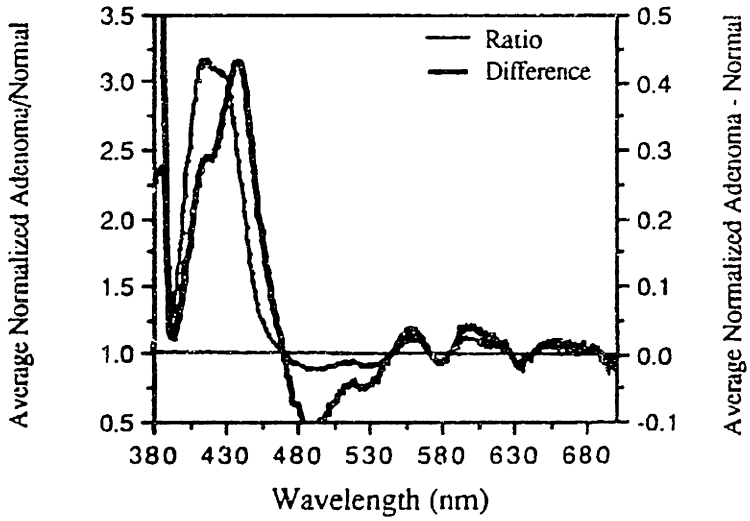

Figure 12: Ratio (solid line) of the average normal and adenomatous colon spectra obtained with 370 nm excitation. The average normal spectrum has been divided by the average adenomatous tissue spectrum. Difference (bold line) of the average normal and adenomatous colon spectra obtained with 370 nm excitation. The average adenomatous tissue spectrum has been subtracted from the average normal spectrum.

Figure 12 also shows the difference of the two average spectra, where the average normal spectrum has been subtracted from the average adenoma spectrum. Qualitatively this difference spectrum is similar to the ratio spectrum in Fig. 12. Peaks and valleys are located at the same locations as in the average ratio spectrum above 470 nm. However, the largest peak exhibits some interesting differences. In the average difference spectrum, this peak nas a shoulder at 418 nm and a main peak at 443 nm, compared to the average ratio spectrum in which there is a single broad peak at 420 nm. Table 6 summarizes the local minima and maxima found in the average ratio and difference spectra.

Table 6: Peaks in Average 370 nm Excited Difference and Ratio Spectra of Normal and Adenomatous Colon Tissue

Emission λ	Maxima or Minima	Ratio, Difference or Both
422 nm	Max	Ratio
418 nm	Max	Difference
443 nm	Max	Difference
480 nm	Min	Both
530 nm	Min	Both
559 nm	Max	Both
580 nm	Min	Both
601 nm	Max	Both
634 nm	Max	Both

An effective algorithm could not be found by considering data at any single emission wavelength. For this reason, binary diagnostic algorithms were considered. All possible binary emission wavelength combinations represented in Table 6 were considered. Here, we present the two sets of emission wavelength combinations with the lowest misclassification rate for the 38 individual samples. The emission wavelength combinations {418, 559 nm}, {422, 559 nm} and {443, 559 nm} performed similarly, each correctly classifying 84% of the 38 samples. Similarly, utilizing either the combination {558, 600 nm} or {558, 635 nm}, 84% of the 38 samples were classified correctly. As an example, the algorithm for the combination {443, 559 nm} is shown in Figure 13. This is a scatter plot containing data from each of the individual samples, with the decision surface represented by the solid line. The specificity of this algorithm for detecting adenoma is 85%; its sensitivity is 84%.

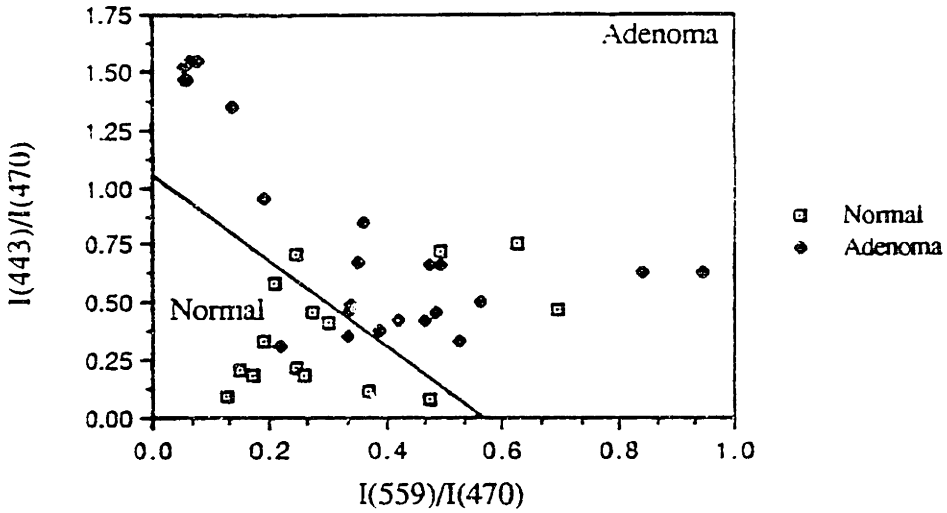

Figure 13: Scatter plot of fluorescence intensities at the emission wavelengths {443, 559 nm} relative to the fluorescence intensity at 470 nm from the 38 individual 370 nm excited spectra. The algorithm represented by the straight line correctly diagnoses 84% of the samples shown. Its specificity for detecting adenoma is 85%; its sensitivity is 84%.

In addition, fluorescence emission spectra were collected from this same set of samples at 330 and 470 nm excitation. Due to space and time considerations, an analysis of this data will not be presented here; however, for reference, the average, normalized spectra of normal and adenomatous colon at these excitation wavelengths are shown in Figs. 14 and 15 respectively.

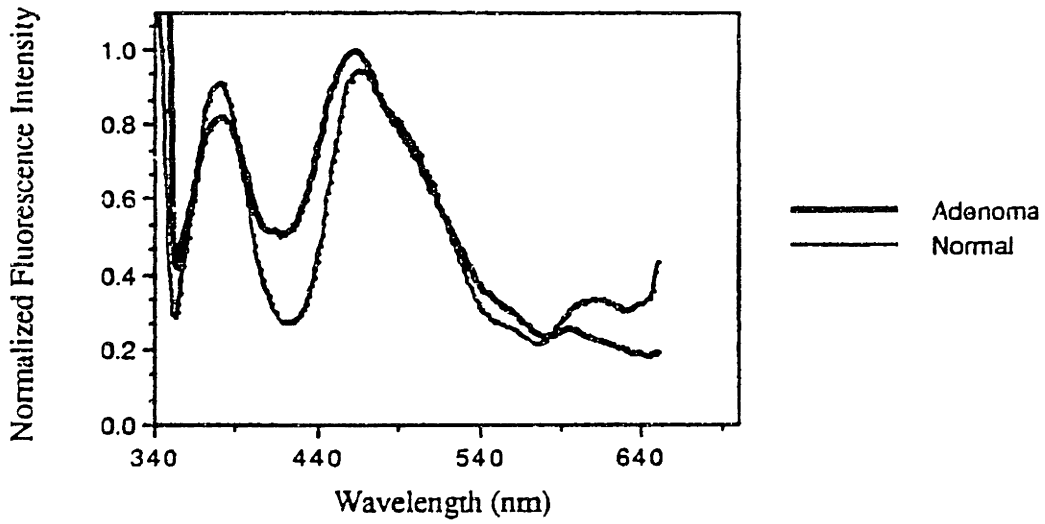

Figure 14: Average, normalized spectra of normal and adenomatous colon obtained with 330 nm excitation.

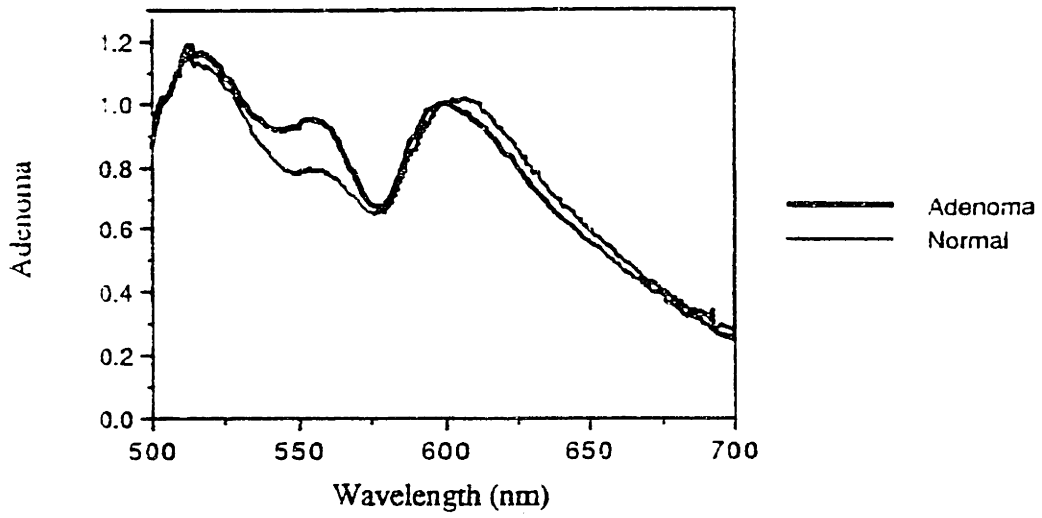

Figure 15: Average, normalized spectra of normal and adenomatous colon obtained with 470 nm excitation.

4:4.1.2: Catheter data

Similar 370 nm excited emission spectra were collected using the spectral catheter system of Chapter Two. This data is presented and analyzed here to illustrate the advantages of this detection system. Figure 16 shows the average fluorescence emission spectrum of 11 samples of normal colon obtained with the spectral catheter system; the excitation wavelength was 369.9 nm. Two intense emission peaks are present near 460 and 480 nm. Valleys can be observed near 420, 540 and 580 nm. The small peak at 520 nm is an artifact due to a large decrease in the spectral response of the detection system at this wavelength. This spectrum is fairly similar to that obtained with the fluorimeter for normal tissue at 370 nm excitation (Fig. 11), except that the peaks are slightly blue shifted here, the 480 nm peak is slightly more pronounced and the valleys are much less pronounced.

These differences can be understood in terms of the different collection geometries of the two systems. The collection geometry of the catheter system is well defined, that of the fluorimeter is not; thus, the attenuation contributions to spectra obtained with the fluorimeter will be greatly enhanced relative to those obtained with the catheter system [36, 36]. It will later be demonstrated that the valleys at 420, 540 and 580 nm are due to the attenuation effects of oxy-hemoglobin. They are more pronounced in spectra obtained with the fluorimeter. The attenuation contribution at 420 nm affects the

observed maximum of the the peak near 470 nm - in the spectrum obtained with the fluorimeter, there is relatively more attenuation at 420 nm, and the peak is observed at 470 nm. In the spectrum obtained with the catheter, there is relatively less attenuation at 420 nm, thus the observed position of the peak is blue shifted to 460 nm. This blue shift allows for better resolution of the second maximum at 480 nm in spectra obtained with the catheter.

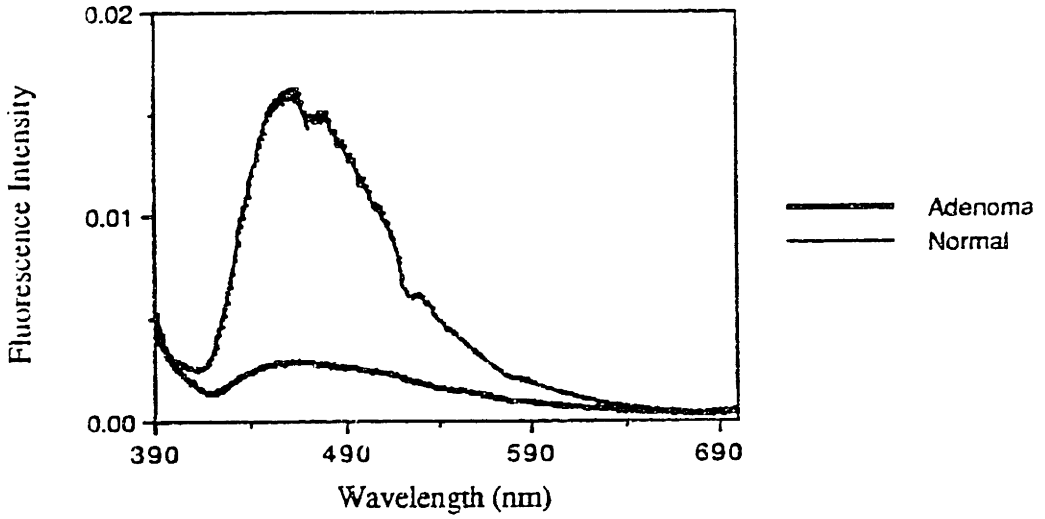

Figure 16: Average fluorescence emission spectra of 11 samples of normal colon (solid line) and 15 samples of adenomatous colon (bold line). Spectra were obtained with the catheter system described in Chapter Two. The excitation wavelength was 369.9 nm. Fluorescence intensity is reported here in arbitrary units relative to a standard as described in Chapter Two.

Figure 16 also shows the average fluorescence emission spectrum of 15 samples of adenomatous colon. The excitation wavelength was 369.9 nm. Here, absolute fluorescence intensities have been preserved. This spectrum shows fluorescence peaks at 460 and 500 nm with valleys near 420, 540 and 580 nm. This spectrum is similar to that obtained with the fluorimeter except the valleys are less pronounced. Although, there is relatively more fluorescence in the 400-460 nm region of the adenoma spectra obtained with the catheter, the shoulder present at 450 nm in the spectra some of the adenomas obtained with the fluorimeter is not prominent in the adenoma spectra obtained with the catheter. It is not believed that this is due to any differences in collection geometry, but rather due to differences in the sample handling procedure for the first few adenomas investigated with the fluorimeter.

The differences in the average spectra presented in Fig. 16 include a larger fluorescence intensity in normal colon at 460 nm, a difference in the position of the second largest peak, at 480 in normal tissue and 500 nm in adenomatous tissue, and more pronounced valleys at 420, 540 and 580 nm in adenomatous tissue. These differences are characterized quantitatively in Fig. 17, which shows the ratio of the average adenoma spectrum to the average normal tissue spectrum. This ratio spectrum is characterized by four regions: a downward sloping region from 400-420 nm where the ratio is <1, a flat region from 420-480 nm where the ratio is <1, an upward sloping region from 480-650 nm where the ratio is <1 and an upward sloping region from 650-700 nm where the ratio is >1.

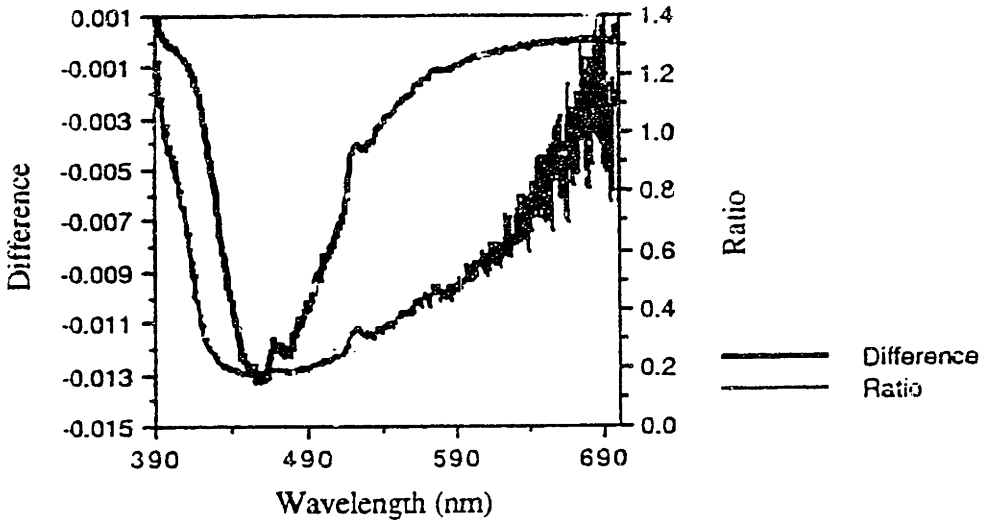

Figure 17: Ratio (solid line) and difference (bold line) of the average adenoma and normal tissue spectrum shown in Fig. 16. The excitation wavelength was 369.9 nm.

These can be related to the differences in the average fluorescence spectra discussed qualitatively above. The downward sloping region from 400-420 nm reflects the blue region of the spectrum in which the relative fluorescence intensity of the adenomas is relatively greater than that of normal tissues. The flat region from 430-460 nm represents peak at 460 nm, where the fluorescence intensity of normal tissue is greater than that of adenomatous tissue. The relatively flat ratio in this region indicates that the fluorescence lineshape of this peak is similar in normal and adenomatous tissue The upward sloping region from 480-650 nm represents a region where the absolute difference in the fluorescence intensity of normal and adenomatous tissue is decreasing, and is due to the red shift in the position of the second most intense maximum in the

spectra of adenomatous tissues. Above 680 nm, the absolute fluorescence intensity in the adenoma spectrum is slightly greater than that in the normal spectrum. This difference peaks near 680 nm.

Figure 17 also shows the difference of the average adenoma and normal tissue spectra. This spectrum essentially reflects the same features observed in the ratio spectrum, except that the differences observed at 680 nm in the ratio spectrum are not a feature of the difference spectrum. Table 7 lists the locations of the local maxima and minima in the ratio and difference spectra shown in Fig. 17.

Table 7: Peaks in Average 370 nm Excited Difference and Ratio Spectra of Normal and Adenomatous Colon Tissue

Emission λ	Maxima or Minima	Ratio, Difference or Both
404 nm	Max	Both
460 nm	Min	Both
480 nm	Min	Both
516 nm	Min	Difference
532 nm	Min	Difference
600 nm	Min	Ratio
680 nm	Max	Ratio

A comparison of Tables 6 and 7 shows that many of the same emission wavelengths (± 10 nm) were identified as diagnostically useful from data collected with the conventional fluorimeter and the spectral catheter. An exception is 460 nm which was identified from the catheter data but not the fluorimeter data. Essentially this is because the fluorimeter data was normalized in this region, eliminating an important piece of information. Empirical algorithms for the presence of adenoma were defined with the fluorescence intensities at emission wavelengths listed in Table 7 using the method outlined in Chapter Two.

Figure 18 shows three of the most effective diagnostic algorithms which could be defined with this method. For this data set, the emission intensity at 480 nm proved to be an effective diagnostic algorithm for adenoma. Figure 18(a) shows that a simple algorithm represented by a straight line at I(480) = .003 is capable of correctly diagnosing 96% of the 26 samples as normal or adenoma. Equally effective binary diagnostic algorithms could also be defined using the emission intensity at 480 nm with that at either 404 nm or 680 nm. These are shown in Figs 18(b) and 18(c) respectively. Here, again the algorithms represented by the two straight line segments correctly classify 96% of the 25 samples as normal or adenomatous. It should be pointed out, that, with this data set,

the addition of another parameter does not improve the performance of the algorithm. However, in the binary scatter plots there are fewer data points which fall near the decision surface. Thus, as the size of the data set is increased, these algorithms may prove to be more effective than the algorithm based on fluorescence intensity at a single emission wavelength. The specificity, sensitivity and predictive value of these algorithms for detecting adenoma are 93%, 100% and 100% respectively. In all cases the same adenomatous sample is incorrectly diagnosed as normal.

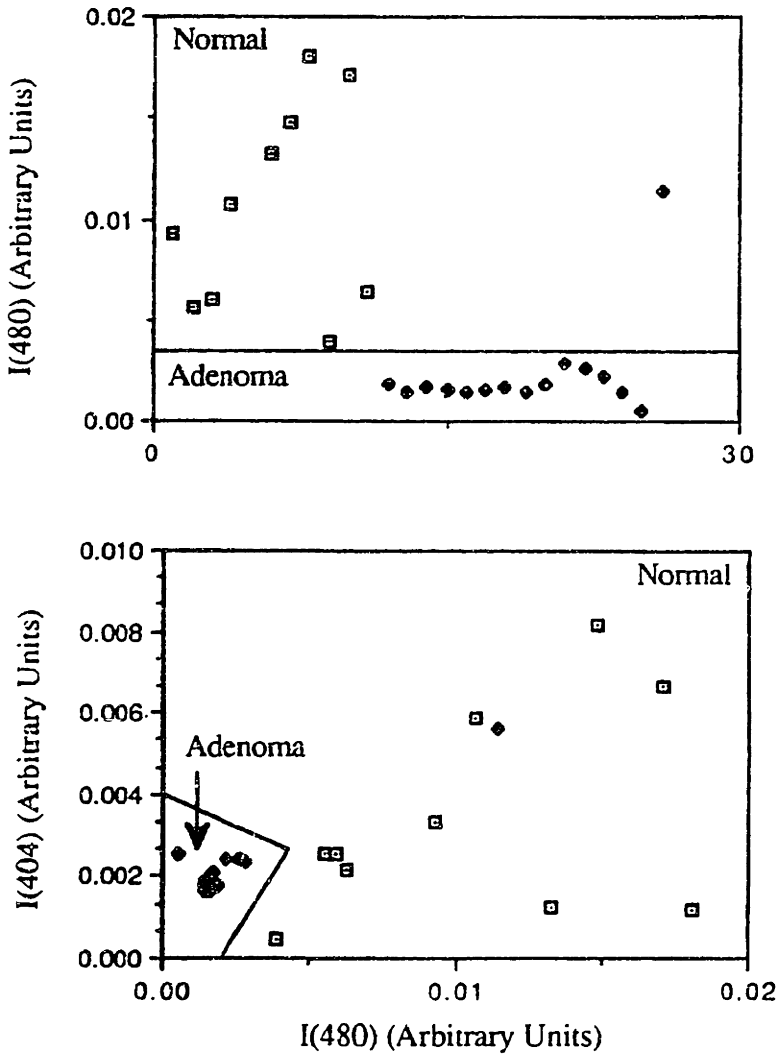

Figure 18: Empirical diagnostic algorithms for adenoma based on emission spectra excited at 369.9 nm.

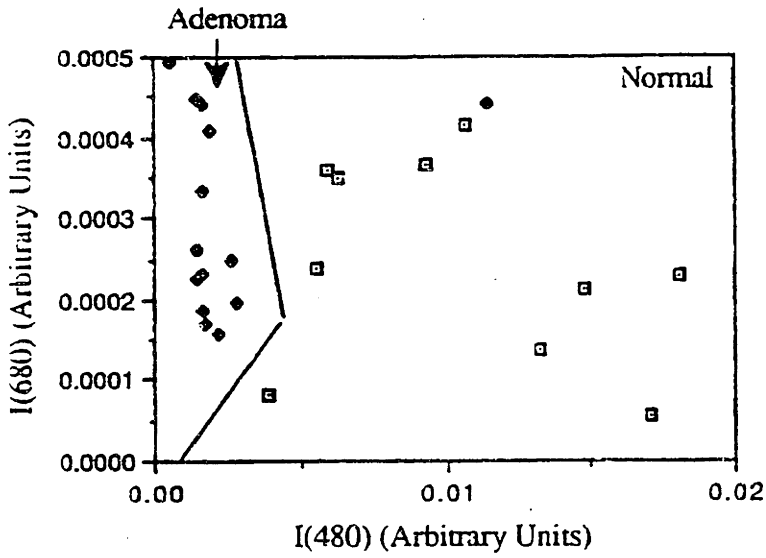

Figure 18 (cont.).

In addition, fluorescence emission spectra were collected from this same set of samples at 319.9 and 435.7 nm excitation. Although because of time and space considerations, an analysis of this data will not be presented here, for reference, the average, normalized spectra of normal and adenomatous colon at these excitation wavelengths are shown in Figs. 19 and 20 respectively.

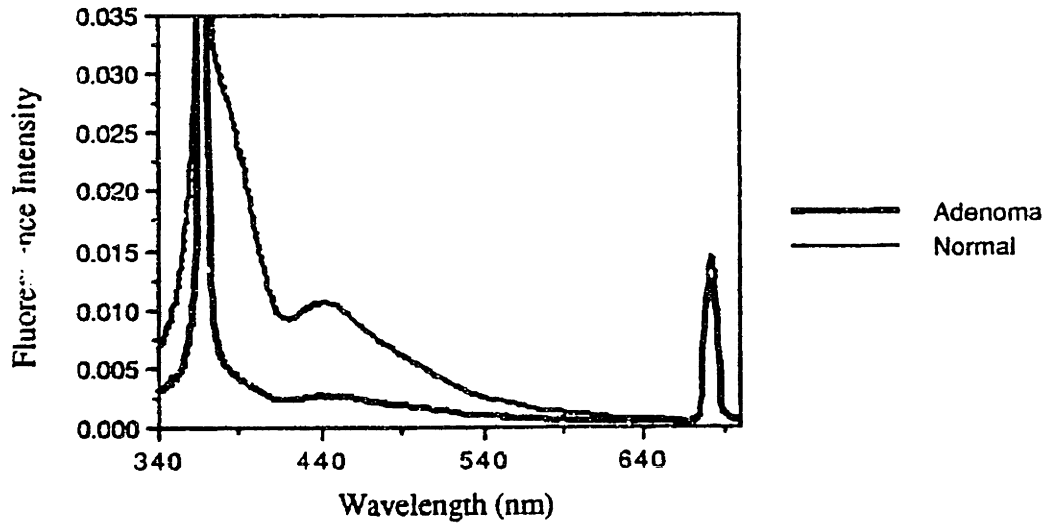

Figure 19: Average, normalized spectra of normal (solid line) and adenomatous colon (bold line) obtained with 319.9 nm excitation. The sharp peaks at 369.9 and 682.9 nm represent scattered light at other wavelengths produced by stimulated Raman scattering of 532 nm light by H_2 gas. In later experiments these were eliminated by use of an interference filter centered at the desired excitation wavelength.

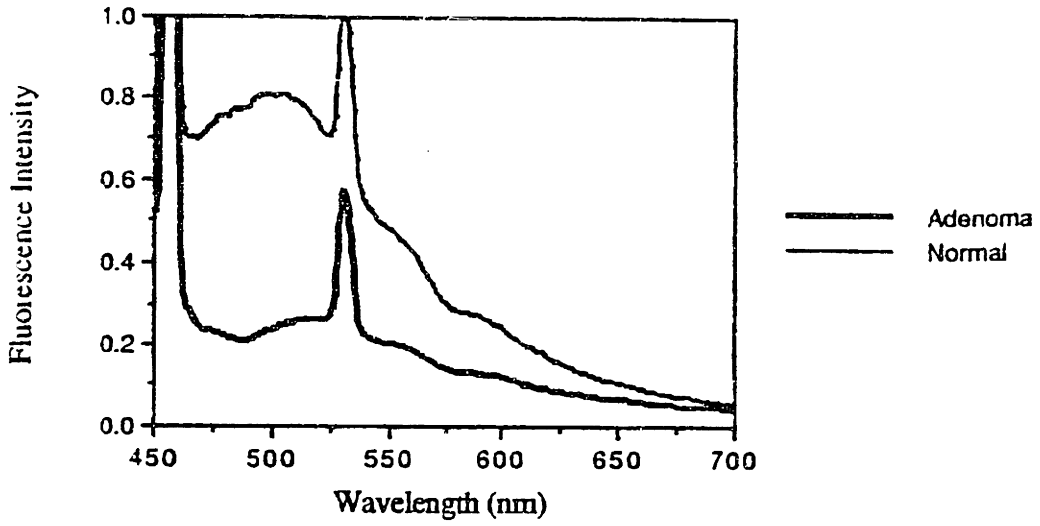

Figure 20: Average, normalized spectra of normal (solid line) and adenomatous colon (bold line) obtained with 435.7 nm excitation. the sharp peak at 532 nm represents scattered light from the Nd:YAG laser. In later experiments these were eliminated by use of an interference filter centered at the desired excitation wavelength.

4:4.2: *In vivo* Adenomatous Polyp Model at 370 nm Excitation[2]

Based on the success of algorithms for colonic adenoma based on empirical features of fluorescence emission spectra collected *in vitro* with 370 nm excitation, an *in vivo* trial of the technique was commenced. 370 nm excited fluorescence emission spectra were collected using an optical fiber catheter *in vivo* during colonoscopy. Spectra were obtained from normal mucosa, adenomatous polyps and hyperplastic polyps from patients with a history of polyp formation.

The goal of this study was threefold:

1. to demonstrate that fluorescence emission spectra could be collected *in vivo* during colonoscopy with good S/N in near real time;

2. to determine whether models of normal colon and colonic adenoma studied *in vitro* yielded data representative of normal colon and sporadic adenomatous polyps *in vivo*; and

---

[2] The work described in this section was a collaborative effort with Cleveland Clinic Foundation. Rim Cothren, Tom Ivanc, Maryann Fitzmaurice, Robert Petras and Michael Sivak all participated in this study. Their contributions are gratefully acknowledged.

3. to determine whether fluorescence could be used *in vivo* to distinguish neoplastic and non-neoplastic colon with similar architectural features - i.e. could fluorescence spectroscopy be used to differentiate hyperplastic and adenomatous polyps.

4:4.2.1: Experimental Methods

Figure 21 shows the spectrofluorimeter used to collect mucosal fluorescence spectra of colon *in vivo*. An optical fiber probe was constructed that could be passed through the accessory channel of a standard colonoscope. The probe delivered monochromatic light produced at 370 nm with a nitrogen pumped dye laser through a centrally placed optical fiber. This light formed a 1 mm diameter excitation spot at the distal tip of a 1 mm diameter transparent quartz shield. At 370 nm excitation, the laser furnished an average power of 270 μW at the distal tip, delivered in 3 ns pulses at 20 Hz. Nine smaller, peripherally placed optical fibers surround the central excitation fiber. These collect the emitted tissue fluorescence from a surface area of tissue only slightly greater (10%) than that directly illuminated by excitation light. The system thus has a well defined collection geometry [36, 37].

The proximal ends of the nine collection fibers were imaged at the entrance slit of an imaging spectrograph coupled to a gated optical multichannel analyzer under computer control. A 399 nm long pass, low fluorescence filter was used to block scattered excitation radiation from the detector. A 1 μs collection gate synchronized to the laser pulse effectively eliminated the effects of the colonoscope's white illumination light during collection of the much weaker tissue fluorescence.

The patients studied with this spectroscopic system were selected from a group of patients referred for follow-up colonoscopy for suspected colonic adenomas seen at flexible sigmoidoscopy or with barium enema. Informed consent was obtained from each patient and the project was reviewed and sanctioned by the Institutional Review Board of the Cleveland Clinic and the Committee on Use of Humans as Experimental Subjects at the Massachusetts Institute of Technology.

The patients were prepared for colonoscopy by ingestion of an oral lavage solution (Colyte). Intravenous sedatives and analgesic, most often midazolam (1-2 mg) and meperidine (50-100 mg) were administered at the start of the procedure. At 370 nm excitation, it was determined that Colyte did not fluoresce appreciably.

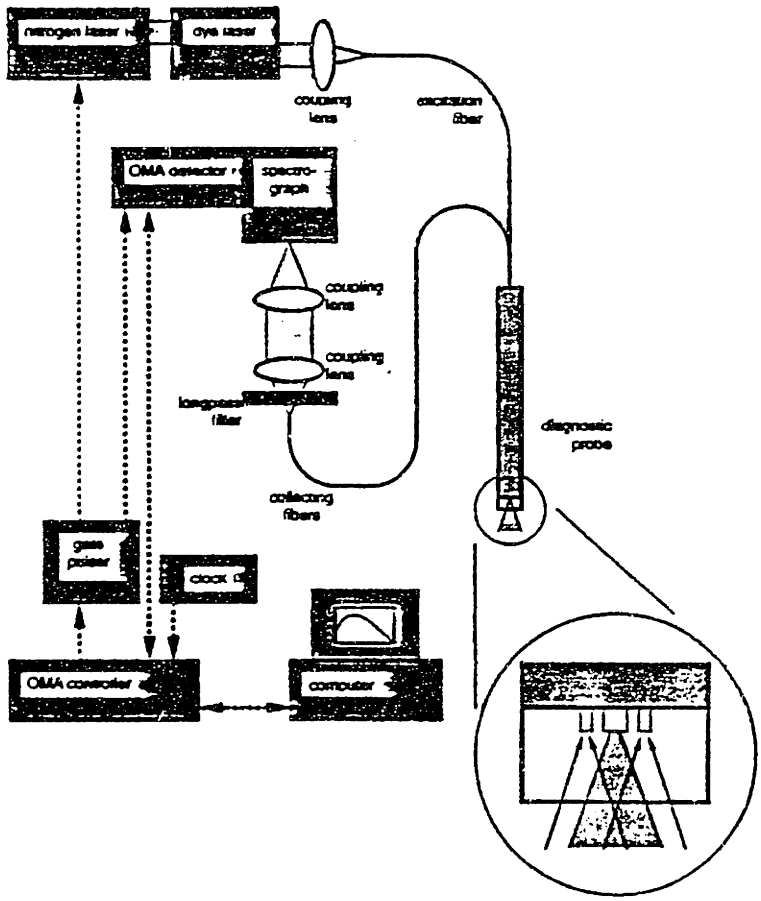

Figure 21: Block diagram of the system used to collect fluorescence spectra of colonic mucosa *in vivo* during colonoscopy. The inset shows an enlarged schematic of the optical fiber catheter.

Colonoscopy was performed in the usual fashion using a standard colonoscope. In each patient, the spectroscopy probe was passed through the accessory channel of the colonoscope and its outer shield was placed in direct contact with the surface of mucosal polyps and/or control non-polypoid normal-appearing mucosa. This contact displaced residual colonic contents and/or mucous. In addition, direct contact was provided a fixed distance between the mucosa and the distal ends of the probe's optical fibers, so that reliable calibrated fluorescence intensity information could be obtained.

Fluorescence emission spectra were collected from 400 - 700 nm with a resolution of 0.6 nm. After three spectra were obtained, the probe was removed and then replaced two to four additional times with three spectra obtained at each placement. This process yielded nine to fifteen individual spectra per site. No appreciable fluorescence photobleaching was observed. The S/N achieved in these individual spectra was on the order of 30. A biopsy for histologic examination was then performed at the mucosal site analyzed by the probe. Polyps were treated by standard electro-surgical snare polypectomy or coagulation biopsy ("hot biopsy") in the case of diminutive polyps. Tissues were categorized histologically as normal, hyperplastic polyp, tubular adenoma, tubulovillous adenoma, villous adenoma, benign lymphoid aggregate[3] or as tissue insufficient for diagnosis.

Spectra were corrected for non-uniform spectral response of the detection system by using a calibrated lamp. The fluorescence intensity of a standard fluorescence paper was measured prior to study in each patient and was used to calibrate the fluorescence intensity of the tissue spectra. The spectral background was corrected to zero by subtracting dark current.

Data were reduced by computing an average spectrum and a standard deviation from the nine to fifteen corrected spectra obtained from each site. The average spectrum per site was used in all further data manipulations. These average per site spectra were grouped according to histologic categories. For each histologic category the average and standard deviation spectra were calculated.

4:4.2.2: Description of Data

LIF spectra were obtained *in vivo* and analyzed from 31 adenomas, 4 hyperplastic polyps, 12 benign lymphoid aggregates and 32 histologically normal areas from 20 patients. The adenomas ranged in size from 2-11 mm (average 5 mm) while the hyperplastic polyps measured 2-5 mm (average 3 mm). Twenty three of the adenomas were classified as tubular, while two were villous and six were tubulovillous. The laser caused no tissue damage that could be detected at the light microscopic level.

[3]Here, benign lymphoid aggregate refers to small (0.5-1.0 mm) clusters of lymphoid tissue, comprised mainly of lymphocytes. These aggregates are commonly found in the gastro-intestinal tract of normal individuals, and may be perceived by the endoscopist as a polyp.

Figure 22(a) shows six of the individual fluorescence spectra obtained from a representative normal specimen and a tubular adenoma. Although the three spectra corresponding to each placement of the fiber optic probe are discernible, there is relatively small variation between sets of spectra corresponding to different probe placements. This is illustrated in Figure 22(b), which shows the average spectra corresponding to these two tissue samples as well as average spectra ± standard deviation spectra. The standard deviation was less than 20% of the average at all wavelengths for these two samples; this was a typically observed result.

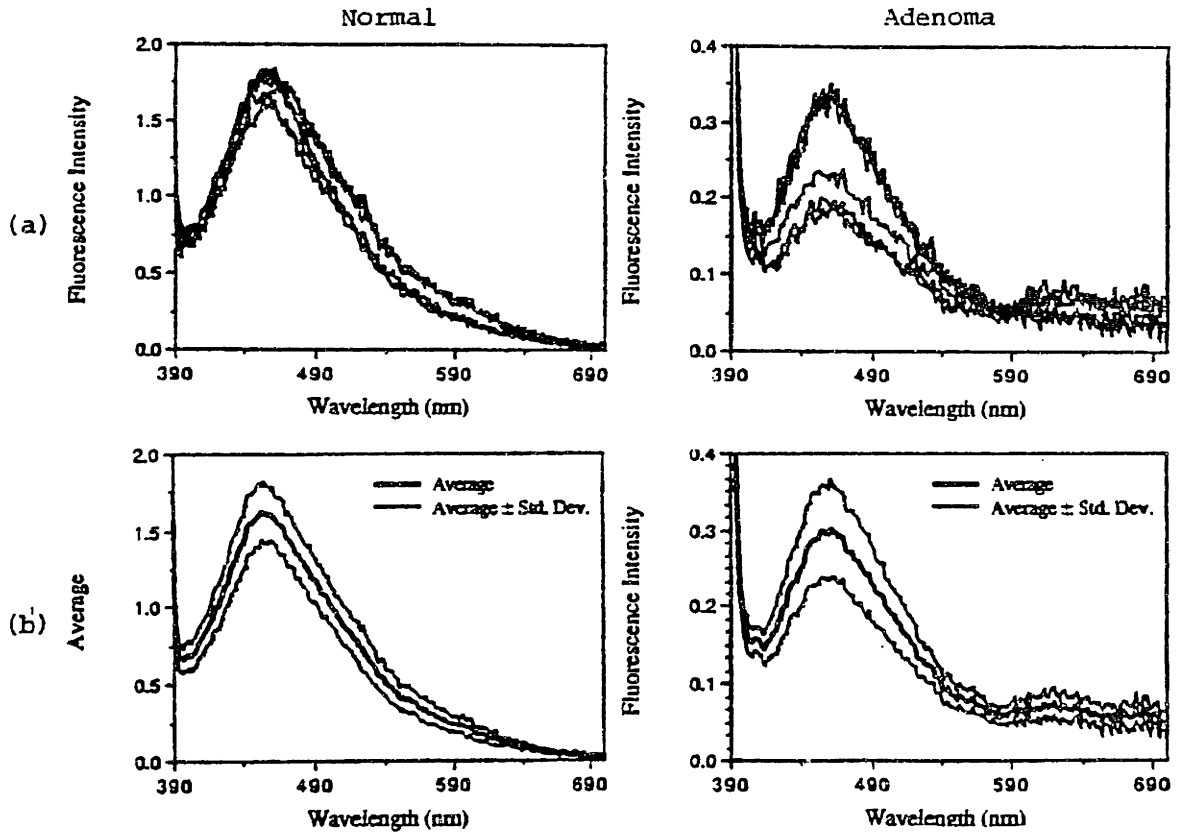

Figure 22: (a) Six of the individual spectra collected from a specimen of (a) normal colonic mucosa and a tubular adenoma. (b) Average and average ± standard deviation spectra of the 9-12 individual spectra for the normal colonic mucosa and tubular adenoma samples shown in Fig. 22(a).

Figure 23 shows the average spectra corresponding to each histologic category. Average spectra ± standard deviation are also shown here. In all categories except benign lymphoid aggregate the standard deviation was less than approximately 30% of the average at all wavelengths. The spectra of all histologic categories showed features which were generally similar; the maximum fluorescence intensity was observed at approximately 460 nm, two less intense maxima were found at 560 and 620 nm. Valleys were present at 540 and 580 nm. The average spectra of tubular adenomas, tubulovillous adenomas and benign lymphoid aggregates also exhibited maxima near 620 and 680 nm.

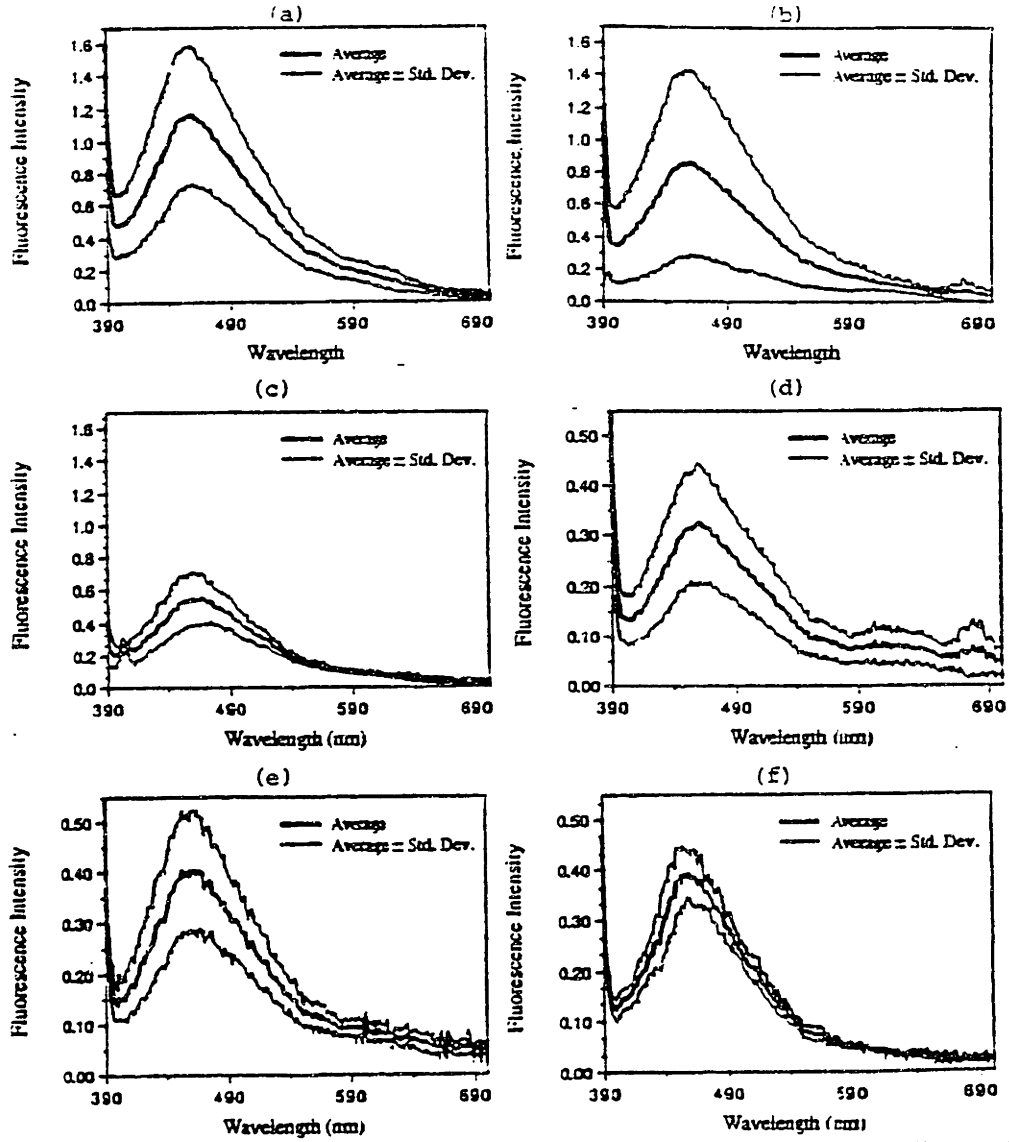

Figure 23: Average spectrum and average ± standard deviation spectra for all samples histologically classified as (a) normal, (b) benign lymphoid aggregate, (c) hyperplastic polyp, (d) tubular adenoma, (e) tubulovillous adenoma, and (f) villous adenoma.

Differences in the average spectra of these histologic categories were twofold. The average intensity of the peak found at 460 nm varied; it was greatest for normal tissues (1.15 units), and decreased in order of benign lymphoid aggregate (.85), hyperplastic polyp (.54), tubulovillous adenoma (.4), villous adenoma (.39) and tubular adenoma (.32). The average intensity of the subsidiary maximum at 680 nm also varied; it exhibited similar higher intensities for tubular adenomas (.07), tubulovillous adenomas (.05) and benign lymphoid aggregates (.06), while normal samples (.04), hyperplastic polyps (.03) and villous adenomas (.02) exhibited similar lower intensities at these peaks.

Figure 24 illustrates these trends; shown are a comparison of the average normal and adenoma spectra. The approximately fourfold difference in the intensity of the 460 nm peak is shown in Fig. 24(a). In the two peaks at 620 and 680 nm, however, the fluorescence intensity of the adenomas is relatively greater, and the fluorescence curves actually cross near 650 nm. This relative difference in fluorescence intensity at longer wavelengths is highlighted in Fig. 24(b), where these average spectra have been normalized to unity at 460 nm.

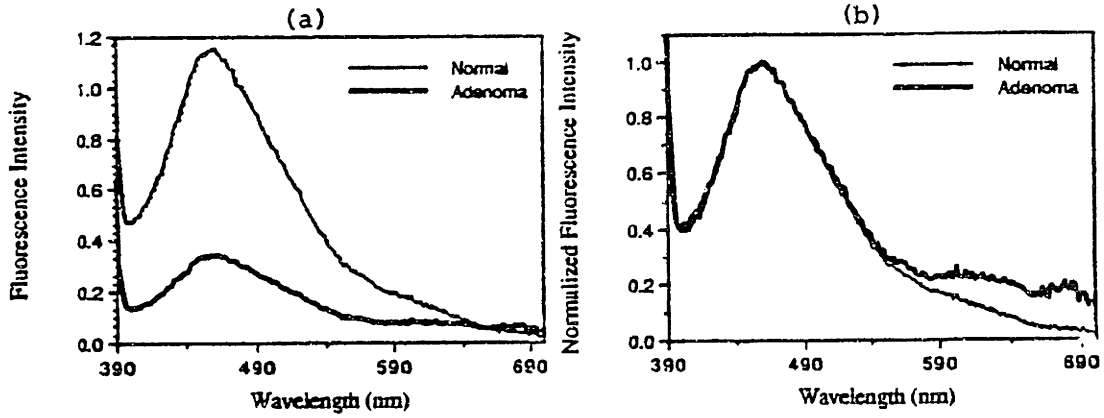

Figure 24: (a) Average spectrum of normal colonic mucosa and colonic adenoma. (b) The same average spectra of normal colonic mucosa and normal tissue, with fluorescence intensity normalized to unity at 460 nm.

These differences are illustrated quantitatively in Fig. 25, which shows the ratio of the average adenoma spectrum to the average normal spectrum. The differences in the 460 nm peak are reflected here; from 400-560 nm the ratio spectrum exhibits a flat region,

where the fluorescence intensity of adenoma is less than that of normal tissue. At wavelengths greater than 560 nm, the relatively increased fluorescence of adenomas is indicated as an upward sloping curve, peaking near 680 nm.

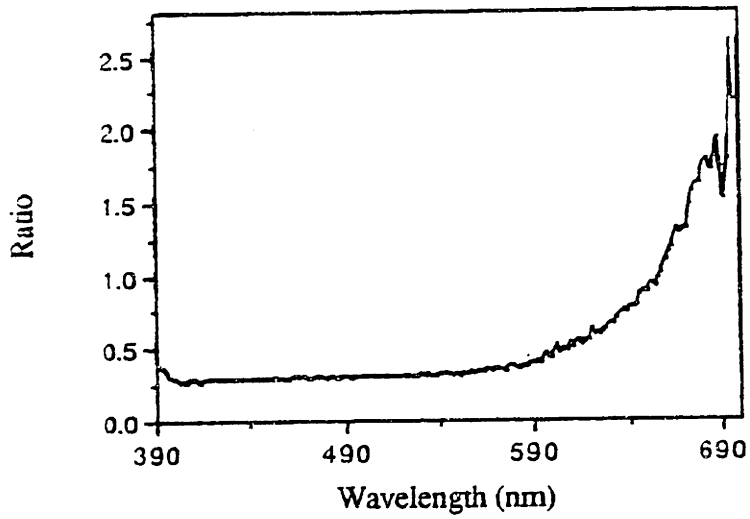

Figure 25: Average ratio spectra of adenoma to normal colonic mucosa.

4:4.2.3: Scatter Plot Diagnostics

This suggests that, for diagnostic purposes, we can reduce our spectroscopic data to fluorescence intensities at two wavelengths, one in the region 400 to 560 nm, the other greater than 560 nm. We have chosen these wavelengths as 460 nm and 680 nm. Below 560 nm, the ratio spectrum is flat, indicating that there is similar diagnostic information at all wavelengths in this region. Experimentally, we can obtain this information most accurately at 460 nm, the peak of colon tissue fluorescence. The ratio spectrum peaks at 680 nm, thus the fluorescence intensity at this wavelength provides the most useful diagnostic information above 560 nm. Table 8 lists the average and standard deviations of the fluorescence intensities at these wavelengths from samples in each histologic category.

Table 8: Average fluorescence intensities ± standard deviations at 460 nm and 680 nm for all histologic categories.

Histologic Category	Average I(460) ± Standard Deviation	Average I(680) ± Standard Deviation
Normal	1.15± 0.43	0.37 ± 0.023
Benign Lymphoid Aggregate	0.85 ± 0.58	0.06 ± 0.07
Hyperplastic Polyp	0.54 ± 0.16	0.03 ± 0.02
Tubular Adenoma	0.32 ± 0.12	0.07 ± 0.05
Tubulovillous Adenoma	0.40 ± 0.11	0.05 ± 0.02
Villous Adenoma	0.39 ± 0.05	0.02 ± 0.005
Non-Adenomatous Tissue	1.03 ± 0.49	0.04 ± 0.04
Adenoma	0.34 ± 0.12	0.06 ± 0.05

Data at these emission wavelengths were utilized in defining and evaluating diagnostic algorithms for the presence of adenoma. Although differences were observed in the fluorescence spectra of tissues from all histologic categories, initially we attempt only to distinguish adenomas from all other types of colonic mucosa (normal, benign lymphoid aggregates and hyperplastic polyps). This is the most clinically relevant histologic distinction, and we observed the largest spectroscopic differences between tissues from these two categories.

Algorithms were defined in two ways; the first method utilized scatter plots of fluorescence parameters of each of the individual samples. Scatter plots were divided into regions corresponding to adenomatous and non-adenomatous tissue using straight line segments to represent the decision surface. Decision surfaces were chosen to minimize the number of samples which were misclassified. Algorithms for identifying adenoma were evaluated by noting specificity, sensitivity and predictive value [38].

Given the fluorescence intensities at two wavelengths, four types of scatter plots can be defined; three one dimensional plots: I(460), I(680) and I(680)/I(460) for all samples, and one two dimensional plot: I(460) vs I(680) for all samples. This two dimensional plot, shown in Fig. 26, resulted in the most accurate classification scheme. The decision surface shown correctly classifies 95% of the 77 samples as adenomatous or non-adenomatous. The algorithm has a specificity of 91%, a sensitivity of 100% and a predictive value of 89%.

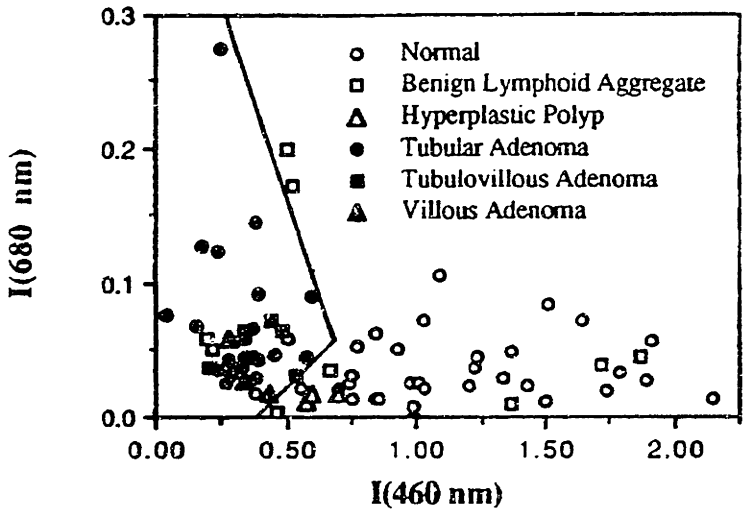

Figure 26: Two dimensional scatter plot of the fluorescence intensity at 460 nm vs. that at 680 nm for all 77 samples. The straight lines represent the a decision surface which minimizes the number of samples misclassified.

One normal sample, one hyperplastic polyp and two benign lymphoid aggregates were misclassified. No adenomas were misclassified. The proportionately higher misclassification rate for hyperplastic polyps and benign lymphoid aggregates can be understood simply in terms of the average values of the fluorescence intensities at 460 and 680 nm for these tissue types. Normal tissues exhibit a greater fluorescence intensity at 460 nm and a lower fluorescence intensity at 680 nm than adenomas. The fluorescence of hyperplastic polyps, however, while lower than that of adenomas at 680 nm, is more similar to adenomas at 460 nm. Benign lymphoid aggregates have a fluorescence intensity at 680 nm that is more similar to adenomas.

Although the diagnostic algorithm presented in Fig. 26 is simple to define, it suffers from two fundamental problems. First, the diagnostic implications of samples with data points near the decision surfaces are unclear. The algorithm incorrectly classifies a small number of samples, most of which fall near the decision surfaces, implying that the closer a data point is to the decision surface, the less likely the classification is accurate. This uncertainty, however, is difficult to quantify. The second problem associated with this method of algorithm development is that the algorithm minimizes the sample misclassification rate only for the sample set with which it was defined. Because the decision surfaces are drawn 'around' discrete points representing individual samples, the resulting algorithm may not be optimized for other data sets, even

those whose fluorescence properties are similarly distributed. Furthermore, this type of algorithm is not optimized for data sets which have largely different proportions of adenomatous and non-adenomatous tissue than the defining data set.

4:4.2.4: Probability Algorithm

Our second method of algorithm development relies on statistical techniques to overcome these problems. This method, described in detail in Chapter Two, is based on posterior probabilities, the probability that an unknown sample is either adenomatous or non-adenomatous given its individual fluorescence properties [38]. Unknown samples are allocated to the histologic category for which they have the highest posterior probability. In other words, the decision surface represents the surface where the posterior probabilities for adenoma and non-adenomatous tissue are equal.

We used this statistical method to recalculate the decision surfaces for the two dimensional plot of the fluorescence intensity at 460 nm vs that at 680 nm shown in Fig. 26. The posterior probabilities for adenoma and non-adenoma given the fluorescence intensities at these two wavelengths can be calculated according to Bayes rule as:

$$(1)\ P(NA \mid I(460), I(680)) = \frac{p(NA)P(I(460), I(680) \mid NA)}{p(NA)P(I(460), I(680) \mid NA) + p(A)P(I(460), I(680) \mid A)}$$

$$P(A \mid I(460), I(680)) = \frac{p(A)P(I(460), I(680) \mid A)}{p(NA)P(I(460), I(680) \mid NA) + p(A)P(I(460), I(680) \mid A)}$$

Calculating the posterior probability requires two additional probabilities. The prior probabilities, p(NA) and p(A), denote the proportion of unknown samples which are non-adenomatous and adenomatous respectively. For our data set, these are 0.6 and 0.4, respectively. The probability distributions of the fluorescence intensities at these two wavelengths given non-adenomatous and adenomatous samples, P(I(460),I(680) | NA) and P(I(460),I(680) | A), must also be known. Assuming the fluorescence intensities at these two wavelengths are independent quantities[4], these multi-wavelength distributions are the product of the single wavelength distributions:

[4]The scatter plot of I(460) vs I(680) exhibited little correlation between the variables, and the square of the correlation coefficient of I(460) with I(680) was calculated to be .067, indicating that 6.7% of the variation in I(680) could be accounted for by variation in I(4600).

$$(2)\ P(I(460),I(680) \mid NA) = P(I(460) \mid NA)\ P(I(680) \mid NA)$$

$$P(I(460),I(680) \mid A) = P(I(460) \mid A)\ P(I(680) \mid A)$$

Here, we assume that these single wavelength distributions can be approximated by the truncated normal distribution, which is given by:

$$(3)\quad P(x) = \frac{\frac{1}{\sqrt{2\pi}\,\sigma}\exp\left(\frac{(x-m)^2}{2\sigma^2}\right)}{1 - \int_{-\infty}^{0}\exp\left(\frac{(x-m)^2}{2\sigma^2}\right)dt}$$

In this formulation, m and σ represent parameters of the distribution which can be related to the mean and standard deviation [39]. This distributions is frequently used to describe concentrations in chemical and biological species. Although we use it here for fluorescence intensities, in principle, if the emission of individual chromophores is well separated, these fluorescence intensities are proportional to the concentrations and quantum yields of tissue chromophores.

We calculated these four individual distributions, P(I(460) | NA), P(I(460) | A), P(I(680) | NA) and P(I(680) | A), for our data set by adjusting these parameters in an iterative fashion, until the mean and standard deviation of the distributions were within 1% of the mean and standard deviation of our data. Figure 27 compares these distributions to histograms of our data, and demonstrates that they describe our data reasonably well.

These single wavelength distributions were used to calculate the joint probability distributions P(I(460),I(680) | NA) and P(I(460),I(680) | A) according to Eq. (2); these are shown in Fig. 28. Finally, the posterior probabilities for adenoma and non-adenoma were calculated for the prior probabilities of our data set according to Eq. (1). The posterior probability is shown for adenoma in Fig. 29; that for non-adenoma is simply 1 minus that for adenoma.

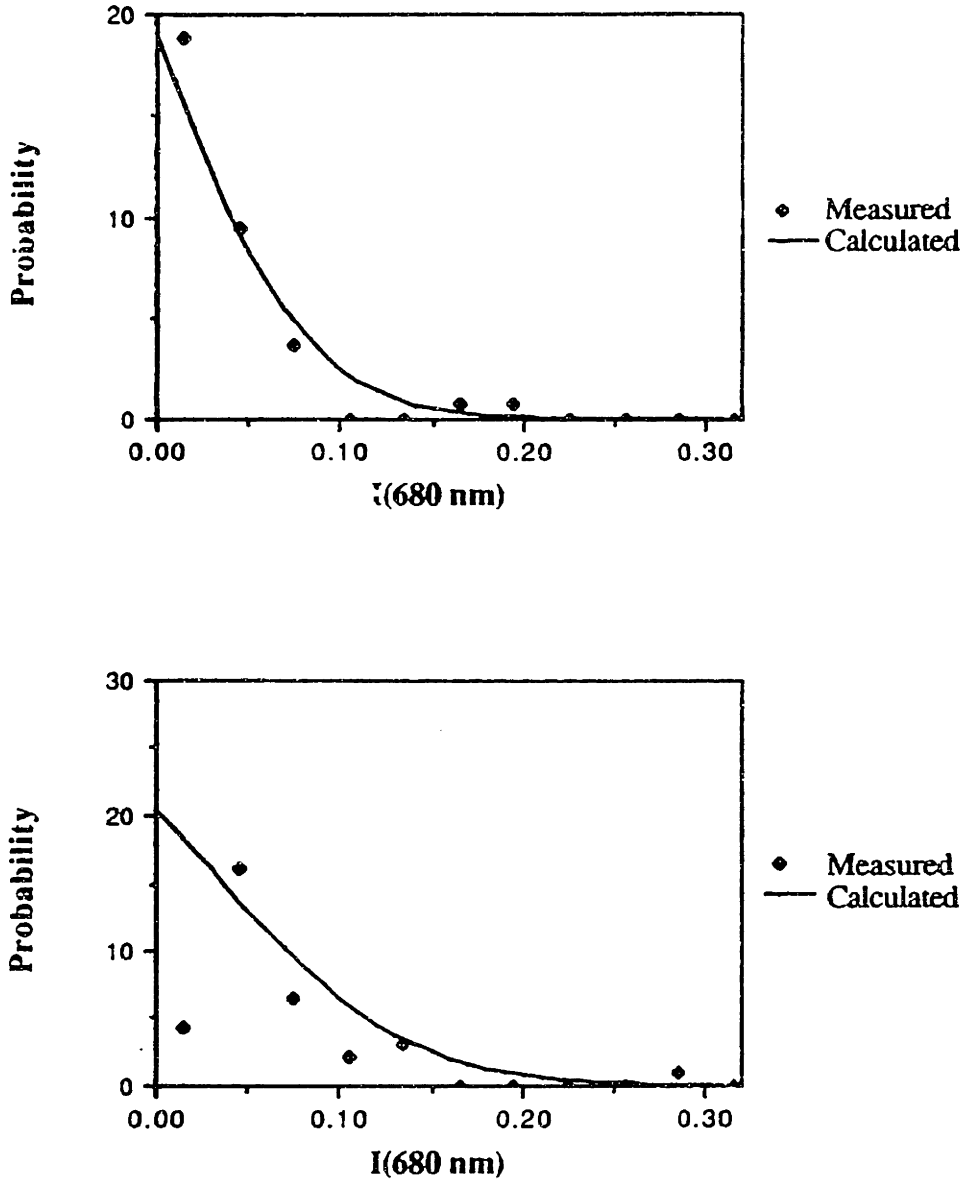

Figure 27 (cont.): (b) Comparison of experimentally measured and calculated probability distributions, P(I(680) | NA) and P(I(680) | A). Distributions were calculated according to Eq. (3).

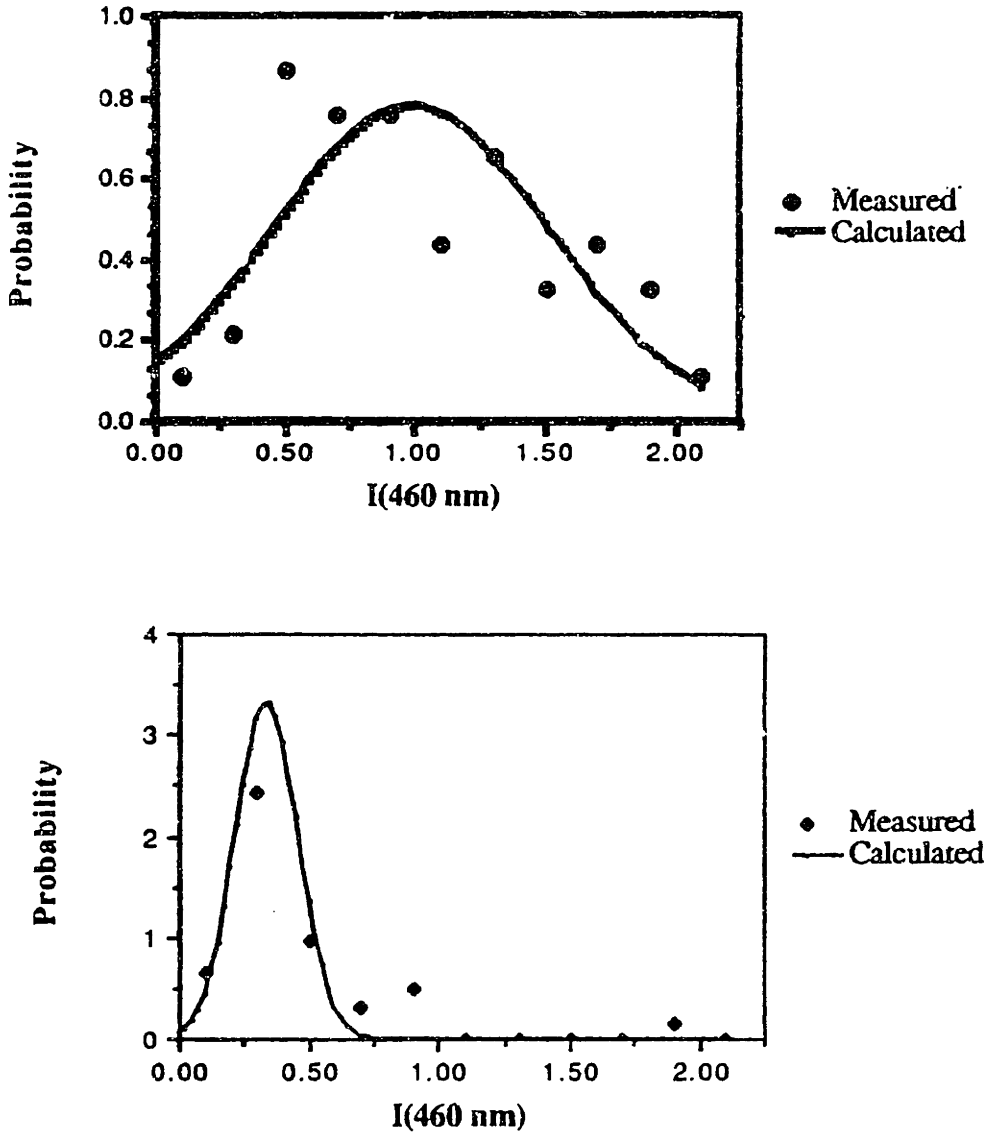

Figure 27: (a) Comparison of experimentally measured and calculated probability distributions, P(I(460) | NA) and P(I(460) | A).

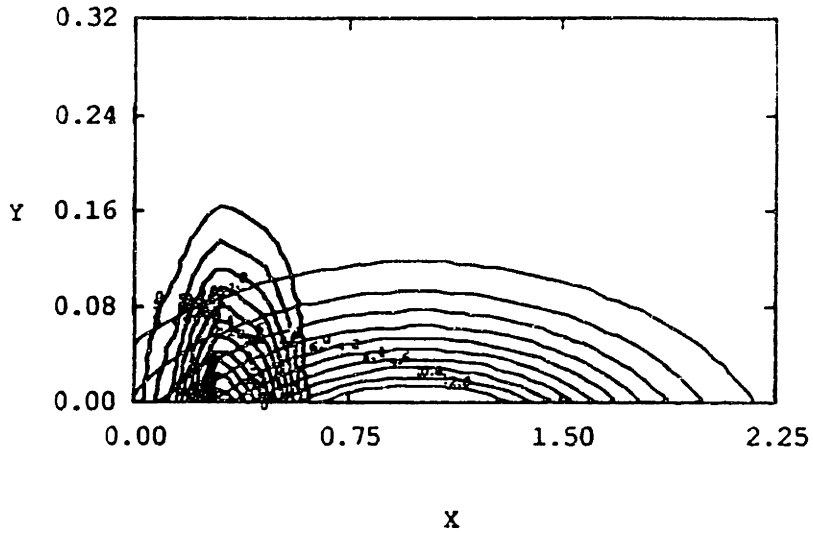

Figure 28: Joint probability distributions P(I(460),I(680) | NA) and P(I(460),I(680) | A). In each case, 10 linearly spaced contours are shown from the maximum probability to zero.

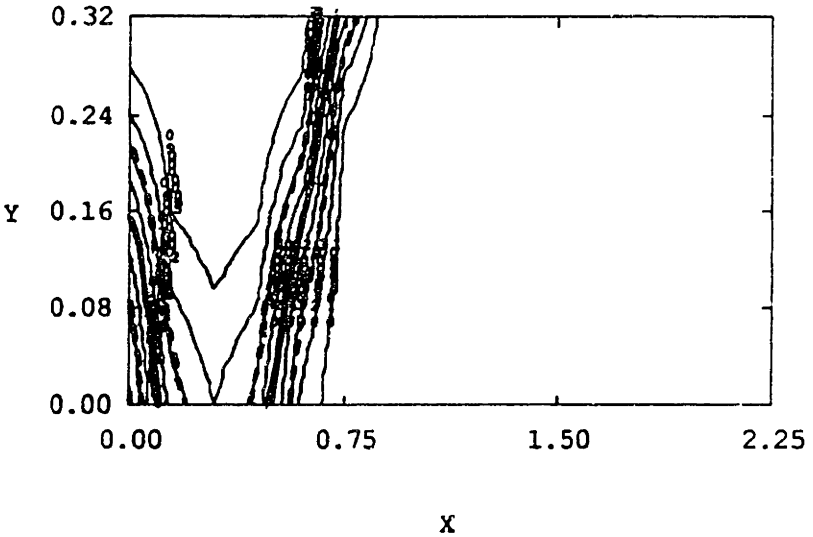

Figure 29: Posterior probability distribution, P(A | I(460),I(680). P(NA | I(460),I(680)) is not shown but is given simply by 1 - P(A | I(460),I(680)). 10 linearly spaced contours are shown from 0.1 to 1.0. The bold line indicates the equal probability contour at 0.5. The dashed lines represent the .7/.3 probability contours.

Equation (1) and Figure 29 represent the key to calculating statistically meaningful decision surfaces. In Fig. 29, the equal probability surface (0.5) is shown in bold; this represents the decision surface. The other contours shown in Fig. 29 provide a method of interpreting the diagnostic implications of points close to the decision surface. The dotted lines on either side of the decision surface indicate the surface for which the posterior probability for adenoma:non-adenoma is in the ratio 0.7:0.3 or 0.3:0.7. Unknown samples with posterior probabilities outside these lines have a greater than 70% probability of belonging to the histologic category to which they are allocated by the decision surface.

Figure 30 shows the scatter plot of Fig. 26 with the decision surface and confidence limits defined from the posterior probabilities in Fig. 30. This decision surface correctly classifies 86% of the 77 samples. It has a specificity of 85%, a sensitivity of 87% and a predictive value of 79%. It is important to note that nearly all (87%) of the 77 samples fall outside the confidence limits on our decision surface.

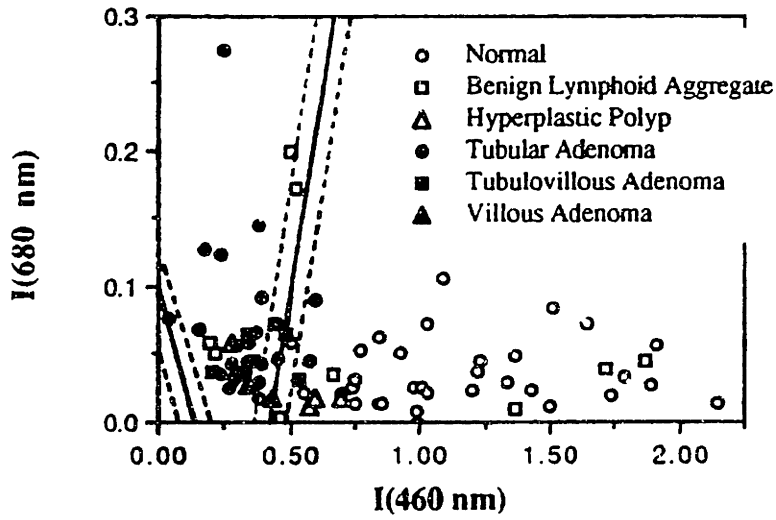

Figure 30: Scatter plot of Fig. 26 with the decision surface and confidence limits defined from the posterior probabilities in Fig. 29.

This algorithm misclassifies the same 4 samples that were misclassified in Fig. 26; however, an additional 3 tubular adenomas and 1 villous adenoma are also misclassified. This poorer performance is a reflection of the fact that the decision surfaces here are drawn according to probability distributions, rather than 'around' discrete data points. The performance of this statistically based algorithm is likely a more realistic estimate of the diagnostic capabilities of algorithms based on these fluorescence

parameters with data sets other than the one used to define it. In addition, it is important to point out that this algorithm can be easily generalized for data sets with different proportions of adenomatous and non-adenomatous tissues, by adjusting the prior probabilities in Eq. (1).

The performance of the decision surfaces shown in Fig. 30 can be easily extrapolated to data sets with different prior probabilities using Eq. (4), which gives the positive and negative predictive values as a function of prior probability of disease [38].

$$(4)\quad PV_{+} = \frac{(1-p)SP}{(1-p)SP + p(1-SE)}$$

$$PV_{-} = \frac{pSE}{pSE + (1-p)(1-SP)}$$

Figure 31 shows a plot of positive and negative predictive value as a function of the prior probability of encountering adenoma. This figure is drawn for the decision surfaces in Fig. 30, and illustrates that the predictive value of this algorithm depends strongly on the prior probability of encountering adenoma. The predictive values of our data set are shown with arrows at prior probability of adenoma, p = 0.39.

This curve puts limits on the incidence of adenoma for which the decision surfaces in Fig. 30 are useful, and indicates for which prior probabilities these surfaces will need to be adjusted. The positive and negative predictive values are quite high over a wide range of prior probabilities (0.25 < prior probability < 0.75). The positive predictive value reaches 0.5 at p = .15, while the negative predictive value reaches 0.5 at p = .85. As the predictive value gives the probability that we have made a correct diagnosis, these values of the prior probability of adenoma indicate the regions over which the performance of the algorithm in Fig. 30 is better than chance. For prior probabilities outside the region where the positive and negative predictive values are high, it is necessary to redraw the decision surfaces of Fig. 30 according to Eq. (1).

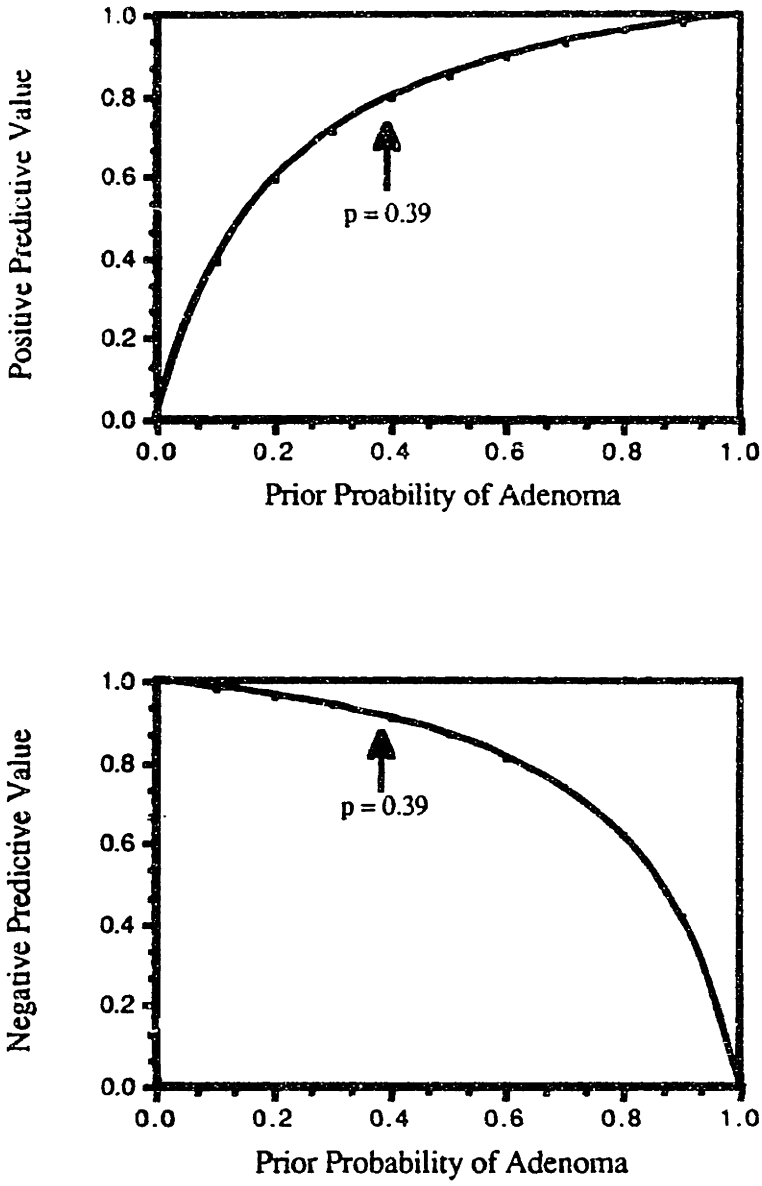

Figure 31: (a) Positive and (b) negative predictive value as a function of prior probability of adenoma for the decision surfaces of Fig. 30.

It is useful to compare the incidence of the various tissue classifications in our defining data set to that typically encountered in different clinical settings. In one series of 105 patients with 201 sporadic epithelial polyps at the Cleveland Clinic Foundation, adenoma was found in 53.7%, 21.9% were hyperplastic, 12.9% were normal, and 5.5% were grouped together with non-specific diagnoses of benign lymphoid aggregate, chronic inflammation, lamina propria muciphages, lamina propria edema and submucosal

lipoma. The remaining 6% included diagnoses of adenoma plus adenocarcinoma, adenocarcinoma, hyperplastic polyps with adenoma, juvenile polyp, carcinoid tumor and samples insufficient for diagnosis. The incidence of normal (41%), adenomatous (39%), and hyperplastic (5%) tissues, and benign lymphoid aggregates (12%) in our defining data set was similar. However, in screening for dysplasia by selected mucosal biopsy in patients with MUC, dramatically different incidence rates have been reported. In one series of 77 biopsies from 16 patients with MUC at the Cleveland Clinic Foundation, low or high grade dysplasia was reported in 6.5%. 90.9% were negative for dysplasia and 2.6% were indeterminant for dysplasia. This suggests that in screening for dysplasia in this condition, it will be necessary to modify the decision surfaces in Fig. 30 for more appropriate prior probabilities.

4:4.2.5: Differences Between *in vitro* and *in vivo* Data

At 370 nm excitation, the spectra of normal colon and tubular adenomas obtained *in vivo* were in general similar to those obtained *in vitro* with the spectral catheter system at 369.9 nm excitation. The peak fluorescence intensity of normal tissues was approximately 4 times greater than that of tubular adenomas both *in vivo* and *in vitro*. However, above 650 nm, *in vivo*, adenomatous tissues displayed greater fluorescence intensity than normal tissues. *In vitro*, this difference was much less pronounced.

There were also subtle differences appreciated in the fluorescence lineshapes of these tissues *in vivo* and *in vitro*. Spectra of both normal and adenomatous colon obtained *in vivo* displayed less structure in the region from 400 to 600 nm. In general, only a single peak was present at 460 nm with valleys at 420, 540 and 580 nm. However, *in vitro*, subsidiary maxima were present at 480 nm in normal tissue and 500 nm in adenomatous tissue. In some cases (Fig. 22(a)), these subsidiary maxima were observed in a few of the nine to fifteen individual spectra obtained from a single site *in vivo*. However, they were rarely present in the average per site spectrum. This suggests that in this averaging procedure, some information is lost. Finally, the valley at 420 nm was more pronounced in the fluorescence spectra of normal and adenomatous colon obtained *in vitro*. In particular, below 420 nm, *in vitro* the fluorescence intensity of adenomas was relatively greater than that of normal tissue. *In vivo*, this difference was not observed.

These differences are all reflected in a comparison of the ratio of the average adenoma spectrum to the average normal spectrum calculated for data obtained *in vivo*

and *in vitro*. Despite these differences, it must be pointed out that very similar empirical diagnostic algorithms can be defined for the presence of adenoma *in vitro* (Fig. 20) and *in vitro* (Fig. 26). This demonstrates that many of the diagnostically significant features are observed both *in vivo* and in the research laboratory, and that, in addition, there are differences observed in spectra of normal and adenomatous tissues *in vivo* and *in vitro*.

4:5: Morphologic/Biochemical Basis of Fluorescence

The previous sections have demonstrated that fluorescence spectroscopy is a promising technique for diagnosing the presence of colonic adenoma. However, the diagnostic algorithms presented thus far have employed an empirical analysis of tissue fluorescence spectra. In this section, we demonstrate that the fluorescence spectra of tissue are directly related to its histochemical composition. We compare the fluorescence EEMs of tissue presented earlier to fluorescence EEMs of pure biomolecules to obtain a potential identification of tissue fluorophores at the chemical level. In addition, we identify tissue fluorophores at 370 nm excitation at the morphologic level, using fluorescence and light microscopy of stained and unstained sections of tissue. The optical properties of these morphologic constituents of tissue are measured with 370 nm excited fluorescence microspectroscopy. This work provides the basis for applying models of tissue fluorescence to the fluorescence spectra of colonic tissue.

4:5.1: EEMs

In general, tissue fluorescence spectra contain contributions from both intrinsic fluorescence and attenuation. In order to compare the EEMs of pure biomolecules to tissue EEMs, it is first necessary to separate the effects of attenuation from tissue EEMs.

Total reflectance spectra provide a measure of the attenuation contributions to tissue EEMs. In a total reflectance spectrum, valleys indicate peaks in attenuation. These attenuation peaks can be related to the tissue EEMs in the following way. Attenuation peaks act to produce valleys in the fluorescence spectra of optically thick tissue samples [36, 37]. As attenuation effects are important both for exciting and emitted radiation, valleys will be produced in both excitation and emission spectra. Thus, at the location of these attenuation peaks, one expects to see symmetrically located valleys in the tissue EEMs parallel to both the excitation and emission axes.

Attenuation effects, which include both scattering and absorption, were recorded independently by measuring total reflectance spectra of eight (four normal, four adenoma)

full thickness colonic specimens from four patients using a standard absorption spectrophotometer equipped with an integrating sphere. Three of the normal samples were matched controls from patients with familial adenomatous polyposis. Percent total reflectance was recorded from 250 - 700 nm with a resolution of 5 nm FWHM. Figure 32 shows average total reflectance spectra of four samples of normal colon and four colonic adenomas. In both types of tissues, reflectance valleys are located at 270, 355, 420, 540, 575, and 635 nm. These valleys are superimposed on a gently upward sloping background, which is slightly steeper for normal tissue.

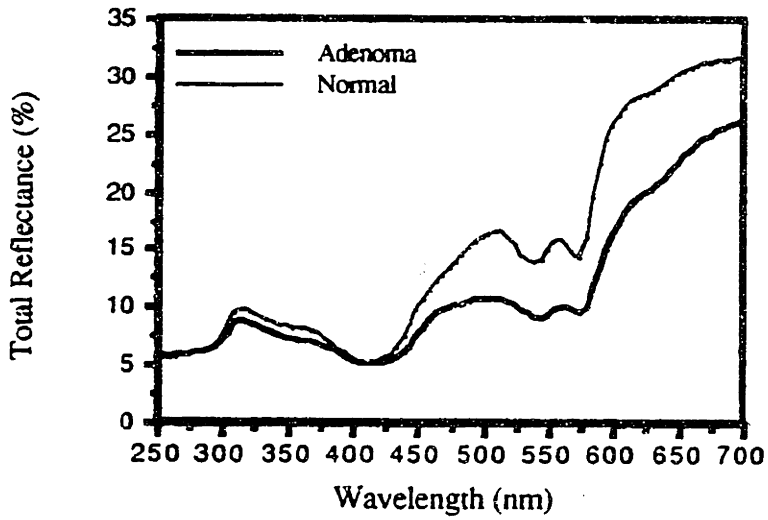

Figure 32: Average total reflectance spectrum of four normal colon samples (solid line), and average total reflectance spectrum of four adenomatous colon samples (bold line).

The valleys in the total reflectance spectra can be correlated with the valleys in the average EEMs shown in Figs. 3 and 4. The strongest attenuation peak at 420 nm gives rise to valleys in the tissue EEMs at 420 nm along both the excitation and emission axes. Although not as prominent, valleys are also present along the emission axis at 540 and 575 nm. A small valley along the excitation axis near 355 nm can also be appreciated.

It is well known that the absorption spectrum of oxy-hemoglobin exhibits peaks near 280, 350, 420, 540 and 580 nm [40]. Thus, nearly all of the attenuation peaks noted in the total reflectance spectra of normal and adenomatous colon in Fig. 32 could be ascribed to oxy-hemoglobin. The presence of oxy-hemoglobin could be attributed to the vascularity of the bowel wall [3]. The gently upward sloping background in the tissue

reflectance spectra is likely due to attenuation of other proteins. In general, protein absorption is strong in the UV region, but falls off strongly above 320 nm [41]. However, protein crosslinks, or other chromophores associated with extracellular structural proteins (i.e. collagen and elastin) and cellular proteins could contribute to this sloping attenuation.

Potential tissue fluorophores were identified by comparing excitation/emission peaks in tissue EEMs to those in EEMs of individual tissue constituents as well as peaks cited in the literature. EEMs of these molecules were obtained using the method outlined for gastrointestinal tissue in Chapter Two. Excitation/emission maxima are presented here for 1 mM buffered (pH = 7.4) isotonic (140 mM NaCl) aqueous solutions of tryptophan, NADH, NADPH, 4-pyridoxic acid, and pyridoxal 5'-phosphate. Data from dry powders of collagen I (bovine achilles tendon), collagen III (calf skin) and elastin (bovine neck ligament) are also given.

Table 9 contains a compendium of excitation/emission maxima from the EEMs of each of the biochemical compounds considered which might contribute to normal and adenomatous colon tissue EEMs [42, 43]. This list should not be considered exhaustive. Tables 2-5 list the local excitation/emission peaks in the colon tissue EEMs as well as our preliminary assignment of tissue fluorophores to these peaks based on comparison with Table 9.

Note, however, that the band positions in Table 9 do not exactly match the band positions in Tables 2-5. Two effects may be responsible for these differences. Attenuation acts to alter both the observed location of the excitation/emission maxima and observed lineshape of individual tissue fluorophores in the multi-component tissue EEMs. Similarly, the observed lineshapes and positions of chromophore maxima can be altered in multi-component tissue EEMs when the excitation and emission of individual chromophores closely overlap. For these reasons, our identifications should be considered preliminary.

Table 9: Summary of Excitation-Emission Maxima in Selected Biological Molecules

Chromophore/ Chromomorph	1 mM Solution/ Dry Powder?	(λ_{exc},λ_{em}) Maxima[a]
Tryptophan	Solution	(275, 350 nm)
NADH	Solution	(350, 460 nm)
NADPH	Solution	(350, 460 nm)
4-Pyridoxic Acid	Solution	(300, 435 nm)
Pyridoxal 5'-phosphate	Solution	(305, 375 nm) (410,520 nm)
Collagen I	Powder	(340, 395 nm) (270, 395 nm) (285, 310 nm)
Collagen III	Powder	(275, 310 nm) (330, 390 nm) (370, 450 nm)
Elastin	Powder	(460, 520 nm) (360, 410 nm) (425, 490 nm) (260, 410 nm)
Pyridoxic acid lactone [42]		(360, 430 nm)
Porphyrins [43]		(400, 675 nm) (400, 610 nm)

[a] Where more than one maxima is given, they are listed in order of decreasing fluorescence intensity.

The largest peak in the tissue EEMs near (290, 330 nm) has been assigned to the aromatic amino acid tryptophan, which has a maximum at (275, 350 nm) when in aqueous solution. The small difference in intensity of the tryptophan peak in normal and adenomatous tissues could be due either to a difference in the concentration of tryptophan or its environment [44].

Potential fluorophores for the tissue peak at (345, 465 nm) include NADH and NADPH. These molecules function as co-enzymes in oxidation-reduction reactions, and both have an excitation/emission maximum at (350, 460 nm) in aqueous solution. It should be noted that the (345, 465 nm) peak is bounded by attenuation valleys at 420 nm along the excitation and emission axes. Thus, the precise location of its excitation/emission maximum may be significantly shifted, and our preliminary assignment of this peak to NADH/NADPH should be regarded with this caveat.

Several peaks which appear in tissue EEMs are near peaks associated with chromophores related to vitamin B_6. The peak unique to normal tissue at (315, 430 nm) is near that of 4-pyridoxic acid at (300, 430 nm). The shoulder in adenomatous tissue at (370, 420 nm) is near the reported maximum of pyridoxic acid lactone at (370, 440 nm)

[42]. Although three peaks are present in the normal and adenomatous tissue EEMs at (460, 530 nm), (465, 555 nm) and (470, 595 nm), they are likely due to a single peak with superimposed oxy-hemoglobin attenuation valleys at 540 and 580 nm. Pyridoxal 5'-phosphate represents a potential candidate for this peak. Its largest excitation/emission maximum is at (410, 520 nm); the shift in the tissue excitation maximum could be attributed to the Soret band attenuation of oxy-hemoglobin. The effects of oxy-hemoglobin attenuation are reduced in the ratio map, and the peak assigned to pyridoxal 5'-phosphate is observed at (400, 480 nm). In addition, pyridoxal 5'-phosphate exhibits a second peak at (305, 385 nm) which is near the peak found at (330, 385 nm) in the normal tissue EEM.

These peaks assigned to pyridoxal 5'-phosphate could also be due to structural protein fluorescence. Elastin fluorescence exhibits a maximum at (460, 520 nm). Collagen I and collagen III fluorescence show peaks at (340, 395 nm) and (330, 390 nm), respectively. Microspectrofluorimetry studies, described later, can separate contributions of extra- and intra-cellular fluorescence, and provide the definitive answer.

Finally, the peaks unique to adenomatous tissue fluorescence at (430, 600 nm) and (430, 670 nm) could be due to the presence of endogenous porphyrins. Hematoporphyrin derivative, for example, which is a mixture of several biologically relevant porphyrins, exhibits fluorescence excitation emission maxima near (400, 610 nm) and (400, 675 nm) [43].

As noted above, comparison of EEMs from individual biochemical compounds with optically thick tissue EEMs does not always lead to definitive fluorophore identification, because of potential difficulties created by attenuation and overlapping excitation and emission. Both of these difficulties can be overcome by modeling the tissue EEM in terms of the attenuation and fluorescence properties of individual chromophores.

It is interesting to note that the fluorophores preliminarily assigned here have been previously associated with pre-cancerous and cancerous states. For example, the peak assigned to NADH or NADPH is twice as intense in normal tissue as in adenomatous tissue EEMs. Schwartz et al found that the absolute concentrations of NAD+ and NADH decreased 2-3 fold following murine sarcoma virus transformation in rat kidney fibroblasts [45]. The peaks assigned to pyridoxal 5'-phosphate are also approximately twice as intense in the normal tissue as in adenomatous tissue EEMs. Several workers

have reported decreased levels of serum pyridoxal 5'-phosphate in cancer patients [46]. The peaks assigned to porphyrins were most prominent in the adenomatous tissue EEM. An increased content of endogenous porphyrins has been noted in neoplasms of other organ systems [47].

This has important implications for the interpretation of the tissue emission spectra excited at 370 nm presented earlier. Near 370 nm excitation, potential chromophores identified from the EEMs include the structural proteins, elastin, and type I and III collagen, NADH, NADPH, pyridoxal 5' phosphate and pyridoxic acid lactone. Figure 33 shows emission spectra of each of these chromophores (except pyridoxic acid lactone) excited at 370 nm. These spectra represent the 370 nm excited spectrum from the corresponding chromophore fluorescence EEM.

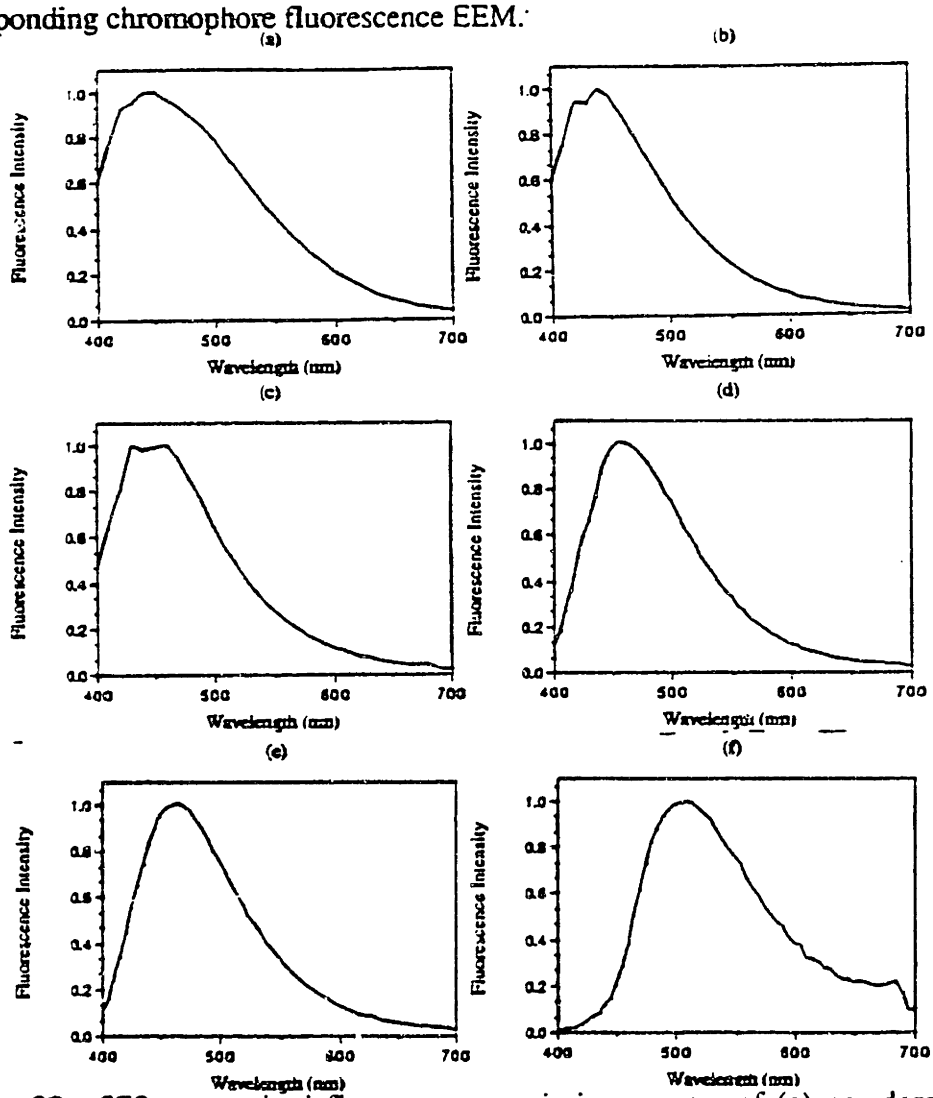

Figure 33: 370 nm excited fluorescence emission spectra of (a) powdered bovine elastin, (b) powdered bovine collagen, type I, (c) powdered bovine collagen, type III, (d) 1 mM NADH, (e) 1 mM NADPH, and (f) 1 mM pyridoxal 5' phosphate.

At 370 nm excitation, the emission spectrum of elastin peaks near 450 nm. At this excitation wavelength, collagen I and III show similar emission lineshapes, peaking near 430 nm. NADH and NADPH show similar fluorescence emission spectra at this excitation wavelength, with a peak at 455 nm. The 370 nm excited emission spectrum of pyridoxal 5' phosphate peaks near 510 nm.

With these identifications, we can preliminarily interpret the chemical information contained in the 370 nm tissue fluorescence spectra presented earlier. We will concentrate on data obtained with the spectral catheter, for two reasons. As the collection geometry was carefully controlled in this system, the effects of reabsorption were minimized in the resulting spectra. Furthermore, the absolute fluorescence intensity information was preserved in this data.

Both normal tissue and adenomatous tissue exhibited a peak at 460 nm. The potential chromophores/chromomorphs for this peak include the structural proteins and NADH or NADPH. The peak emission of NADH and NADPH and NADPH more closely matches that of the tissue peak; however, the tissue attenuation peak at 420 nm could significantly red shift the observed emission maximum of the structural proteins to 460 nm. This peak was approximately four times less intense in the adenoma spectra; this could be due to a decrease in NADH or NADPH in the adenoma [45]. This observation could also be consistent with structural protein fluorescence, as the submucosa contains much of the structural protein in the colon. In adenomatous polyps, the mucosa becomes much thicker, thus the relative contribution of structural proteins in the submucosa to the tissue fluorescence spectrum could decrease. Again, microspectroscopy can provide the answer to this question.

The emission spectrum of pyridoxal 5' phosphate peaks near 510 nm. The fluorescence spectrum of adenomatous tissue showed a subsidiary maximum near 510 nm, this chromophore represents a possible explanation for this peak. Although decreased levels of pyridoxal 5' phosphate have been reported in the serum levels of cancer patients [46], no studies have reported tissue levels of this chromophore in neoplasia.

4:5.2: Fluorescence Microscopy at 370 nm Excitation

The previous studies have shown that fluorescence EEMs can be used to provide a chemical interpretation of tissue fluorescence spectra. In this section, we will show that

fluorescence microscopy and microspectroscopy can be used to provide a morphologic interpretation of the basis of tissue fluorescence. These methods of interpreting tissue fluorescence spectra provide complimentary information, which ultimately will allow us to model tissue fluorescence spectra in order to extract parameters from fluorescence spectra which are related to the histochemical composition of tissue.

4:5.2.1: Identification of Chromomorphs[5]

A combination of fluorescence microscopy and light microscopy were used to morphologically identify the fluorescent structures contributing to the 370 nm excited fluorescence emission spectra of colon. Autofluorescent structures within normal and adenomatous colon were identified from unstained frozen sections of tissue using a fluorescence microscope. Serial sections were then stained with various histochemical stains and viewed under the light microscope in order to identify these fluorescent structures at the morphologic level.

Ten specimens of normal colon were obtained from uninvolved areas of resection specimens from 10 patients with rectal adenocarcinoma, diverticular disease or hyperplastic polyps. Six tubular adenomas were collected from colectomy specimens of four patients with familial adenomatous polyposis. Specimens were snap frozen in liquid nitrogen and isopentane and stored at -70°C until use. Later, specimens were serially cut into 8 µm thick sections with a cryostat microtome and stored at -20°C. Before study with the fluorescence microscope, slides were coverslipped with a non-fluorescent aqueous mounting medium (glycerin and phosphate buffered saline, 9:1). Before study with the light microscope, serial sections were stained with hemotoxylin and eosin (H&E) and Movat's pentachrome stains.

Tissue autofluorescence was viewed using an inverted fluorescence microscope adapted for laser illumination, diagrammed in Fig. 34. Multi-line excitation light from 351 - 364 nm was provided from a CW argon ion laser via a quartz optical fiber. As shown in Fig. 34, the distal tip of the fiber was positioned at an angle of approximately 30° to the stage, achieving approximately trans-illumination. A 250 µm diameter field of view was illuminated with this system, the excitation intensity was 100 mW/mm^2. At this excitation intensity, visible photo-bleaching was observed within several minutes. To control for this, each field of view was studied as rapidly as possible. A barrier filter

[5]The studies described in this section were largely the work of Tjeerd Romer and Maryann Fitzmaurice. Their contributions are gratefully acknowledged.

(long-pass filter) with a 50% transmission at 420 nm was used to view fluorescence. The morphology, distribution, color and intensity of autofluorescence were recorded for each fluorescent structure in each cryostat section studied.

In normal colon, four layers of the colon could be distinguished based on their autofluorescence: the mucosa, muscularis mucosa, submucosa and muscularis propria. With the 420 nm barrier filter, the submucosa demonstrated an intense, finely fibrillar, blue autofluorescence (Fig. 35(a)). This fluorescence could be attributed to collagen fibers in the submucosa, which stain yellow with the Movat's pentachrome stain. In the muscularis mucosa and muscularis propria, occasional collagen fibers were present on Movat's stain; these also demonstrated a similar blue, fibrillar fluorescence.

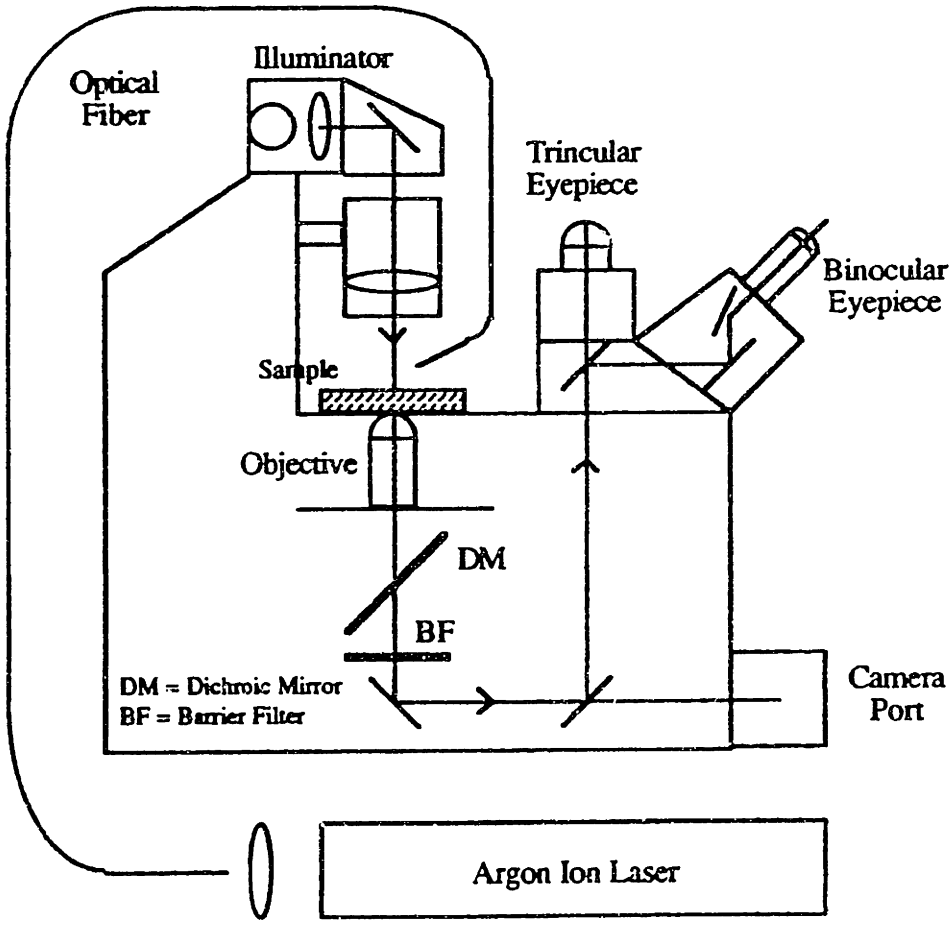

Figure 34: Block diagram of the inverted fluorescence microscope used to view the 351-364 nm nm excited autofluorescence of colon.

In the mucosa, three distinctly fluorescent structures could be observed. Collagen fibers in the connective tissue of the lamina propria contributed a blue fibrillar

autofluorescence, similar in color, but of weaker intensity relative to that of the submucosa. Yellow-amber, granular fluorescent deposits were also present in the lamina propria, most numerous near the lumenal surface. These were correlated to the presence of eosinophils in serial sections stained with H&E and Movat pentachrome stains. The granules of eosinophils have been previously described as intensely autofluorescence with green excitation [48]. An extremely faint blue-green fluorescence was associated with the fluorescence of absorptive cells. This fluorescence was most prominent near the base and membranes of these cells.

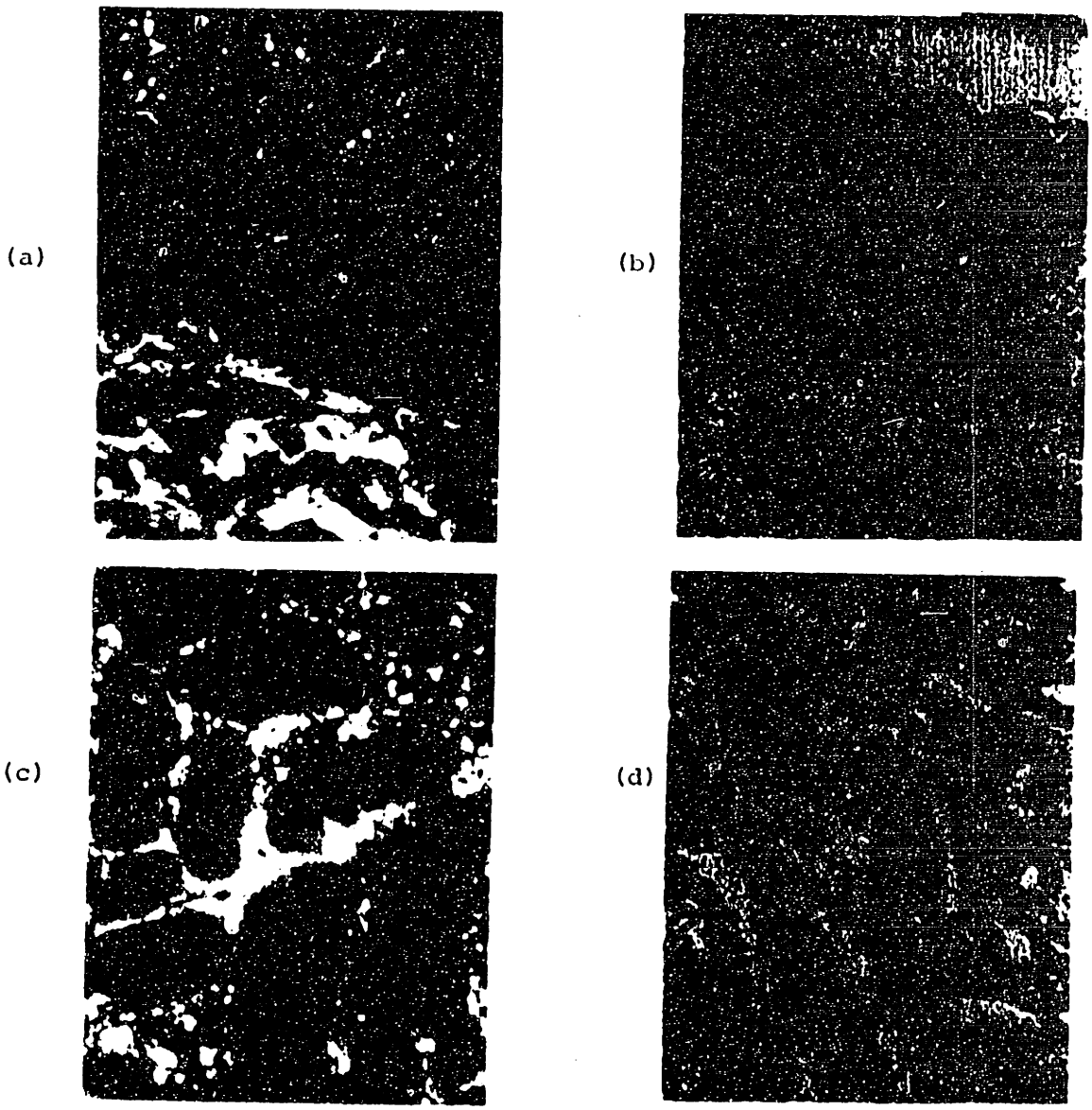

Figure 35: (a) Autofluorescence of normal colon as observed through the fluorescence microscope in Fig. 34. (b) Serial section of normal colon stained with H&E. (c) Autofluorescence of adenomatous polyp. (d) Serial section of adenomatous polyp stained with H&E.

In adenomatous polyps, again all layers of the bowel wall could be distinguished through the fluorescence microscope. The fluorescence of all layers except the mucosa resembled that of normal colon. In the mucosa of adenomatous polyps, again three distinctly fluorescent structures could be recognized. A faint, blue, fibrillar fluorescence, very similar to that observed in the mucosa of normal tissue was observed in the adenomatous mucosa (Fig 35(c)). This fluorescence again correlated to the presence of collagen fibers in the lamina propria by Movat's pentachrome stain. Again, yellow - amber fluorescent granules were observed in the mucosa of adenomatous polyps. These were similar in color and intensity to those observed in normal mucosa; however, they were more numerous and more evenly distributed in adenomatous mucosa. These were correlated to the presence of eosinophils in serial sections stained with H&E and Movat's pentachrome stains. This increase in the number of eosinophils is consistent with observations of other groups [15], and may be of prognostic significance.

The fluorescence of non-dysplastic absorptive cells within the polyp was quite similar to that of normal tissue. However, the fluorescence of dysplastic epithelial cells differed remarkable from that of non-dysplastic cells. A relatively homogeneous blue green fluorescence was observed within the cytoplasm of these cells. The intensity of this fluorescence appeared to correlate with the grade of dysplasia as determined from serial sections stained with H&E.

4:5.2.2: Fluorescence Microspectroscopy

In order to interpret tissue fluorescence spectra in terms of contributions from these chromomorphs, it is necessary to measure their emission spectra at 370 nm excitation. This was accomplished using the fluorescence microspectrometer described in Chapter Two. Using this system, 370 nm excited fluorescence emission spectra were recorded from two samples of normal colon from uninvolved areas of resection specimens of two patients colonic adenocarcinoma or diverticular disease. Fluorescence spectra were also recorded from four adenomatous polyps obtained from resection specimens of four patients with familial adenomatous polyposis. For each sample, several fluorescence emission spectra were recorded for each of the chromomorphs described in the previous section. The 40X objective was used in all cases except for recording fluorescence spectra from absorptive cells, in which case the 100X objective was used.

Each fluorescence spectrum was normalized to unity at the emission wavelength corresponding to peak emission. An average, normalized spectrum was calculated for each chromomorph in normal and adenomatous tissue. In cases where no significant differences were observed in the average normal and adenomatous chromomorph spectrum, an average spectrum was computed for all data. Figure 36 shows the resulting average spectrum for each chromomorph.

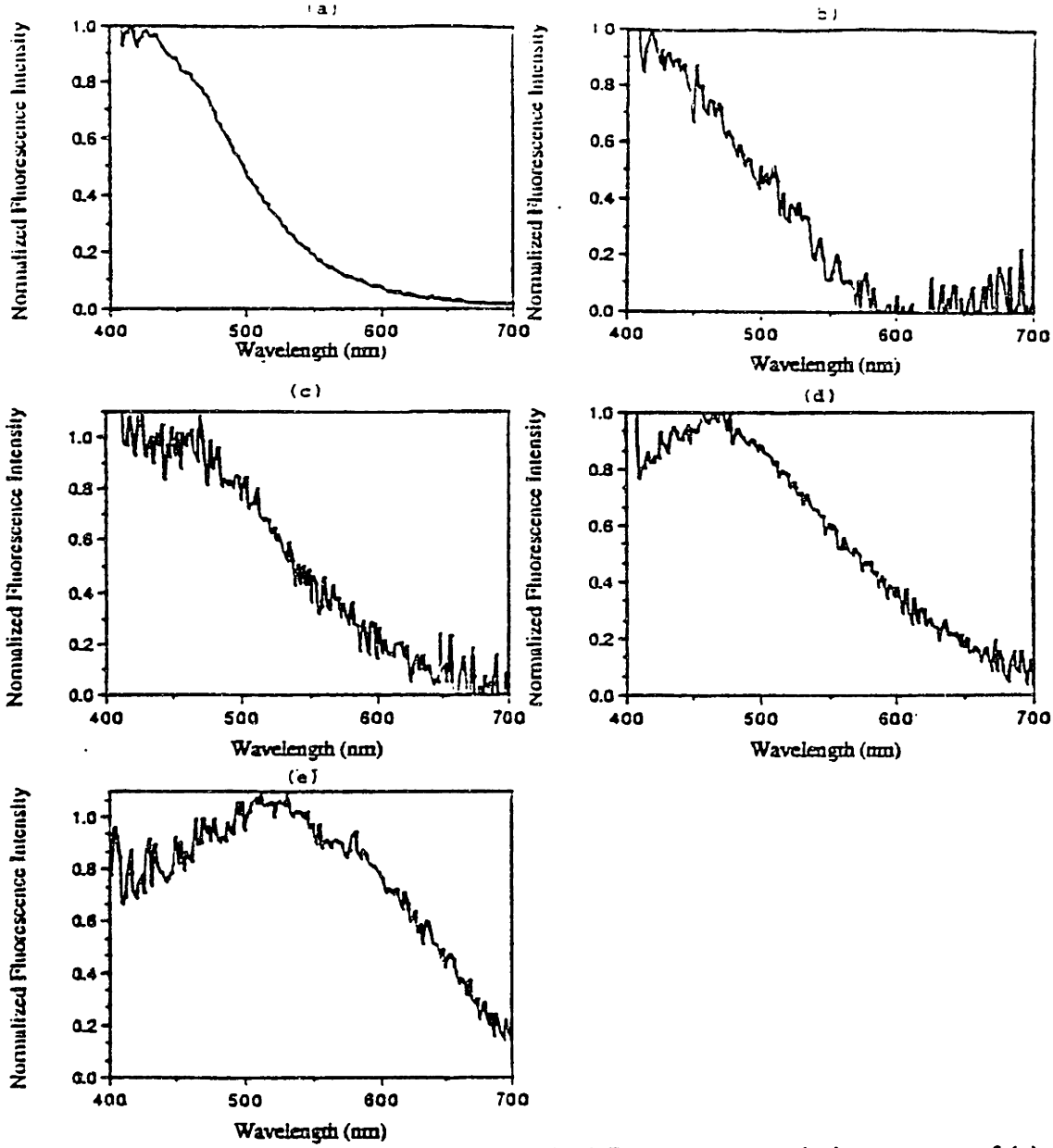

Figure 36: Average, normalized, 370 nm excited fluorescence emission spectra of (a) submucosal collagen, (b) collagen fibers in the lamina propria of normal mucosa, (c) collagen fibers in the lamina propria of adenomatous mucosa, (d) mucosal eosinophils, and (e) adenomatous mucosal absorptive cells.

The fluorescence lineshape recorded from collagen fibers in the submucosa of normal and adenomatous tissues was the same, peaking near 430 nm. The fluorescence lineshape of collagen fibers in the lamina propria of normal mucosa exhibited an identical lineshape. However, the fluorescence lineshape of collagen fibers in adenomatous mucosa was unique, exhibiting a broader fluorescence peak, with a maxima near 460 nm. Mucosal eosinophils in normal and adenomatous colon showed similar fluorescence lineshapes, consisting of a broad peak, centered at 480 nm. Absorptive cells in adenomatous mucosa displayed a broad fluorescence peak, with a maximum near 520 nm. The fluorescence emission spectra of absorptive cells in normal mucosa was exceedingly weak. The recorded signal was indistinguishable from that of lamina propria connective tissue, indicating possibly that the signal was too weak to be accurately recorded with this system.

These lineshapes can be used to interpret the fluorescence spectra of tissue presented earlier at a morphologic level. The spectra obtained with the catheter system will be discussed as the effects of attenuation are minimized in this data. In the average spectrum of normal colon obtained with this system, the peak at 460 nm can be attributed to the emission of collagen fibers in the submucosa and lamina propria. Although these chromomorphs have an emission which peaks around 430 nm, the Soret absorption band of oxyhemoglobin acts to shift the observed location of the maximum. The subsidiary maxima at 480 nm in this average spectrum is likely due to the fluorescence of eosinophils within the mucosa.

In the average adenoma spectrum, the peak at 460 nm can also be attributed to collagen fibers within the submucosa and lamina propria. Relative to normal colon, the intensity of this peak is decreased in adenomatous tissues. This is likely due to the increase in mucosal thickness of adenomatous polyps. The brightly fluorescent collagen fibers in the submucosa are further from the lumen, and thus, contribute less to the overall spectrum. Again, the Soret band of oxy-hemoglobin acts to shift the observed position of this maximum. Eosinophil fluorescence also contributes to the fluorescence spectrum of adenomatous colon. Finally, the peak at 520 nm peak observed in the adenoma spectrum can be attributed to the fluorescence of dysplastic absorptive cells.

Although microspectroscopy can be used to identify and characterize tissue chromomorphs, this technique provides limited insight about the chemical basis of tissue fluorescence. However, using EEMs, we were able to provide potential chemical

identification of tissue fluorophores. A comparison of these identifications should provide valuable insight into definitively establishing the histochemical basis of tissue fluorescence. Essentially by comparing the 370 nm excited fluorescence spectrum of individual chromomorphs (Fig. 36) with those of chromophores presented earlier (Fig. 33), the self consistency of these suggested chemical identifications can be tested.

A comparison of the fluorescence lineshape of submucosal collagen and collagen in the normal lamina propria shows that this emission is consistent with that of type I collagen. The emission lineshape of collagen in the adenomatous lamina propria more closely matches that of type III collagen. Although this emission spectrum is also consistent with that of NADH and NADPH, the localization that we can achieve with microspectroscopy shows that this is not likely the correct identification.

None of the potential fluorophores identified chemically matches the emission lineshape observed from eosinophils at this excitation wavelength. Eosinophil autofluorescence has been described previously, where it has been shown that this autofluorescence is associated with eosinophil granules [48-50]. Extracts of eosinophil granules demonstrate two excitation maxima at 370 and 450 nm; when fluorescence emission is excited at 450 nm, a single emission peak is observed at 520 nm [49]. Although this fluorescence has been associated with the granules, the identity of the associated fluorophore remains obscure [49, 50]. When examined under the electron microscope, eosinophil granules are composed of two regions: an electron dense core with a crystalline lattice structure, and an electron radio-lucent matrix [50]. The major component of the electron dense core is major basic protein (MBP); the amino acid sequence of this protein is known, and it contains 4% tryptophan [50]. The matrix is composed of several other proteins listed in Table 10 [50]. Many of these also contain tryptophan [50]. Table 10 also summarizes the functions of these proteins. In addition, the granules contain several enzymes; two of the major enzymes include eosinophil peroxidase and collagenase. Eosinophil peroxidase has a heme prosthetic group, with a Soret band absorption maximum at 412 nm, and molar absorption coefficient of 110 $mM^{-1}cm^{-1}$ [50]. The granules also contain several sulfated complex carbohydrates, including chondroitin 4-sulfate, chondroitin 6-sulfate and dermatan sulfate [50].

Table 10: Properties of Principle Eosinophil Granule Proteins. Adapted from [50].

Name	Site	Activities
MBP	Core	Toxic to parasites, murine tumor cells, many mammalian cells; causes histamine release from basophils and rat mast cells, neutralizes heparin.
ECP	Matrix	Shortens coagulation time, alters fibrinolysis; toxic to parasites; potent neurotoxin; inhibits cultures of peripheral blood lymphocytes; causes histamine release from rat mast cells.
EDN(EPX)	Matrix	Potent neurotoxin; toxic to parasites; inhibits cultures of peripheral blood lymphocytes.
EPO	Matrix	In the presence of H_2O_2 + halide kills microorganisms and tumor cells, initiates mast cell secretion, inactivates leukotrienes, causes histamine release, causes histamine release from rat mast cells.

Finally, the emission maxima of dysplastic absorptive cells matches that of pyridoxal 5' phosphate. However, there is more fluorescence observed in the blue region of this chromomorph than is observed in the chromophore. The weak level of fluorescence of this chromomorph makes it difficult to definitively rule out this possible chemical identification.

4:6: Model of Adenoma Fluorescence at 370 nm Excitation

We have demonstrated that the important chromomorphs contributing to the fluorescence spectra of normal and adenomatous colon at 370 nm excitation include the structural protein collagen in the lamina propria and submucosa of normal colon (Ca), the structural protein collagen in the lamina propria of adenomatous colon (Cb), the eosinophil granules (E) and the cytoplasm of dysplastic epithelial cells in mucosal glands (G). With these identifications, we can write an expression for the 370 nm excited fluorescence intensity of colon as a function of emission wavelength. In doing so we assume exponential attenuation of light in a single, optically thick layer of tissue with homogeneously distributed chromophores. From Chapter 2 this is:

$$(5)\quad S(\lambda) = \frac{\beta_{Ca}F_{Ca}(\lambda)+\beta_{Cb}F_{Cb}(\lambda)+\beta_{E}F_{E}(\lambda)+\beta_{G}F_{G}(\lambda)}{\sum_{j=1}^{M} x_j A_j(\lambda)}$$

In order to interpret our fluorescence data using this equation, it is also necessary to identify the attenuators which contribute to the tissue spectra and measure their

attenuation properties. A consideration of the structure of the colon implies that most attenuation effects will occur within the mucosal layer, as this layer is nearest the lumen and its thickness (100 - 500 μm) approximates the penetration depth of 370 nm light in tissue. We utilized the fluorescence microspectrofluorimeter described in Chapter 2 to measure mucosal attenuation spectra of normal and adenomatous colon. 370 nm excited fluorescence spectra were measured from three samples of optically thick normal and adenomatous colon using the inverted fluorescence microspectrofluorimeter. These bulk specimens were inverted on a glass coverslip and placed on the microscope stage. Fluorescence spectra were collected from the three samples and averaged, yielding $S_{Thick}(\lambda)$. 10 μm thick frozen sections of the mucosa of these samples were then cut, mounted on glass slides, and coverslipped with buffered (50 mM TRIS), pH = 7.4, isotonic (140 mM) saline. Fluorescence spectra were recorded from these samples under identical experimental conditions as for the optically thick samples. These three spectra were averaged yielding $S_{Thin}(\lambda)dz$, where dz is the sample thickness.

These spectra can be related to each other mathematically according to the one layer model of tissue fluorescence presented in Chapter 2 as:

$$(6)\quad S_{Thick}(\lambda) = \frac{S_{Thin}(\lambda)}{\sum_{j=1}^{M} x_j A_j(\lambda)}$$

The mucosal attenuation spectrum was then calculated as:

$$(7)\quad \sum_{j=1}^{M} x_j A_j(\lambda) = \frac{S_{Thin}(\lambda)}{S_{Thick}(\lambda)}$$

Figure 37 shows the average mucosal attenuation spectrum of normal colon, where attenuation is given in m^{-1}. The mucosal attenuation spectrum of adenomatous colon was similar. This spectrum exhibits peaks at 420, 540 and 580 nm, and is nearly identical to the attenuation spectrum of oxy-hemoglobin, except for a constant background [51]. There are at least two contributions to this constant background. $A_j(\lambda)$ is the sum of the attenuation coefficient at the excitation wavelength and the attenuation coefficient at the emission wavelength of interest. Thus, one contribution to this constant background is the oxy-hemoglobin attenuation coefficient at 370 nm. The background can also include contributions from other attenuators. For example, it is likely that the structural protein

collagen also contributes to the tissue fluorescence spectra through attenuation. These identifications are consistent with our earlier qualitative interpretation of tissue fluorescence spectra at this excitation wavelength. We noted the attenuation effects of oxy-hemoglobin at 420, 540 and 580 nm.

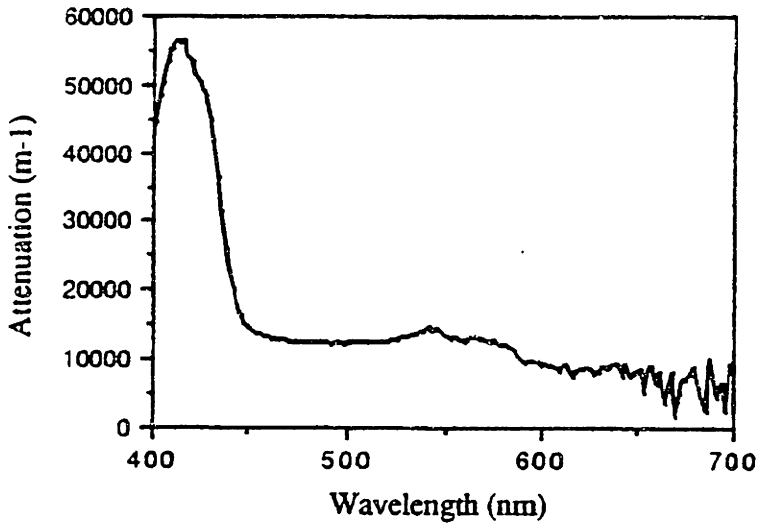

Figure 37: Average attenuation spectrum of normal colonic mucosa.

Here, we assume that the attenuation spectrum of colon can be represented as the sum of the oxy-hemoglobin attenuation and a constant attenuation as

$$(8)\ \sum_{j=1}^{M} x_j A_j(\lambda) = x_{Hb} A_{Hb}(\lambda) + x_C.$$

With this, we can then write Eq. (5) as

$$(9)\ S(\lambda) = \frac{\beta_{Ca} F_{Ca}(\lambda) + \beta_{Cb} F_{Cb}(\lambda) + \beta_E F_E(\lambda) + \beta_G F_G(\lambda)}{x_{Hb} A_{Hb}(\lambda) + x_C}.$$

This provides the key for quantitative interpretation of 370 nm excited spectra of human colon.

4:6.1: Application to *In Vitro* Data

Here we illustrate the application of this model to several typical 370 nm excited fluorescence spectra of normal and adenomatous colon. These spectra were obtained *in vitro* using the conventional fluorimeter described in Chapter Two, and were presented in Section 4:4.1.1 of this chapter. These spectra have been normalized to unity at 470 nm. The adenoma samples were selected from the larger subset of data without a peak at 445 nm.

These data were modeled according to Eq. (9). The parameters of the model included β_{Ca}, β_{Cb}, β_E, β_G, x_{Hb} and x_C, and were restricted to positive values. The fluorescence lineshapes were those presented in Fig. 36. The attenuation lineshape $A_{Hb}(\lambda)$ was that of normal mucosa attenuation, normalized at 420 nm. In fitting the data, the parameters were varied in order to minimize χ^2, the square of the difference between experimental and calculated fluorescence signal divided by the standard deviation. Thirty data points at 10 nm intervals from 410 - 700 nm intervals were compared.

Fits to data for four typical spectra are shown in Fig. 38. Table 11 lists the associated model parameters for these fits. The agreement of the model and the calculated spectra, as judged by χ^2, is best for the two samples of normal colon ($\chi^2 \sim 30$)[6]. The spectra of these two samples are quite similar, and the the associated model parameters are also similar. The spectra of these samples could be described in terms of the fluorescence contributions of collagen and eosinophil granules and the attenuation contributions of oxy-hemoglobin. The contribution of the collagen in the normal lamina propria and submucosa (Ca) dominated these spectra.

---

[6]The goodness of the fit can be judged by calculating the probability that a non-zero value of χ^2 arises from chance fluctuations in the data rather than due to an inappropriate model. For thirty degrees of freedom as in our data there is a 90% chance that χ^2 will be greater than 20 due to random fluctuations, but only a 1% chance that it will be greater than 50 due to random fluctuations [52].

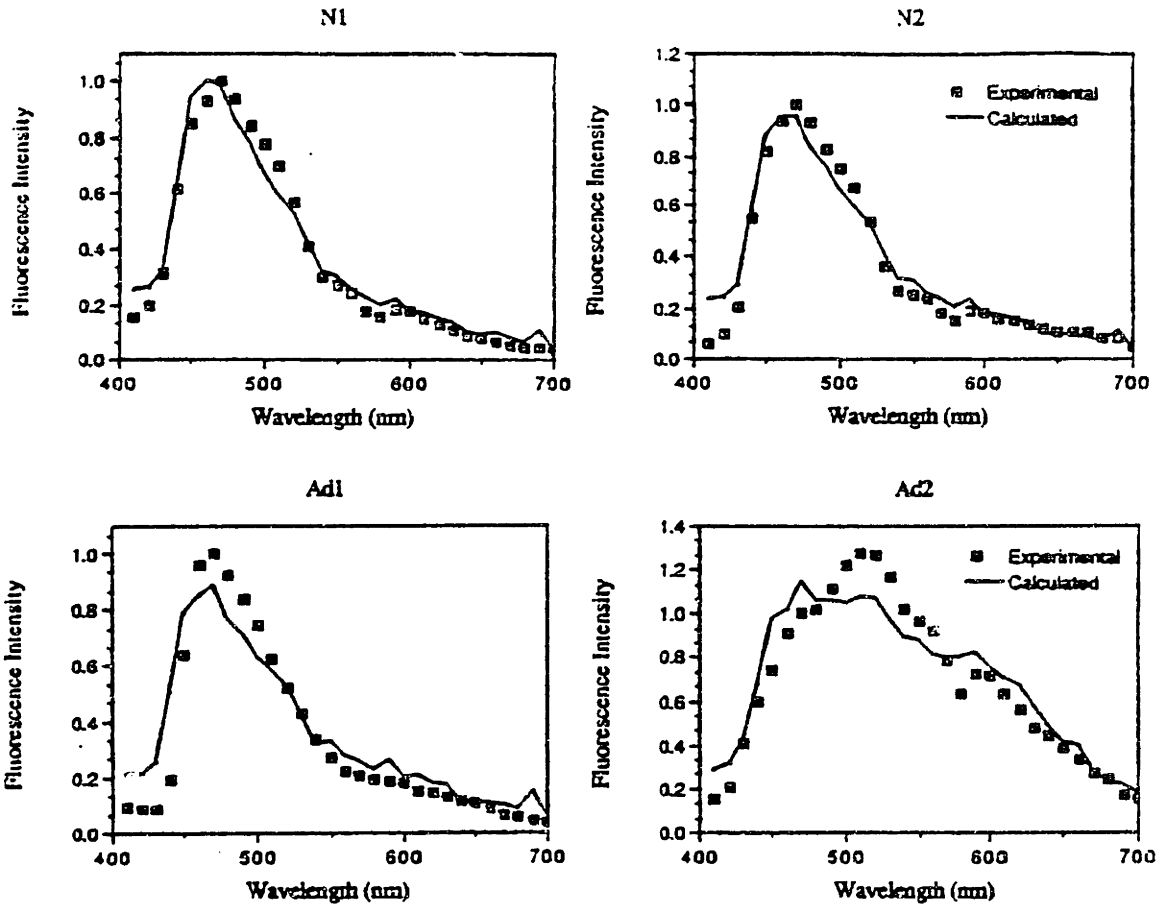

Figure 38: Typical fits to data for two samples of normal colon, N_1 and N_2, and two samples of adenomatous colon, A_1 and A_2. The associated model parameters for each sample are shown in Table 11.

Table 11: Parameters for fits to Eq. (9) shown in Fig. 38.

Sample	ßCa	ßCb	ßE	ßG	xHb	xC	χ^2
N_1	1.38	0.24	0.17	0	6.66	0	30
N_2	1.42	0.40	0.25	0	8.28	0	47
Ad_1	1.27	0.81	0.46	0	11.68	0	120
Ad_2	0	0	0.67	0.64	2.81	0.52	96

Two adenoma spectra were also fit to Eq. (9); however, the spectra of these two tissues are quite different. In general, more variability was observed in the spectra of adenomatous tissues than in normal tissues. The spectrum of Ad_1 resembles that of normal tissue, except that the peak emission wavelength is slightly shifted towards longer wavelengths. This shift was earlier attributed to an increased number of eosinophils in adenomas. In the spectrum of Ad_2, there is a shoulder at 520 nm. This shoulder was earlier attributed to the fluorescence of dysplastic epithelial cells in our qualitative interpretation of these spectra.

Although both spectra could be fit to Eq. (9), the agreement of model and data was less satisfactory with χ^2 on the order of 100.[7] Despite this, it is instructive to consider the model parameters for these two samples. In the spectrum of Ad_1, the contribution of collagen in the submucosa (Ca) still dominates; however, collagen in the adenomatous lamina propria (Cb) and eosinophils (E) contribute relatively more to this spectrum than in the spectra of normal tissues. In the spectrum of Ad_2, collagen does not contribute; rather, the contributions (E) of eosinophils and dysplastic epithelial cells (G) dominate. This is consistent with the histologic changes that occur in adenoma formation. As mucosal hyperplasia occurs, the relative contribution of collagen in the submucosa (Ca) decreases. Increased eosinophils and dysplastic cytoplasm give rise to increased values of ßE and ßG. Thus, with the model of tissue fluorescence, we can quantitatively interpret these fluorescence spectra, and this interpretation is consistent with our earlier qualitative interpretation.

---

[7]The goodness of the fit can be judged by calculating the probability that a non-zero value of χ^2 arises from chance fluctuations in the data rather than due to an inappropriate model. For thirty degrees of freedom as in our data there is a 90% chance that χ^2 will be greater than 20 due to random fluctuations, but only a 1% chance that it will be greater than 50 due to random fluctuations [52].

4:6.2: Model Based Algorithms

In order to exploit the differences in these model parameters in a diagnostic algorithm, several steps must be taken. These include:

1. Fitting spectra acquired *in vitro* with the spectral catheter to Eq. (9).

2. Establishing how all parameters of the model vary with tissue type for this data. Developing an algorithm for the presence of adenomas using these parameters based on the methods presented in Chapter 2.

3. Fitting data acquired *in vivo* with the spectral catheter to Eq. (9).

4. Comparing the parameters of this fit to those measured *in vitro* and adjusting the algorithms developed *in vitro* as necessary.

This will certainly be the subject of future work; however, before proceeding with these studies, it is first necessary to improve the agreement of the calculated and experimentally measured spectra. As discussed earlier,[6] reasonable agreement would be indicated by χ^2 on the order of 20. We have identified several possible reasons which can account for our higher values of χ^2. Here we list them along with steps which can be taken to eliminate these problems.

1. Some fluorescence and attenuation lineshapes may be slightly incorrect. Experimentally, the lineshapes $F_{Ca}(\lambda)$ and $F_E(\lambda)$ exhibited the least sample to sample variability and the greatest S/N. The lineshapes $F_{Cb}(\lambda)$ and $F_G(\lambda)$ exhibited lower S/N and greater sample to sample variability. More fluorescence microspectroscopy experiments, with increased excitation intensity, are needed to improve our confidence in these lineshapes.

Although little variation was observed in the attenuation lineshape $A_{Hb}(\lambda)$, it was obtained for a collection geometry equivalent to that of the spectral catheter. It is not unreasonable to assume that the wavelength dependent effects of scattering may be different for the collection geometry of the conventional fluorimeter. Thus, in fitting data acquired with the catheter to Eq. (9), χ^2 may improve.

2. The fluorescence and attenuation lineshapes in Eq. (9) were obtained with the microspectrofluorimeter, which has a non-uniform spectral response. Similarly tissue spectra fit to Eq. (9) were obtained with the conventional spectrofluorimeter which

has a non-uniform spectral response. Although these were corrected with a calibrated spectral lamp in all cases, in our experience, even slight miscalibrations can dramatically affect the quality of the fit. The calibration curves for these instruments need to be carefully rechecked against one another.

When these steps have been taken, further studies, to develop a histochemically based diagnostic algorithms for colonic dysplasia should proceed.

4:7: References

1. American Cancer Society, 1986 Cancer Facts and Figures, American Cancer Society, New York, 1986.

2. Astler VB, Coller FA. The Prognostic Significance of Direct Extension of Carcinoma of the Colon and Rectum, Ann Surg, 139:846, 1954.

3. Robbins SL, Cotran RS, Kumar V, Pathologic Basis of Disease, 3rd ed, WB Saunders Co., Philadelphia, 1984.

4. Gilbertsen VA, Colon Cancer Screening - the Minnesota Experience, Gastrointes Endosc, 26S:31s-32s, 1980.

5. Neugut AI, Forde K, Screening Colonoscopy: Has the Time Come?, Am J Gastroenterol, 83:295-97, 1988.

6. Rosai J, Ackerman's Surgical Pathology, Mosby, p. 594-627, 1988.

7. Gilbertsen VA, Proctosigmoidoscopy and polypectomy in reducing the incidence of rectal cancer, Cancer, 34:936-39, 1974.

8. Gilbertsen VA, McHugh R, Schuman L, Williams SE, The Earlier Detection of Colorectal Cancers. A Preliminary Report of the Results of the Occult Blood Study, Cancer, 45:2889-2901, 1980.

9. Spiro HM, Clinical Gastroenterology, 2nd ed., MacMillan Publishing Co, New York, 1977.

10. Smith JN, Lee KR, Essentials of Gastroenterology, CV Mosby Co., St. Louis, 1969.

11. Williams CB, Price AB, Colon Polyps and Carcinoma, Ch.45 in Sivak M, Gastroenterologic Endoscopy, WB Saunders Co., Philadelphia, p. 921-45, 1987.

12. Ham AW, Cormack DH, Histology, 8th Ed., JB Lippincott Co., Philadelphia, 1979.

13. Whitehead, Normal Appearances in Colonic Biopsy Specimens, Ch. 16 in, Mucosal Biopsy of the Gastro-Intestinal Tract.

14. Wheater KR, Burkitt HG, Daniels VG, Functional Histology, 2nd ed, Churchill Livingston, Edinburgh, 1987.

15. Horny HP, Horst HA, Lymphoreticular Infiltrates in Adenocarcinoma of the Large Intestine, Pathol Res Pract 182:222-27, 1987.

16. Muto T, Bussey JR, Morson BC, The Evolution of Cancer of the Colon and Rectum, Cancer, 36:2251-70, 1975.

17. Shamsuddin AM, Kato Y, Kunishima N, Sugano H, Trump BF, Carcinoma in situ in Nonpolypoid Mucosa of the Large Intestine, Report of a Case with Significance in Strategies for Early Detection, Cancer 56:2849-54, 1985.

18. Norfleet RG, Ryan ME, Wyman JB, Adenomatous and Hyperplastic Polyps Cannot be Reliably Distinguished by Their Appearance Through the Fiber Optic Sigmoidoscope, Dig Dis Sci 33:1175-77, 1988.

19. Kewenter J, Ahlman H, Hulten L, Cancer Risk in Extensive Ulcerative Colitis, Ann Surg, 188:824-28, 1978.

20. Collins RH Jr, Feldman M, Fortran FS, Colon Cancer, Dysplasia and Surveillance in Patients with Ulcerative Colitis, NEJM, 316:654, 1987.

21. Devroede GJ, Tayler WF, Saver WB, et al, Cancer Risk and Life Expectancy of Children with Ulcerative Colitis, NEJM, 285:17, 1971.

22. Greenstein AJ, Sachar DB, Smith H, et al, Cancer in Universal and Left-sided Ulcerative Colitis: Factors Determining Risk, Gast End 77:290, 1979.

23. Ritchie JK, et al, Prognosis of Carcinoma in Ulcerative Colitis, Gut, 22:752, 1981.

24. Bonnevie O, Binder V, Anthonisen P, Riis P, The Prognosis of Ulcerative Colitis, Scand J Gastroenterol, 9:81-91, 1974.

25. Bauer JJ, Gelernt IM, Salky B, Kreel I, Sexual Dysfunction after Protocolectomy for Inflammatory Bowel Disease, Gastroenterology 78:1138A, 1980.

26. Morson BC, Pang LSC, Rectal Biopsy as an Aid to Cancer Control in Ulcerative Colitis, Gut 8:423-34, 1967.

27. Kewenter J, Hulten L, Ahren Chr, The Occurrence of Severe Epithelial Dysplasia and Its Bearing on the Treatment of Longstanding Ulcerative Colitis, Ann Surg, 195:209-13, 1982.

28. Riddell RH, Hodman H, Ransohoff DF et al, Dysplasia in Inflammatory Bowel Disease: Standardized Classification with Provisional Clinical Applications, Hum Pathol, 14:931, 1983.

29. Lennard-Jones JE, Ritchie JK, Morson BC, Williams CB, Cancer Surveillance in Ulcerative Colitis Experience over 15 Years, Lancet, July 16:149-52, 1983.

30. Rosenstock E, Farmer RG, Petras RE, et al, Surveillance for Colonic Carcinoma in Ulcerative Colitis, Gast End, 89:1342, 1985.

31. Petras RE, Non-Neoplastic Intestinal Disease, in Sterburg SS, ed, Diagnostic Surgical Pathology, New York, p. 993-95, 1989.

32. Kapadia CR, Cutruzolla FW, O'Brian KM, Stetz ML, Enriquez R, Deckelbaum LI, Detection of Adenomatous Transformation of Colonic Mucosa by Fiber Optic Laser Induced Fluorescence Spectroscopy, Gastroenterol 94:A216, 1988.

33. Yakshe PN, Bonner RF, Patterson R, Leon M, Fleischer DE, Laser Induced Fluorescence Spectroscopy. Can it Be Used in the Diagnosis and Treatment of Colonic Malignancy? Am J Gastroenterol 84:1199, 1989.

34. Hirano T, Ishizuka M, Suzuki K, Ishida K, Suzuki S, Miyaki S, Honma A, Suzuki M, Aizawa K, Kato H, Hayata Y, Photodynamic Cancer Diagnosis and Treatment System Consisting of Pulse Lasers and an Endoscope Spectro-Image Analyzer, Lasers in the Life Sciences, 3:99-116, 1989..

35. Riddel RH, Goldman H, Ransohoff DF, et al, Dysplasia in Inflammatory Bowel Disease: Standardized Classification with Provisional Clinical Applications, Hum Pathol 11:931-69, 1983.

36. Richards-Kortum RR, Mehta AV, Hayes G, Cothren R, Kolubayev T, Kittrell C, Ratliff NB, Kramer JR, Feld MS, Spectral Diagnosis of Atherosclerosis Using an Optical Fiber Laser Catheter, American Heart Journal 118:381-91, 1989.

37. Keijzer M, Richards-Kortum RR, Jacques SL, Feld MS, Fluorescence Spectroscopy of Turbid Media: Autofluorescence of Human Aorta, Applied Optics 28:4286-92, 1989.

38. Harris EK, Albert A, Multivariate Interpretation of Clinical Laboratory Data, Decker, New York, 1987.

39. Johnson NL, Kotz S, Distributions in Statistics, Houghtin Mifflin, Boston, 1970.

40. Van Assendelft OW. Spectrophotometry of Hemoglobin Derivatives. Royal Vangorcum Ltd, Assen, The Netherlands, p. 58, 1970.

41. Campbell ID, Dwek R. Biological Spectroscopy. Benjamin Cummings Publishing Co., P. 69-70, 1984.

42. Wolfbeiss OS, Leiner MJ. Mapping of the Total Fluorescence of Human Blood Serum as a New Method for its Characterization. Anal. Chim. Acta. 1985; 167:203-215.

43. Chung-Ho S, Duzman E, Mellott J, Liaw LH, Berns MW. Spectroscopic, Morphologic, and Cytotoxic Studies on Major Fractions of Hematoporphyrin Derivative and Photofrin II. Lasers in Surgery and Medicine 1987; 7:171-79.

44. Bent DV, Hayon E. Excited State Chemistry of Aromatic Amino Acids and Related Peptides. III. Tryptophan. J Am Chem Soc 1975; 97:2612-19.

45. Schwartz JP, Possoneau JV, Johnson GS, Pastan I. The Effect of Growth Conditions on NAD+ and NADH Concentration and the NAD+:NADH Ratio in Normal and Transformed Fibroblasts. J Biol Chem 1974; 249:4138.

46. Merril AH, Henderson JM. Diseases Associated with Defects in Vitamin B6 Metabolism. Ann. Rev. Nutr. 1987; 7:137-156.

47. Yuanlong Y, Yanming Y, Fuming L, Yuten L, Paozhong M. Characteristic Autofluorescence for Cancer Diagnosis and its Origin. Lasers in Surgery and Medicine 1987; 7:528-32.

48. Samoszuk MK, Espinoza FP, Deposition of Autofluorescent Eosinophil Granules in Pathologic Bone Marrow Biopsies, Blood, 70:597-99, 1987.

49. Weil GJ, Chused T, Eosinophil Autofluorescence and its Use in Isolation and Analysis of Human Eosinophils Using Flow Microfluorometry, Blood 57:1099-1104, 1981.

50. Gleich GJ, Adolphson CR, The Eosinophilic Leukocyte: Structure and Function, Adv Immunology 39:177-253, 1986.

51. Van Assendelft OW, Spectrophotometry of Haemoglobin Derivatives, Royal VanGorcum Ltd, 1970.

52. Young HD, Statistical Treatment of Experimental Data, McGraw Hill, New York, p. 163, 1962.

5: Spectroscopic Diagnosis of Transitional Cell Carcinoma in the Urinary Bladder

This chapter contains a characterization of the spectroscopic properties of normal urinary bladder and several types of transitional cell carcinoma (TCC). This data is discussed in terms of developing a spectroscopic diagnostic algorithm for TCC in the urinary bladder. As discussed in detail below, better diagnostic techniques are needed to identify those patients with superficial TCC at most risk for developing invasive bladder cancer, in order that superficial TCC can be treated with the least aggressive form of therapy effective for preventing the development of invasive disease.

The first section of this chapter contains a brief review of the histologic features of normal and neoplastic urinary bladder. The clinically relevant features of TCC are also reviewed here. The second section includes fluorescence EEMs of normal urinary bladder and TCC. Here, optimal excitation wavelengths for the spectroscopic diagnosis of TCC are established. The third section contains average fluorescence emission spectra of normal and neoplastic bladder obtained at these excitation wavelengths. Empirical diagnostic algorithms for the presence of TCC are defined and evaluated in this section as well. Finally, in the fourth section, a preliminary understanding of the morphologic and biochemical basis of bladder fluorescence at one of these excitation wavelengths is developed based on a comparison of tissue fluorescence EEMs to those of pure biomolecules.

5:1: Neoplasia in the Urinary Bladder

There are approximately 40,000 new cases of cancer of the urinary bladder each year in the United States; the disease is responsible for about 10,000 deaths annually [1]. In order to illustrate important clinical issues in the diagnosis and management of this disease, here, we first present an overview of the morphology and histology of normal and neoplastic urinary bladder.

5:1.1: Morphology and Histology of Normal and Neoplastic Urinary Bladder

5:1.1.1: Normal Bladder

The urinary bladder functions primarily as a storage reservoir for urine [2]. Physiologically, the bladder must be able to accommodate great changes in volume [3].

A consideration of the histologic features of the bladder demonstrates how this is possible. The normal bladder, depicted in Fig. 1, is a layered structure, consisting of a transitional epithelium, a lamina propria, three alternating layers of smooth muscle, and an adventitia [3].

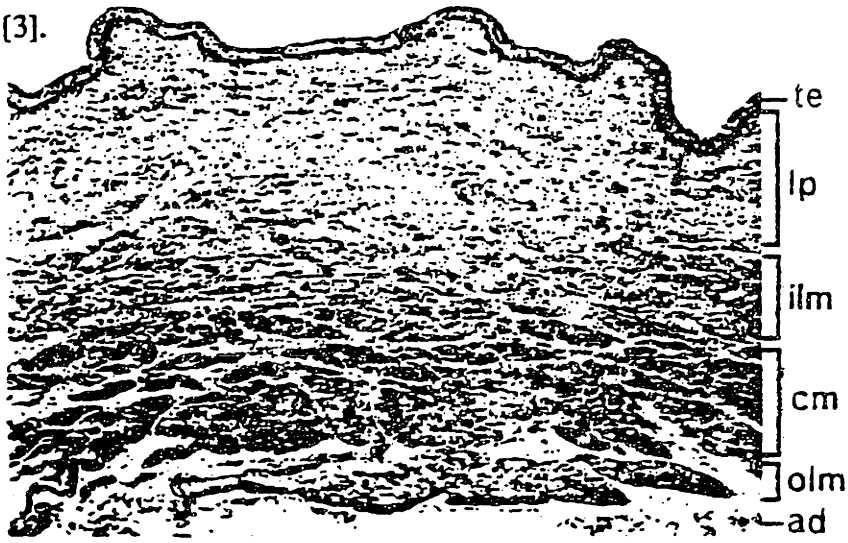

Figure 1: Histologic photograph of normal bladder, indicating the various layers: the transitional epithelium, the lamina propria, the inner longitudinal, the circular and the outer longitudinal layers of smooth muscles, and the adventitia.

The muscular layers contract and relax effecting the change in volume of the urinary bladder [2, 3]. The lamina propria, consisting mainly of loose, collagenous, connective tissue [3], is elastic, and can accommodate itself to these changes in volume. The urothelium is highly specialized to allow bladder distention without leakage of urine [3]. It normally consists of about seven to eight layers of cells [4]. The lumenal layer of cells consists of large flattened cells, referred to as umbrella cells, which cover relatively large areas [4]. The intermediate zone of the urothelium consists of 4-5 layers of cells when the bladder is maximally distended, and 6-8 layers of cells when fully contracted [4]. The layer of epithelial cells situated on the basement membrane consists of small cells which are cylindrical in the contracted bladder and flattened in the distended bladder [4]. In this way, the integrity of the urothelium can be maintained even when the bladder is fully distended [3].

Diseases of the bladder frequently affect the histologic structure of the urothelium. Most neoplasms of the urinary bladder, in fact, are epithelial in nature [4]. Tumors of the urinary bladder must be considered in the context of other pathologies which can alter the structure of the urothelium. Inflammatory disorders are particularly common both in patients with and without bladder tumors [4].

The most common inflammatory disorders of the urinary bladder are acute and chronic cystitis [4]. In the normal patient, these are often the result of bacterial agents; however, in the cancer patient they can result from the application of cytotoxic antitumor drugs or radiation therapy [4]. In either case, cystitis results in a non-specific acute or chronic inflammation [4]. In the acute stage, the initial inflammatory reaction is characterized by mucosal hyperemia [4]. In more advanced cases, focal or diffuse mucosal hemorrhages may occur [4]. In some cases, large areas of mucosal ulceration can result [4].

In long-standing cases of chronic inflammation, nests of normal transitional bladder mucosa called Von Brunn's nests may become enveloped within the lamina propria. This condition is known as proliferative cystitis. Over time, these nests may dilate giving rise to small cysts or clusters of cysts [4, 5]. This condition, known as cystitis cystica, can sometimes be recognized on gross examination, as these cysts appear from the surface as small (0.1 - 0.5 cm) clear vesicles [4].

5:1.1.2: Transitional Cell Carcinoma

The majority of bladder tumors (~90%) are of epithelial origin [4, 5]. Only a few of these are benign in nature [4]. Benign epithelial neoplasms of the urinary bladder, papillomas, are uncommon, and represent less than 1% of the papillary tumors of the bladder [4]. Papillomas may arise anywhere within the bladder [4]. They are small (0.5-2.0 cm diameter), delicate, branching structures, covered with papillae [4, 5]. Each papillae consists of a central core of fibrovascular tissue covered by no more than seven layers of normal appearing transitional cells [4, 5].

Epithelial hyperplasia, in which the number of epithelial cell layers is increased beyond the normal seven, is a benign form of epithelial neoplasia [5]. This condition is often found in conjunction with other tumors of the bladder, or in chronic inflammation [5]. In some cases, nuclear abnormalities can be observed in the epithelial cells, this condition is referred to as atypical hyperplasia [5].

There are three types of malignant epithelial neoplasms of the urinary bladder: transitional cell carcinoma, squamous cell carcinoma and adenocarcinoma [4]. The majority of bladder cancers (~90%) are transitional cell carcinoma, and our discussion of bladder cancer will focus on TCC [4]. Transitional cell carcinomas are characterized according to their architectural and histologic features [5]. Architecturally, TCCs are divided according to whether the associated lesion is papillary or flat [4]. In addition,

lesions are characterized based on whether or not the atypical cells have penetrated the mucosal basement membrane [5]. Histologically, TCC is classified into three grades of epithelial cell atypia [4, 5].

Most tumors of the bladder are papillary in nature [5], and consist of polypoid lesions, 1 - 5 cm in diameter, which are attached to the mucosa via a stalk [4]. Papillary carcinomas can be either invasive or non-invasive [4, 5]. On gross examination, non-invasive papillary carcinomas closely resemble benign papillomas, and microscopic examination is required to determine the malignant potential of the lesion [4]. However, when invasion occurs, the underlying bladder wall becomes thickened, and the malignant nature of the lesion can be determined on gross inspection [4].

Three grades of cellular atypia are recognized in TCC; these are characterized in Table 1 [4]. Grade I tumors are differentiated from papillomas primarily on the basis of architecture alone [5]. The epithelial cells of higher grade lesions display recognizable atypia [5]. In grade II lesions, there is often epithelial hyperplasia, and nuclear abnormalities are by definition present [5]. The cells however are still recognizable as transitional cells [4]. Tumor cells of grade III lesions are barely recognizable as transitional cells, and there is often cellular disarray [4]. Papillary lesions are most commonly grade I or II; however, they may contain grade III epithelial cells [4].

Table 1: Morphology of Urothelial Transitional Cell Neoplasms. Adapted from [4, 5].

Grade	# of Epithelial Cell Layers	Nuclear Enlargement	Hyper-chromasia	Mitoses
Papilloma	No more than 7	None	Absent	Rare
TCC-I	More than 7	Slight to Moderate	Slight in occasional cell	Uncommon
TCC-II	More than 7 (usually marked increase)	Moderate to marked	Slight to moderate in 25-50% of cells	Common
TCC-III	More than 7 (often marked increase)	Marked, Extreme variability of sizes	Marked in 50% or more of cells	Prominent

Non-papillary transitional cell carcinomas are also found, in which the carcinoma takes the form of a plaque-like thickening of the mucosa [4]. These lesions can also be invasive or non-invasive; however, they are more commonly invasive, and tend to contain more atypical cells than papillary lesions [4]. Typically, these invasive lesions are characterized by ulcerations or areas of hemorrhage [5]. Non-invasive flat lesions containing anaplastic epithelial cells, sometimes referred to as carcinoma in situ, are often found near areas of invasive cancers [4, 5].

5:1.2: Clinical Issues

It is of central importance in the diagnosis and management of bladder neoplasia to understand the interrelationships and prognostic implications of each of the forms of neoplasia discussed in the preceding section.

5:1.2.1: Dysplasia Carcinoma Sequence

It is generally accepted that all carcinoma of the bladder originates from abnormal urothelium [5, 6]. Figure 2 contains histologic evidence to support this hypothesis; shown are schematic diagrams of histologic tissue type across the surface area of a surgically excised bladder from several patients with TCC [6]. Papillary tumors of low histologic grade are believed to originate from urothelial hyperplasia, while those papillary tumors of higher grade develop from atypical hyperplasia or non-papillary carcinoma *in situ* [5]. Invasive non-papillary carcinomas probably have their origin in flat CIS as well [5].

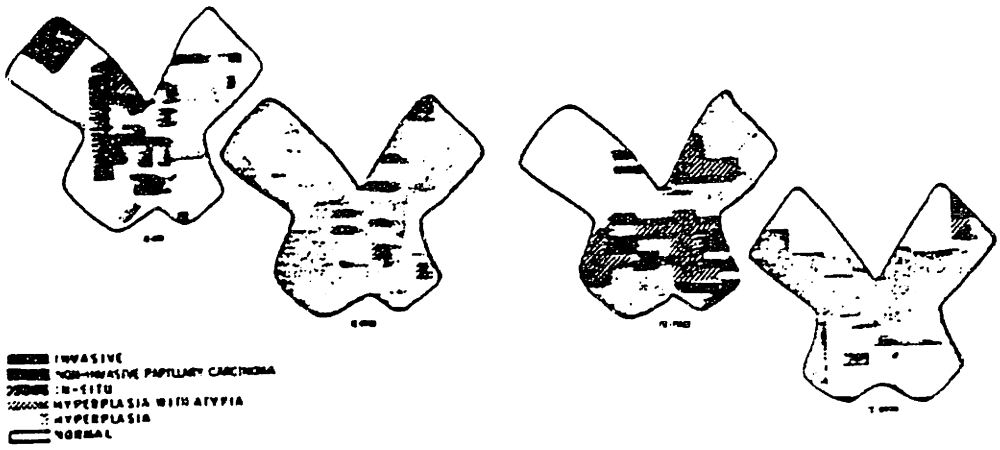

Figure 2: Diagrammatic representation of epithelial histology in surgically removed cancerous bladders. This illustrates that carcinoma of the bladder likely has its origins in abnormal urothelium. Adapted from [5].

This progression has been termed the dysplasia-carcinoma sequence, and is of considerable importance in the diagnosis, management and prognosis of bladder cancer [4, 5]. In the following sections the diagnosis and treatment of bladder cancer will be considered with emphasis given to the impact of the dysplasia-carcinoma sequence.

5:1.2.2: Initial Diagnosis and Prognosis

The primary symptom produced by bladder tumors is painless hematuria [4]. In some cases, hematuria may be accompanied by frequency, urgency or dysuria [4]. These symptoms are non-specific; many other diseases, including cystitis, can produce some combination of them [7]. However, cases of hematuria, particularly in individuals at most risk (males in fifth to sixth decades of life [4]) must be investigated in order to rule out the presence of neoplasia. Such investigation should be timely, as it is known that even short delays in the diagnosis of invasive bladder cancer can result in significantly worse prognosis for the patient [8].

In patients suspected to have a bladder tumor, several diagnostic techniques can be employed. These include urine cytology, radiographic studies such as the intravenous urogram, and cystoscopy [9-13]. Urine cytology consists of observing the histologic features of desquamated urothelial cells collected from the urine sediment [10-12]. Papillomas and low grade papillary carcinomas cannot be diagnosed by urine cytology [10]; however, with this technique, it is possible to detect the presence of grade II and III malignancies [10-12]. Unfortunately, using this technique, the location of the tumor within the bladder cannot be determined [10-12].

Cystoscopy is a widely used technique to determine the location of bladder tumors, and with biopsy can be used to carefully assess the histologic grade of the tumor [13]. A cystoscope consists of a rigid, coherent, fiber optic bundle which can be inserted in the urethra, and used to view the interior of the urinary bladder with reflected white light [13]. With this instrument, bladder tumors can be identified based on changes in gross architecture of the urothelium [13]. Papillary neoplasms can be identified on gross examination, although papillomas cannot be distinguished from true papillary carcinomas [13]. Flat invasive carcinomas can also be identified on gross examination, based on the ulceration and thickening of the bladder wall they produce; however, the degree of cellular atypia and invasion cannot be determined [13]. Flat CIS, epithelial hyperplasia or atypical hyperplasia cannot be identified by gross inspection alone [13]. Because cystoscopy relies on changes in gross morphology to identify neoplasia, it is most often

supplemented with mucosal biopsies, in order to accurately grade and stage bladder tumors [14].

The prognosis of TCC depends on the histologic grade of the neoplasm and on the clinical stage when first diagnosed. For the benign papilloma, the 5 year survival rate approaches 100% with only local resection [4, 5]. For the malignant lesions, the mortality rate has been correlated with the degree of cellular atypia [5]. In grade II papillary tumors the mortality approached 50% in one study, for grade III tumors mortality was over 90% [15]. In all forms of bladder cancer, death is usually caused by progressive infiltration of the ureters leading to obstructive renal disease or dissemination of the cancer [4].

5:1.2.3: Treatment and Follow Up

The management of TCC of the urinary bladder is dictated in large part by the natural history of the disease - the dysplasia carcinoma sequence. Here, we will review the therapies for benign papillomas, superficial and invasive TCC, and consider the diagnostic techniques used to monitor treatment.

Benign papillomas and non-invasive papillary transitional cell carcinomas can be simply removed by resection or fulguration at cystoscopy [16]. Benign papillomas are believed to have no malignant potential, and the recurrence rate of these lesions is quite low [4]. However, patients with a previous history of papilloma are at slightly increased risk for eventual development of bladder cancer [4]. Non-invasive papillary TCCs treated in this manner rarely lead to death; however, at least 60% of such patients develop a recurrence [16], and in many cases the recurrence shows greater cellular atypia, and implies worse prognosis [4].

Invasive transitional cell carcinomas are commonly treated with radiation therapy, by partial or total cystectomy, or some combination [17, 18], depending primarily on the size of the tumor, and the degree of invasion. In any case, the 5 year survival rates for invasive TCC are discouragingly low, indicating the crucial role early diagnosis may play in decreasing the mortality of TCC [5]. However, the high rate of recurrence for non-invasive TCC treated by fulguration or resection at cystoscopy suggests that early initial diagnosis will not be sufficient to achieve this goal. To reduce the mortality of TCC, both improved methods of early diagnosis and improved methods for preventing recurrences or identifying them and treating them at an early stage must be developed.

It has been suggested that recurrences of TCC develop from abnormal urothelium, as part of the dysplasia-carcinoma sequence. Thus, one method of preventing recurrences would be to develop techniques to selectively destroy this abnormal epithelium. Chemotherapeutic agents represent one method of selectively destroying neoplastic cells, and many trials in which these agents are locally applied to the entire bladder mucosa have been conducted [18]. Certain patients respond to this treatment, resulting in near complete disappearance of carcinoma cells; however, in others, markedly atypical cells persist [10]. In one study, following resection of a single non-invasive papillary TCC, patients given intravesical adriamycin over 14 months exhibited approximately 50% less recurrences than did untreated controls over a three year follow up period [18].

Another method of selectively destroying such neoplastic cells is to use immunotherapy, in which the natural immunity of the host is manipulated to achieve this result [19]. The most widely used form of this treatment is active, non-specific immunotherapy, in which the patient's immune system is stimulated locally, in the hopes that it will elicit a response of the patient to his own tumor [19]. Bacille Calmette-Guerin (BCG) is a widely use non-specific immunotherapeutic agent, which can be applied intravesically to the bladder mucosa, eliciting a non-specific inflammatory response. Again, however, BCG appears to be effective at eliminating or reducing recurrences for only a portion (50-80%) of patients with superficial TCC [20]. The risk of recurrence is extremely high in patients for whom these types of treatments fail; thus, careful follow up is necessary to screen for the presence of recurrences in patients treated in these manners [18, 19]. Typically, this screening is achieved through cystoscopy with selected mucosal biopsy [13].

A second approach to managing recurrences is to screen for neoplastic changes in the urothelium following removal of an initial non-invasive papillary carcinoma [13]. The dysplasia-carcinoma sequence suggests that such changes precede recurrence [5]. Clinical experience bears this out - patients with abnormal epithelial biopsies are more likely to develop subsequent recurrences [21]. If discovered, therapeutic steps can be taken in an attempt to avoid ultimate recurrence. Techniques of intravesical chemotherapy or immunotherapy described above are successful in some cases [18, 19]. However, in other cases partial or total cystectomy can be used to remove the abnormal epithelium [9].

A problem with this approach is that early diagnosis of these epithelial abnormalities is difficult. The most commonly used technique is cystoscopically directed

biopsy [13]. Because cystoscopy identifies epithelial abnormalities on the basis of gross architecture, locating histologic abnormalities with cystoscopically directed biopsy is largely a matter of chance [23]. In one series of 399 biopsies obtained from normal appearing mucosa, it was found that 4.5% contained CIS, and an additional 13.5% contained dysplasia [22]. When cystoscopic appearance was flat and erythematous, abnormalities were observed in 51% of biopsies, 14% containing carcinoma, and with the typical endoscopic appearance of CIS was observed, 42% of biopsies contained carcinoma, with 11% indicating severe dysplasia [22].

One of the most crucial issues in the treatment and follow up of patients with superficial bladder carcinoma is the role of total cystectomy [23]. While cystectomy can cure a certain portion of TCC patients, it is an operative procedure which is accompanied by significant morbidity and mortality [24]. The mutilation and functional loss associated with this procedure is a significant burden for these patients [24]. Therefore, there is much interest in improving techniques for the detection of dysplasia and CIS, in order to accurately separate those patients at most risk for developing invasive bladder cancer, requiring radical cystectomy and patients who can be treated effectively with less aggressive intravesical therapies.

5:1.2.4: Potential Role of Fluorescence Spectroscopy

Spectroscopic diagnosis of these conditions has the potential to reduce the sampling error associated with cystoscopy and biopsy, either through better direction of biopsy placement or by allowing the entire surface area of the bladder to be screened without the need for biopsy. There is much evidence to indicate that fluorescence spectroscopy can be used to diagnose mucosal carcinoma in a variety of organs [25-27]. The remainder of this chapter is devoted to developing a spectroscopic diagnostic algorithm for the presence of TCC and associated neoplastic changes in the urinary bladder.

Here, we consider the spectroscopic properties of normal and neoplastic human urinary bladder recorded *in vitro*. Our goal is to develop diagnostic algorithms for epithelial neoplasia, which can be used to improve cystoscopically directed biopsy. Spectra are presented from normal urinary bladder, CIS, papillary and non-papillary TCC. In addition, the fluorescence spectra of non-neoplastic urinary bladder with two inflammatory conditions, chronic cystitis, and chronic cystitis with cystitis cystica are presented. We demonstrate, that *in vitro*, empirical algorithms based on fluorescence

emission intensities obtained at 476 nm excitation can be used to differentiate neoplastic bladder from non-neoplastic bladder, and non-neoplastic inflammatory bladder from normal bladder. The histochemical basis of this fluorescence is explored using fluorescence EEMs and fluorescence microscopy.

5:2: Survey of Spectroscopic Properties of Normal and Pathologic Bladder

The first step in our procedure is to compare the UV and visible fluorescence properties of normal and pathologic tissues to select excitation wavelengths optimal for the differentiation of these tissues. We again utilize fluorescence EEMs to achieve this goal.

5:2.1: Fluorescence EEMs

Fluorescence EEMs of normal, non-neoplastic, and neoplastic urinary bladder were recorded *in vitro* using the method described for bladder in Chapter Two. Samples of urinary bladder were obtained from resection specimens of patients with TCC. Full thickness specimens of normal appearing bladder, papillary and non-papillary TCC were collected. Samples were snap frozen in liquid nitrogen and isopentane and stored at -70° C until study. The specimens were thawed at room temperature, kept moist with 140 mM buffered saline, pH 7.4 and mounted in a quartz cuvette for spectroscopic studies. Following study, the tissues were fixed in 4% formalin solution, paraffin embedded, cut into 4 μm thick sections and stained with hemotoxylin and eosin. The resultant slides were examined by a single genitourinary pathologist to histologically assess tissue type.

Fluorescence EEMs were recorded for 26 samples of urinary bladder from 20 patients. Eighteen of these were negative for tumor: seven were normal, seven displayed chronic cystitis, three showed chronic cystitis and cystitis cystica, and one displaying chronic cystitis with extensive fibrosis was discarded. Eight specimens were positive for neoplasia: one was a non-invasive papillary TCC, two showed focal CIS, and four were invasive, non-papillary TCC. A deep lymphatic tumor was present in one specimen which was discarded from further data analysis.

A complete characterization of the UV and visible fluorescence properties of normal and neoplastic urinary bladder is presented in Figs. 3 and 4. Figure 3 shows the average fluorescence EEM of normal urinary bladder, urinary bladder with chronic cystitis, and urinary bladder with both chronic cystitis and cystitis cystica. Figure 4

shows average EEMs of tissue samples displaying focal CIS, non-invasive, papillary TCC and invasive non-papillary TCC.

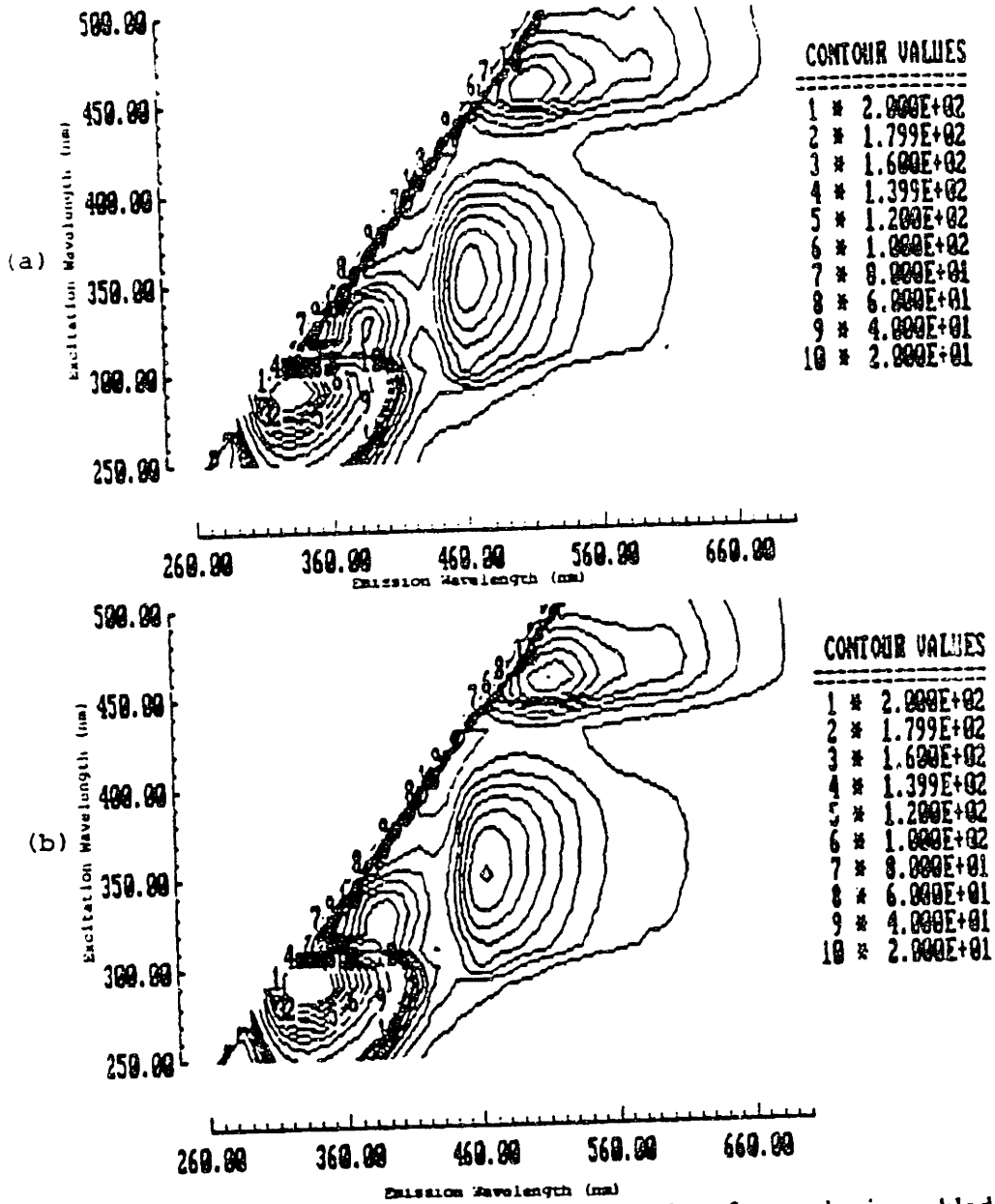

Figure 3: Average fluorescence EEMs of (a) seven samples of normal urinary bladder, (b) seven samples of urinary bladder with chronic cystitis, and (c) four samples of urinary bladder with chronic cystitis and cystitis cystica. Two sets of linearly spaced contours are shown: ten from 200 to 20 units and nine from 18 to 2 units. Here fluorescence intensities are reported in the same set of arbitrary units maintained for fluorescence EEMs throughout this thesis.

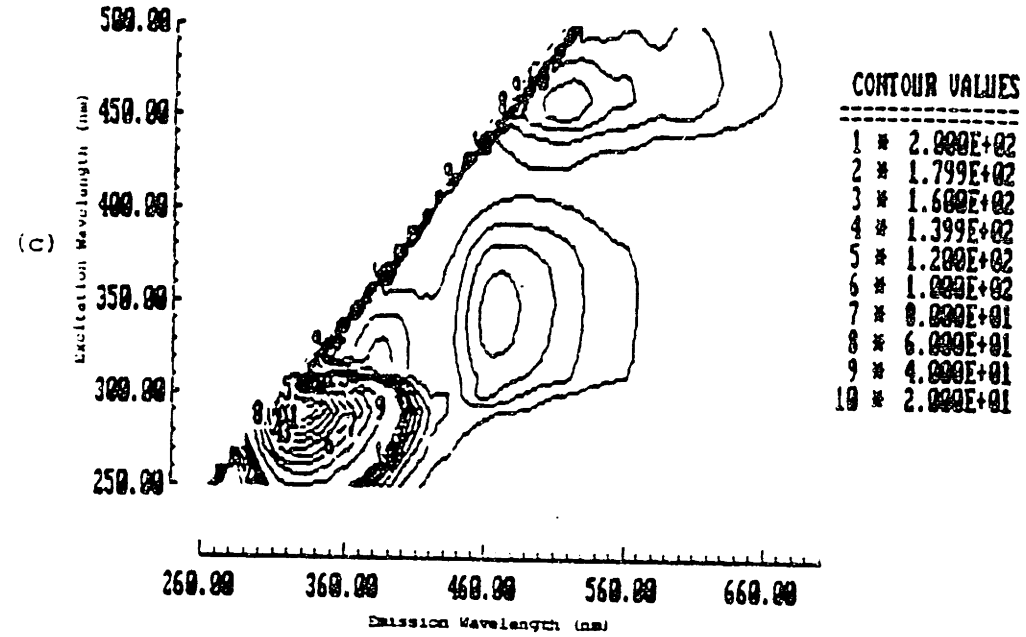

Figure 3 (Cont.):

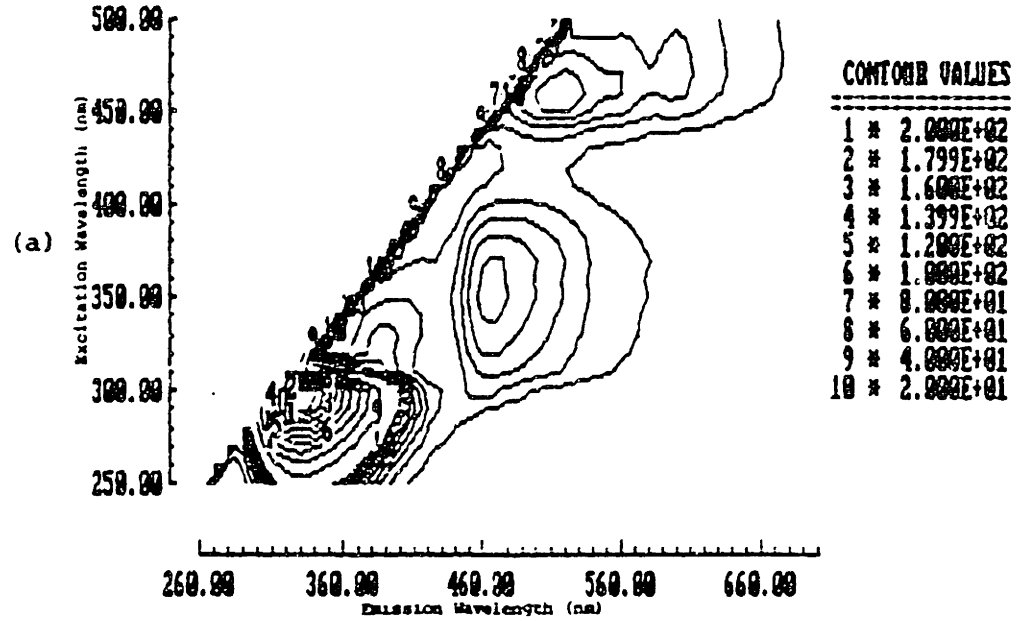

Figure 4: Average fluorescence EEMs of (a) two samples of focal CIS, (b) one non-invasive papillary TCC, and (c) four samples of invasive, non-papillary TCC. Two sets of linearly spaced contours are shown: ten from 200 to 20 units and nine from 18 to 2 units. Here fluorescence intensities are reported in the same set of arbitrary units maintained for fluorescence EEMs throughout this thesis.

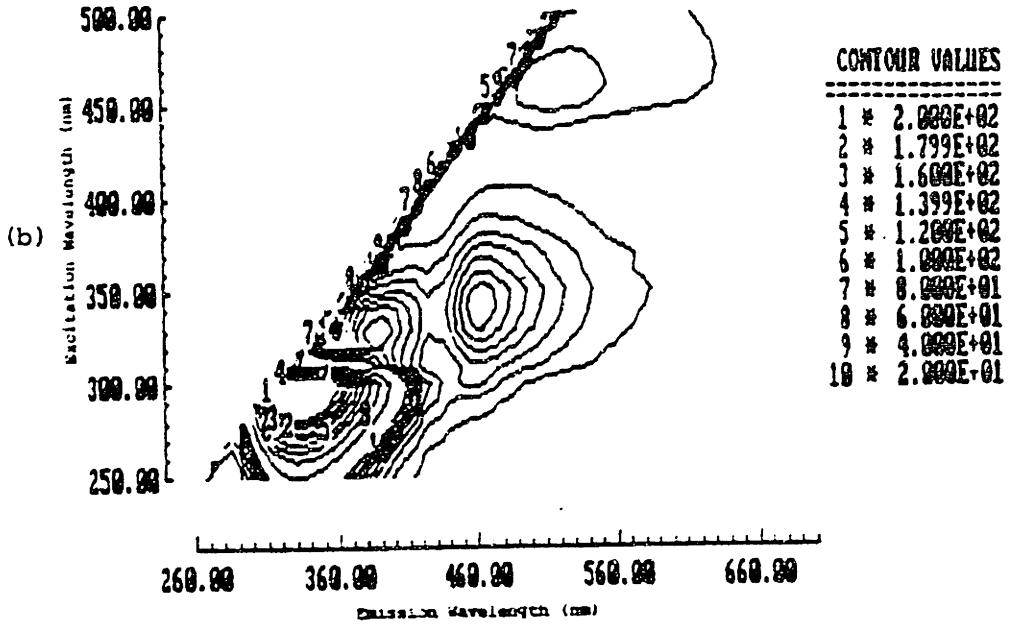

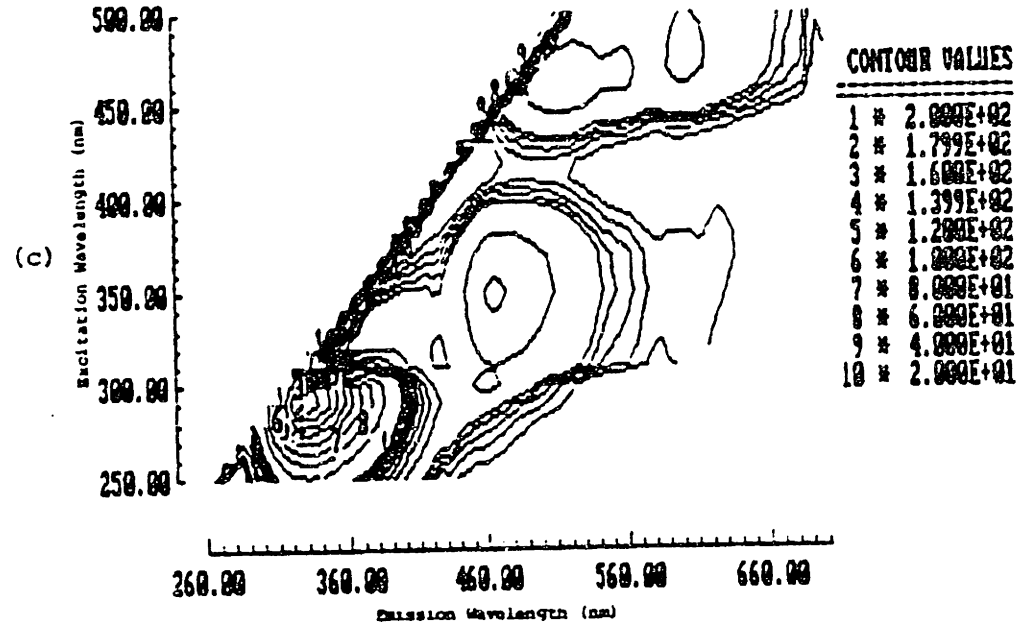

Figure 4 (cont.):

Each of these fluorescence excitation-emission matrices can be characterized by the locations and intensities of the excitation-emission maxima. For each tissue type, maxima of varying fluorescence intensities were found in similar locations, as characterized in Table 2.

Table 2: Excitation-emission maxima in the average fluorescence EEMs of human urinary bladder.

Excitation-Emission Maxima	Normal	Normal Chronic Cystitis	Normal Chronic Cystitis Cystitis Cystica	CIS	Non-Invasive Papillary TCC	Invasive TCC	Potential Chromophore/ Chromomorph (See Table 3)
(290, 330 nm)	200	200	200	200	200	180	Tryptophan
(300, 470 nm)	10	8	6	4	6	4	?
(315, 425 nm)	6	14	-	-	6	4	4-pyridoxic acid
(325, 385 nm)	16	12	8	10	14	6	Pyridoxal 5'-phosphate, Collagen I, Collagen III
(350, 465 nm)	16	16	8	10	14	4	NADH, NAD(P)H
(460, 515 nm)	14	16	8	10	4	4	Pyridoxal 5'-phosphate, Elastin
(470, 560 nm)	10	8	6	8	-	4	Pyridoxal 5'-phosphate, Elastin
(470, 590 nm)	8	6	4	6	2	4	Pyridoxal 5'-phosphate, Elastin

The fluorescence EEMs of normal bladder and bladder with chronic cystitis were most similar, differing primarily in the intensity of the narrow peaks at (315, 425 nm) and (325, 385 nm). The fluorescence EEMs of inflammatory bladder with cystitis cystica was substantially different than that of other non-neoplastic bladder. Specifically, all peaks except that due to tryptophan at (290, 330 nm) were approximately a factor of two less intense in bladder displaying cystitis cystica relative to normal bladder and bladder with chronic cystitis. The fluorescence intensities at the excitation-emission maxima of neoplastic bladder differed from that of normal bladder, as characterized in Table 1. The intensities of these maxima also varied for different types of neoplasia; the fluorescence EEMs of CIS, papillary TCC and invasive TCC exhibited significant differences.

5:2.2: Choice of Optimal Excitation Wavelength

These differences indicate that fluorescence spectroscopy has potential to differentiate neoplastic and non-neoplastic urinary bladder. Furthermore, the EEMs provide a method of selecting excitation wavelengths at which this differentiation is greatest. A consideration of Table 1 indicates that, at any of the excitation wavelengths corresponding to excitation maxima except 290 nm, there are differences in the intensity of the emission peaks which can be used, on average, to differentiate normal bladder, chronic cystitis, cystitis cystica, CIS, papillary TCC and invasive TCC. In particular, intensities of the emission maxima at 315 and 325 nm excitation, on average, can be used to distinguish each of these tissue categories. Similarly, the intensities of the emission maxima at 460-470 nm excitation can be used to distinguish each of these tissue categories on average.

As described in Chapter Two, a more comprehensive method of comparing fluorescence intensities at all excitation and emission wavelengths is to construct the ratio of the average fluorescence EEMs[1]. Figure 5 shows the ratio of the average EEMs of chronic cystitis, cystitis cystica, CIS, non-invasive papillary TCC and invasive TCC, to the average EEM of normal urinary bladder. Figure 5(a) illustrates the ratio of the average EEM bladder with chronic cystitis to that of normal bladder, and shows that the fluorescence properties of these tissues are quite similar. Although several local maxima and minima are present, they range in value only from 1.2 to 0.8.

There are significantly greater differences in the fluorescence EEMs of cystitis cystica and neoplastic bladder as compared to normal urinary bladder. In the region of tryptophan emission, the ratio maps of cystitis cystica and invasive TCC are similar, exhibiting local maxima near (270, 360 nm), 0.9 times as intense as the fluorescence of normal tissue. In addition, in all neoplastic tissues, a local maximum near (300, 340 nm) was present which was approximately 1.3 times as intense as the fluorescence of normal tissue. Leiner has previously demonstrated that there are similar differences in the excitation-emission profile of serum tryptophan in cancer patients [28].

---

[1]Here, we construct only the ratio maps as prior studies (Chapters Three and Four) have shown that, in general, they contain all the information of the difference map, and are more sensitive to the presence of small lineshape differences on top of similar intense backgrounds.

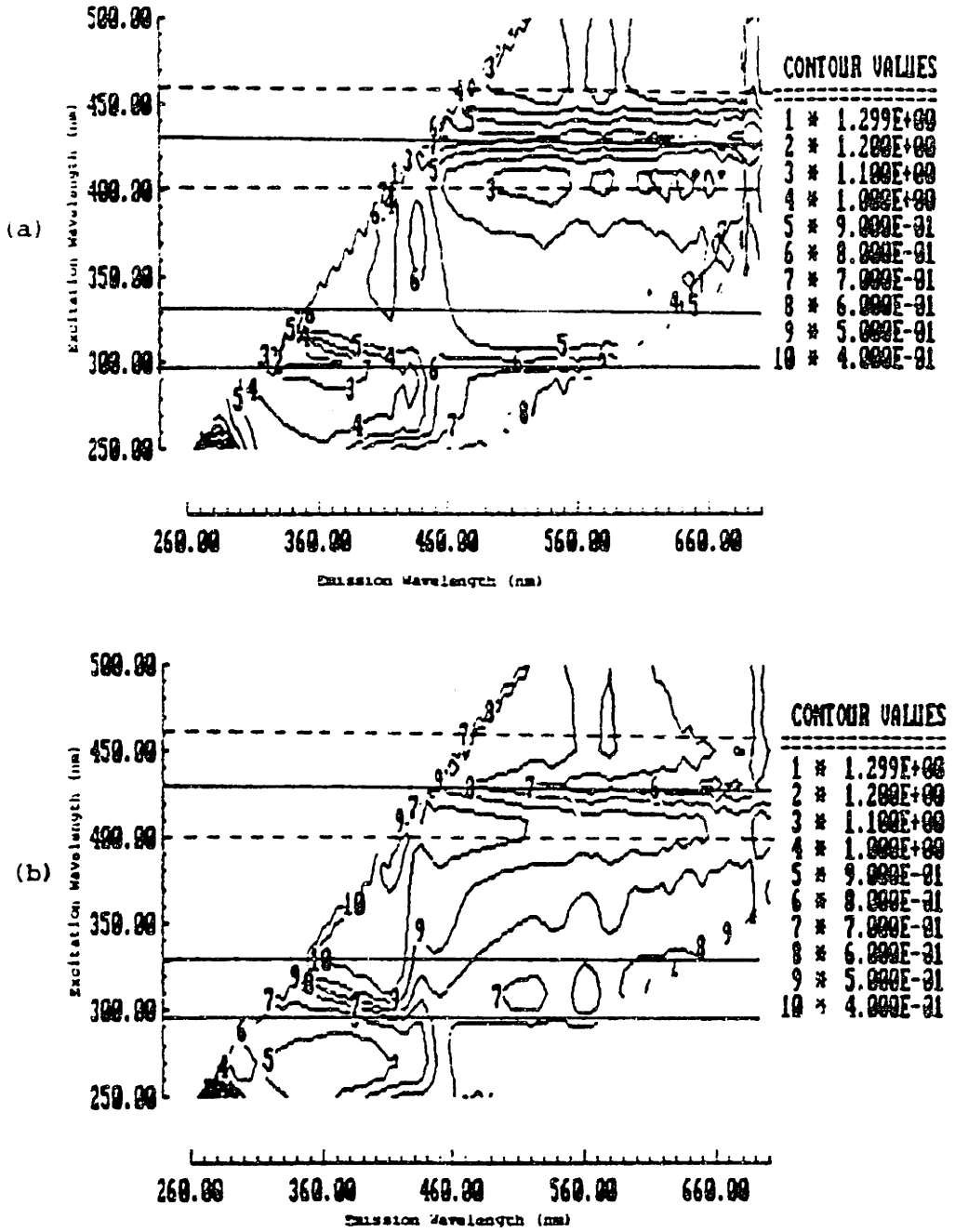

Figure 5: Contour map representations of the ratio of the average fluorescence EEMs of (a) chronic cystitis, (b) cystitis cystica, (c) CIS, (d) non-invasive papillary TCC, and (e) invasive TCC to normal urinary bladder. Thirteen linearly spaced contours are shown from 0.1 to 1.3.

(c)

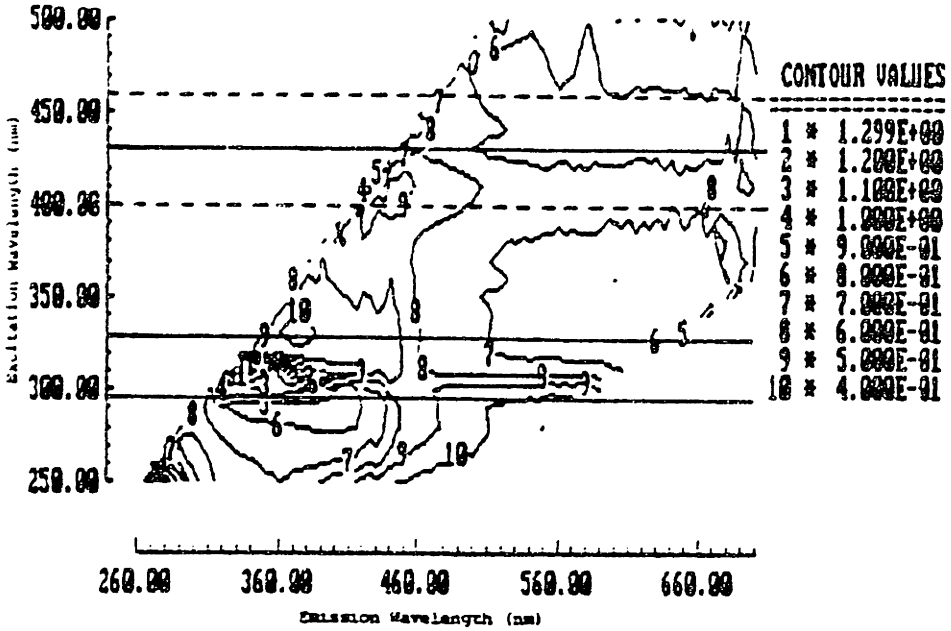

(d)

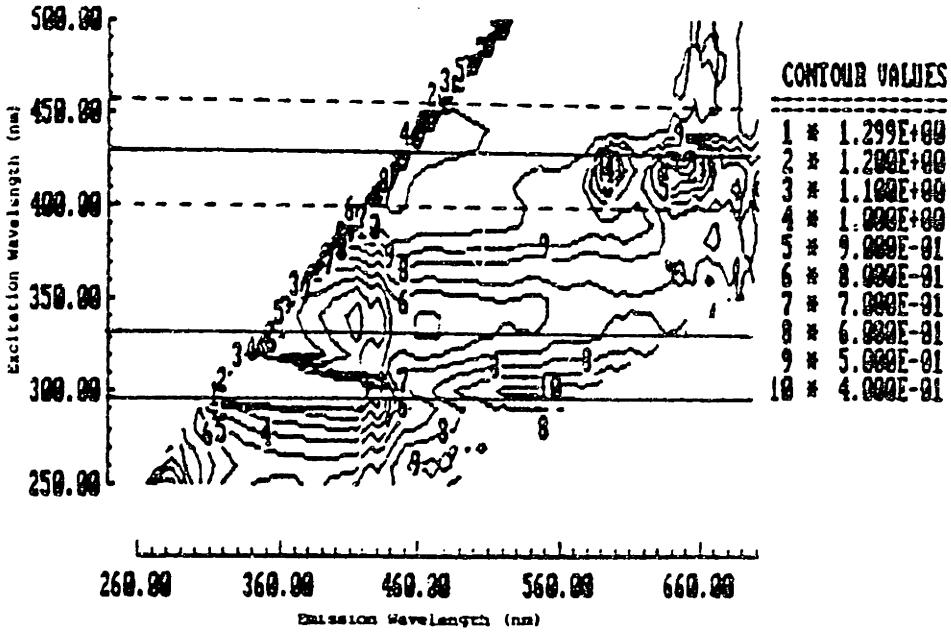

Figure 5 (Cont.):

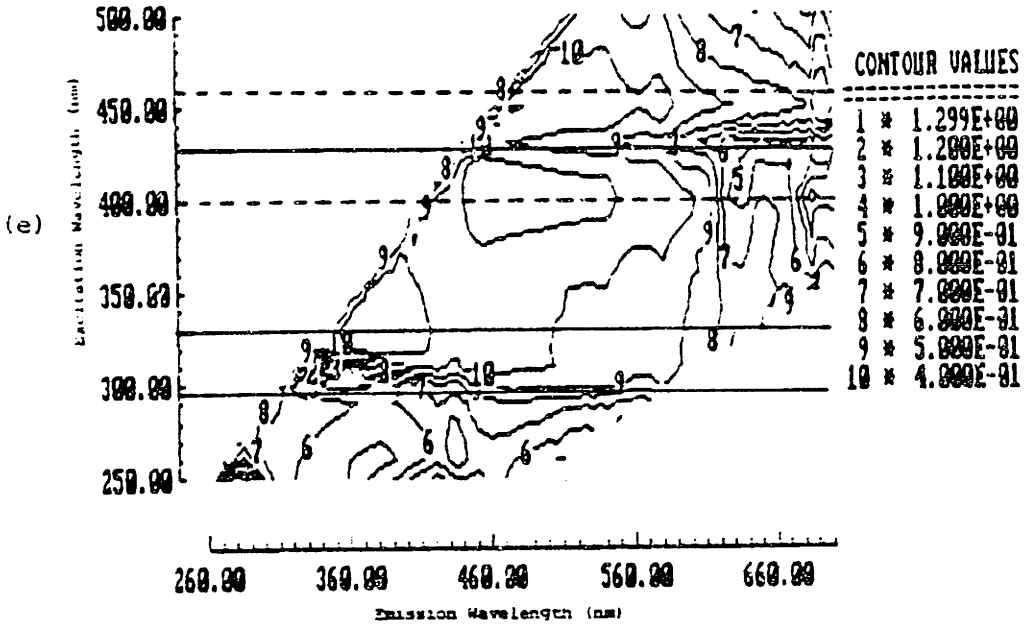

Figure 5 (Cont.):

The ratio of the EEMs of cystitis cystica, CIS and invasive TCC all exhibited local minima of approximately 0.4 at (330, 390 nm), consistent with the previously reported differences in intensity of the peak at this location in Table 1. The fluorescence EEM of papillary TCC did not differ from that of normal tissue in this region. However, in the ratio of the EEM of the papillary TCC to the normal bladder, two local maxima were observed at 340 nm excitation and 420 and 460 nm emission, with values of 1.1 and 0.9, respectively.

The ratio EEMs of all these tissues to normal bladder exhibited several broad local minima near 400 and 450 nm excitation ranging in emission from 460 to 600 nm. These peaks are separated by valleys running parallel to the excitation and emission axes at 420, 540 and 580 nm, due to the absorption of oxyhemoglobin (see Sec. 5:4.1). It is likely then, that all these local minima are due to the emission of one or perhaps several chromophores, possibly pyridoxal 5'-phosphate, NADH or NAD(P)H, and/or elastin.

Finally, the ratio of the average EEM of papillary TCC exhibits two unique local maxima at 430 nm excitation and 590 and 650 nm emission. It is likely that these are due to the emission of porphyrins [29], which have been previously reported to accumulate in neoplastic tissues in several organs [27].

Because these local maxima and minima are broad, they can all be sampled with a small number of excitation wavelengths. An excitation wavelength near 290-300 nm can sample the differences reported in the region of tryptophan emission. Similarly, an excitation wavelength near 320-340 nm will detect differences in the emission of the band at (325, 380 nm) potentially due to collagen. The local maxima and minima in the visible region of the EEMs are extremely broad, and can be sampled with a single excitation wavelength at 425-435 nm. These differences could also be sampled with two excitation wavelengths in the region 390-410 nm and 450-470 nm. As these more closely match excitation maxima of bladder tissue, they will result in greater signal.

These excitation wavelengths optimal for the diagnosis of neoplastic bladder tissue are illustrated as bold horizontal lines in Fig. 5, at 295 nm, 330 nm, and 430 nm. Excitation wavelengths at 400 and 460 nm represent another method of obtaining the information in the visible region of the spectrum, and are shown as dashed lines in Fig. 5.

5:3: Empirical Diagnostic Algorithms at These Excitation Wavelengths

Fluorescence emission spectra were recorded from many samples of urinary bladder at excitation wavelengths in each of these regions. Two spectrometers, described in Chapter Two, were used: a conventional fluorimeter, and a laser spectrometer utilizing an optical fiber catheter. The laser spectrometer has several important advantages - unlike the conventional fluorimeter, it provides a well defined collection geometry [30, 31], and it can, with minimal modifications, be used to collect tissue fluorescence spectra *in vivo* [32]. Despite its disadvantages, however, the conventional spectrofluorimeter was initially utilized because of its simplicity and availability. Most samples were studied with this system, so these results are reported here.

Data were collected *in vitro* from full thickness samples of human urinary bladder obtained from resection specimens of patients with TCC. Upon removal, specimens were snap frozen in liquid nitrogen and isopentane and stored at -70° C until study. The specimens were thawed at room temperature, and kept moist with 140 mM buffered saline, pH 7.4. For studies with the fluorimeter, samples were mounted in a quartz cuvette. Following study, the samples were fixed in 4% formalin solution, paraffin embedded, cut into 4 μm sections and stained with hemotoxylin and eosin. The resultant slides were examined by a single genitourinary pathologist.

Using the conventional fluorimeter as described in Chapter Two, fluorescence emission spectra were collected at three excitation wavelengths corresponding to three of the regions identified from the EEMs: 290 nm, 330 nm, and 476 nm. Spectra were collected from 37 samples of urinary bladder from 28 patients. Twelve samples had histologically normal urothelium, five displayed chronic cystitis, two showed both chronic cystitis and cystitis cystica. Two samples displayed focal CIS, three non-invasive papillary TCC, and ten were high grade invasive TCC. Spectra from three samples were not analyzed because of significant autolysis, or the presence of deep lymphatic tumor. With the conventional fluorimeter, because of variations in incident spot size, a consistent measurement of absolute fluorescence intensity was not obtained, therefore, spectra obtained with this instrument were normalized to one at the wavelength corresponding to the peak emission intensity of normal bladder.

Using the optical fiber catheter as described in Chapter Two, fluorescence emission spectra were collected from eight samples of human urinary bladder from eight patients at two excitation wavelengths corresponding to regions identified from the EEMs previously: 319.9 nm and 435.7 nm. Four of these samples had histologically normal urothelium, two showed evidence of chronic cystitis, one displayed focal CIS, and the other displayed invasive TCC. With this system, an accurate measurement of absolute fluorescence intensities was obtained; fluorescence intensities are reported here in arbitrary units relative to a standard, as described in Chapter Two.

At each excitation region surveyed with the conventional fluorimeter, empirical diagnostic algorithms for the presence of TCC and inflammation were defined and evaluated in order to determine which excitation regions provided the most useful diagnostic information. In all cases, the same method of algorithm development was used. This method utilizes scatter plots of fluorescence intensities at various wavelengths, and is described in detail in Chapter Two.

Briefly, this method consists of comparing the fluorescence intensity of all normal, inflammatory, and cancerous specimens at one or two emission wavelengths in a one or two dimensional scatter plot. Diagnostic algorithms were defined from these plots by using straight line segments to divide the plot into regions classified as normal, inflammation or TCC. The emission wavelengths where the fluorescence intensities of normal, inflammatory, and cancerous tissues are most different are those corresponding to local maxima and minima in the ratio of the average fluorescence emission spectra of

these classifications of urinary bladder[2]. In principle, if the emission of individual tissue chromophores is well separated, the intensities at the emission wavelengths identified with this method are correlated to the concentration and quantum yield of individual chromophores. Thus, the empirical algorithms presented here are crudely related to the biochemically based algorithms we hope to ultimately achieve.

Here, at 290, 330 and 476 nm excitation, we present the average spectra of each classification of urinary bladder, the ratio spectra, and the most effective one or two dimensional classification scheme. Data obtained with the laser spectrometer are also presented; however, because of the small number of samples studied, diagnostic algorithms for the presence of disease were not defined. Instead, these spectra are compared to those obtained with the conventional fluorimeter, to illustrate the advantages of catheter based fluorimeters.

5:3.1: Fluorimeter data

Figure 6(a) shows the average, normalized, fluorescence emission spectrum of normal urinary bladder at 290 nm excitation. Also shown are the average spectrum ± the standard deviation. Figure 6(b) again shows this average spectrum, with the average spectrum of the other tissue classifications (chronic cystitis, chronic cystitis with cystitis cystica, CIS, non-invasive, papillary TCC and invasive TCC) superimposed. All spectra show similar general features - an intense emission peak at 310 nm, and a much less intense peak at 480 nm, with an intervening valley at 420 nm.

Although these spectra all share similar features, there are differences in the lineshape of the 310 nm peak, and in the relative intensity of the 480 nm peak. These are best illustrated in Fig. 7, which shows the ratio of the average spectra of pathologic bladder to that of normal bladder. These ratios can be characterized by three regions, one near 420 nm, and two adjacent regions, one each above and below this. Above 450 nm, the difference in relative intensity of the 480 nm peak can be seen by a relatively flat region. All pathologic categories exhibited relatively less fluorescence than normal tissue at 480 nm. Below 400 nm, differences in the lineshape of the 310 nm peak can be observed. Peaks and valleys can be observed both at the long and short wavelength edge of this peak. These are consistent with possible shifts in the emission profile of the aromatic

[2]Here, we construct only the ratio spectra as prior studies (Chapters Three and Four) have shown that , in general, they contain all the information found in the difference spectra.

amino acid tryptophan [33]. Near 420 nm, all of these ratio spectra have peaks, reflecting possible differences in the hemoglobin content of these tissues relative to normal bladder.

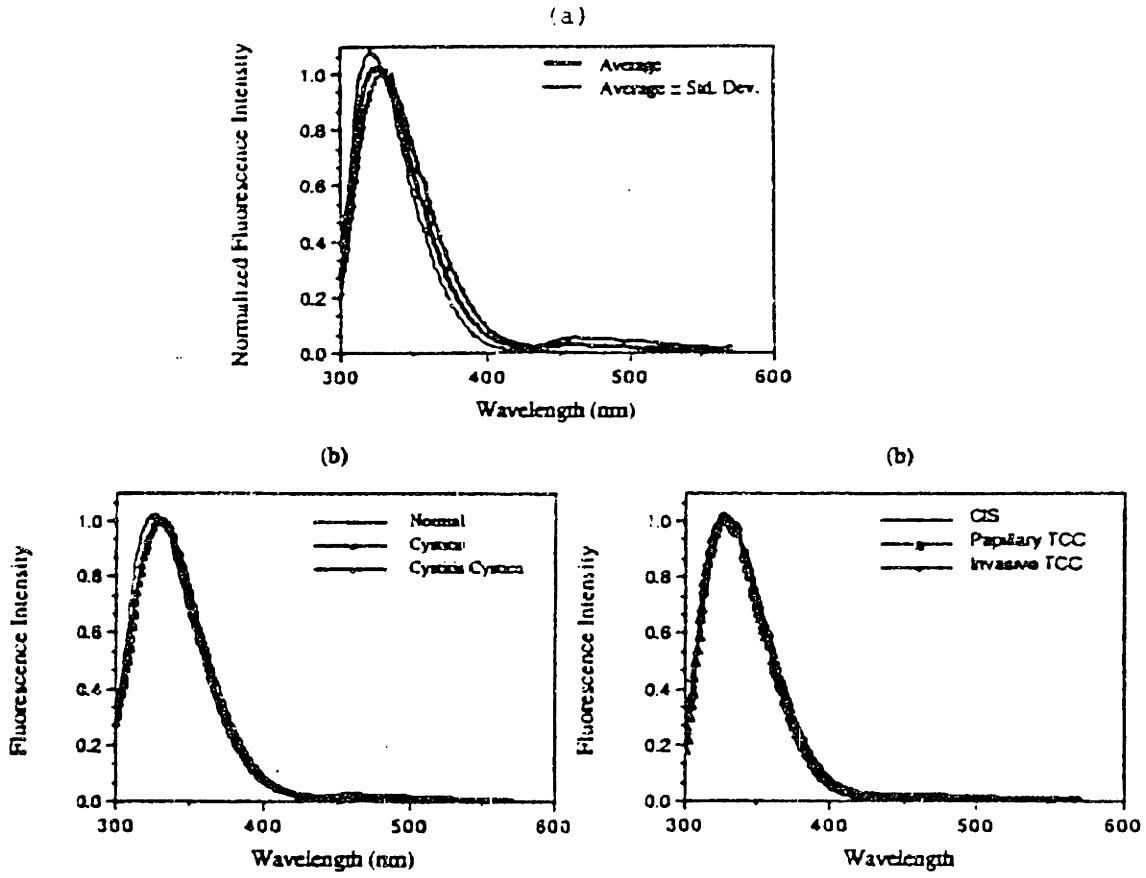

Figure 6: (a) Average emission spectrum ± standard deviation of normal urinary bladder. (b) Average emission spectra of normal urinary bladder, chronic cystitis, chronic cystitis with cystitis cystica, CIS, non-invasive papillary TCC, and invasive TCC. The excitation wavelength is 290 nm. Spectra have been normalized at 320 nm.

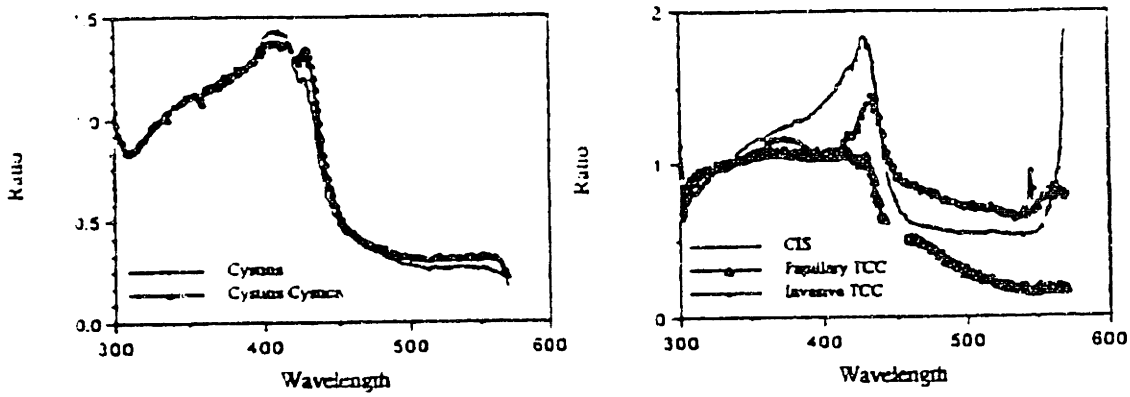

Figure 7: Ratio of the average spectra of chronic cystitis, chronic cystitis with cystitis cystica, CIS, non-invasive papillary TCC and invasive TCC to normal urinary bladder. The excitation wavelength was 290 nm.

Empirical algorithms were defined for the presence of inflammation and TCC using fluorescence intensities at emission wavelengths corresponding to local maxima and minima in the ratio spectra of Fig. 7, using the method outlined in Chapter Two. Using data at a single emission wavelength, no effective diagnostic algorithms could be defined. However, the emission wavelengths of 310 and 373 nm were most effective for differentiating normal tissue from all other categories. Similarly, any of the closely spaced emission wavelengths, 413, 420, 428, or 433, were the most effective for diagnosing the presence of inflammation, and 483 nm was most effective for identifying TCC. Two dimensional algorithms were thus defined from fluorescence intensities at combinations of these three sets of emission wavelengths.

Two effective two-dimensional algorithms were defined to separate bladder with normal urothelium from that with TCC and inflammation. These are shown in Fig. 8; that in Fig. 8(a) utilizes fluorescence intensities at 310 and 483 nm, and that in Fig. 8(b) 373 and 483 nm. In both cases, the algorithms misclassify one non-invasive papillary TCC and two invasive TCCs. The algorithm in Fig. 8(a) misclassifies two normal samples, that of 8(b) misclassifies one normal. This corresponds to a specificity, sensitivity and positive predictive value of 87%, 82%, and 87% respectively for the algorithm in Fig. 8(a), and 87%, 90% and 93% respectively for that in Fig. 8(b).

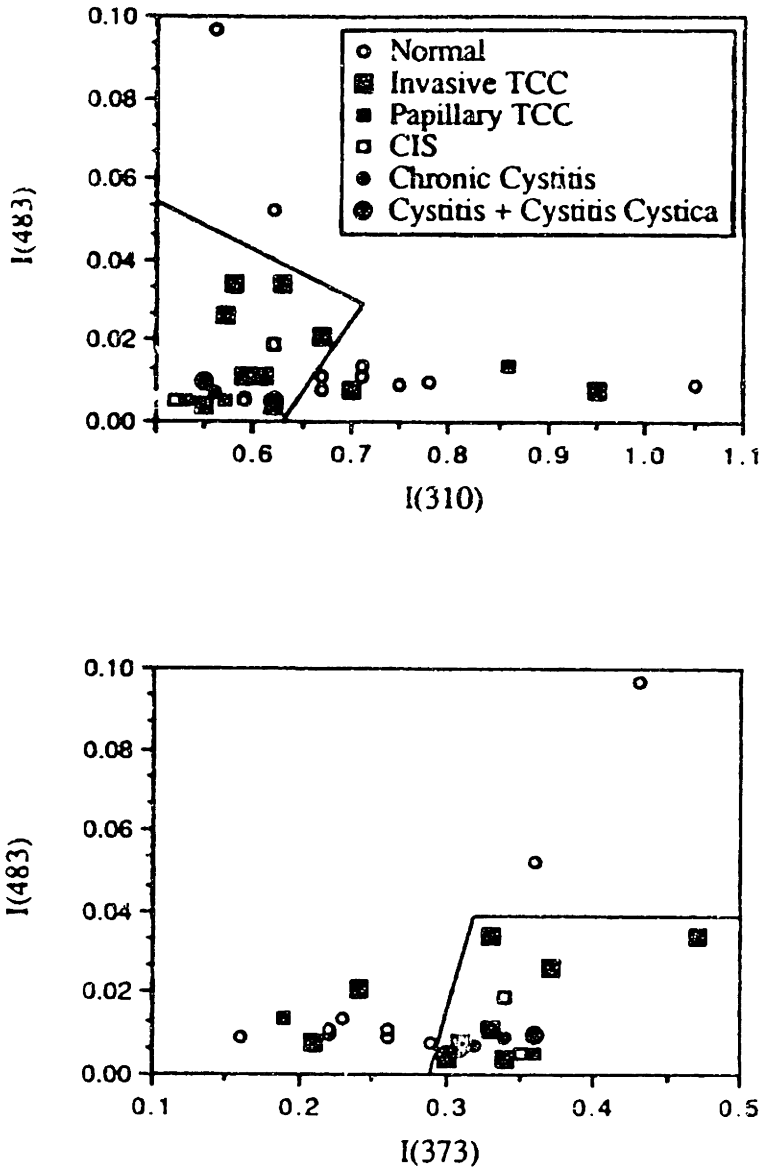

Figure 8: Two dimensional algorithms to separate bladder with normal urothelium from that of inflammation and TCC. That in (a) utilizes fluorescence intensities at 310 and 473 nm, while that of (b) utilizes 373 and 483 nm.

While these algorithms are effective at identifying those samples with normal urothelium, it is desirable to identify those pathologic samples displaying TCC. As illustrated in Fig. 9, the fluorescence properties of these tissue types are significantly different at these excitation-emission wavelength pairs. Figure 9 shows a two dimensional scatter plot of the fluorescence intensity at 413 nm vs that at 483 nm for all samples displaying epithelial inflammation or TCC. Although the fluorescence properties

of these tissue types are different, the scatter in the data precludes definition of an effective two dimensional empirical algorithm from this data to separate these two categories of tissue. This suggests that more information is required to achieve an effective classification scheme. Reliable measurement of absolute fluorescence intensities or higher order classification schemes represent two potential methods of improving these algorithms.

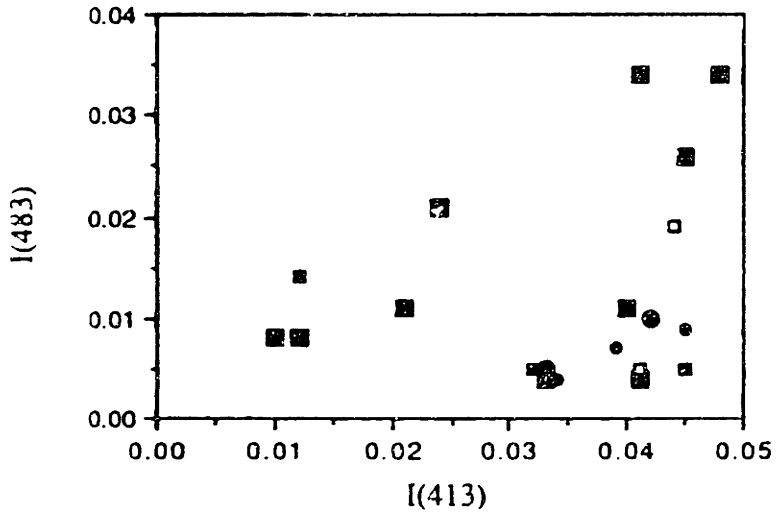

Figure 9: Two dimensional scatter plot of florescence intensities at 413 and 483 nm for samples displaying epithelial inflammation and TCC.

Figure 10(a) shows the average, normalized fluorescence emission spectrum of normal urinary bladder obtained at 330 nm excitation. The average spectrum ± standard deviations are also shown. Figure 10(b) shows the average, normalized spectra of all tissue categories at this excitation wavelength. All spectra show similar features: emission maxima at 380 nm, 470 nm, 560 and 610 nm with valleys at 420, 540 and 580 nm. Differences in the relative intensity of the peaks at 380, 560 and 610 nm and the valley at 420 nm are apparent in the various categories of tissue. In addition, there are differences in the lineshape of the peak at 470 nm.

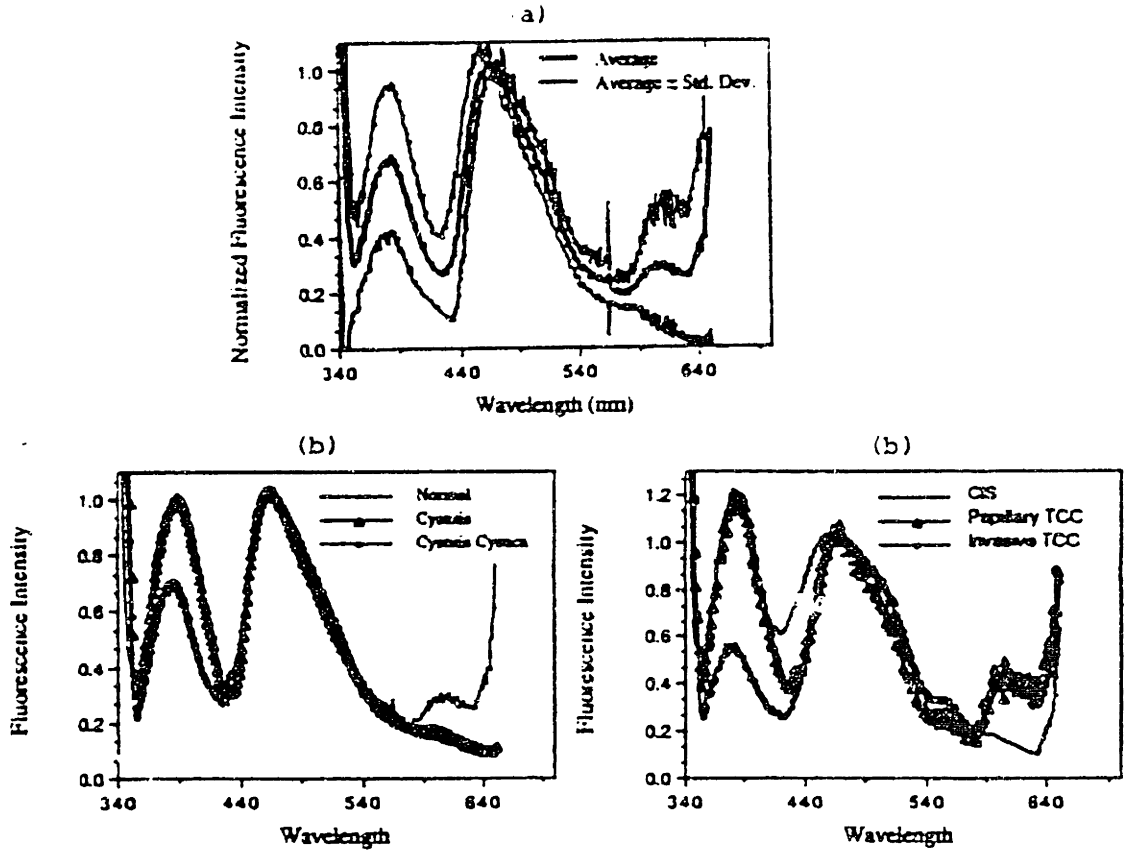

Figure 10: (a) Average spectrum and average ± standard deviation of normal urinary bladder. (b) Average spectra of normal urinary bladder, bladder with chronic cystitis, chronic cystitis and cystitis cystica, CIS, non-invasive papillary TCC and invasive TCC. The excitation wavelength was 330 nm. Spectra have been normalized at 470 nm.

These differences are quantified in Fig. 11, which shows the ratio of the average spectra of the categories of abnormal bladder to that of normal urinary bladder. These ratio spectra can be divided into five regions. The region from 340 - 400 nm illustrates variations in the relative intensity and lineshape of the peak at 380 nm, previously assigned to collagen. The region from 400 - 440 nm illustrates differences in the contribution of hemoglobin absorption. These differences are also apparent from 540 - 580 nm. The region from 440 - 540 nm illustrated differences in the lineshape of the

peak at 470 nm, which are most pronounced for invasive TCC. Finally, the region above 600 nm illustrates differences in the relative intensity of the peak at 610 nm. This peak is most pronounced in papillary and invasive TCC.

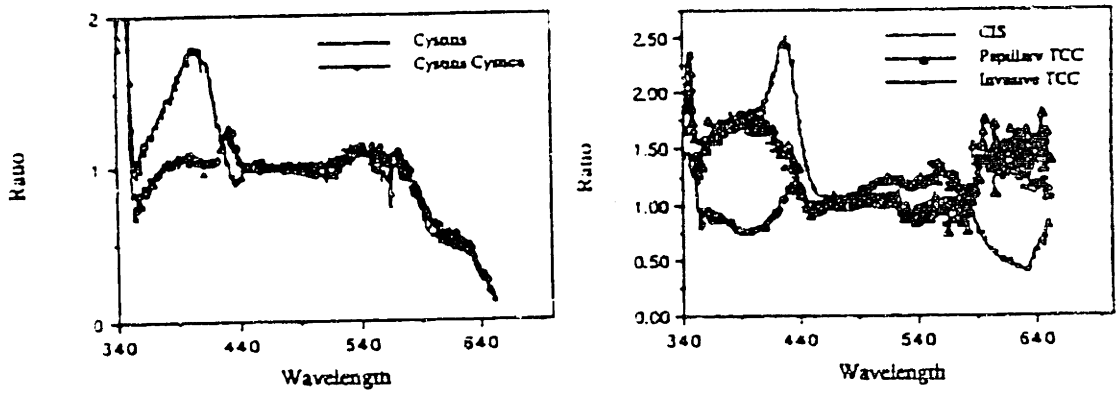

Figure 11: Ratio of the average spectra of bladder with chronic cystitis, chronic cystitis with cystitis cystica, CIS, non-invasive, papillary TCC and invasive TCC to that of normal urinary bladder. The excitation wavelength was 330 nm.

Empirical diagnostic algorithms were defined using fluorescence intensities corresponding to local maxima and minima in the ratio spectra of Fig. 11. No effective diagnostic algorithms could be identified using intensities at a single emission wavelength. However, data at emission wavelengths of 366 and 458 nm were most effective for separating tissue with TCC from other tissue categories. Similarly, emission intensities at 406 nm were most effective for separating inflamed tissues from other samples, and data at 430 nm was most effective for separating normal samples from other tissue types. Two dimensional algorithms utilizing emission intensities at these three sets of emission wavelengths were thus considered.

Figure 12 shows the two most effective two dimensional algorithms for the presence of TCC defined from this data. That in Fig. 12(a), based on emission intensities at 386 and 430 nm misclassifies only one non-invasive papillary TCC and one normal sample. The second, in Fig. 12(b) is based on emission intensities at 430 and 456 nm, and misclassifies one non-invasive, papillary TCC, one normal sample and one sample with chronic cystitis and cystitis cystica. The performance of these algorithms was

characterized by their specificity, sensitivity and positive predictive value, which are given by 94%, 89% and 89% respectively for that of Fig. 12(a), and 88%, 90% and 85% respectively for that in Fig. 12(b).

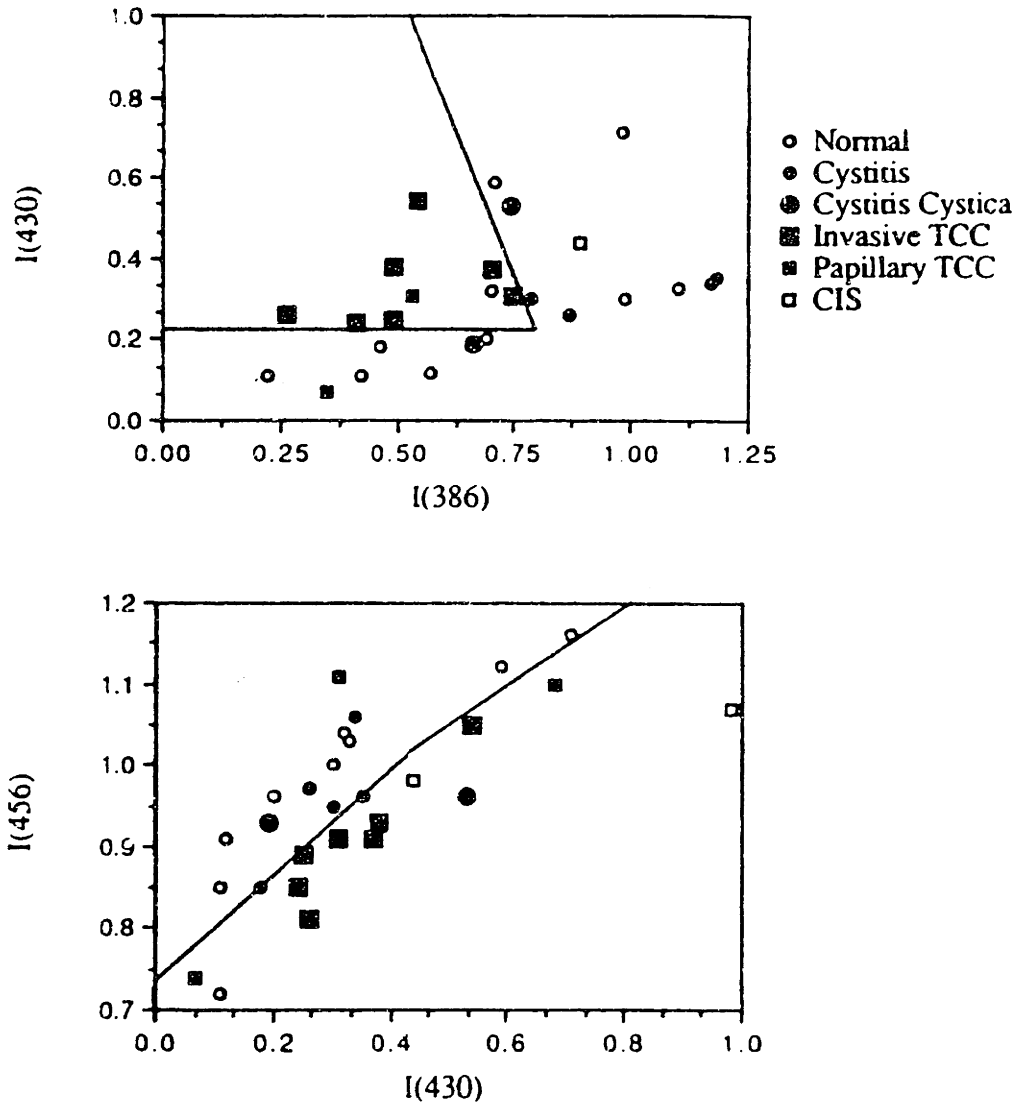

Figure 12: Two dimensional algorithms for the presence of TCC in urinary bladder. That in (a) is based on emission intensities at 386 and 430 nm, that in (b) utilizes 430 and 456 nm.

These algorithms represent an improvement over those presented in Fig. 8 for 290 nm excitation, in that tissues with TCC are separated from all other tissue categories. However, again, it is desirable to separate those samples which are histologically normal from those which have urothelial inflammation. Figure 13 shows a two dimensional scatter plot of the fluorescence intensity at 406 nm vs that at 430 nm for all samples

without TCC. This shows that the spectroscopic properties of these tissue types are different, but is not diagnostically useful. Again, this suggests that additional information must be incorporated in these algorithms, perhaps either via higher order classification schemes or reliable measurement of absolute fluorescence intensities.

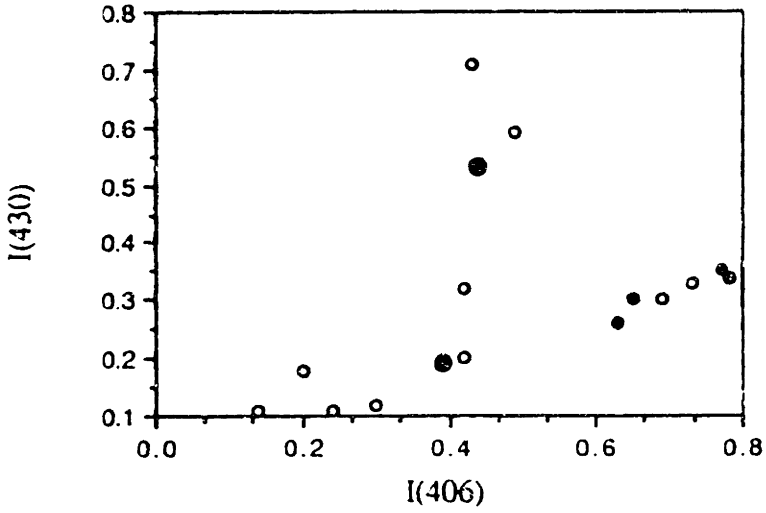

Figure 13: Two dimensional scatter plot of the fluorescence intensities at 406 and 430 nm of all samples of urinary bladder without TCC. The excitation wavelength was 330 nm.

Figure 14(a) shows the average normalized emission spectrum of normal urinary bladder at 476 nm excitation. The average spectrum ± standard deviations are also shown here. Figure 14(b) shows this average spectrum with the average spectra of bladder with chronic cystitis, chronic cystitis with cystitis cystica, CIS, non-invasive papillary TCC, and invasive TCC superimposed. These spectra are again characterized by similar features. All tissue spectra show peaks at 510, 560 and 600 nm, with intervening valleys at 540 and 580 nm. However, the emission spectra of the various tissue categories differ, both in the relative intensity of the various peaks and valleys and in fluorescence lineshape.

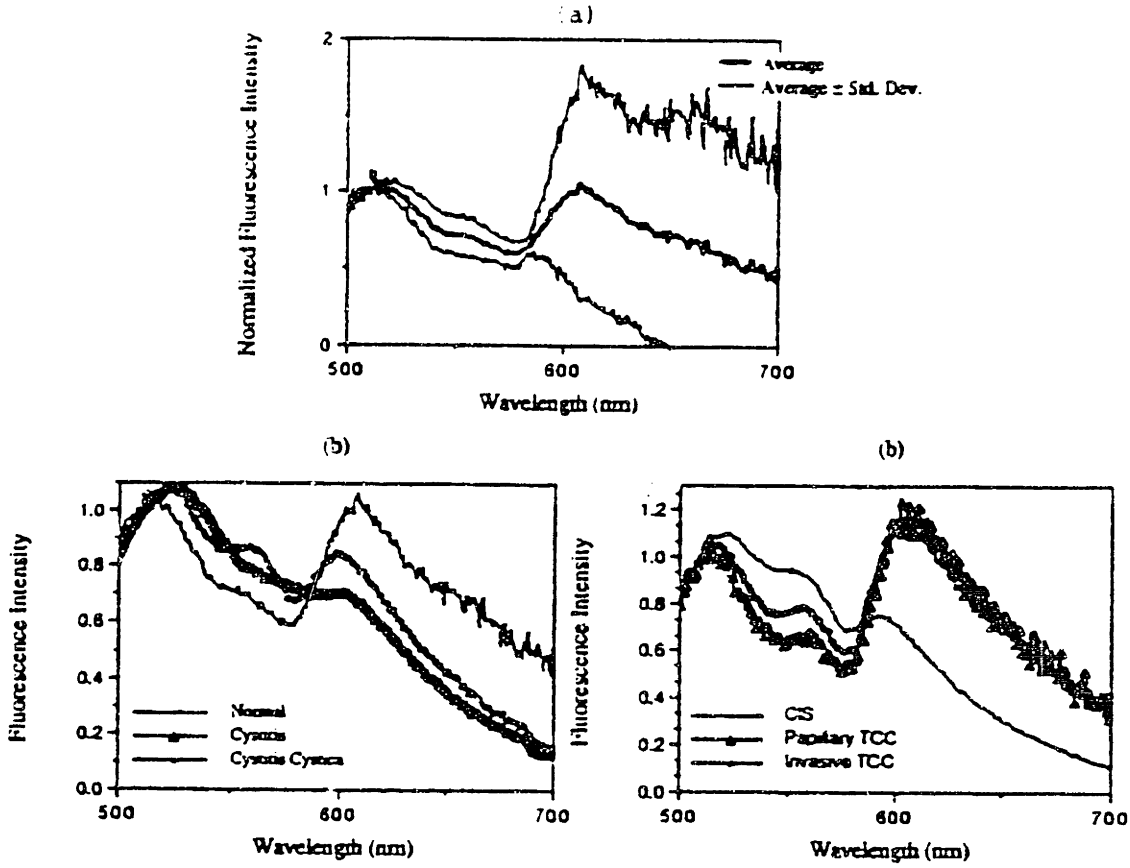

Figure 14: (a) Average normalized fluorescence emission spectra of normal urinary bladder, ± standard deviations. (b) Average fluorescence emission spectra of normal urinary bladder, bladder with chronic cystitis, chronic cystitis with cystitis cystica, CIS, non-invasive papillary TCC, and invasive TCC. The excitation wavelength was 476 nm. Spectra have been normalized at 500 nm.

These differences are illustrated more quantitatively in Fig. 15, which shows the ratio of the various categories of abnormal bladder to normal urinary bladder. These spectra exhibit peaks and valleys at 540 and 580 nm, due to differences in the contribution of oxy-hemoglobin absorption. Differences in the relative intensities of the peaks at 520, 560 and 600 nm are apparent as local maxima in the ratio spectra. Finally, local maxima are present at 634 and 680 nm in many of the ratio spectra.

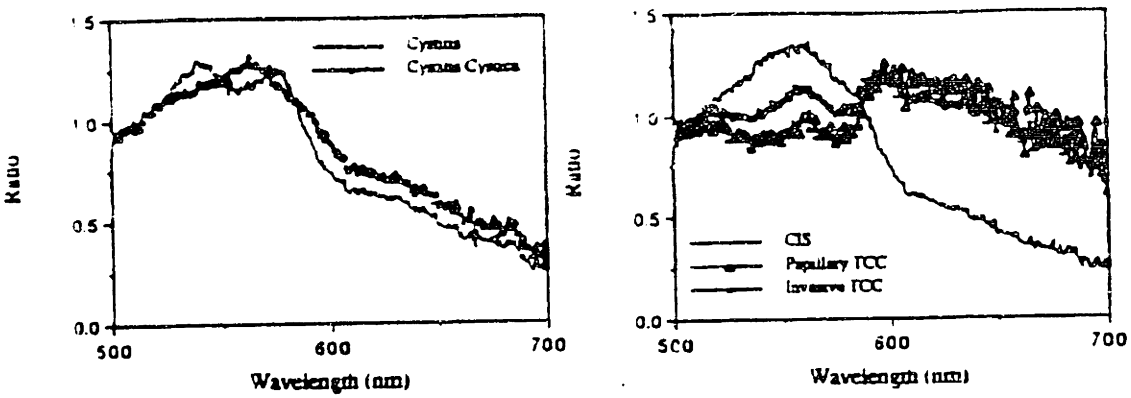

Figure 15: Ratio of the average spectra of bladder with chronic cystitis, chronic cystitis with cystitis cystica, CIS, non-invasive papillary TCC and invasive TCC to the average spectrum of normal urinary bladder. The excitation wavelength was 476 nm.

Empirical algorithms were defined based on fluorescence intensities at emission wavelengths corresponding to local maxima and minima in the ratio spectra. Again, no effective algorithms could be found from a consideration of data at a single emission wavelength. However, algorithms based on emission intensities at 634 and 680 nm were particularly effective at differentiating those samples with TCC from all others. Algorithms based on intensities at 562 and 588 were most effective at separating normal samples from all others, and intensities at 520 and 540 nm were most effective at separating those samples with urothelial inflammation from others. Therefore, two dimensional algorithms were defined and evaluated from data at combinations from these three sets of emission wavelengths.

Figure 16 shows shows the most effective two dimensional algorithm for the presence of TCC. This algorithm utilizes fluorescence intensities at 562 and 680 nm, and misclassifies one normal sample, two samples of invasive TCC, and one sample of chronic cystitis and cystitis cystica. The specificity, sensitivity and predictive value of this scheme are all 87%. At this excitation wavelength, an effective algorithm could also be found to separate those samples without TCC according to the presence or absence chronic cystitis and chronic cystitis with cystitis cystica. Figure 17 shows a two dimensional algorithm based on fluorescence intensities at 540 and 588 nm, which separates samples without TCC effectively into these three categories.

in Fig. 16 are also plotted in Fig. 17. This procedure results in an overall misclassification rate of 6/34, or 18%.

In conclusion, at 330 and 476 nm excitation, empirical algorithms can be defined to separate those bladder tissues with CIS, papillary or invasive TCC from non-neoplastic bladder. In addition, at 476 nm, empirical algorithms can be defined to separate those non-neoplastic bladder tissues with inflammation from those without, suggesting that 476 nm excitation represents a region at which further study is indicated.

Although these algorithms were defined from a relatively small sample set, the incidence of disease in this data set was similar to that encountered in clinical applications. In one series of 200 cystoscopic biopsies from 71 patients to rule out TCC at the Cleveland Clinic Foundation the following incidence figures were found. TCC was observed in 30% of biopsies, 16% of tissues were normal, 12% exhibited proliferative cystitis, and 30% were given a non-specific diagnosis including acute or chronic inflammation, lamina propria edema or hemorrhage, ulceration, fibrosis, squamous metaplasia or denuded epithelium. 7% demonstrated urothelial atypia or dysplasia and 2% showed metastatic non-transitional cell carcinoma. The incidence figures for our data set were: 35% normal urothelium, 21% chronic inflammation, 44% TCC.

5:3.2: Catheter data

Tissue emission spectra were recorded at two excitation wavelengths corresponding to regions identified from the EEMs using the spectral catheter system described in Chapter Two. Figure 18 shows average emission spectra of normal urinary bladder, cystitis, cystitis cystica , CIS and invasive TCC at 319.9 nm excitation[3]. This can be compared to the emission spectra obtained at 330 nm excitation with the conventional fluorimeter presented in Fig. 10. In general, these spectra show similar features: two emission peaks at 380 and 470 nm; however, the valleys due to hemoglobin absorption are less prominent in the spectra obtained with the fiber optic catheter. In addition, with this system, the absolute fluorescence intensity could be easily recorded. This represents an additional piece of information, which may have diagnostic significance.

---

[3]The S/N in the spectra obtained at this excitation wavelength was approximately 10. This is lower than the desired minimum value of 20 stated earlier. The low S/N is primarily due to the weak excitation intensity used to record these spectra. In future experiments this S/N can be improved either by increasing the excitation intensity or the integration time without producing laser induced alteration of tissue spectral properties.

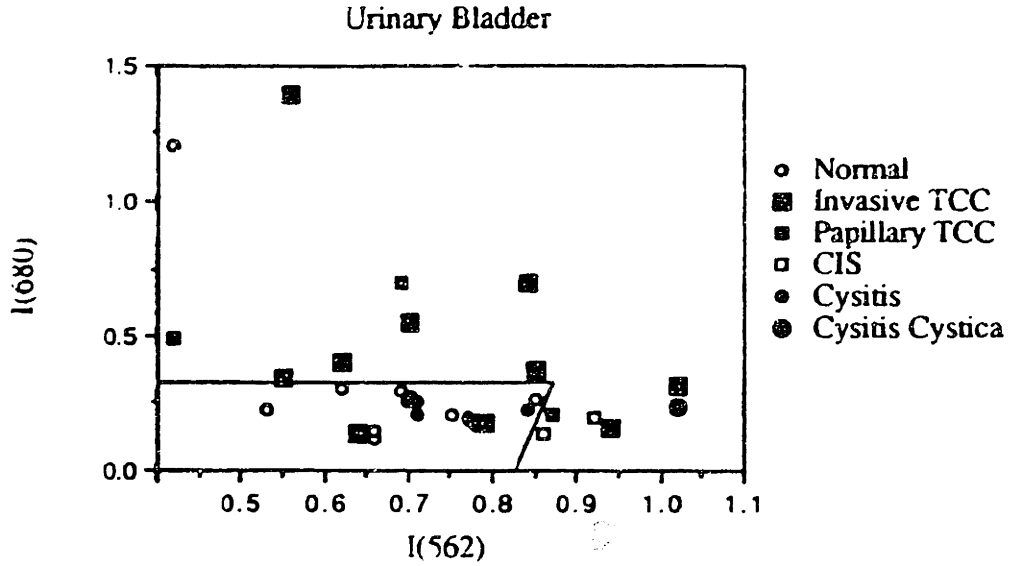

Figure 16: Two dimensional classification scheme for the presence of TCC in urinary bladder. This algorithm is based 476 nm excitation and on fluorescence intensities at 562 and 680 nm.

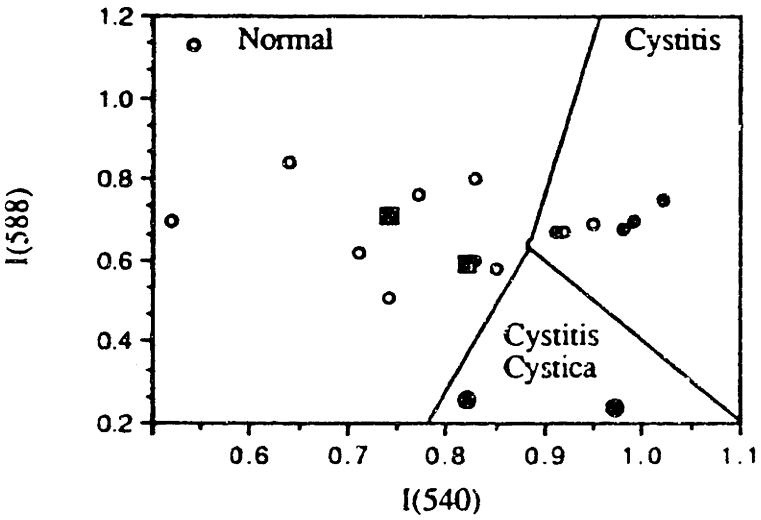

Figure 17: Two dimensional classification scheme for the presence of cystitis and cystitis cystica in those samples without TCC. This scheme is based on 476 nm excitation and emission wavelengths of 540 and 588 nm.

Thus, at this excitation wavelength, we can construct a two step algorithm to diagnose tissue type into these three categories. Step 1 consists of applying the algorithm in Fig. 16 to identify those samples with TCC. Step 2 then consists of applying the algorithm in Fig. 17 to those samples identified as non-cancerous in Step 1. For our defining data set, we have followed this procedure; those samples with TCC misclassified

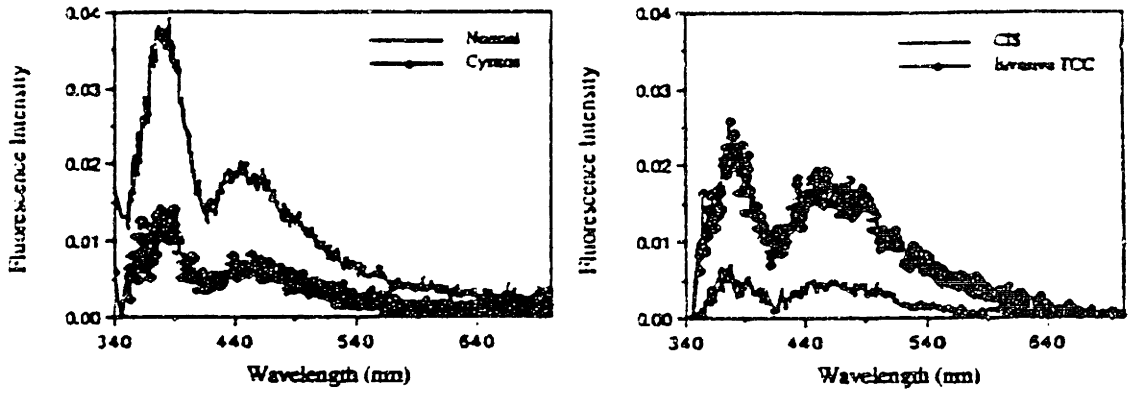

Figure 18: Average fluorescence emission spectra of normal urinary bladder, chronic cystitis, CIS and invasive TCC. The excitation wavelength was 319.9 nm, and the spectra were obtained with a fiber optic catheter system. Fluorescence intensities are reported in arbitrary units relative to a fluorescence standard as described in Chapter Two. The same set of arbitrary units is maintained for data collected with this system throughout this thesis.

Figure 19 shows the average emission spectrum of the same samples obtained at 435.7 nm excitation. These can be compared to the average spectra obtained with the conventional fluorimeter at 476 nm excitation shown in Fig. 14. Again, the features of these spectra are similar, with at broad peak at 510 nm, and subsidiary minima at 540 and 580 nm. However, these valleys are much less pronounced in the data obtained with the fiber optic catheter, due to its specially designed collection geometry [31, 32]. The absolute fluorescence intensities are quite different for the various categories of tissue, and represent an additional piece of diagnostic information, which should be considered in future algorithm development.

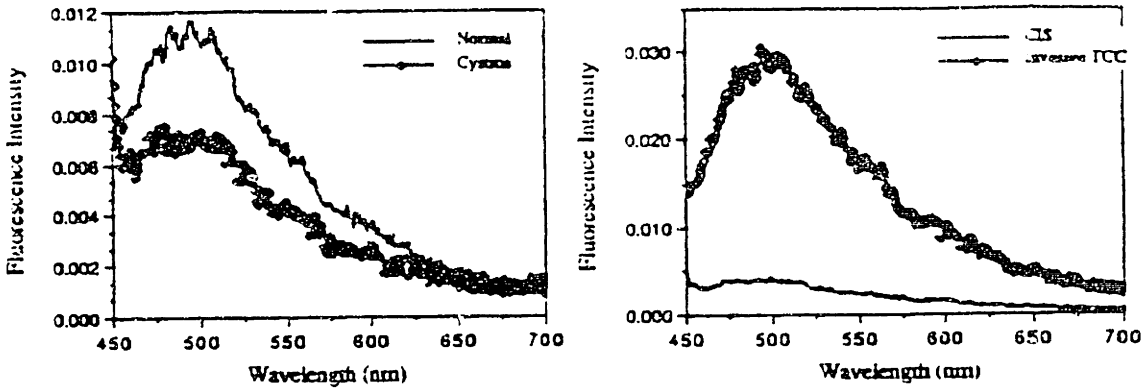

Figure 19: Average fluorescence emission spectra of normal urinary bladder, chronic cystitis, CIS and invasive TCC. The excitation wavelength was 435.7 nm, and the spectra were obtained with a fiber optic catheter system. Fluorescence intensities are reported in arbitrary units relative to a fluorescence standard as described in Chapter Two. The same set of arbitrary units is maintained for data collected with this system throughout this thesis.

The algorithms presented earlier for data obtained with the conventional fluorimeter could likely be improved if spectra were collected with a catheter based system, allowing absolute fluorescence intensities to be recorded.

In the next section, we attempt to develop a preliminary understanding of the morphologic and chemical features of TCC which are amenable to detection with fluorescence spectroscopy, and provide the basis for the algorithms presented here. This is achieved by a closer consideration of the chemical information contained in the fluorescence EEMs presented in Section 5:1 of this chapter.

5:4: Morphologic/Biochemical Basis of Tissue Fluorescence

5:4.1: EEMs

Here, we compare the fluorescence EEMs of urinary bladder presented earlier to fluorescence EEMs of pure biomolecules in order to obtain a potential identification of tissue fluorophores at the molecular level. As described previously, tissue fluorescence spectra contain contributions from both intrinsic fluorescence and attenuation, and to

compare the EEMs of pure biomolecules to tissue EEMs it if first necessary to separate the effects of attenuation from tissue EEMs.

Total reflectance spectra provide a measure of the attenuation contributions to tissue EEMs. Again, in a total reflectance spectrum, valleys indicate peaks in attenuation. Attenuation peaks act to produce valleys in the fluorescence spectra of optically thick tissue samples [30, 31]. Attenuation effects are important both for exciting and emitted radiation, and valleys will be produced in both excitation and emission spectra. At the location of these attenuation peaks, valleys, parallel to the excitation and emission axes, will be present in the tissue EEMs.

Attenuation effects, which include both scattering and absorption, were recorded independently by measuring total reflectance spectra of 26 samples of urinary bladder from 20 patients, using a standard absorption spectrophotometer equipped with an integrating sphere. Percent total reflectance was recorded from 200 - 700 nm, with a resolution of 5 nm FWHM. Figure 20 shows total reflectance spectra of a typical sample of normal urinary bladder and invasive TCC. In both types of tissue, reflectance valleys are located at 270, 355, 420, 540, 575, and 635 nm. Other types of bladder tissue exhibited reflectance valleys at similar locations. These valleys are superimposed on a gently upward sloping background, which is slightly steeper for normal tissue.

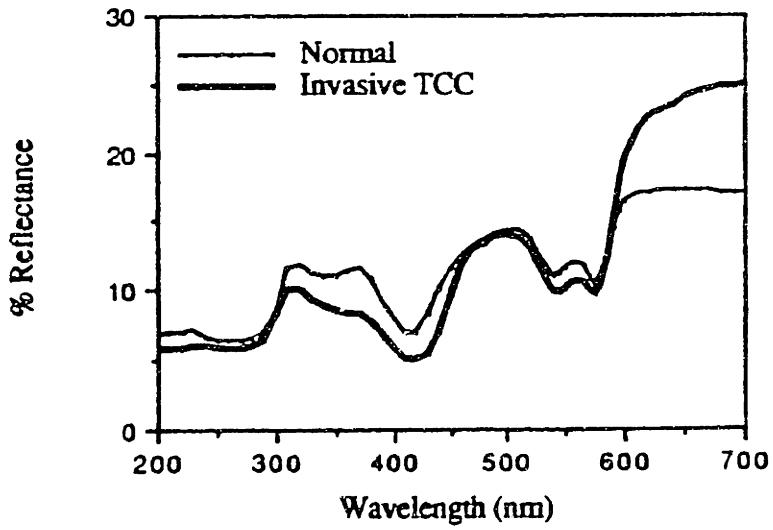

Figure 20: Typical total reflectance spectra of normal urinary bladder and invasive TCC of the bladder.

The valleys in the total reflectance spectra can be correlated with the valleys in the average EEM shown in Figs. 3 and 4. The attenuation peak at 420 nm gives rise to valleys in the tissue EEMs at 420 nm along the excitation and emission axes. Although not as prominent, valleys are also present along the emission axis at 540 and 575 nm.

It is well known that the absorption spectrum of oxy-hemoglobin exhibits peaks near 280, 350, 420, 540 and 580 nm [34]. Thus, nearly all of the attenuation peaks noted in the total reflectance spectra of urinary bladder in Fig. 20 could be attributed to oxy-hemoglobin. The presence of hemoglobin could be attributed to the vascularity of the bladder wall [4]. The gently upward sloping background in the tissue reflectance spectra is likely due to the attenuation of other proteins. In general, protein absorption is strong in the UV region, but falls off strongly in the visible [35]. Both extracellular structural proteins (i.e. collagen and elastin) and cellular proteins could contribute to this sloping attenuation.

The lineshape of the total reflectance spectrum is strikingly similar in all tissues studied here - arterial, gastro-intestinal and urinary bladder. In large part, this is because these tissues all contain varying degrees of oxyhemoglobin and structural proteins [4]. This similarity in attenuation is partly responsible for the similarities in the fluorescence EEMs of these tissues. In all, attenuation valleys of varying depth are present parallel to the excitation and emission axes at 420, 540 and 580 nm.

Potential tissue fluorophores were identified by comparing excitation/emission peaks in tissue EEMs to those in EEMs of pure biomolecules as well as peaks cited in the literature. EEMs of these molecules were previously described in Chapter 4:5.1. Table 3 contains a compendium of excitation-emission maxima from the EEMs of each of the biochemical compounds considered which might contribute to urinary bladder fluorescence [28, 29]. This list should not be considered exhaustive. Table 2 lists the local excitation-emission maxima in urinary bladder EEMs as well as our preliminary assignment of tissue fluorophores to those peaks based on comparison with Table 3.

Note, again, that the band positions in Table 3 do not exactly match the band positions in Table 2. Two effects may be responsible for these differences. Attenuation acts to alter both the observed location of the excitation/emission maxima and observed lineshape of individual tissue fluorophores in the multi-component tissue EEMs. Similarly, the observed lineshapes and positions of chromophore maxima can be altered

in multi-component tissue EEMs when the excitation and emission of individual chromophores closely overlap. For these reasons our identification should be considered preliminary.

Table 3: Summary of Excitation-Emission Maxima in Selected Biologically Important Molecules

Chromophore/ Chromomorph	1 mM Solution/ Dry Powder?	(λ_{exc},λ_{em}) Maximaa
Tryptophan	Solution	(275, 350 nm)
NADH	Solution	(350, 460 nm)
NADPH	Solution	(350, 460 nm)
4-Pyridoxic Acid	Solution	(300, 435 nm)
Pyridoxal 5'-phosphate	Solution	(305, 375 nm) (410,520 nm)
Collagen I	Powder	(340, 395 nm) (270, 395 nm) (285, 310 nm)
Collagen III	Powder	(275, 310 nm) (330, 390 nm) (370, 450 nm)
Elastin	Powder	(460, 520 nm) (360, 410 nm) (425, 490 nm) (260, 410 nm)
Pyridoxic acid lactone [28]		(360, 430 nm)
Porphyrins [29]		(400, 675 nm) (400, 610 nm)

[a] Where more than one maxima is given, they are listed in order of decreasing fluorescence intensity.

Again, the similarity of chromophore/chromomorph assignments in arterial, gastro-intestinal and urinary bladder tissues should be noted. The largest peak in the EEMs of all these tissues has been assigned to the aromatic amino acid tryptophan. In bladder tissue with TCC, significant differences were observed in the excitation emission profile of this peak. This could be due to differences in the tryptophan environment in these tissues. Interestingly, other workers have shown that bladder cancer is associated

with defects in tryptophan metabolism [4]. Certain metabolites of tryptophan-kynurenine are excreted in increased amounts in patients with bladder cancer [4].

The EEMs of arterial, gastro-intestinal, urinary bladder tissues all exhibited peaks near (345, 465 nm), which closely matches the excitation-emission maximum of both NADH and NAD(P)H. It should be noted that the (345, 465 nm) peak is bounded by attenuation valleys at 420 nm along the excitation and emission axes. Thus, the precise location of its excitation-emission maximum may be significantly shifted, and our preliminary assignment of this peak should be regarded with this caveat.

Several peaks which appear in the EEMs of arterial, gastro-intestinal, urinary bladder tissues are near peaks associated with chromophores related to vitamin B_6. The peak most intense in non-neoplastic bladder with chronic cystitis at (315, 430 nm) is near that of 4-pyridoxic acid at (300, 430 nm). Although three peaks are present in the normal and cancerous bladder tissue EEMs at (460, 530 nm), (465, 555 nm) and (470, 595 nm), again they are likely due to a single peak with superimposed oxy-hemoglobin attenuation valleys at 540 and 580 nm. Pyridoxal 5'-phosphate represents a potential candidate for this peak. Its largest excitation/emission maximum is at (410, 520 nm); the shift in the tissue excitation maximum could be attributed to the Soret band attenuation of oxy-hemoglobin.

These peaks assigned to pyridoxal 5'-phosphate could also be due to structural protein fluorescence. Elastin fluorescence exhibits a maximum at (460, 520 nm). Collagen I and collagen III fluorescence show peaks at (340, 395 nm) and (330, 390 nm), respectively. Fluorescence microscopy studies, described later, are required to make a definitive identification.

Finally, the prominent peaks were observed in the ratio of the EEMs of some types of TCC to that of normal bladder at (430, 600 nm) and (430, 630 nm). These peaks could be due to the presence of endogenous porphyrins. Hematoporphyrin derivative, for example, which is a mixture of several biologically relevant porphyrins, exhibits fluorescence excitation emission maxima near (400, 610 nm) and (400, 675 nm) [29]. Peaks at these locations were noted in the ratio of the EEMs of adenomatous colon to that of normal colon.

As noted above, comparison of EEMs from individual biochemical compounds with optically thick tissue EEMs does not always lead to definitive fluorophore

identification, because of potential difficulties created by attenuation and overlapping excitation and emission. Both of these difficulties can be overcome by modeling the tissue EEM in terms of the attenuation and fluorescence properties of individual chromophores.

The similarity in the fluorescence EEMs of neoplastic colon and urinary bladder suggest that the features of the florescence of these neoplastic tissues may be due to chromophores common to many neoplasms. In part, this is due to the fact that much of the observed fluorescence may be due to the structural proteins collagen and elastin. Similar architectural transformations occur in papillary neoplasms of these organs. However, many of the fluorophores assigned here have been previously associated with cancerous and precancerous states. NADH levels have been reported to decrease 2-3 fold following murine sarcoma virus transformation in rat kidney fibroblasts [36]. Decreased serum pyridoxal 5'-phosphate levels have been reported in cancer patients [37]. Increased porphyrin content has been reported in neoplasms of many organ systems [38].

In summary, the EEMs provide information about optimal excitation wavelengths for the differentiation of normal and neoplastic urinary bladder and about the identity of the chromophores and chromomorphs which contribute to tissue fluorescence spectra. Here, preliminary results have shown that fluorescence spectroscopy is promising for ultimately improving methods for early detection of neoplasia in the urinary bladder.

5:5: References

1. American Cancer Society, 1986 Cancer Facts and Figures, American Cancer Society, New York, 1986.

2. Schmidt RF, Thews G, Human Physiology, Springer-Verlag, Berlin, 1983.

3. Ham AW, Cormack DH, Histology, 8th ed., JB Lippincott Co., Philadelphia 1979.

4. Robbins SL, Cotran RS, Kumar V, Pathologic Basis of Disease, Third Edition, WB Saunders Co, Philadelphia, 1984.

5. Koss LG, Tumors of the Urinary Bladder, Armed Forces Institute of Pathology, Washington DC, 1975.

6. Koss LG, Tiamson EM, Robbins MA, JAMA 227:281-86, 1974.

7. Braunwald E, Isselbacher KJ, Petersdorf RG, Wilson JD, Martin JB, Fauci AS, Harrison's Principles of Internal Medicine, 11th ed, McGraw-Hill, New York, 1987.

8. Hendry WF, Manning N, Perry NM, Whitfield HN, Wickham JEA, The Effects of a Haematuria Service on the Early Diagnosis of Bladder Cancer, Chapt. 3, in Oliver RTD, Hendry WF, Bloom HJG, Bladder Cancer, Principles of Combination Therapy, Butterworths, London, p. 19-26, 1981.

9. Oliver RTD, Hendry WF, Bloom HJG, Bladder Cancer, Principles of Combination Therapy, Butterworths, London, 1981.

10. Esposti, Urinary Cytology for Diagnosis, Grading and Monitoring Response to Treatment, Chapt. 2 in Oliver RTD, Hendry WF, Bloom HJG, Bladder Cancer, Principles of Combination Therapy, Butterworths, London, p. 9-18, 1981.

11. Farrow GM, Utz DC, Rife CC, Greene LF, Clinical Observations in 69 Cases of *in situ* Carcinoma of the Urinary Bladder, Cancer Res 37:2794-98, 1977.

12. Farrow GM, Pathologist's Role in Bladder Cancer, Seminars in Oncol, 6:198-206, 1979.

13. Kennedy TJ, Flexible Cystoscopy, Urol Clin North Am, 15:525-8, 1988.

14. Soloway MS, Bicknell L, Role of Selected Mucosal Biopsy in the Evaluation of Patients with Bladder Cancer, in Bladder Cancer, Part A: Pathology, Diagnosis and Surgery, Alan R. Liss, New York, p. 275-81, 1984.

15. Bergkvist A, Ljungqvist A, Moberger G, Classification of Bladder Tumors Based on the Cellular Pattern. Preliminary Report of a Clinical-Pathological Study of 300 Cases with a Minimum Follow-up of Eight Years, Acta Chir Scand 130:371-78, 1965.

16. Pryor JP, Introduction to the Management of Superficial Bladder Tumors, Chapt. 6 in Oliver RTD, Hendry WF, Bloom HJG, Bladder Cancer, Principles of Combination Therapy, Butterworths, London, p. 59-61, 1981.

17. Hope-Stone HF, Blandy JP, Oliver RTD, England H, Radical Radiotherapy and Salvage Cystectomy in the Treatment of Invasive Carcinoma of the Bladder, Chapt. 15 in Oliver RTD, Hendry WF, Bloom HJG, Bladder Cancer, Principles of Combination Therapy, Butterworths, London, p. 127-38, 1981.

18. Jacobi GH, Thuroft JW, Prophylactic Intravesical Doxorubicin Instillation after TUR of Superficial Transitional Cell Tumours: 3 Years' Experience, Chapt 10 in Oliver RTD, Hendry WF, Bloom HJG, Bladder Cancer, Principles of Combination Therapy, Butterworths, London, p. 85--88, 1981.

19. Oliver RTD, Immunity in Malignant Disease, Chapt. 28 in Oliver RTD, Hendry WF, Bloom HJG, Bladder Cancer, Principles of Combination Therapy, Butterworths, London, p. 263-77, 1981.

20. Morales A, Intravesical and Systemic BCG Treatment for superficial Bladder Cancer: Results and Method of Evaluation, Chapt. 31 in Oliver RTD, Hendry WF, Bloom HJG, Bladder Cancer, Principles of Combination Therapy, Butterworths, London, p. 297-304, 1981.

21. Murphy WM, Nagy GK, Rao MK, Soloway MS, Parija GC, Cox CE, Friedel GH, "Normal" Urothelium in Patients with Bladder Cancer, in Bladder Cancer Part A: Pathology, Diagnosis and Surgery, Alan R. Liss, New York, p. 275-81, 1984.

22. Wallace DMA, Hindmarsh JR, Webb JN, Busuttil A, Hargrave TB, Newsam JE, Chisholm GD, The Role of Multiple Mucosal Biopsies in the Management of Patients with Bladder Cancer, Br J Urol 51:535-40, 1979.

23. Soloway MS, Bicknell L, Role of Selected Mucosal Biopsy in the Evaluation of Patients with Bladder Cancer, in Bladder Cancer Part A: Pathology, Diagnosis and Surgery, Alan R Liss, p 275-81, 1984.

24. Paulson DF, Avoiding Complications with Radical Cystectomy in Bladder Cancer Part A: Pathology, Diagnosis and Surgery, Alan R Liss, New York, p 409-34, 1984

25. Alfano RR, Tang GC, Pradhan A, Lam W, Choy DSC, Opher E, Fluorescence Spectra from Cancerous and Normal Human Breast and Lung Tissues, IEEE JQE QE23:1806-11, 1987.

26. Kapadia CR, Cutruzzolo FW, O'Brien KM, Stetz ML, Enriquez R, Deckelbaum LI, Detection of Adenomatous Transformation of Colonic Mucosa by Fiber-Optic Laser-Induced Fluorescence Spectroscopy, (Abstract), Gastroenterol 94:A216, 1988.

27. Yuanlong Y, Yanming Y, Fuming L, Yufen L Paozhen M, Characteristic Autofluorescence for Cancer Diagnosis and its Origin, Lasers in surgery and Medicine 7:528-32, 1987.

28. Wolfbeiss OS, Leiner MJ, Mapping of the Total Fluorescence of Human Blood Serum as a New Method for its Characterization, Anal Chim Acta 167:203-15, 1985.

29. Chung-Ho S, Duzman E, Mellott J, Liaw LH, Berns MW, Spectroscopic, Morphologic and Cytotoxic Studies on Major Fractions of Hematoporphyrin Derivative and Photofrin II, Lasers in Surgery and Medicine 7:171-79, 1987.

30. Richards-Kortum RR, Mehta AV, Hayes G, Cothren R, Kolubayev T, Kittrell C, Ratliff NB, Kramer JR, Feld MS, Spectral Diagnosis of Atherosclerosis Using an Optical Fiber Laser Catheter, American Heart Journal, 118:381-91, 1989.

31. Keijzer M, Richards-Kortum R, Jacques SL, Feld MS, Fluorescence Spectroscopy of Turbid Media: Autofluorescence of Human Aorta, Applied Optics 28:4286-92, 1989.

32. Cothren RM, Richards-Kortum RR, ... Gastrointestinal Endoscopy, in press.

33. Bent DV, Hayon E. Excited State Chemistry of Aromatic Amino Acids and Related Peptides. III. Tryptophan. J Am Chem Soc 1975; 97:2612-19.

34. Van Assendelft OW. Spectrophotometry of Hemoglobin Derivatives. Royal Vangorcum Ltd, Assen, The Netherlands, p. 58, 1970.

35. Campbell ID, Dwek R. Biological Spectroscopy. Benjamin Cummings Publishing Co., P. 69-70, 1984.

36. Schwartz JP, Possoneau JV, Johnson GS, Pastan I. The Effect of Growth Conditions on NAD+ and NADH Concentration and the NAD+:NADH Ratio in Normal and Transformed Fibroblasts. J Biol Chem 1974; 249:4138.

37. Merril AH, Henderson JM. Diseases Associated with Defects in Vitamin B6 Metabolism. Ann. Rev. Nutr. 1987; 7:137-156.

38. Yuanlong Y, Yanming Y, Fuming L, Yuten L, Paozhong M. Characteristic Autofluorescence for Cancer Diagnosis and its Origin. Lasers in Surgery and Medicine 1987; 7:528-32.

6: Conclusions and Future Directions

6:1: Summary of Results

In summary, we have demonstrated that fluorescence spectroscopy has the potential to improve current methods of diagnosis (and ultimately therapy) for three specific diseases: atherosclerosis, dysplasia in ulcerative colitis and transitional cell carcinoma (TCC) in the urinary bladder. This thesis has shown that, in these tissues, it is possible to spectroscopically diagnose the presence of pathology based on its histochemical features in near real time with a method that can easily be utilized *in vivo*. It is important to note that these algorithms were developed using a general, stepwise method, which can easily be applied to detecting disease in any tissue system.

In the following sections, the important conclusions which can be drawn from the application of this method to each of the three clinical conditions will be summarized. Future studies and experiments to improve these methods will then be proposed.

6:1.1: Chapter Three - Detection of Atherosclerosis

The method of algorithm development outlined in Chapter One was applied to the problem of diagnosing atherosclerosis in the elastic and muscular arteries. Fluorescence EEMs of normal and atherosclerotic muscular and elastic arteries demonstrated that three excitation wavelength regions were optimal for identifying atherosclerosis: 310, 350 and 450 ± 10 nm.

Much more extensive studies of the fluorescence properties of these tissues were carried out at 476 nm excitation. A combination of fluorescence and light microscopic studies showed that, in both elastic and muscular arteries, the primary structures contributing to the fluorescence spectrum were collagen fibers, elastin fibers and ceroid. The fluorescence lineshapes of these structures were measured at 476 nm excitation *in vitro* in aorta. In addition, it was demonstrated that the attenuation of these structures as well as oxy-hemoglobin contributed to the fluorescence spectrum of these tissues. These attenuation spectra were measured *in vitro* for aorta at 476 nm excitation.

A general, one-layer model of tissue fluorescence was developed and was applied to the 476 nm excited LIF spectra of these tissues, in order to extract parameters proportional to the concentration of structural proteins, ceroid and oxy-hemoglobin from

the fluorescence spectra. The structural protein and ceroid parameters formed the basis for diagnostic algorithms for the presence of atherosclerosis in these tissues. In elastic arteries, normal vessel wall could be differentiated from atherosclerotic vessel wall with a high degree of accuracy. In muscular arteries, normal vessel wall, non-calcified atherosclerotic plaque and calcified atherosclerotic plaque could be differentiated with a high degree of accuracy. Statistically optimized algorithms based on these parameters were derived for the presence of non-calcified and calcified atherosclerotic plaque in muscular arteries.

Studies of the 476 nm excited fluorescence properties of elastic and muscular arteries were conducted *in vivo*. In these studies it was established that fluorescence spectra with reasonable S/N could be obtained *in vivo* quickly, and that the fluorescence properties of normal and atherosclerotic vessel wall were similar *in vivo* and *in vitro*, except for differences in the relative contribution of oxy-hemoglobin attenuation to the fluorescence spectra. In addition, it was shown that the model of tissue fluorescence developed *in vitro* could be applied to fluorescence spectra of muscular arteries collected *in vivo*. Diagnosis of atherosclerosis based on the decision surfaces developed *in vitro* was in relatively good agreement with angioscopic assessment of tissue type.

6:1.2: Chapter Four - Detection of Dysplasia in Ulcerative Colitis

The method of algorithm development presented in Chapter One was applied to the problem of diagnosing dysplasia in ulcerative colitis. Initial studies with fluorescence EEMs were carried out *in vitro* utilizing normal colon and non-neoplastic colon with ulcerative colitis as models of non-neoplastic colon, and adenomatous polyps from patients with familial adenomatous polyposis as a model of dysplasia. These studies showed that the excitation regions of 290, 330, 370 and 430 ± 10 nm were optimal for identifying the presence of dysplasia.

More extensive studies of colon fluorescence were carried out at 370 nm excitation. *In vitro*, it was shown that empirical algorithms based on the fluorescence intensities at 480 and 680 nm could be used to differentiate normal colon from adenomatous polyps in patients with familial adenomatous polyposis. Fluorescence spectra were collected *in vivo* at this excitation wavelength from many samples of normal colon, sporadic adenomatous polyps and hyperplastic polyps. It was shown that a similar diagnostic algorithm, based again on fluorescence intensities at 460 and 680 nm, could be used to differentiate adenomatous polyps from normal colon and hyperplastic

polyps. This algorithm was statistically optimized, and was discussed in terms of the incidence of dysplasia expected to be encountered in several clinical settings.

The histochemical basis of fluorescence of these tissues at 370 nm excitation was investigated *in vitro* using fluorescence and light microscopy. It was demonstrated that collagen fibers in the submucosa and the lamina propria contributed to the fluorescence spectrum in the blue region. Eosinophils present in the lamina propria contributed in a more yellow region of the spectrum, and the cytoplasm of dysplastic epithelial cells contributed in the green region of the spectrum. Using a fluorescence microspectrofluorimeter, emission spectra were recorded from each of these structures: the fluorescence of collagen fibers in the submucosa and normal lamina propria exhibited a single maximum at 430 nm, while that of collagen fibers in the lamina propria of adenomas peaked near 460 nm. The fluorescence spectrum of eosinophils exhibited a single maximum at 480 nm. The fluorescence spectrum of dysplastic epithelial cells peaked near 520 nm, consistent with the emission spectrum of pyridoxal 5'-phosphate. In addition, the attenuation of oxy-hemoglobin and structural proteins was determined to be important from an examination of tissue total reflectance spectra. These identifications could be correlated to the various maxima in the spectra of these tissues obtained *in vitro* with the spectral catheter. Furthermore, it was shown that with these identifications, the general, one-layer model of tissue fluorescence could be used to interpret these spectra quantitatively.

6:1.3: Chapter Five - Detection of TCC in Urinary Bladder

The method of algorithm development presented in Chapter One was finally applied to the problem of diagnosing the presence of TCC in the urinary bladder. Here, the fluorescence properties of both normal and inflammatory bladder were compared to that of several forms of TCC using fluorescence EEMs. These studies were conducted *in vitro*, and showed that either three or four excitation wavelength regions could be used to sample all the diagnostically relevant information in the UV and visible portions of the spectrum. These regions include 290, 330 and 430 nm ± 10 nm, or 290, 330, 400 and 460 nm ± 10 nm.

Fluorescence spectra were obtained at 290, 330 and 476 nm excitation *in vitro* from normal and inflammatory urinary bladder and several stages of TCC, using the conventional spectrofluorimeter. Empirical algorithms were defined from this data, in an attempt to differentiate these three classes of tissue. At 290 nm excitation, only normal

bladder could be differentiated effectively from inflammatory bladder and bladder with TCC. At 330 nm excitation, bladder with TCC could be accurately differentiated from normal and inflammatory bladder. However, at 476 nm excitation, algorithms could be defined to separate all three classes of tissue.

Spectra of several tissue samples were also obtained with the spectral catheter at 330 and 430 nm excitation. These were compared to those obtained with the conventional fluorimeter to illustrate the superiority of the catheter based fluorimeter.

6:2: Future Directions

6:2.1: Proposed Studies and Experiments

This thesis has demonstrated an effective method for developing spectroscopic diagnostic algorithms for the presence of pathology in a variety of tissues. However, there are many improvements that could be made in the general method. Some of these include:

- Improve the conventional spectrofluorimeter used to record tissue spectra and fluorescence EEMs *in vitro* in order that its collection geometry is well defined and the same as that of the spectral catheter.

- Improve our method of extracting information from tissue fluorescence EEMs. First, the simple one layer model of tissue fluorescence based on exponential attenuation of light can be applied at all excitation wavelengths sampled in the EEM. The application of this model will make it possible to quantitatively extract contributions to the EEMs of various fluorophores and attenuators. In addition it will make it possible to study the apparent asymmetry noted in the contributions of attenuation to excitation and emission spectra.

- Improve the simple models of tissue fluorescence presented in Chapter Two. Primarily this would consist of treating light attenuation in a more sophisticated method. Two models to be considered include the transport equation with and without the diffusion approximation.

- Develop more sophisticated methods of studying tissue fluorescence *in vivo* - both at single excitation wavelengths or at many excitation wavelengths as in an EEM. In both arterial and gastro-intestinal tissues, differences were reported in

the fluorescence spectra obtained *in vivo* and *in vitro*. Collecting all data *in vivo* represents one possible method of avoiding this complication. Alternatively, better methods of tissue handling *in vitro* could be developed in an attempt to avoid these differences. For example, using oxygenated perfusion solutions, it may be possible to keep excised tissues alive for periods of several hours.

• Develop methods of spectroscopic imaging, which can be applied to implement spectroscopic diagnostic algorithms for pathology over larger surface areas of tissue than can be sampled with the spectral catheter.

In addition to these improvements in the general method, there are many studies required to develop the algorithms presented here for clinical use *in vivo*. These are summarized below for each disease studied in this thesis.

6:2.1.1: Atherosclerosis

Although effective diagnostic algorithms for the presence of atherosclerosis were developed with 476 nm excitation *in vitro* much work remains to be done. Proposed studies include:

• Studying the other excitation regions indicated by the EEMs in detail, and relating this information to that which can be obtained at 476 nm excitation.

• Applying more sophisticated models of tissue fluorescence, including the two layer model presented in Chapter Two, or models eventually developed with more sophisticated treatments of light attenuation.

• Conducting studies of arterial fluorescence *in vivo*, in which the results of the algorithm classification of tissue type can be compared to that determined histologically.

• Conducting studies of 476 nm excited LIF *in vivo* in order to determine whether this technique can be used to measure ceroid and calcium content *in vivo* to predict those lesions treated with PTCA that are most likely to restenose.

• Conducting studies of 476 nm excited LIF *in vivo* in an animal model to study the progression of atherosclerotic lesions.

- Conducting studies of 476 nm excited LIF in order to determine whether this technique can be used *in vivo* to guide laser angiosurgery catheters, in order to prevent arterial perforation during this technique. Before clinical trials of these combined techniques can be conducted, several *in vitro* studies are required, including:

    - Determine the decision surface in order to separate atherosclerotic plaque from underlying media in muscular arteries.

    - Determine the effects of laser ablation at the ablation wavelength of interest on the spectroscopic properties of normal muscular artery, non-calcified and calcified plaque.

    - Given the results of these two studies, develop an algorithm which can be used to control laser ablation of atherosclerotic plaque in muscular arteries. Apply this algorithm first in intact arteries *in vitro*, then ultimately *in vivo*.

6.2.1.2: Dysplasia in Ulcerative Colitis

Effective, empirically derived, spectroscopic diagnostic algorithms were developed at 370 nm excitation for the presence of adenomatous polyps both *in vitro* and *in vivo*. In order to achieve our final goal of diagnosing dysplasia in ulcerative colitis with this method several steps remain to be taken. These include:

- Extending our EEM studies to include dysplastic colon in ulcerative colitis patients in order to determine whether the optimal excitation wavelengths have been established for diagnosing dysplasia in this condition.

- Applying the simple model of colon tissue fluorescence presented in Chapter Four to the 370 nm excited spectra collected with the spectral catheter *in vitro* and *in vivo*. Developing histochemically based algorithms from these model parameters should provide improved algorithms for the identification of adenomatous polyps.

- Increasing the number of hyperplastic polyps studied *in vivo* at 370 nm excitation in order to determine whether the algorithms developed at this excitation wavelength can accurately differentiate these tissues.

• Studying the 370 nm excited LIF properties of non-neoplastic and dysplastic colon from patients with MUC in more detail. It is necessary to determine if any modifications need to made to the algorithms presented here for differentiating adenomatous polyps from hyperplastic polyps and normal colon.

• Studying the other excitation wavelength regions indicated from the tissue EEMs in more detail to determine whether this information can be used separately, or in conjunction with 370 nm excitation in order to improve the diagnostic capability of this technique.

6:2.1.3: TCC in Urinary Bladder

In this system, although several preliminary studies were carried out, many steps remain in order to achieve a clinically useful diagnostic algorithm for TCC in the urinary bladder. Many of these steps are simply related to carrying out the methods developed in Chapter One to completion. They include:

• Record spectra of many samples of urinary bladder *in vitro* at 476 nm excitation using a spectral catheter system. Develop empirical diagnostic algorithms for the presence of inflammation and TCC.

• At 476 nm excitation, determine the histochemical basis of urinary bladder fluorescence. Utilize this in order to model tissue spectra obtained at this excitation wavelength. Develop diagnostic algorithms for inflammation and TCC based on the parameters of this model.

• At this excitation wavelength, obtain fluorescence spectra of normal and neoplastic bladder *in vivo*. Compare these spectra to those obtained *in vitro*, and determine whether algorithms and models developed *in vitro* need to be modified for clinical application.

• Determine whether the other excitation wavelength regions indicated from the EEMs provide significantly different diagnostically useful information.

6:2.2: New Diseases

It is important to note that the method of algorithm development presented in this thesis is a general one, which can easily be applied to detecting disease in any tissue system. In particular, it would be of particular value to investigate other epithelial

neoplastic diseases, in order to determine whether the similarities noted in neoplasms of urinary bladder and the colon are more general in nature.

6:3: Conclusions

In conclusion, it appears that fluorescence spectroscopy may become an important adjunct to pathology in diagnostic medicine. It promises to be particularly useful in those clinical situations where the use of pathology is limited because potentially diseased tissue cannot be located or removed. We have shown here that fluorescence spectroscopy can be used to non-invasively sample some features of the histochemical composition of tissue. In addition to providing this information, ultimately, fluorescence spectroscopy may be used to sample features of disease that pathology currently cannot. Respiration, metabolism, ischemia, and even necrosis can all potentially be monitored non-invasively as a function of time with spectroscopy by studying NADH, NAD(P)H, the flavins, ceroid and/or oxy-hemoglobin for example. This additional information may provide even better methods of diagnosis as well as expanding our knowledge of the etiology and pathogenesis of various diseases.